DEVELOPMENT AND APPLICATION OF ELECTROCHEMICAL SENSORS FOR STUDYING NEUROMUSCULAR SIGNALING IN THE GASTROINTESTINAL TRACT

By

Skye Antoinette Henderson

A DISSERTATION

Submitted to
Michigan State University
in partial fulfillment of the requirements
for the degree of

Chemistry – Doctor of Philosophy

2023

ABSTRACT

Alzheimer's disease (AD) is the most common cause of dementia and is hallmarked by the presence of amyloid beta (Aβ) plaques and neurofibrillary tangles which cause memory deficits and gradual cognitive decline. Studies looking at AD typically focus on central nervous system dysfunction, however, there has been an increasing number of studies that suggest the gut is involved in AD pathology. The enteric nervous system is a division of the autonomic nervous system that contains specific neural networks to control important gastrointestinal tract function such as digestion, motility, nutrient absorption, blood flow, and secretion. Intestinal motility is regulated through the synchronized activity of enteric neurons, interstitial cells of Cajal, and smooth muscle cells which lie within the musculature of the gastrointestinal (GI) tract. Acetylcholine is released from excitatory motor neurons to contract smooth muscle while nitric oxide and ATP—or a similar purine—are released from inhibitory motor neurons to relax smooth muscle. Disruption in these signaling mechanisms which mediate the peristaltic reflex could lead to GI dysfunction in AD.

Electrochemical tools are incredibly useful for studying neurotransmission events owed to their spatial and temporal resolution. To determine if nitric oxide or acetylcholine release is altered in AD, we measured the real time release of nitric oxide and acetylcholine from mouse myenteric ganglia *in vitro* using electrochemical sensors and pharmacological tools. Nitric oxide was detected directly as oxidation current using continuous amperometry along with a boron-doped diamond microelectrode modified with platinum (Pt) nanoparticles and a Nafion coating. Acetylcholine/choline was detected using an enzyme-based sensor which consisted of a platinized-Pt microelectrode modified with a permselective poly(*m*-phenylenediamine) coating and multienzyme film consisting of choline oxidase and acetylcholinesterase immobilized using inert

protein bovine serum albumin and glutaraldehyde to cross-link the amino groups of the enzymes together. We applied these sensors *in vitro* to determine if nitrergic or cholinergic neuromuscular signaling are altered in a 5xFAD and APP/PS1 transgenic mouse model, which mimic major AD pathology. This work focuses primarily on the development, characterization, and application of these sensors *in vitro*. We also report on the development and characterization of an enzyme-based ATP biosensor and preliminary data using optogenetics and blue light stimulation for the selective stimulation of nitrergic neurons from a $NOS1^{cre}$/ROSA transgenic mouse and electrochemical detection of nitric oxide using the modified BDD microelectrodes. This work is foundational is better understanding the neural circuitry which mediates GI motility.

ACKNOWLEDGEMENTS

I would like to acknowledge my advisor, Dr. Greg Swain and my committee: Dr. Gary Blanchard, Dr. Liangliang Sun, and Dr. Jim Galligan for their guidance and support throughout my project. A special thank you Dr. Galligan and his group for welcoming me into their group and treating me as one of their own: especially Dr. Hui Xu, who was a wizard and could magically find a solution to almost any problem, and Roxanne Fernandes, whose hard work kept the lab running and operational. Thank you to Dr. Serban Peteu: you were a great mentor and I appreciate your willingness to pass down your many years of knowledge. Thank you to the IPSTP program and the faculty who ran it: the knowledge I gained throughout this training grant was invaluable and the program was such a positive experience. Thank you to my group members, whose company made the last five years much more tolerable: Dr. Sarah McFall-Boegeman, Dr. Jack Walton, Dr. Fatemeh Parvis, Isuri Dammulla, and Shashika Sabaragamuwejayasundara. I can't wait to see what you all accomplish in your careers.

Thank you to my family and friends for their support over the years. I wouldn't be able to do this without you. A very special thank you to my husband Austin, who has stuck by my side through thick and thin. You helped keep me sane through the craziness that is grad school, whether that be staying up late with me while writing into the night, going on emergency coffee runs, or acting as a sound board to vent. You are my rock.

Lastly, thank you to my dad: I wish you could have been here to see me complete this, but I hope I made you proud.

TABLE OF CONTENTS

CHAPTER 1. INTRODUCTION

1.1 Enteric Nervous System

The enteric nervous system (ENS) is a division of the peripheral nervous system containing 400-600 million neurons that form an intricate circuitry for controlling gastrointestinal (GI) tract activity.[1] The ENS is responsible for directing motility patterns, regulating the peristaltic reflex, controlling fluid balance between the gut lumen and body fluid compartments, regulating blood flow and gastric secretion, facilitating nutrient absorption, and interacting with the immune and endocrine systems of the gut.[1,2] Commonly referred to as the "brain in the gut," The ENS is unique in that it contains its own population of sensory neurons, which allows it to mediate reflex responses independently of central nervous system (CNS) input.[2] GI motility, or the coordinated contraction and relaxation of muscles used to mix and propel food content in the gut, is controlled through the synchronized activity of enteric neurons, interstitial cells of Cajal (ICCs), and smooth muscle cells which lie within the musculature of the GI tract.[2,3] ICCs serve as a non-neuronal pacemaker system, in which slow electrical waves are generated that are electrically coupled to smooth muscle.[3] Enteric neurons, enteric glial cells, and ICCs are clustered within two types of ganglia: the submucosal plexus and the myenteric plexus, which can be seen in Figure 1.1.

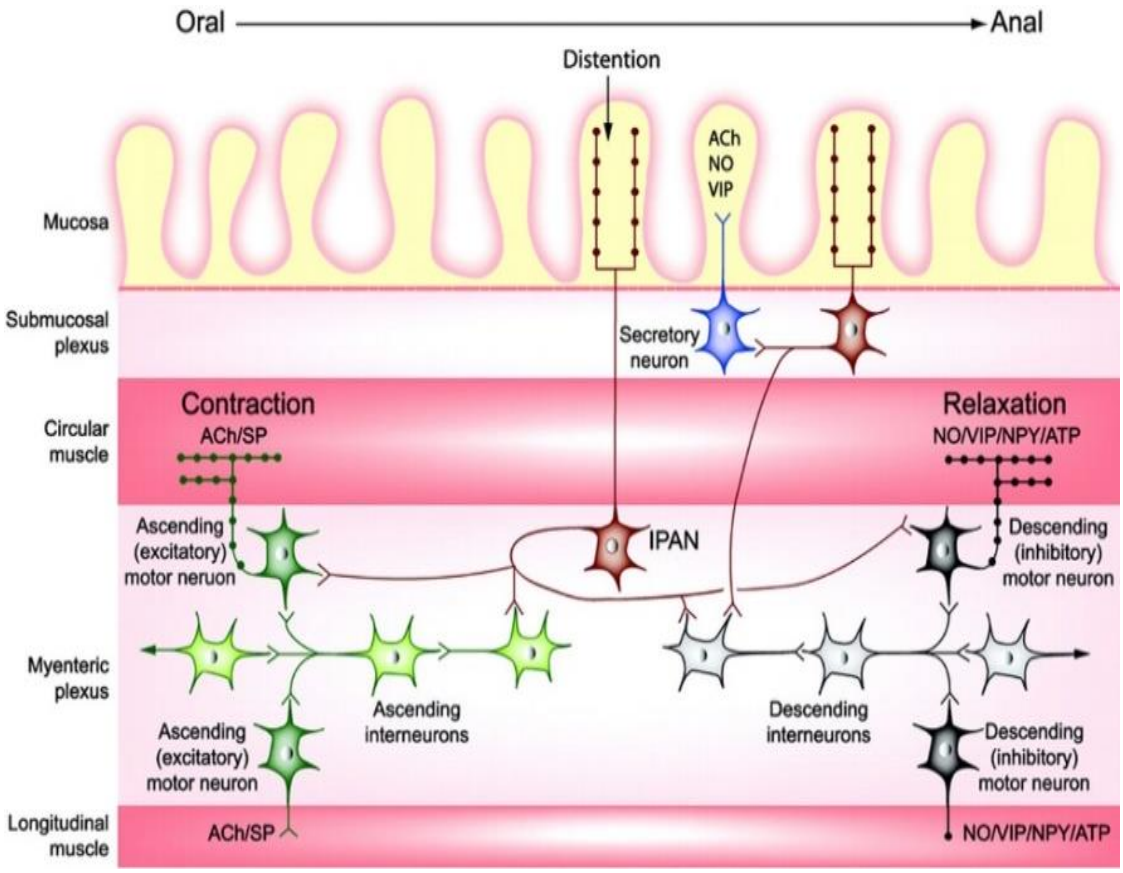

Figure 1.1. Schematic showing the different layers of the gastrointestinal tract and the neural circuitry involved in enteric reflexes. A stimulus activates IPANS in the submucosal plexus and myenteric plexus to synapse with interneurons, motor neurons, and sensory neurons in both the oral and anal direction to produce a contraction or relaxation response, aiding in peristalsis. Reproduced from Ref[4] with permission from Wolters Kluwer Health, Inc.

The submucosal plexus lies within the connective tissue of the submucosal gut layer and regulates mucosal secretion and blood flow. The myenteric plexus is sandwiched between the longitudinal and circular muscle layers in the outermost gut wall and controls smooth muscle activity.[1] Enteric neurons are categorized by their function and include afferent (or sensory) neurons, interneurons, and motor neurons.[5] Intrinsic primary afferent neurons (IPANs) have cell bodies located in the submucosal plexus and myenteric plexus with nerve fibers that project to the intestinal mucosa.[5] Motor reflex is triggered when IPANs receive a chemical or mechanical stimulus to project nerve impulses to interneurons and motor neurons.[5] Interneurons can be either

ascending or descending, and act to either orally activate excitatory motor neurons or aborally activate inhibitory motor neurons. Motor neurons in the longitudinal and circular muscle layers act as the final output pathway to produce an excitatory (contraction) or inhibitory (relaxation) response that aids in propulsion.[5] The primary excitatory neurotransmitter released at the neuromuscular junction is acetylcholine (ACh) acting on muscarinic receptors on the surface of smooth muscle.[6] The primary inhibitory neurotransmitters released at the neuromuscular junction are nitric oxide (NO) and ATP, the latter binds to guanylate cyclase and $P2Y_1$ receptors expressed by smooth muscle cells, respectively.[7-9] It has been argued that β-nicotinamide adenine dinucleotide (β-NAD), or another purine, serve as the purinergic transmitter at inhibitory neuromuscular junctions, rather than ATP, however these claims are controversial as they often rely on indirect evidence and thus remain inconclusive.[10-13]

1.2 Neurogenic Dysfunction in the ENS and the Gut Brain Connection

A properly regulated ENS is critical to one's health, and any dysfunction in signaling could result in a wide range of enteric neuropathies. These neuropathies are typically congenital, developmental, sporadic, associated with other disease states, or drug induced such as constipation caused as a side effect of narcotics.[1,3] GI diseases have a strong impact on today's healthcare system. In 2015, annual healthcare expenditures totaled $135.9 billion for GI conditions and are expected to grow.[14] Motility based gastrointestinal disorders—such as gastroparesis, irritable bowel syndrome, and chronic constipation—affect more than 20% of the general population and can have a dramatic impact on the patient's quality of life.[15] It is important to understand the neural circuitry and the mechanisms by which neurogenic gut motility is regulated to explain and potentially treat functional GI disorders.

The gut is controlled through both intrinsic and extrinsic innervation. Intrinsic innervation

is achieved through the integrated system of neurons in the submucosal and myenteric plexus while extrinsic innervation is achieved through splanchnic (sympathetic) and vagal-sacral (parasympathetic) nerves.[16] The vagus nerve is the major pathway that connects the gut to the brain, and relays information between the viscera and brain stem, innervating the entire gut down to the mid colon.[16] There is constant bidirectional communication between the gut and brain. This communication is essential for proper maintenance of GI homeostasis and digestion as well as emotional and cognitive function.[17] On the other hand, these afferent and efferent nerves which connect the brain to the gut could also act as a conduit for disease to spread from one system to the other.[18] For instance, there has been growing evidence of the involvement of the ENS with diseases that primarily affect the CNS such as Autism, Parkinson's disease (PD), Alzheimer's disease (AD), and amyotrophic lateral sclerosis.[18]

The GI abnormalities that manifest in PD, a debilitating condition causing tremors and rigidity, have long been studied. The main hallmark of PD is the loss of dopaminergic neurons in the substantia nigra and presence of α-synuclein containing cytoplasmic inclusions called Lewy bodies. These aggregates of misfolded α-synuclein have also been found in the ENS, and appear before manifesting in the brain.[19] The bulk of the work done on PD research involving the gut is an extension on Braak's hypothesis, which was put forward about 20 years ago. This hypothesis states that sporadic PD is caused by an unknown pathogen that enters the body through the nasal cavity, is subsequently swallowed thereby reaching the gut and initiating Lewy pathology, and then spreading to the brain via the vagus nerve.[20,21] Although there is much clinical and experimental evidence supporting Braak's hypothesis including GI symptoms such as constipation, loss of smell implying olfactory involvement, presence of Lewy bodies in the olfactory tract, and severe Lewy pathology in the gut positively correlating with constipation and motor impairment, there are still

criticisms.[22]

The connection between AD and the gut is much less studied than it is in PD. AD is another neurodegenerative disease resulting in a gradual decline in memory and cognition, eventually leading to the inability to perform even the most basic of daily tasks. AD is hallmarked by the presence of extracellular amyloid β (Aβ) plaques and Tau protein tangles, which are used for pathological diagnosis.[23] Aβ is formed as a cleavage product from the amyloid precursor protein (APP), which is a glycoprotein that plays an important role in neuronal development, neurotransmission, intracellular transport, and neuronal homeostasis.[24] APP is cleaved by β-secretase and γ-secretase, and the Aβ peptides that are formed can rapidly aggregate to form oligomers, protofibrils, and fibrils which become insoluble and lead to the deposition of amyloid plaques and neurotoxicity.[24] Tau neurofibrillary tangles, on the other hand, are formed when the highly soluble Tau protein becomes hyperphosphorylated and misfolded, disrupting its critical role in tubulin assembly and stabilization of microtubules.[25] AD-related protein deposition, changes in intestinal function, and dysbiosis have all been indicated in various transgenic mouse models that mimic major AD pathology.[26-28] In one study, intra-GI administration of Aβ oligomers into a general-purpose strain of mice lead to Aβ aggregation in the brain, most likely through the vagus nerve, causing memory impairments.[29]

1.3 Electrochemical Tools in Neurochemical Analysis

Electrochemical techniques have been used to detect neurotransmitters for decades. Neurochemical sensing is a hot topic in the field of neuroscience as the disruption of normal neurosignaling events can lead to the development of a host of neurological disorders including AD, PD, Huntington's disease, clinical depression, and schizophrenia among many others.[30] Accurate and sensitive detection of signaling molecules in an *in vitro* or *in vivo* setting is critical

for better understanding the complex neural circuitry which controls basic to complex neurological function as well as examining how neurotransmission may be altered in a diseased state. Ideally, such a technique would be minimally invasive, inexpensive, and possess sufficient spatial and temporal resolution such that the dynamic events of neurotransmitter release could be captured near the sites of release. HPLC-combined with microdialysis sampling is a common technique for probing neurotransmission. Microdialysis involves inserting a dialysis probe with a semipermeable membrane into the brain tissue or region of interest. The probe is then perfused with an electrolyte that mimics the ionic composition of the extracellular fluid. Molecules of interest can then freely diffuse across this semipermeable membrane and flow with the perfusate to the outlet to be separated and detected. Although this method offers excellent selectivity, temporal resolution is at best one minute.[31] Because of this limited temporal resolution, this technique is unable to capture the rapid dynamics of neurotransmission and instead is better suited for measuring basal levels of neurotransmitters over prolonged periods of time.[31] Furthermore, microdialysis probes are somewhat large—usually hundreds of micrometers wide—making spatial resolution limited.[31] Moreover, a larger probe entails a greater risk of causing tissue damage upon surgical insertion.[31] Microelectrode sensors, however, offer minimal tissue damage and excellent spatial resolution, as they possess critical dimensions typically ≤ 25 μm in size.[32] These electrode diameters can shrink even more down to the nanometer range, but once the critical dimension becomes approximately equal to the thickness of the double layer (~10 nm), experimental behavior and electrochemical theory deviates.[32]

Many neurotransmitters such as dopamine (DA), norepinephrine (NE), and serotonin (5-HT) contain phenol groups or other electron-rich functional groups that can be readily oxidized with the appropriate overpotential. In cases where neurotransmitters such as ACh and glutamate

cannot be oxidized or reduced, an enzyme-based sensor can be utilized. These sensors typically involve the coating of an oxidase enzyme, which generates reactive oxygen species like hydrogen peroxide, which can then be oxidized (or reduced) at the electrode interface.[31,33] This voltammetric current can then be used to identify and quantify neurotransmitters. When miniaturizing the electrode to the micro or nanometer scale, this technique offers excellent spatial and temporal resolution and becomes the method of choice for detecting neurotransmitters near their sites of release and action.

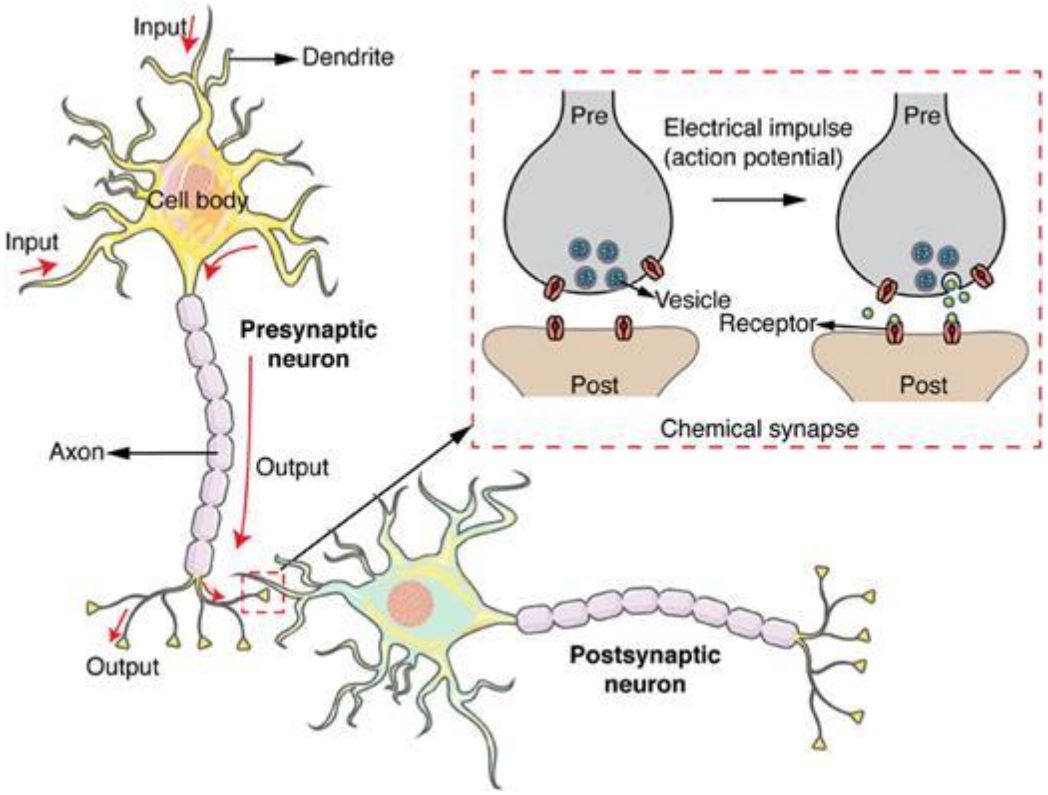

Figure 1.2. Schematic showing neurotransmission between a presynaptic and postsynaptic neuron. An electrical impulse or action potential triggers the exocytotic release of neurotransmitters from the axon terminal across the synaptic cleft. These neurotransmitters can then bind to receptors on the postsynaptic cell. Reproduced from Ref[31] with permission from the American Vacuum Society.

Chemical signaling or neurotransmission occurs from neuron to neuron or from neuron to effector cell. This process can be seen in Figure 1.2. Neurotransmitters are synthesized and stored in vesicles in the presynaptic neuron. Chemical signaling is triggered when an action potential

reaches the presynaptic terminal, and the depolarization causes Ca^{2+} channels to open. The sudden influx of Ca^{2+} into the presynaptic terminal then promotes the migration and fusion of vesicles to the presynaptic membrane. The neurotransmitters stored in those vesicles are released through exocytosis into the synaptic space.[34] (Frohlich 2010). Not all neurotransmitters are stored in vesicles and released through exocytosis, however. For example, NO is synthesized on demand by neuronal nitric oxide synthase (nNOS) in response to an action potential generation.[35] When neurotransmitters are released across a synaptic cleft, they can either bind to receptors on these post-synaptic neurons, become metabolized or recycled by esterases and transporters, or simply diffuse away.[36] If the neurotransmitter binds to a receptor on another neuron, the generation of an additional action potential can either be promoted (from an excitatory input) or inhibited (from an inhibitory input).[34] Whether the response is excitatory or inhibitory depends on the neurotransmitter that is released. As these synaptic clefts are only about 13-16 nm wide.[37] it is uncommon to probe neurotransmitter release from individual synapses unless using carefully fabricated nanoelectrodes.[38] Most measurements probe the spillover of neurotransmitters into the extracellular space from release of multiple neurons.

There are two electrochemical methods that are most used in neurochemical analysis: continuous amperometry (CA) and fast scan cyclic voltammetry (FSCV). In both methods, either the electroactive neurotransmitter or enzymatically generated electroactive product is oxidized or reduced. These electrochemical reactions are carried out at the working electrode in either a three electrode (CA) or two electrode (FSCV) system. In both techniques, a reference electrode (usually an Ag/AgCl electrode) is used to control the potential that is applied to the working or sensing electrode. For CA, a third auxiliary or counter electrode is used to act as electron sink to balance current gained or lost at the working electrode. As current passed at ultramicroelectrodes in FSCV

is so low, the reference electrode also acts as the counter electrode in these measurements.[39] In CA, a fixed potential is applied to a working or recording electrode and current flow is measured in respect to time. The potential which is applied is experimentally determined such that the rate of electrochemical oxidation or reduction of the analyte of interest is mass transport limited. The faradaic current measured is dependent on the flux of the analyte as well as any electroactive species to the electrode surface. Other experimental factors—such as electrode-tissue distance and convection—also affect the measured oxidation current and are controlled by the experimenter. This method offers excellent temporal resolution constrained only to the sampling time. However, CA is susceptible to local ionic concentration changes and selectivity is limited, which necessitates the use of pharmacological methods to help confirm the identity of the species being oxidatively or reductively detected. Data typically appears as a current spike which is dependent on the amount of neurotransmitter released, its corresponding rate of release, and the rate of clearance of that signaling molecule from the extracellular space. By integrating the peak area, one can determine the number of moles of analyte oxidized using Faraday's law:

$$Q = nFN$$

Where Q is the charge passed (coulombs), n is the number of electrons transferred per molecule in the electrochemical reaction, F is Faraday's constant, and N is the number of moles electrolyzed.

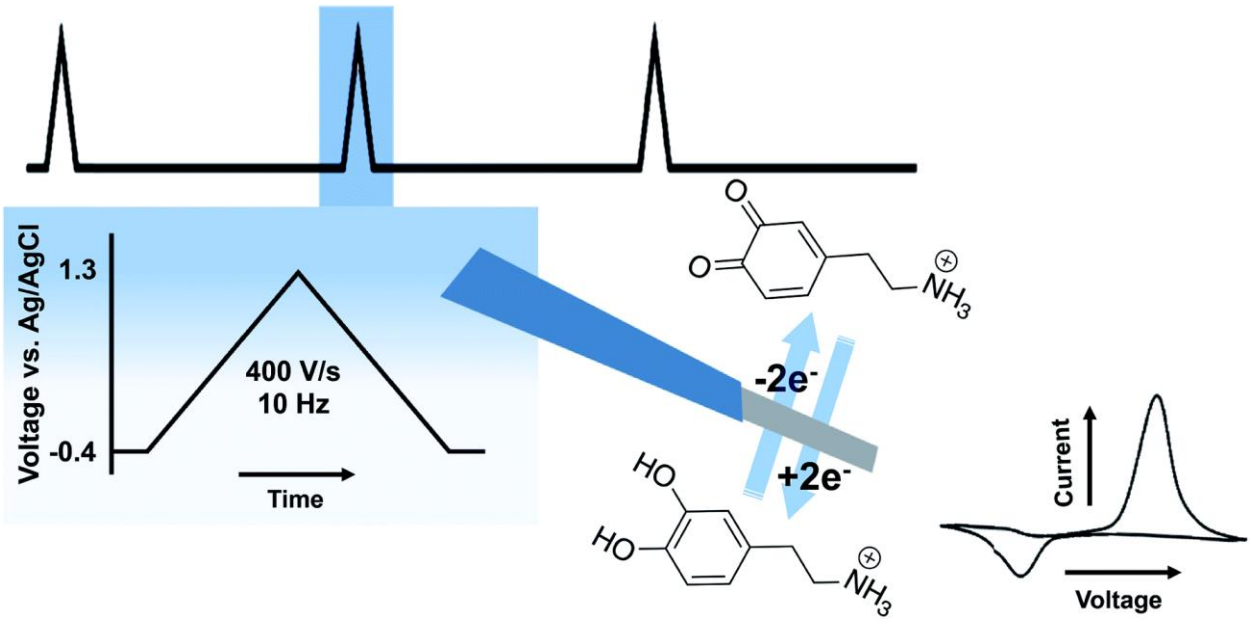

Figure 1.3. Schematic showing FSCV and its use for electrochemical detection of dopamine (DA). At the top is the waveform with the blue box showing the parameters used to generate the waveform. DA detection is achieved via a two-electron oxidation and two-electron reduction of the dopamine-*o*-quinone which is generated. A representative voltammogram can be seen on the right, which plots current in respect to the applied potential. Reproduced from Ref[36] with permission from the Royal Society of Chemistry.

FSCV on the other hand involves rapidly ramping the potential of a working electrode to a switching potential and then back, typically at scan rates in the range of hundreds of volts per second. This produces a voltammogram with an oxidation and reduction peak that can be used for both identification and quantification. An example of what kind of data is generated from these measurements can be seen in Figure 1.3. These oxidation and reductions peaks vary from typical voltammograms performed at lower scan rates in that the peaks are more spread out and the peak separation is larger. These peak distortions are owed to the increased scan rate, rate of electron transfer, and high current density at microelectrodes.[40] This results in a unique "fingerprint" for electrochemical compounds which varies based on the thermodynamic properties of the electroactive compound, respective rates of electron transfer, and chemical stability of the electrochemically oxidized or reduced products that can be used as qualitative data.[41] The

background or charging current, in which ions and solvent dipoles rearrange to counterbalance the charge at surface of the electrode, scales proportionally with scan rate and is consequently 10-100 times greater than faradaic currents for carbon fiber microelectrodes.[40] This necessitates the use of background subtraction to discriminate faradaic current from background current. Because this background subtraction makes FSCV a differential technique, it cannot be used to determine basal levels of neurotransmitters and instead functions more appropriately for measuring transient changes in neurotransmitter levels.[40] The amplitude of these background subtracted currents can be monitored in respect to time to obtain temporal information on neurotransmitter concentration changes with respect to time. Unlike CA, the extrapolated *i vs. t* traces cannot be integrated to determine the number of moles of analyte present. This is because the same redox molecules can be continually oxidized and reduced, therefore peak integration may count the same recycled molecule several times.[40] Although FSCV has better temporal resolution than analytical techniques which rely on microdialysis sampling, temporal resolution is less that of CA. Both techniques offer valuable information on the rate of neurotransmitter release and clearance. As these rates of release and clearance can be influenced by alterations in neurotransmitter release rate, changes in transporter function, autoregulation processes, metabolism, and use of pharmacological agents, electrochemical methods are a very useful tool for explaining the dynamics of specific signaling mechanisms and how those signaling mechanisms can be altered.[42]

1.4 Electrochemical Studies in the Gastrointestinal Tract

There are a limited number of studies which utilize electrochemical tools within the GI tract. As there are only a handful of electroactive compounds released in the gut, selectivity is often not an issue and therefore CA is typically utilized for these measurements.[42] The first record of using microelectrode sensors to monitor 5-HT overflow from enterochromaffin cells (ECs) in the gut was

done in the guinea pig ileum using Nafion coated carbon fiber microelectrodes.[43] The bulk of 5-HT (>90%) in the human body is produced by ECs which line the digestive tract.[44] As 5-HT release activates IPANs which project to enteric nerve circuits, the neurotransmitter plays an important role in regulating GI motility.[44] 5-HT is electrochemically oxidized through a multi-step two-electron, two-proton transfer, and increasing concentration of 5-HT is measured as oxidation current.[45,46] The Nafion film, which is a negatively charged ionomer, electrostatically repels anionic species, such as ascorbic acid and 5-HT metabolites, while attracting positively charged 5-HT.[43] Both mechanical stimulation through contact of the electrode with the mucosal epithelium and chemical stimulation through the application of ACh or carbachol were used to elicit 5-HT release, which was measured directly as oxidation current.[43] One caveat with this work is that carbon fiber microelectrodes are highly susceptible to electrode fouling.[47] Although the authors utilized a Nafion overcoat, an alternate electrode material that is resistant to electrode fouling would be a more practical solution.

Boron-doped diamond (BDD) is an excellent alternative to carbon fiber, especially for neurochemical analysis. Diamond is a sp^3 hybridized carbon structure that when made *p-type* by doping with boron, becomes conductive. Diamond has many beneficial properties including chemically inertness; low background current, which enhances the signal to background ratio and decreases detection limits; wide working potential window of solvent stability; good biocompatibility; resistance to molecular adsorption and biofouling; mechanical stability; and good electrochemical activity for a variety of redox systems and electrolyte media.[48,49] Marcelli and Patel[50] developed a unique approach for measuring extracellular 5-HT concentration by using a BDD microelectrode to detect 5-HT overflow from the colon and ileum using CA. They employed a distance-approach tactic for measuring 5-HT oxidation currents that was accomplished by

decreasing the electrode-tissue distance in a step-wise fashion. The natural log of the current can then be plotted as a function of the electrode-tissue distance. By taking the reciprocal of the slope of this fitted line, one can measure relative rates of 5-HT uptake and from the ratio of the intercept to the reciprocal of the slope, one can measure the rate of 5-HT release.[50] This is assuming that 5-HT is produced at a zero-order reaction rate and uptake occurs at a first order reaction rate.[50] The authors found that 5-HT release was greater in the colon than the ileum, but because the rate of 5-HT clearance is also greater in the colon, this results in overall lower extracellular concentrations of 5-HT in the colon.[50] Our group applied this approach in a mouse model of diet-induced obesity along with other GI functional studies and bioassays to reveal important sex-related differences in how obesity is linked to intestinal dysfunction in obesity.[51] These measurements can be seen in Figure 1.4.

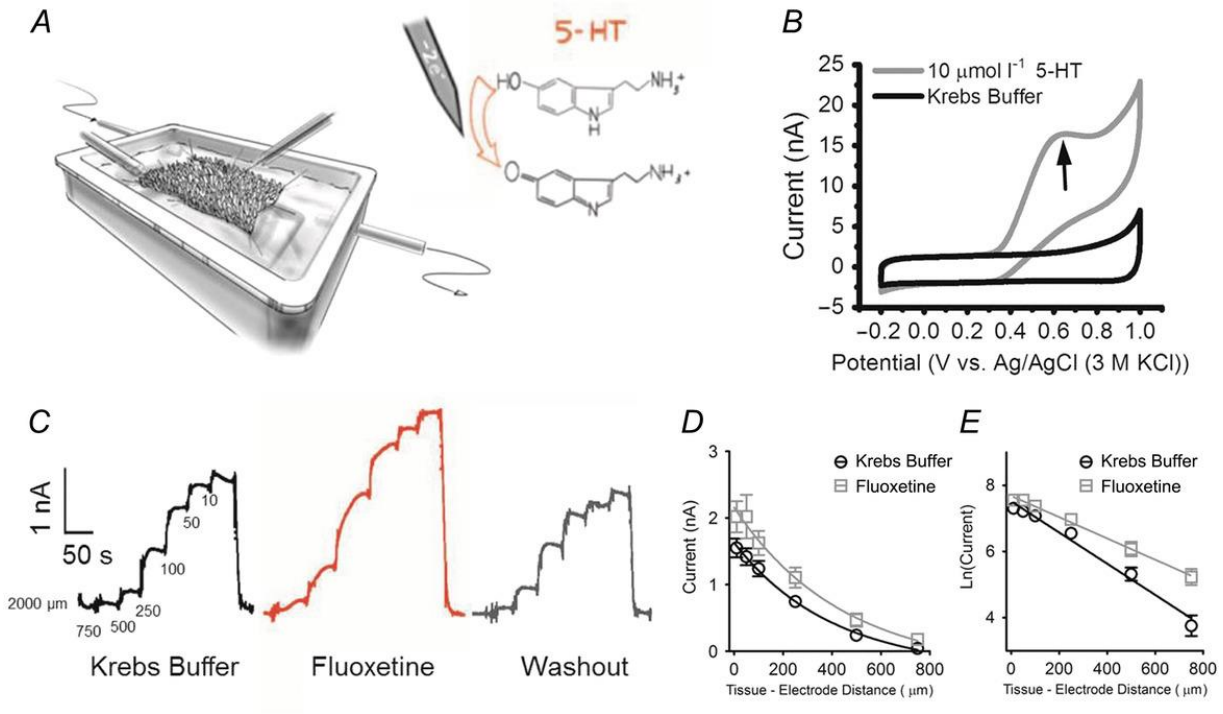

Figure 1.4. Schematic showing the BDD microelectrode and its use for electrochemical measurement of 5-HT from the gut mucosa. The jejunal mucosa preparation used in CA measurements, in which 5-HT released from EC cells is directly oxidized at the electrode interface (A). The potential at which 5-HT is oxidized at a mass transport limited rate was determined using

Figure 1.4. (cont'd)

cyclic voltammetry (CV), in which potential was scanned from -0.2 to 1.0 V at 100 mV s^{-1} (B). Current approach curves were used as a measure of 5-HT release and clearance. The electrode-tissue distance was decreased in a stepwise manner from 2000 µm (where no 5-HT is oxidized) to 10 µm from an individual villus (C). These measurements were performed in Krebs buffer (black trace) before perfusing the 1 µmol L^{-1} fluoxetine, repeating measurements (red trace), and rinsing out the drug to verify restoration of current (grey trace). Current-distance plots before and after fluoxetine administration (D) were log transformed (E) to reveal any changes in rate of 5-HT release or clearance. Reproduced from Ref[51] with permission from John Wiley and Sons.

The measurement of 5-HT overflow from the mucosal epithelium of the intestinal wall has been a popular research theme. One group developed a 3D-printed carbon black/polylactic acid sensor that was fabricated to mimic the natural diameter of a fecal pellet. This electrode was inserted into the bowel to simultaneously measure 5-HT overflow and circular muscle contractions *ex vivo* in guinea pigs.[52] Other researchers used a creative and novel approach to studying the gut-brain connection and created a tissue-mimicking, stretchable "NeuroString" sensor to simultaneously measure monoamine levels in the brain using FSCV and 5-HT overflow in the colon using CA.[53] These sensors were prepared by laser patterning a metal-complexed polyimide into an interconnected graphene/nanoparticle network embedded in an elastomer matrix. The sensors were chronically implanted with minimal tissue damage to monitor neurotransmitter level changes with animal learning tasks.[53]

5-HT is not the only neurotransmitter one can measure in the mucosa. Another group of researchers used carbon fiber microelectrodes to simultaneously measure 5-HT and melatonin release from mouse ileum and distal colon to determine the effects of melatonin supplementation in aged mice.[54] Amperometric measurements of 5-HT (E_{app} = +400 mV) and melatonin (E_{app} = +800 mV) were used to measure evoked 5-HT and melatonin release by slightly compressing the epithelium with the carbon fiber microelectrode, while differential pulse voltammetry was used to measure the steady state concentrations at the mucosal surface.[54] The authors found that the

availability of gut 5-HT and melatonin both increase with increasing age and that melatonin supplementation suppresses natural production of 5-HT and melatonin in aged mice.[54] It is thought that ATP has a significant influence on GI motility by regulating serotonin release, therefore one group designed an enzyme-based sensor for detecting ATP to moniter ATP release from guinea pig ileum and colon.[55] The sensor consisted of glucose oxidase (GOx) and hexokinase (Hex) immobilized within a poly-phenol film on a Pt microelectrode, and ATP was amperometrically detected by positioning the microelectrode 0.5 mm above the mucosa. There is a stable oxidation current in the presence of a constant concentration of glucose, which is oxidized in the presence of GOx to produce H_2O_2 which is electrochemically oxidized. When ATP is introduced to the solution, glucose is consumed as ATP is dephosphorylated by hexokinase, which decreases the amount of glucose available for the first enzymatic reaction. This decreases the amount of H_2O_2 produced and consequently results in a decrease in oxidation current with increasing ATP concentration. The authors found that ATP release was greater from the mucosal surface in the ileum compared to the colon.[55] Another group utilized BDD microelectrodes to study histamine's role in gastric acid secretion in the stomach.[56] The researchers used an iridium oxide pH microelectrode in the potentiometric mode to measure the pH decreases associated with gastric acid secretion while simultaneously using a BDD microelectrode in the amperometric mode to detect histamine overflow from isolated guinea pig stomachs.[56]

Within the musculature, BDD has also been used to measure NO release from myenteric neurons in the guinea pig ileum. NO was measured directly as oxidation current using CA and nicotine applied to the tissue through a superfusion pipette to stimulate NO release from longitudinal muscle myenteric plexus and circular muscle strip preparations.[57] The nicotine acts as an agonist on nicotinic acetylcholine receptors expressed on interneurons and motor neurons in the

myenteric plexus, which also express nNOS the rate limiting enzyme responsible for on demand NO synthesis.[57] The authors found that NO release from the circular muscle—which contains a dense network of nNOS containing nerve fibers—without myenteric plexus attached were almost 3x greater than NO released from longitudinal muscle myenteric plexus preparations.[57] A similar tactic was used combined with immunohistochemistry and western blot to determine that NO signaling to the longitudinal muscle layer in the ileum is stronger in neonatal *vs.* adult guinea pigs.[58] As CA is limited in selectivity, various tactics were employed to verify that the measured oxidation currents were from NO and that the NO released was of neurogenic origin. The nNOS inhibitor nitro-L-arginine was bath applied to prevent NO synthesis and confirm that the measured oxidation currents originated from NO.[57,58] Additionally, other pharmacological agents like the NO scavenger myoglobin were used to verify NO oxidation currents as well as manipulating the applied potential in CA to a potential insufficient to drive NO oxidation, but sufficiently positive to drive oxidation of other electroactive interferents such as serotonin.[57,58] Tetrodotoxin (TTX), a sodium-channel blocker that acts to prevent action potential propagation, was also used to verify neural dependence of nicotine-stimulated NO release.[57,58]

1.5 Research Objectives and Specific Aims

There is limited knowledge on the pathology of AD in the ENS, and it is unknown whether the formation of Aβ plaques directly disrupts enteric neuron function. Current methodology for studying neuromuscular signaling in the gut is limited as the methods provide no quantitative information and rely solely on pharmacological manipulations to obtain information. To date, there are no studies that utilize the direct detection of NO and ACh/Ch as a tool for examining changes in nitrergic and cholinergic neuromuscular signaling in the gut in AD. By developing and applying electrochemical sensors and biosensors to measure the real-time release of these signaling

molecules within the periphery using a transgenic mouse model that mimics major AD pathology, a goal of this research was determining if and how nitrergic and cholinergic signaling is altered in AD in the gut, and how those alterations connect with GI dysfunction.

A loss of nitrergic and cholinergic neurons in the myenteric plexus of APP/PS1 transgenic mice has been reported[26] as well as reduced neurogenic and cholinergic-mediated contractions in the colon of SAMP8 mice.[59] Additionally, a decrease of acetylcholinesterase (AChE), an enzyme which is used in ACh-mediated neurotransmission in the ENS, has been found in the small intestine of 5xFAD transgenic mice[27] as well as internalization of Aβ into enteric cholinergic neurons upon Aβ injection into the GI tract of a general purpose strain of ICR mice.[29] Furthermore, nitrergic neurons are particularly vulnerable to neuropathy,[60] so it is not unreasonable to hypothesize that NO and ACh/Ch release are impaired in AD and that this impairment is a cause of GI dysfunction observed in clinical cases of AD. This leads to the two specific aims of this research:

Specific Aim 1. To better understand the neural circuitry which regulates gastrointestinal motility by developing and applying electrochemical sensors and biosensors for measuring key neurotransmitters involved in regulating gastrointestinal motility.

Specific Aim 2. To determine if and how nitrergic and cholinergic neuromuscular signaling in the enteric nervous system is altered in Alzheimer's disease and how those changes connect with GI function.

Electrochemical sensors and biosensors sensitive and selective for NO, ATP, and ACh/Ch were prepared from modified BDD and Pt microelectrodes and characterized using voltammetric and amperometric techniques, Raman spectroscopy, and scanning electron microscopy. The NO chemical sensor and ACh/Ch biosensor were then applied *in vitro* to detect electrically stimulated

neurotransmitter release from nitrergic and cholinergic neurons from the mouse colon. These sensors were then used in transgenic animal models which mimic major AD pathology to determine if nitrergic or cholinergic signaling is altered in the gut in AD. These studies were performed alongside several GI motility, immunohistochemical, and neuromuscular assays to determine if and how gut function is altered in AD.

REFERENCES

1. Furness, J. B. The Enteric Nervous system and Neurogastroenterology. *Nat. Rev. Gastroenterol. Hepatol*. **2012**, *9*, 286-294.

2. Spencer, N. J.; Hu, H. Enteric Nervous System: Sensory Transduction, Neural Circuits and Gastrointestinal Motility. *Nat. Rev. Gastroenterol. Hepatol*. **2020**, *17*, 338-351.

3. Wood, J.D. Enteric Nervous System: Neuropathic Gastrointestinal Motility. *Digest. Dis. Sci*. **2016**, *61*, 1803–1816.

4. Benarroch, E.E. Enteric Nervous System. *Neurology*. **2007**, *69*(20), 1953-1957.

5. Gallego, D.; Mañé, N.; Gil, V.; Martínez-Cutillas, M.; Jiménez, M. Mechanisms Responsible for Neuromuscular Relaxation in the Gastrointestinal Tract. *Rev. Esp. Enferm. Dig*. **2016**, *108*(11), 721-731

6. Lino, S.; Nojyo, Y. Muscarinic M(2) Acetylcholine Receptor Distribution in the Guinea-Pig Gastrointestinal Tract. *Neuroscience* **2006**, *138*(2), 549-559.

7. Shah, V.; Lyford, G.; Gores, G.; Farrugia, G. Nitric Oxide in Gastrointestinal Health and Disease. *Gastroenterol.* **2004**, *126*(3), 903-913.

8. Burnstock, G. Purinergic Signaling in the Gastrointestinal Tract and Related Organs in Health and Disease. *Purinergic Signal.* **2014**, *10*, 3–50.

9. Perez-Medina, A.; Galligan, J. J. Nitrergic and Purinergic Nerves in the Small Intestinal Myenteric Plexus and Circular Muscle of Mice and Guinea Pigs. In *The Enteric Nervous System II. Advances in Experimental Medicine and Biology*, Vol. 1383; Springer, Cham, 2022; pp 33-43.

10. Mutafova-Yambolieva, V.N.; Hwang, S. J.; Hao, X.; Chen, H.; Zhu, M. X.; Wood, J. D.; Ward, S. M.; Sanders, K. M. β-Nicotinamide Adenine Dinucleotide is an Inhibitory Neurotransmitter in Visceral Smooth Muscle. *Proc. Natl. Acad. Sci. U S A.* **2007**, *104*(41), 16359-16364.

11. Goyal, R.K.; Sullivan, M.P.; Chaudhury, A. Progress in understanding of inhibitory purinergic neuromuscular transmission in the gut *Neurogastroenterol Motil*. **2013**, *25*, 203-207.

12. Durnin, L.; Hwang, S. J.; Kurahashi, M.; Mutafova-Yambolieva, V. N. Uridine Adenosine Tetraphosphate is a Novel Neurogenic P2Y1 Receptor Activator in the Gut. *Proc. Natl. Acad. Sci.* **2014**, *111*(44), 15821-15826.

13. Mutafova-Yambolieva, V.N.; Durnin, L. The Purinergic Neurotransmitter Revisited: A Single Substance or Multiple Players? *Pharmacol Ther*. **2014**, *144*, 162–191.

14. Peery, A.F.; Crockett, S. D.; Murphy, C. C.; Lund, J. L.; Dellon, E. S.; Williams, J. L.;

Jensen, E. T.; Shaheen, N. J.; Barritt, A. S.; Lieber, S. R.; Kochar, B.; Barnes, E. L.; Fan, Y. C.; Pate, V.; Galanko, J.; Baron, T. H.; Sandler, R. S. Burden and Cost of Gastrointestinal, Liver, and Pancreatic Diseases in the United States: Update 2018. *Gastroenterol*. **2019**, 1*56*(1), 254-272.

15. Lacy, B.E.; Weiser, K. Gastrointestinal Motility Disorders: An Update. *Dig Dis* **2006**, *24*(3-4), 228–242.

16. Aziz, Q.; Thompson, D. G. Brain-Gut Axis in Health and Disease. *Gastroenterol.* **1998**, *114*(3), 559-578.

17. Mayer, E. A. Gut Feelings: The Emerging Biology of Gut-Brain Communication. *Nat. Rev. Neurosci.* **2011**, *12*, 453-466.

18. Rao, M.; Gershon, M. The Bowel and Beyond: The Enteric Nervous System in Neurological Disorders. *Nat. Rev. Gastroenterol. Hepatol.* **2016**, *13*(9), 517-528.

19. Liddle, R. A. Parkinson's Disease From the Gut. *Brain Res.* **2018**, *1693*(B), 201-206.

20. Hawkes, C. H.; Del Tredici, K.; Braak, H. Parkinson's Disease: A Dual-Hit Hypothesis. *Neuropathol. Appl. Neurobiol*. **2007**, *33*(6), 599–614.

21. Hawkes, C. H.; Del Tredici, K.; Braak, H. Parkinson's Disease: The Dual Hit Theory Revisited. *Ann. N. Y. Acad. Sci*. **2009**, *1170*, 615–22.

22. Rietdijk, C. D.; Perez-Pardo, P.; Garssen, J.; van Wezel, R. J. A.; Kraneveld, A. D. Exploring Braak's Hypothesis of Parkinson's Disease. *Front. Neurol.* **2017**, *8*, 37.

23. DeTure, M. A.; Dickson, D. W. The Neuropathological Diagnosis of Alzheimer's Disease. *Mol. Neurodegen.* **2019**, *14*(1), 32

24. Chen, G.; Xu, T.; Yan, Y.; Zhou, Y.; Jiang, Y.; Melcher, K.; Xu, H. E. Amyloid Beta: Structure, Biology and Structure-Based Therapeutic Development. *Acta Pharmacol. Sin.* **2017**, *38*, 1205-1235.

25. Chong, F. P.; Ng, K. Y.; Koh, R. Y.; Chye, S. M. Tau Proteins and Tauopathies in Alzheimer's Disease. *Cell. Mol. Neurobiol*. **2018**, *38*, 965-980.

26. Han, X.; Tang, S.; Dong, L.; Song, L.; Dong, Y.; Wang, Y.; Du, Y. Loss of Nitrergic and Cholinergic Neurons in the Enterc Nervous System of APP/PS1 Transgenic Mouse Model. *Neurosci. Lett*. **2017**, *646*, 59-65.

27. Stoye, N. M.; dos Santos Guilherme, M.; Endres, K. Alzheimer's Disease in the Gut—Major Changes in the Gut of 5xFAD Model Mice with ApoA1 as Potential Key Player. *FASEB J.* **2020**, *34*(9), 11883-11899.

28. Menden, A.; Hall, D.; Hahn-Townsend, C.; Broedlow, C. A.; Joshi, U.; Pearson, A.; Crawford, F.; Evans, J. E.; Klatt, N.; Crynen, S.; Mullan, M.; Ait-Ghezala, G. Exogenous

lipase administration alters gut microbiota composition and ameliorates Alzheimer's disease-like pathology in APP/PS1 mice. *Sci. Rep*. **2022**, *12*, 4797.

29. Sun, Y.; Sommerville, N. R.; Liu, J. Y. H.; Ngan, M. P.; Poon, D.; Ponomarev, E. D.; Lu, Z.; Kung, J. S. C.; Rudd, J. A. Intra-Gastrointestinal Amyloid-β1–42 Oligomers Perturb Enteric Function and Induce Alzheimer's Disease Pathology. *J. Physiol*. **2020**, *598*(19), 4209-4223.

30. Nimgampalle, M.; Chakravarthy, H.; Sharma, S.; Shree, S.; Bhat, A. R.; Pradeepkiran, J. A.; Devanathan, D. Neurotransmitter Systems in the Etiology of Major Neurological Disorders: Emerging Insights and Therapeutic Implications. *Aging Res. Rev.* **2023**, *89*, 101994.

31. Beyene, A. G.; Yang, S. J.; Landry, M. P. Review Article: Tools and Trends for Probing Brain Neurochemistry. *J. Vac. Sci. Technol. A* **2019**, *37*, 040802.

32. Bard, A. J.; Faulkner, L. R. Basic Potential Step Methods. In *Electrochemical Methods: Fundamentals and Applications;* 2nd ed.; Wiley, New York, 2001; pp 156-225.

33. Pan, C.; Wei, H.; Han, Z.; Wu, F.; Mao, L. Enzymatic Electrochemical Biosensors for In Situ Neurochemical Measurement. *Curr. Opin, Electrochem.* **2020**, *19*, 162-167.

34. Fröhlich, E. The Neuron: The Basis for Processing and Propagation of Information in the Nervous System. *NeuroQuantology* **2010**, *8*(3), 403-415.

35. Esplugues, J. V. NO as a Signaling Molecules in the Nervous System. *Br. J. Pharmacol.* **2002**, *135*(5), 1079-1095.

36. Ou, Y.; Buchanan, A. M.; Witt, C. E.; Hashemi, P. Frontiers in Electrochemical Sensors for Neurotransmitter Detection: Towards Measuring Neurotransmitters as Chemical Diagnostics for Brain Disorders. *Anal. Methods* **2019**, *11*, 2738-2755.

37. Südhof, T. C. The Synaptic Vesicle Cycle: A Cascade of Protein-Protein Interactions. *Nature* **1995**, *375*, 645-653.

38. Mariani, F.; Gualandi, I.; Schuhmann, W.; Scavetta, E. Micro- and Nano-Devices for Electrochemical Sensing. *Microchim. Acta* **2022**, *189*, 459.

39. Wipf, D. O.; Kristensen, E. W.; Deakin, M. R.; Wightman, R. M. Fast-Scan Cyclic Voltammetry as a Method To Measure Rapid, Heterogenous Electron-Transfer Kinetics. *Anal. Chem*. **1988**, *60*(4), 306-310.

40. Venton, B. J.; Cao, Q. Fundamentals of Fast-Scan Cyclic Voltammetry for Dopamine Detection. *Analyst* **2020**, *145*, 1158-1168.

41. Heien, M. L. A. V.; Johnson, M. A.; Wightman, R. M. Resolving Neurotransmitters Detected by Fast-Scan Cyclic Voltammetry. *Anal. Chem*. **2004**, *76*(19), 5697-5704.

42. Patel, B. A. Electroanalytical Approaches to Study Signaling Mechanisms in the Gastrointestinal Tract. *Neurogastroenterol Motil.* **2011**, *23*(7), 595-605.

43. Bertrand, P. P. Real-Time Detection of Serotonin Release from Enterochromaffin Cells of the Guinea-Pig Ileum. *Neurogastroenterol. Motil.* **2004**, *16*(5), 511-514.

44. Gershon, M. D. 5-Hydroxytryptamine (Serotonin) in the Gastrointestinal Tract. *Curr. Opin. Endocrinol. Diabetes Obes.* **2013**, *20*(1), 14-21.

45. Patel, A. N.; Unwin, P. R.; Macpherson, J. V. Investigation of Film Formation Properties During Electrochemical Oxidation of Serotonin (5-HT) at Polycrystalline Boron Doped Diamond. *Phys. Chem. Chem. Phys.* **2013**, *15*(41), 18085-18092.

46. Wrona, M. Z.; Dryhurst, G. Electrochemical Oxidation of 5-Hydroxytryptamine in Aqueous Solution at Physiological pH. *Bioorg. Chem.* **1990**, *18*(3), 291–317.

47. Güell, A. G.; Meadows, K. E.; Unwin, P. R.; Macpherson, J. V. Trace Voltammetric Detection of Serotonin at Carbon Electrodes: Comparison of Glassy Carbon, Boron Doped Diamond and Carbon Nanotube Network Electrodes. *Phys. Chem. Chem. Phys.* **2010**, *12*, 10108– 10114.

48. Dong, H.; Wang, S.; Galligan, J. J.; Swain, G. M. Boron-Doped Diamond Nano/Microelectrodes for Bio-Sensing and *In Vitro* Measurements. *Front. Biosci. (Schol. Ed.)* **2011**, *3*, 518-540.

49. Purcell, E. K.; Becker, M. F.; Guo, Y.; Hara, S. A.; Ludwig, K. A.; McKinney, C. J.; Monroe, E. M.; Rechenberg, R.; Rusinek, C. A.; Saxena, A.; Siegenthaler, J. R.; Sortwell, C. E.; Thompson, C. H.; Trevathan, J. K.; Witt, S.; Li, W. Next-Generation Diamond Electrodes for Neurochemical Sensing: Challenges and Opportunities. *Micromachines* **2021**, *12*(2), 128

50. Marcelli, G.; Patel, B. A. Understanding Changes in Uptake and Release of Serotonin From Gastrointestinal Tissue Using a Novel Electroanalytical Approach. *Analyst* **2010**, *135*(9), 2340-2347.

51. France, M.; Skorich, E.; Kadrofske, M.; Swain, G. M.; Galligan, J. J. Sex-Related Differences in Small Intestinal Transit and Serotonin Dynamics in High-Fat-Diet-Induced Obesity in Mice. *Exp Physiol*. **2016**, *101*, 81–99.

52. Hamzah, H. H.; Keattch, O.; Yeoman, M. S.; Covil, D.; Patel, B. A. Three-Dimensional-Printed Electrochemical Sensor for Simultaneous Dual Monitoring of Serotonin Overflow and Circular Muscle Contraction. *Anal. Chem.* **2019**, *91*(18), 12014-12020.

53. Li, J.; Liu, Y.; Yuan, L.; Zhang, B.; Bishop, E. S.; Wang, K.; Tang, J.; Zheng, Y.; Xu, W.; Niu, S.; Beker, L.; Li, T. L.; Chen, G.; Diyaolu, M.; Thomas, A.; Mottini, V.; Tok, J. B.; Dunn, J. C. Y.; Cui, B.; Pasca, S. P.; Cui, Y.; Habtezion, A.; Chen, X.; Bao, Z. A Tissue-Like Neurotransmitter Sensor for the Brain and Gut. *Nature* **2022**, *606*, 94-101.

54. Bertrand, P. P.; Bertrand, R. L.; Camello, P. J.; Pozo, M. J. Simultaneous Measurement of Serotonin and Melatonin from the Intestine of Old Mice: The Effects of Daily Melatonin Supplementation. *J. Pineal Res.* **2010**, *49*(1), 23-34.

55. Patel, B. A.; Rogers, M.; Wieder, T.; O'Hare, D.; Boutelle, M. G. ATP Microelectrode Biosensor for Stable Long-Term *In Vitro* Monitoring From Gastrointestinal Tissue. *Biosens. Bioelectron*. **2011**, *26*, 2890-2896.

56. Bitziou, E.; O'Hare, D.; Patel, B. A. Simultaneous Detection of pH Changes and Histamine Release from Oxyntic Glands in Isolated Stomach. *Anal. Chem.* **2008**, *80*, 8733–8740.

57. Patel, B. A.; Galligan, J. J.; Swain, G. M.; Bian, X. Electrochemical Monitoring of Nitric Oxide Released by Myenteric Neurons of the Guinea Pig Ileum. *Neurogastroenterol. Motil*. **2008**, *20*(11), 1243-1250.

58. Patel, B. A.; Dai, X.; Burda, J. E.; Zhao, H.; Swain, G. M.; Galligan, J. J.; Bian, X. Inhibitory Neuromuscular Transmission to Ileal Longitudinal Muscle Predominates in Neonatal Guinea Pigs. *Neurogastroenterol. Motil.* **2010**, *22*(8), 909-e237.

59. Pellegrini, C.; Daniele, S.; Antonioli, L.; Benvenuti, L.; D'Antongiovanni, V.; Piccarducci, R.; Pietrobono, D.; Citi, V.; Piragine, E.; Flori, L.; Ippolito, C.; Segnani, C.; Palazon-Riquelme, P.; Lopez-Castejon, G.; Martelli, A.; Colucci, R.; Bernardini, N.; Trincavelli, M. L.; Calderone, V.; Martini, C.; Blandizzi, C.; Fornai, M. Prodromal Intestinal Events in Alzheimer's Disease (AD): Colonic Dysmotility and Inflammation Are Associated with Enteric AD-Related Protein Deposition. *Int. J. Mol. Sci.* **2020**, *21*(10), 3523.

60. Bódi, N.; Szalai, Z.; Bagyánszki, M. Nitrergic Enteric Neurons in Health and Disease—Focus on Animal Models. *Int. J. Mol. Sci.* **2019**, *20*(8), 2003.

CHAPTER 2. EXPERIMENTAL METHODS

2.1 Electrode Preparation

2.1.1 Boron-Doped Diamond Electrodes

The boron-doped diamond (BDD) disk macroelectrode (4 mm diam., 0.13 cm^2), sealed in Kel-F (Fraunhofer USA Center for Coatings and Diamond Technologies, MSU), was pretreated using a light polish with 0.05 μm diam. alumina powder slurried in ultrapure water on a felt pad and a 20 min ultrasonic cleaning in ultrapure isopropyl alcohol (IPA). The BDD microelectrodes were prepared by overcoating a sharpened 76 μm diam Pt wire with a layer of boron-doped nanocrystalline diamond using microwave-assisted chemical vapor deposition. Further detail of the BDD microelectrode preparation can be found elsewhere.[1,2] Ultrahigh-purity methane (CH_4), hydrogen (H_2), and diborane (B_2H_6) were used. The deposition conditions were generally a 1% v/v CH_4/H_2 source gas ratio, 600 W power, 35 Torr system pressure, a total gas flow rate of 200 sccm, and 10 ppm of B_2H_6 added for boron doping. B_2H_6 was 0.05% v/v diluted in ultrapure H_2. The BDD electrodes were cleaned prior to each use by a 15 min immersion in ultrapure IPA.

2.1.2 Platinum Microelectrodes

Platinum (Pt) microelectrodes were prepared in two ways. For ATP biosensor preparation, a 50 μm diameter Teflon-coated Pt wire (AM Systems, Sequim, WA). was used with the coating removed on both ends. One end was glued to a copper wire with conductive Ag epoxy for electrical connection. The other end was inserted into a polypropylene pipet tip with several millimeters of the wire protruding. The polypropylene was then gently heated to melt the polymer to form a seal around the wire with the exposed Pt forming the sensing region. The wire was secured in place on the opposite end of the pipet tip with a nonconductive epoxy resin plug. For acetylcholine/choline (ACh/Ch) biosensor preparation, Pt microelectrodes were prepared by contacting one end of an 80

μm diam. Pt (Goodfellow, 99.9%) wire to a ~3 in. piece of 0.25 mm diam. Cu (Aldrich, 99.9%) wire using conductive silver epoxy and curing overnight. The next day, the Pt-Cu wires were threaded through glass capillaries (1.2 mm diam.) which were pulled to a taper using a P30 vertical micropipette puller (Sutter Instruments) and cut open so that a small gap of space was present between the opening of the glass capillary and the Pt wire. This end of the microelectrode was then immersed into a two-part epoxy mixture for 30-60 s, which was prepared by mixing equal parts of epoxy resin and hardener (Gorilla Clear Epoxy). Through capillary action, epoxy was drawn into the tip of the capillary to form a resin plug, insulating the electrode. The back end of the capillary was also sealed using the same epoxy. Excess epoxy was quickly wiped from the outside of the capillary using a Kimwipe and the resin was allowed to cure overnight at room temperature. The next day, electrodes were placed in the oven for 1-2 hours at 70°C to further harden the epoxy and the electrodes were then ground at 45º using a BV-10 micropipette beveler (Sutter Instruments) using a course diamond abrasive plate (Cat. #104C, Sutter Instruments). This exposed an elliptical disk area of the Pt wire with a geometric area of 7.1×10^{-5} cm^{-2}. After grinding, the electrodes were ultrasonically cleaned in ultrapure water for 30 min to remove any debris and then cycled potentiodynamically from -0.2 to 1.2 V at 50 mV s^{-1} for 8 cycles in deoxygenated 0.5 mol L^{-1} H_2SO_4. Well-defined features for Pt-oxide formation, Pt-oxide stripping, and hydrogen adsorption/desorption were typically observed after cycling. A schematic showing the steps of the Pt microelectrode construction can be seen in Figure 2.1.

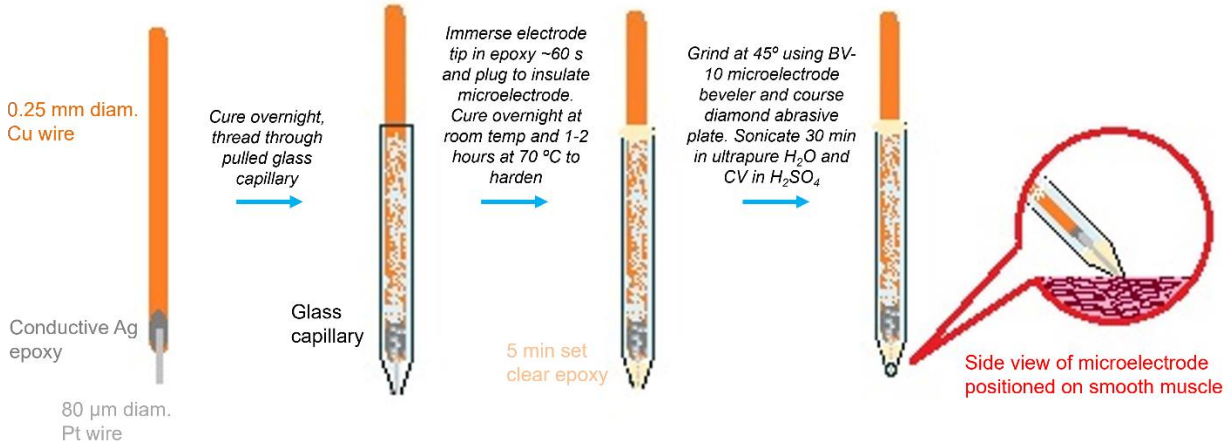

Figure 2.1. Schematic showing the individual steps of Pt microelectrode construction for ACh/Ch biosensor preparation. The result is a microelectrode with a geometric area of 7.1 x 10^{-5} cm^{-2} that can be positioned during in vitro measurements with 100% contact between electrochemically active area of the electrode and the tissue.

2.1.3 ATP Biosensor Preparation

ATP biosensors were prepared using both smooth Pt wire microelectrodes and platinized Pt wire microelectrodes. Platinization was accomplished potentiodynamically using 40 cycles (optimized) between 0.3 and 1.2 V vs. Ag/AgCl in 1 mmol L^{-1} potassium hexachloroplatinate (IV) (K_2PtCl_6) dissolved in 0.1 mol L^{-1} perchloric acid. The scan rate was at 50 mV s^{-1}. The poly(3,4-ethylenedioxythiophene)-glucose oxidase-hexokinase (PEDOT-GOx-Hex) film was formed on the Pt microelectrodes by electropolymerization from a solution containing 10 mg mL^{-1} GOx, 40 mg mL^{-1} Hex, and 4.5 mol L^{-1} 3,4-ethylenedioxythiophene (EDOT), all in 0.1 mol L^{-1} tetrabutylammonium tetrafluoroborate ($TBABF_4$) dissolved in dichloromethane (DCM). Enzyme-loading concentrations were selected based on literature.[3] Note that the electropolymerization with the entrapped enzymes was performed in an organic electrolyte solution. The solution was deoxygenated with N_2 for 15 min before polymer film formation. The polymer film, with entrapped the GOx and Hex enzymes, was formed by potentiodynamically using 100 cycles (optimized) between −1.1 and 1.1 V vs. Ag QRE at 50 mV s^{-1}. After electrocoating, the

microelectrode sensor tip was thoroughly rinsed with ultrapure water to remove excess monomer, electrolyte, and solvent. The sensor was then dried under a stream of N_2 before initial use.

2.1.4 Nitric Oxide Sensor Preparation

For electrochemical detection of nitric oxide (NO), BDD microelectrodes were modified with Pt nanoparticles to reduce the working potential of NO oxidation and a thin film of Nafion to electrostatically repel negatively charged interferents such as the nitrite anion. Pt electrocatalyst particles were formed potentiodynamically on the BDD electrodes in 2.0 mmol L^{-1} K_2PtCl_6 dissolved in deoxygenated 0.5 mol L^{-1} H_2SO_4 under a N_2 gas blanket.[4,5] The potential was cycled between −0.2 and 1.3 V *vs* Ag/AgCl for 10 cycles at 0.01 V s^{-1} with a starting potential of 1.0 V to initiate nucleation. Following platinization, the electrochemically active surface area (ECSA) was determined using cyclic voltammetry (CV) in a deaerated solution of 0.5 mol L^{-1} H_2SO_4. Potential scans (5 cycles) were recorded from −0.25 to 1.25 V at 0.1 V s^{-1}. The integrated charge for hydrogen desorption between −0.25 and 0.20 V *vs* Ag/AgCl was used to calculate the ECSA using the charge density associated with a monolayer of hydrogen adsorbed onto single crystal Pt (210 μC cm^{-2}).[6] The BDD disk macroelectrode was used to optimize the Pt nanoparticle formation as a function of the K_2PtCl_6 concentration (0.1, 0.5, 1, 1.5, and 2 mmol L^{-1}), scan rate (0.01, 0.05, and 0.1 V s^{-1}), and cycle number (5, 10, 15, and 25) used for metallization. After electrodeposition, a Nafion film was formed over the metal-coated electrode by dip-coating the modified electrode in 2.5% (w/v) colloidal Nafion solution diluted with ultrapure IPA. The coated electrodes were dried vertically in an oven overnight at 55 °C in the presence of moisture, which was achieved by suspending the electrodes ~1 cm above water in a parafilm-sealed glass vial. The optimal Nafion solution concentration as well as the optimal drying time was determined using drop-casting experiments with the disk macroelectrode in which 50 μL of 0.1–5% (w/v) Nafion was applied

directly to the electrode surface and dried in the oven in at 55 °C for varying times.

2.1.5 ACh/Ch Biosensor Preparation

Electrochemical ACh/Ch biosensors were prepared by depositing a multienzyme film cross-linked with glutaraldehyde onto a poly(*m*-phenylenediamine) (p*m*PD) modified Pt microelectrode. To increase the electrochemically active area of the electrode and improve adhesion of the multienzyme film,[7-10] the Pt microelectrodes were potential cycled in a solution containing 2 mmol L^{-1} K_2PtCl_6 in 0.5 mol L^{-1} H_2SO_4 from -0.2 to 1.2 V at 10 mV s^{-1} for 10 cycles with an initial potential of 1.0 V scanning cathodically to reduce Pt(IV) and initiate nanoparticle nucleation. This tactic was previously used to enhance the sensitivity and stability of ATP biosensors[11] and to platinize BDD microelectrodes.[12] These electrodeposition conditions produce a disperse coverage of Pt nanoparticles across the substrate with a range of diameters. This is characteristic of a progressive nucleation and growth process, in which new nuclei continuously form while existing Pt nanoparticles grow out from those nucleation sites.[13,14]

To provide selectivity against potential oxidizable interferents, a permselective p*m*PD polymer film was electrodeposited onto the platinized-Pt microelectrode prior to enzyme immobilization. Using a deoxygenated 5 mmol L^{-1} *m*-phenylenediamine (*m*PD) solution dissolved in 0.1 mol L^{-1} PB, pH 7.4, the potential was cycled from 0.2 to 1.0 V at 25 mV s^{-1} for 40 cycles. In optimization experiments, the scan rate (10, 25, 50 mV s^{-1}) and cycle number (10, 20, 40) were optimized for sufficient H_2O_2 permeability and adequate rejection of electroactive interferents ascorbic acid (AA), dopamine (DA), norepinephrine (NE), and serotonin (5-HT).

Following platinization and p*m*PD formation on the Pt microelectrodes, enzyme immobilization was performed by pipetting 1 µL of a multienzyme solution containing equal volumes of 200 U mL^{-1} ChOx, 400 U mL^{-1} AChE, 10% (w/v) BSA to stabilize the enzymes, and

0.75% (v/v) glutaraldehyde onto the electrode surface under aid of a low-power microscope. Figure 2.2 shows a general schematic of the steps following during biosensor preparation. Enzyme immobilization is achieved through the cross-linking of the amino groups of the proteins in the enzyme layer using glutaraldehyde to form cross-linked aggregates that can impregnate the pores and channels of the p*m*PD support for enhanced stability.[15-19] The enzyme unit activity and solution concentration values were identical to literature.[19] The electrodes were allowed to dry for 2 h at room temperature and were then immersed into 0.1 mol L^{-1} phosphate buffer, pH 7.4, and stored in the fridge at 4°C. The volume of multienzyme solution was optimized using 0.5, 1, 2, and 3 µL.

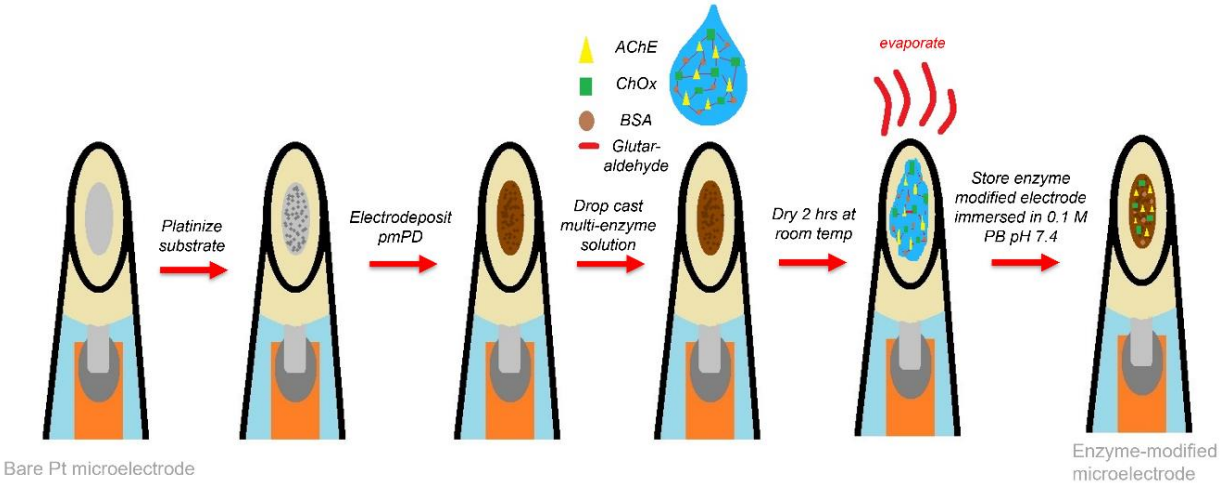

Figure 2.2. Schematic showing the steps followed in ACh/Ch biosensor construction, starting with a bare Pt-microelectrode and ending with a platinized and polymer modified enzyme-coated microelectrode.

2.2 Physical and Electrochemical Characterization

2.2.1 Raman Spectroscopy

Raman spectroscopy was performed using a Renishaw inVia™ Reflex spectrometer consisting of a confocal microscope connected to a continuous wave, diode-pumped solid-state laser. The excitation wavelength used was 532 nm. Raman spectra were recorded along a 50 µm line profile of the diamond film (1 acquisition per 1 µm) and used to evaluate the quality of the

nanocrystalline diamond films and the presence of sp^2 carbon impurities.

2.2.2 Scanning Electron Microscopy

Scanning electron microscopy (SEM) was used to examine microelectrode morphology through various stages of modification. SEM was performed using both a JEOL 6610LV microscope and a JEOL 7500F ultrahigh resolution microscope, both housed at MSU's Center for Advanced Microscopy. The micrographs were constructed from both secondary and backscattered electrons using an accelerating voltage of 2, 5, 10, 12, or 15 keV, depending on the sensitivity of the sample. Energy dispersive x-ray spectroscopy (EDS) for elemental analysis was performed using an Aztec detection system (Oxford Instruments, UK) attached to the SEM. The data was analyzed using the associated software (version 3.1). For non-conductive samples, a 30 s iridium sputter coating was used before imaging.

2.2.3 Electrochemical Characterization

With exception of the *in vitro* measurements, all electrochemical measurements were performed at room temperature (25°C) in a 10 mL single compartment glass cell. The cell was housed inside an electrically grounded Faraday cage to reduce electrical noise. A Pt wire served as the counter electrode and a commercial Ag/AgCl (3 mol L^{-1} KCl) electrode (Bioanalytical Systems Inc., West Lafayette, IN) served as the reference electrode. When voltammetry was performed in DCM, a silver wire served as a pseudo reference electrode (QRE). With exception of the enzyme-based sensor measurements which required O_2 as a cofactor, all solutions were deoxygenated by bubbling N_2 gas for a minimum of 15 mins, maintaining a N_2 blanket over the cell throughout measurements. Cyclic voltammetry (CV), linear sweep voltammetry (LSV), and continuous amperometry (CA) were performed using a computer-controlled electrochemical workstation (Model 832A, CH Instruments, Austin, TX) or a Gamry Instruments Reference 600+

potentiostat/galvanostat (Warminster, PA). For CA measurements, solutions were continuously stirred using a magnetic stir bar and low noise electrical stirrer.

2.3 *In Vitro* Electrochemical Measurements

In vitro electrochemical measurements were made measuring both NO and ACh/Ch release from mouse circular muscle preps using a modified BDD microelectrode and enzyme-based biosensors. For NO measurements, prior to each measurement the Nafion/Pt/BDD microelectrode was potential cycled in 0.5 mol L^{-1} H_2SO_4 to activate and clean the electrode surface and the Nafion film was renewed every three measurements. For ACh/Ch measurements, microelectrodes were prepared in batches using different biosensors for individual measurements. To account for any sensor-to-sensor variability, a calibration was performed in the recording chamber used for *in vitro* measurements by perfusing warmed (36-37°C) Krebs buffer pH 7.4 through a recording chamber at 4 mL min^{-1} and recording the current response to increasing concentrations of ACh (0.1, 0.5, 1, 5, and 10 µmol L^{-1}) perfused through the chamber with the sensor polarized at 0.75 V vs. Ag/AgCl. In cases where two animals were tested within a single day, the same sensor was used, but a second brief calibration was performed using only 1 µmol L^{-1} ACh to verify the current response was unchanged.

For tissue preparations, a small (~1 cm) piece of proximal-mid colon was removed from a euthanized mouse and placed into a dish containing prewarmed (37°C) Krebs buffer, pH 7.4. The fat and connective tissue were carefully removed using microscissors and forceps and the preparation was cut along the mesenteric border, stretched, and pinned flat using steel pins with the mucosa facing up. The mucosa and submucosa were carefully peeled back using fine forceps exposing the circular muscle, and a section of this preparation (~1 cm^2) was cut and transferred to a Sylgard-lined recording chamber using small (0.05 mm diam.) steel pins. The tissue was carefully

stretched and pinned, being careful to avoid tearing. For some optogenetics measurements, the tissue was flipped such that the circular muscle faced down, and strips of serosa/longitudinal muscle were carefully peeled off, exposing myenteric ganglia. These preps are referred to as longitudinal muscle myenteric plexus preps (LMMPs). A reference electrode (Ag/AgCl) and counter electrode (Pt wire) were secured opposite of one another in the recording chamber. Then warmed (36-37°C) and oxygenated (95% O_2, 5% CO_2) Krebs buffer, pH 7.4, containing 1 μmol L^{-1} nifedipine (to block spontaneous longitudinal muscle contractions) and 1 μmol L^{-1} scopolamine (to block muscarinic cholinergic receptors) was perfused over the tissue at 4 mL min^{-1} for 30 min to equilibrate the tissue. The scopolamine was excluded for the Ach/Ch measurements.

After 30 min, the Nafion/Pt/BDD microelectrode or ACh/Ch biosensor was gently touched to a region of the tissue near a myenteric ganglion using a micromanipulator and low-power microscope. To position the microelectrode at "zero distance," the microelectrode was carefully touched to the tissue and backed-off until the tissue was no longer contorted. Using an Omni 90 analog potentiostat (formerly Cypress Systems, Inc.), the working electrode was polarized at 0.8 V (NO) or 0.75 V (ACh/Ch). Once the current stabilized, transmural electrical stimulation was accomplished by placing two Ag/AgCl wires on opposite ends of the tissue preparation. Voltage pulses were then delivered across these wires using an electrically isolated Grass S88 stimulator (Grass Technologies, West Warwick, RI) to stimulate all neurons and nerve fibers (80 V, 10 Hz, 0.5 ms pulse duration). The number of voltage pulses delivered was gradually increased. For optogenetic studies, short pulses of blue light (20 mW/mm^2, 10 Hz, 20 ms pulse duration) were delivered using an LED positioned ~100 μm from the electrode tip using a micromanipulator and microscope. Amperometric *i–t* traces were recorded using an Axon Digidata 1400A Low-Noise Data Acquisition System with Axoscope 10.7 software (Molecular Devices, Sunnyvale, CA). Data

was analyzed using Clampfit 10.7 software (Molecular Devices) after smoothing with a 10 Hz low pass filter. The signal was passed through a 60 Hz notch filter to remove line noise prior to digitization. As it is difficult to visualize myenteric ganglia through the thickness of the circular muscle layer, a "test" stimulation was performed initially to determine if a sufficient response in the form of a current spike was achieved. Microelectrode position is very important for neuroanalytical measurements of this type. If the microelectrode is positioned fortuitously close to a ganglion or multiple ganglia, then the oxidation current response will be higher, due to a higher concentration of neurotransmitter released in the extracellular volume around the microelectrode, than the current response will be if the microelectrode is positioned further away from release sites. The usual course of action in these measurements is to first move the microelectrode to a few regions in the tissue specimen to find a "hot spot" and then conduct the measurement sequence at this location.

Following electrical stimulation, the sodium channel blocker, tetrodotoxin (TTX, 0.3 µmol L^{-1} or 0.5 µmol L^{-1}), was perfused over the tissue for 10 min before repeating stimulations to verify the neurogenic origin of the measured NO and ACh/Ch release. After this, the tissue was rinsed for 15-20 mins and a single stimulation was repeated to verify the restoration of oxidation current. Next, the nitric oxide synthase (NOS) inhibitor L-nitro-N-arginine (L-NNA, 100 µmol L^{-1}) was perfused for through the chamber for 10 mins before repeating stimulations. NOS is the rate-limiting enzyme that synthesizes NO on demand through catalysis of the oxidation of L-arginine to NO plus L-citrulline, thus L-NNA competes for these arginine binding sites consequently preventing NO synthesis and release. For ACh/Ch measurements, the AChE inhibitor neostigmine (10 µmol L^{-1}) was perfused for 10 min prior to repeating stimulations to examine the source of the measured oxidation current.

2.4 Animal Model

2.4.1 Animal Husbandry and Tissue Collection

All procedures were approved by the Institutional Animal Use and Care Committee (IACUC) at Michigan State University (Animal use protocol #PROTO201900058). All animals were housed in a 12-hour light/dark cycle and 68% humidity levels in house, with *ad libitum* access to water and food (Tekla Global 18% protein diet (2918)). Euthanasia was performed in compliance with the Panel on Euthanasia of the American Veterinary Medical Association using 4% isoflurane and cervical dislocation as approved. The brain, small intestine, and colon were collected. Left cerebral hemispheres and a small segment of colon were immediately fixed at 4°C with Zamboni's fixative (4% formaldehyde with 5% picric acid in 0.1 M sodium phosphate buffer, pH 7.2) for 48 h. Brain tissues were immersed into 15% and 35% of sucrose in 0.1 M sodium phosphate buffer for 2–3 days, then embedded in optimal cutting temperature compound (O.C.T.) and stored at −80°C for further cryostat sectioning and immunostaining. Right cerebral hemispheres and a small segment of small intestine were collected and freshly stored at −80°C for further ELISA assay.

2.4.2 5xFAD Mice

The 5xFAD mouse is a widely used Aβ pathogenic model whereby Aβ accumulation in the brain occurs as early as 2 months of age. In addition, neuronal loss in the CNS occurs at 3 months, and cognitive impairment is observed at 5 months of age.[20,21] Literature has reported that 5xFAD mice also present minor GI dysmotility,[22,23] changes in enteric neuronal structure,[23] altered colonic gene expressions and calcium homeostasis, increased enteric neuronal viability,[22] and GI dysbiosis.[24] Male and female 5xFAD mice (B6SJL-Tg [APPSwFlLon, PSEN1*M146L*L286V] 6799Vas/Mmjax, Jackson Laboratories; stock no: 34848-JAX) and control (WT) mice (Jackson Laboratories; stock no. 000664 C57BL/6) were purchased at 8 weeks of age and sacrificed after 6

months.

2.4.3 APP/PS1 Mice

APP/PS1 mice are a double transgenic strain of mice which overexpress two mutations directed toward CNS neurons that are associated with early-onset Alzheimer's disease. These mice start to develop Aβ plaques by 6 months of age which increases up to 12 months of age.[25,26] Neuronal loss adjacent to these plaques occurs between 8 to 10 months.[27] Memory impairments start as early as 6 months of age while spatial learning becomes impaired by 12 months.[28,29] These mice have also shown overexpression of Aβ and phosphorylated Tau protein in myenteric neurons, intestinal dysfunction, inflammation, and increased intestinal permeability.[30-33] Male and female APP/PS1 hemizygotes and genetic control mice (B6C3-Tg(APPswe,PSEN1dE9)85Dbo/Mmjaxries; MMRRC034829, Stock: 004462-JAX)) were purchased from Jackson Laboratory at 8-weeks-old (jax.org/strain/004462) and sacrificed after 12 months. All mice were maintained on a C57BL/6;C3H (B6C3) genetic background.

2.4.5 NOS1^{cre}/ROSA Mice

We used the Cre/lox recombinase system to express ChR2-eYFP in NOS containing neurons by cross breeding homozygote female B6;129S-Gt(ROSA)$^{26Sortm32(CAG-COP4*H134R/EYFP)Hze}$/J mice (ROSA) (Jackson Laboratories; Stock No: 012569) with homozygous male B6.129-NOS1$^{tm1(cre)Mgmj}$/J mice (Nos1^{cre}), which express Cre-recombinase in the neuronal nitric oxide synthase (nNOS) locus (Jackson Laboratory Stock no. 017526). The resulting offspring have the STOP cassette deleted in the Cre-expressing tissue and consequently express the ChR2(H134R)-EYFP fusion protein (which is immunoreactive by eYFP fluorescence) in NOS containing neurons. Mice were bred in-house and euthanized after 2 months.

2.5 GI Motility Assays, Immunohistochemistry, and ELISA

2.5.1 Body Weight, Food Intake, and Fecal Pellet Output

To assess GI motility, we measured body weight, food intake and fecal pellet output every 4 weeks, starting at 9 weeks up to 25 weeks in all mice. After measuring body weight, mice were separated from their original cages and individually housed in a cage with access to 40 g of food and free access to water for 72 h. Total food (g) consumption was measured within 72 h. For fecal pellet output measurements, each mouse was separated from their home cage and individually housed in cages without access to food and water for 2 h, on 3 consecutive days. Fecal pellets were assessed for number and length (mm). Wet pellet weight was assessed immediately after pellet collection, whereas dry weights were measured after 24 h desiccation at room temperature. Fecal water content was calculated by subtracting dry weight from wet weight.

2.5.2 Measurement of Colonic Migrating Motor Complexes

The frequency and propagation velocity of colonic migrating motor complexes (CMMCs) were important in evaluation of colonic GI motility. After euthanasia, the entire colon (6–8 cm) was collected from mice and the lumen was flushed with Krebs' solution. A stainless-steel rod was inserted into the lumen, and surgical ligatures were used to secure the proximal and distal ends of the colon onto the rod. The preparation was then secured in a 60 mL organ bath that contained oxygenated Krebs solution maintained at 37°C. The colonic segment was secured to the rod ~2 cm apart with one at the end of the proximal colon and one at the start of distal colon. Both ends of the threads were attached to separate force transducers (CP122A strain gauge amplifiers, Grass Instruments, Astro-Med, Inc. W. Warwick, RI) and were placed under an initial tension of 2 g. The colon was allowed to rest for 30 min and then CMMC frequency, duration, and propagation speed were analyzed in a 20 min window using LabChart software 8 (AD Instruments, Colorado Springs,

CO).

2.5.3 Isometric Tension Recording in Isolated Organ Bath

Longitudinal smooth muscle contractility was determined pharmacologically and electrophysiologically using isometric tension recording in an organ bath. Following euthanasia, a 1.5 cm length of duodenum, ileum, proximal and distal colon were mounted onto a platinum foil electrode on one end and a stationary isometric force transducer on the other end with silk ligatures. The assembly was placed into a 20 mL organ bath containing oxygenated Krebs solution at 37°C and a resting tension of 1 g was applied to each preparation. To determine smooth muscle contractility for excitatory neurotransmission, bethanechol, a muscarinic receptor agonist, was cumulatively added into each organ bath at 2 min intervals to produce myogenic contractions. Each preparation was washed with Kreb's solution every 10 min and after each drug application. Enteric nerve-evoked contractions were tested by transmural electrical stimuli (30 V, 0.8 ms pulse duration, 10 s train duration, 0.5–10 Hz) with a Grass S88 Stimulator (Grass Technologies). TTX (0.3 μmol L^{-1}), a voltage-gated Na^+ channel inhibitor, was used to block neuromuscular transmission to reveal myogenic responses. All tissues were dried using Kimwipes and tissue weight between ligatures was weighed at the end of experiment. All drug and electrophysiological responses were calculated by subtraction of baseline from peak responses and converted into mg (contraction force)/mg (tissue weight).

2.5.4 Intracellular IJP Recordings from Circular Smooth Muscle Cells

Myenteric neuromuscular transmission modulates GI motility. Colonic myenteric neuromuscular transmission was evaluated electrophysiologically using sharp microelectrode intracellular recordings. Following euthanasia, a 1 cm colon segment was isolated and cut along the mesenteric border, pinned flat on the dish with the mucosa facing upward, and the mucosal and

submucosal layers were removed. A 1 cm^2 exposed circular muscle prep was transferred to a 5 mL silicone elastomer-lined recording chamber with constant perfusion (flow rate 3 mL/min) of oxygenated 37°C Krebs' solution. The tissue was acclimated for 30 min after which microelectrodes (tip resistance, 60–120 MΩ) (borosilicate 1.0 mm × 0.5 mm fiber glass, FHC Inc.,) filled with 2 mol L^{-1} KCl were used to impale circular smooth muscle cells. Transmural electrical stimulation (80 V, 0.5 ms pulse duration, 10 Hz train, and 100–300 ms pulse duration) was performed using a pair of Ag/AgCl wires (A-M Systems,) connected to a Grass S88 stimulator. MRS2179 (10 μmol L^{-1}), a P2Y1 receptor antagonist, was used to block purinergic activation induced membrane hyperpolarization to reveal the nitrergic component of membrane hyperpolarization in smooth muscle cells. Resting membrane potential recordings greater than −40 mV were used for data analysis. Amplitude (mV) was measured from the traces obtained in AxoScope 10.4 (Molecular Devices).

2.5.5 Immunostaining

The expression of Aβ was determined in whole brain, colonic circular muscle myenteric plexus (CMMP) in whole tissue preparation, and in coronal and transverse sections of the colon by immunostaining. The expression of NOS and YFP was determined in brain slices and CMMP preps from the colon and small intestine. Fixed brain tissues were sectioned at 10 μm thickness using a cryostat. For CMMP preparations, a 1 cm^2 segment was cut along the mesenteric border, pinned flat on the petri-dish with the mucosa facing upward, and the mucosal and submucosal layers were removed. The prep was fixed overnight at 4°C with Zamboni's fixative (4% formaldehyde with 5% picric acid in 0.1 M sodium phosphate buffer, pH 7.2). The fixative was washed with 0.1 M phosphate buffer solution (84 mM Na_2HPO_4, 18 mM NaH_2PO_4, pH 7.2), the tissue was flipped over, and the serosa and longitudinal muscle layer were dissected using fine forceps. Coronal and

transverse sections of fixed segment of colon were embedded with paraffin, performed by the histology core at Michigan State University. The colonic sections were cut at 5 μm thickness and dewaxed before immune staining. All preps were incubated overnight at 4°C with primary antibodies followed by 1 h incubation at room temperature with secondary antibodies (See Table 2.1, antibody information). All preps were examined using a Nikon C2+ upright confocal laser scanning microscope (Nikon Instruments, Inc,). Fluorophores were excited using 488 nm and 594 nm lasers and their spectra were captured using Nikon NIS-Elements advanced research software version 4.0. Identical photomultiplier settings were used for image acquisition from all samples. Images for publication were prepared using Adobe Photoshop CS5.

1º AB	Host	Catalog #	Dilution	1º AB Source	2ºAB	Dilution	2ºAB Source
Aβ	Rabbit	71-5800	1:300	Thermo Fisher	Alexa 594	1:500	Thermo Fisher
Aβ	Rabbit	8243	1:500	Cell Signaling	Alexa 594	1:500	Thermo Fisher
HuC/D	Mouse	A21271	1:300	Thermo Fisher	Alexa 488	1:500	Thermo Fisher
NeuN	Mouse	MAB377	1:500	Millipore	Alexa 488	1:500	Thermo Fisher
NOS	Goat	AB1376	1:100	Abcam	Alexa 594	1:1000	Thermo Fisher

Table 2.1. List of antibodies used in immunofluorescence. Primary antibodies (1º AB) and secondary antibodies (2º AB) and their respective dilutions and suppliers of reagents used for immunofluorescence staining.

2.5.6 ELISA Assay for Aβ42 Expression

Expression of Aβ42 (insoluble Aβ isoform) was evaluated in whole brain, ileum and colon from 5xFAD and WT mice by ELISA assay. The segment of ileum (~100 mg) and colon were homogenized in cell extraction buffer (FNN0011, ThermoFisher Scientific) and the following protease inhibitors: 1 mmol L^{-1} PMSF (36978, ThermoFisher Scientific) and 1X protease inhibitor cocktail (P2714, Sigma). Brain tissues were homogenized in 5 mol L^{-1} Guanidine-HCl/50 mmol L^{-}

[1] Tris, pH 8.0 with 1X protease inhibitor cocktail (P2714, Sigma). ELISA detection of Aβ42 was performed with a Mouse Aβ Elisa Kit (KMB3441, ThermoFisher Scientific) per the manufacturer's instructions. The protein concentration of homogenized tissues was measured by protein assay (BCA1 and B9643, Sigma-Aldrich) and the expression of Aβ in tissues was calculated as Aβ42 pg/μg tissue protein.

2.6 Chemical Reagents and Standard Preparation

2.6.1 NO Generation

Standard NO solutions were prepared by two methods. For the macroelectrode experiments, pure NO gas was bubbled through deoxygenated 0.1 mol L^{-1} phosphate buffer (PB) pH 7.2 in a sealed ~50 mL glass vessel designed to exclude atmospheric oxygen. After bubbling for 30 min, the solution became saturated with the dissolved gas to produce an ~2 mmol L^{-1} NO solution under standard conditions.[34] Aliquots of this solution were then removed volumetrically with an airtight syringe and added to an electrochemical cell containing a known volume of deoxygenated 0.1 M PB pH 7.2 blanketed under N_2 gas. For the microelectrode experiments, NO-containing solutions were prepared using the NO donor, DEA-NONOate (Cayman Chemical, Ann Arbor, MI). DEA-NONOate spontaneously dissociates in a pH-dependent, first-order process to liberate 1.5 mol of NO per mole of parent compound at pH = 7.4 with a half-life of 2 min at 37 °C and 16 min at 22-25°C.[35,36] A 50 mmol L^{-1} DEA-NONOate stock solution was prepared by adding 0.96 mL of deoxygenated 0.01 mol L^{-1} NaOH to 10 mg of DEA-NONOate through an airtight syringe. Stock solutions were then prepared by further dilution with deaerated 0.01 mol L^{-1} NaOH and added volumetrically to a N_2-blanketed electrochemical cell containing 0.1 mol L^{-1} PB pH 7.4 through an airtight syringe. Electrochemical measurements were then initiated once the time-dependent NO release reached a maximum solution concentration (no more than 5 min, as verified by CA). DEA-

NONOate stock solutions were stored on ice and used within 24 h of preparation.

2.6.2 Reagents

Hexokinase from yeast (Hex, ≥150 units per mg protein) was purchased from Worthington (Lakewood, NJ) and used as received. Glucose oxidase from *Aspergillus niger* (Gox, 100,000-250,000 units/g solid), acetylcholinesterase from *Electrophorus electricus* (AChE ≥1000 units/mg protein), choline oxidase from *Alcaligenes sp.* (ChOx ≥10 units/mg solid), 5'-triphosphate disodium salt hydrate (ATP), 3,4-ethylenedioxythiophene (EDOT), tetrabutylammonium tetrafluoroborate ($TBABF_4$), dichloromethane (DCM), potassium hexachloroplatinate (K_2PtCl_6), perchloric acid ($HClO_4$), ultrahigh purity sulfuric acid (H_2SO_4, 99.999 %), sodium nitrite ($NaNO_2$), colloidal Nafion solution (5.0 % w/w), *m*-phenylenediamine flakes (*m*PD), bovine serum albumin (BSA), glutaraldehyde (25% in H_2O), acetylcholine chloride (ACh), choline chloride (Ch), L-ascorbic acid (AA), dopamine hydrochloride (DA), DL-norepinephrine hydrochloride (NE), and serotonin hydrochloride (5-HT) were purchased from Sigma Aldrich (St Louis, MO) and used as received. Isopropanol (IPA, 70 %) was distilled and stored over activated carbon prior to use.

2.6.3 Solution Preparation

All solutions were prepared using ultrapure water (>17 MΩcm), which was prepared using a Barnstead E-Pure purification system (Model D3750). Phosphate buffer (PB) was prepared from sodium phosphate monobasic (NaH_2PO_4, ≥ 99.0 %) and sodium phosphate dibasic (Na_2HPO_4, ≥ 99.0 %). Krebs buffer pH 7.4 (117 mmol L^{-1} NaCl, 4.7 mmol L^{-1} KCl, 2.5 mmol L^{-1} $CaCl_2$, 1.2 mmol L^{-1} $MgCl_2$, 1.2 mmol L^{-1} NaH_2PO_4, 25 mmol L^{-1} $NaHCO_3$, and 11 mmol L^{-1} glucose) was prepared fresh daily. For tissue measurements, nifedipine (1 µmol L^{-1}, Aldrich) and scopolamine (1 µmol L^{-1}) was added to the perfusing Krebs buffer and continuously applied throughout measurements. For ACh measurements, the scopolamine was excluded. The sodium channel

blocker tetrodotoxin (TTX, 0.3 or 0.5 μmol L^{-1}, Cayman Chemical, CAUTION: potent neurotoxin, use with extreme care), NOS inhibitor N-nitro-L-arginine (L-NNA, 100 μmol L^{-1}, Aldrich), and AChE inhibitor neostigmine (10 μmol L^{-1}, Aldrich) were also added continuously to the perfusing buffer during drug effect experiments.

2.7 Statistical Analysis

Replicate measurements (n = 3) were used to assess reproducibility and unless otherwise noted, data are presented as mean ± standard deviation (SD). Results from animal studies are reported as mean ± standard error of mean (SEM). Unpaired Student's *t*-tests were used to compare means between two groups, where a p-value < 0.05 was determined to be statistically significant. For animal studies, a sample size of n = 5-6 mice was used in each group. Two-way analysis of variance (ANOVA) and Bonferroni's *post hoc* test was used to compare changes in NO and ACh/Ch release among mice. Data was graphed and analyzed using both Origin 9.0 and GraphPad Prism 9.5.1 software.

REFERENCES

1. Park, J.; Galligan, J. J.; Fink, G. D.; Swain, G. M. *In Vitro* Continuous Amperometry with a Diamond Microelectrode Coupled with Video Microscopy for Simultaneously Monitoring Endogenous Norepinephrine and Its Effect on the Contractile Response of a Rat Mesenteric Artery. *Anal. Chem.* **2006**, *78*, 6756– 6764.

2. Park, J.; Quaiserová-Mocko, V.; Pecková, K.; Galligan, J. J.; Fink, G. D.; Swain, G. M. Fabrication, Characterization, and Application of a Diamond Microelectrode for Electrochemical Measurement of Norepinephrine Release from the Sympathetic Nervous System. *Diamond Relat. Mater.* **2006**, *15*, 761– 772.

3. Patel, B. A.; Rogers, M.; Wieder, T.; O'Hare, D.;. Boutelle, M. G. ATP Microelectrode Biosensor for Stable Long-Term *In Vitro* Monitoring From Gastrointestinal Tissue. *Biosens. Bioelectron.* 2011, **26**, 2890-2896.

4. Song, M. J.; Kim, J. H.; Lee, S. K.; Lim, D. S. Fabrication of Pt Nanoparticles-Decorated CVD Diamond Electrode for Biosensor Applications. *Anal. Sci.* **2011**, *27*, 985– 989.

5. Stoychev, D.; Papoutsis, A.; Kelaidopoulou, A.; Kokkinidis, G.; Milchev, A. Electrodeposition of Platinum on Metallic and Nonmetallic Substrates ─ Selection of Experimental Conditions. *Mater. Chem. Phys.* **2001**, *72*, 360– 365.

6. Zhan, D.; Velmurugan, J.; Mirkin, M. V. Adsorption/Desorption of Hydrogen on Pt Nanoelectrodes: Evidence of Surface Diffusion and Spillover. *J. Am. Chem. Soc.* **2009**, *131*, 14756– 14760.

7. Kucherenko, I. S.; Soldatkin, O. O.; Kucherenko, D. Y.; Soldatkina, O. V.; Dzyadevych, S. V. Advances in Nanomaterial Application in Enzyme-Based Electrochemical Biosensors: A Review. *Nanoscale Adv.* **2019**, *1*, 4560-4577.

8. Kim, C. S.; Oh, S. M. Enzyme Sensors Prepared by Electrodeposition on Platinized Platinum Electrodes. *Electrochim. Acta* **1996**, *41*(15), 2433-2439.

9. Reyes De Corcuera, J. I.; Cavalieri, R. P.; Powers, J. R. Improved Platinization Conditions Produce a 60-Fold Increase in Sensitivity of Amperometric Biosensors Using Glucose Oxidase Immobilized in Poly-*o*-phenylenediamine. *J. Electroanal. Chem.* **2005**, *575*(2), 229-241.

10. Li, Y.; Sella, C.; Lemaître, F.; Collignon, M. G.; Thouin, L.; Amatore, C. Highly Sensitive Platinum-Black Coated Platinum Electrodes for Electrochemical Detection of Hydrogen Peroxide and Nitrite in Microchannel. *Electroanalysis* **2013**, *25*(4), 895-902.

11. Peteu, S. F.; Russell, S. A.; Galligan, J. J.; Swain, G. M. An Electrochemical ATP Biosensor with Enzymes Entrapped within a PEDOT Film. *Electroanalysis* **2021**, *33*, 495– 505.

12. Henderson, S.; Bhardwaj, K.; Perugachi, V.; Espinoza-Montero, P.; Galligan, J. J.; Swain,

G. M. *In Vitro* Monitoring of Nitric Oxide Release in the Mouse Colon Using a Boron-Doped Diamond Microelectrode Modified with Platinum Nanoparticles and Nafion. *Anal. Chem.* **2023**, *95*(2), 1027-1037

13. Bennett, J. A.; Show, Y.; Wang, S.; Swain, G. M. Pulsed Galvanostatic Deposition of Pt Particles on Microcrystalline and Nanocrystalline Diamond Thin-Film Electrodes: I. Characterization of As-Deposited Metal/Diamond Surfaces. *J. Electrochem. Soc.* **2005**, *152*, E184.

14. Bennett, J. A.; Swain, G. M. Investigating the Nucleation and Growth of Electrodeposited Pt on Polycrystalline Diamond Electrodes. *J. Electrochem. Soc.* **2010**, *157*, F89– F95.

15. Barbosa, O.; Ortiz, C.; Berenguer-Murcia, A.; Torres, R.; Rodrigues, R. C.; Fernandez-Lafuente, R. Glutaraldehyde in Bio-Catalysts Design: A Useful Crosslinker and a Versatile Tool in Enzyme Immobilization. *RSC Adv.* **2014**, *4*(4), 1583-1600.

16. Sassolas, A.; Blum, L. J.; Leca-Bouvier, B. D. Immobilization Strategies to Develop Enzymatic Biosensors. *Biotechnol. Adv.* **2012**, *30*, 489-511.

17. Nguyen, H. H.; Kim, M. An Overview of Techniques in Enzyme Immobilization. *Appl. Sci. Converg. Technol.* **2017**, *26*(6), 157-163.

18. Patel, B. A. Electrochemical Biosensors. In *Electrochemistry for Bioanalysis*; Patel, B., Eds.; Elsevier: Amsterdam, 2020, pp 267-284.

19. Mitchell, K. M. Acetylcholine and Choline Amperometric Enzyme Sensors Characterized in Vitro and in Vivo. *Anal. Chem.* **2004**, *76*(4), 1098-1106.

20. Oakley, H.; Cole, S. L.; Logan, S.; Maus, E.; Shao, P.; Crat, J.; Guillozet-Bongaarts, A.; Ohno, M.; Disterhoft, J.; Van Eldik, L.; Berry, R.; Vassar, R. Intraneuronal β-Amyloid Aggregates, Neurodegeneration, and Neuron Loss in Transgenic Mice with Five Familial Alzheimer's Disease Mutations: Potential Factors in Amyloid Plaque Formation. *J. Neurosci*. **2006**, *26*(40), 10129-10140.

21. Ohno, M,; Chang, L.; Tseng, W.; Oakley, H.; Citron, M.; Klein, W. L.; Vassar, R.; Disterhoft, J. F. Temporal Memory Deficits in Alzheimer's Mouse Models: Rescue by Genetic Deletion of BACE1. *Eur. J. Neurosci*. **2006**, *23*(1), 251-260.

22. Stoye, N. M.; Dos Santos, G. M.; Endres, K. Alzheimer's Disease in the Gut-Major Changes in the Gut of 5xFAD Model Mice with ApoA1 as Potential Key Player. *FASEB J*. **2020**, *34*(9), 11883-11899.

23. Nguyen, V. T. T.; Brücker, L.; Volz, A. K.; Baumgärtner, J. C.; dos Santos Guilherme, M.; Valeri, F.; May-Simera, H.; Endres, K. Primary Cilia Structure Is Prolonged in Enteric Neurons of 5xFAD Alzheimer's Disease Model Mice. *Int. J. Mol. Sci*. **2021**, *22*(24), 13564.

24. Valeri, F.; Dos Santos Guilherme, M.; He, F.; Stoye, N. M.; Schwiertz, A.; Endres, K. Impact of the Age of Cecal Material Transfer Donors on Alzheimer's Disease Pathology

in 5xFAD Mice. *Microorganisms* **2021**, *9*(12), 2548.

25. Jankowsky, J. L.; Fadale, D. J.; Anderson, J.; Xu, G. M.; Gonzales, V.; Jenkins, N. A.; Copeland, N. G.; Lee, M. K.; Younkin, L. H.; Wagner, S. L.; Younkin, S. G.; Borchelt, D. R. Mutant Presenilins Specifically Elevate the Levels of the 42 Residue Beta-Amyloid Peptide *In Vivo*: Evidence for Augmentation of a 42-Specific Gamma Secretase. *Hum. Mol. Genet.* **2004**, *13*(2), 159-170.

26. Garcia-Alloza, M.; Robbins, E. M.; Zhang-Nunes, S. X.; Purcell, S. M.; Betensky, R. A.; Raju, S.; Prada, C.; Greenberg, S. M.; Bacskai, B. J.; Frosch, M. P. Characterization of Amyloid Deposition in the APPswe/PS1dE9 Mouse Model of Alzheimer Disease. *Neurobiol. Dis*. **2006**, *24*(3), 516-524.

27. Jackson, R. J.; Rudinskiy, N.; Herrmann, A. G.; Croft, S.; Kim, J. M.; Petrova, V.; Ramos-Rodriguez, J. J.; Pitstick, R.; Wegmann, S.; Garcia-Alloza, M.; Carlson, G. A.; Hyman, B. T.; Spires-Jones, T. L. Human Tau Increases Amyloid β Plaque Size But Not Amyloid β-Mediated Synapse Loss in a Novel Mouse Model of Alzheimer's Disease. *Eur. J. Neurosci*. **2016**, *44*(12), 3056-3066.

28. Kilgore, M.; Miller, C. A.; Fass, D. M.; Hennig, K. M.; Haggarty, S. J.; Sweatt, J. D.; Rumbaugh, G. Inhibitors of Class 1 Histone Deacetylases Reverse Contextual Memory Deficits in a Mouse Model of Alzheimer's Disease. *Neuropsychopharmacology*. **2010**, *35*(4), 870-880.

29. Lalonde, R.; Kim, H. D.; Maxwell, J. A.; Fukuchi, K. Exploratory Activity and Spatial Learning in 12-Month-Old APP(695)SWE/co+PS1/DeltaE9 Mice with Amyloid Plaques. *Neurosci. Lett*. **2005**, *390*(2), 87-92.

30. Han, X.; Tang, S.; Dong, L.; Song, L.; Dong, Y.; Wang, Y.; Du, Y. Loss of Nitrergic and Cholinergic Neurons in the Enterc Nervous System of APP/PS1 Transgenic Mouse Model. *Neurosci. Lett.* **2017**, *646*, 59-65. DOI: 10.1016/j.neulet.2017.01.061

31. Feng, J.; Dong, L.; Zhang, J.; Han, X.; Tang, S.; Song, L.; Cong, L.; Wang, X.; Wang, Y.; Du, Y. Unique Expression Pattern of KIBRA in the Enteric Nervous System of APP/PS1 Mice. *Neurosci. Lett.* **2018**, *675*(14), 41-47.

32. Manocha, G. D.; Floden, A. M.; Miller, N. M.; Smith, A. J.; Nagamoto-Combs, K.; Saito, T.; Saido, T. C.; Combs, C. K. Temporal Progression of Alzheimer's Disease in Brains and Intestines of Transgenic Mice. *Neurobiol. Aging* **2019**, *81*, 166-176.

33. Chen, Y.; Fang, L.; Zhou, H.; Fan, Y.; Lin, L.; Li, J.; Xu, J.; Chen, Y.; Ma, Y.; Chen, Y. Gut Microbiome Alterations Precede Cerebral Amyloidosis and Microglial Pathology in a Mouse Model of Alzheimer's Disease. *Biomed Res. Int*. **2020**, *2020*, 8456596.

34. Archer, S. L.; Shultz, P. J.; Warren, J. B.; Hampl, V.; DeMaster, E. G. Preparation of Standards and Measurement of Nitric Oxide, Nitroxyl, and Related Oxidation Products. *Methods* **1995**, *7*, 21– 34.

35. Amatore, C.; Arbault, S.; Bouret, Y.; Cauli, B.; Guille, M.; Rancillac, A.; Rossier, J. Nitric Oxide Release during Evoked Neuronal Activity in Cerebellum Slices: Detection with Platinized Carbon-Fiber Microelectrodes. *ChemPhysChem* **2006**, *7*, 181– 187

36. Li, Y.; Sella, C.; Lemaître, F.; Guille-Collignon, M.; Thouin, L.; Amatore, C. Electrochemical Detection of Nitric Oxide and Peroxynitrite Anion in Microchannels at Highly Sensitive Platinum-Black Coated Electrodes. Application to ROS and RNS Mixtures prior to Biological Investigations. *Electrochim. Acta* **2014**, *144*, 111– 118.

CHAPTER 3. AN ELECTROCHEMICAL ATP BIOSENSOR WITH ENZYMES ENTRAPPED WITHIN A PEDOT FILM

3.1 Introduction

ATP is a key neurosignaling molecule in the vasculature and the gastrointestinal tract.[1-5] For example, sympathetic nerves supplying blood vessels communicate with surrounding smooth muscle cells using norepinephrine and ATP.[1-4] In the gut, ATP functions as an inhibitory neuromuscular signaling molecule.[5-7] ATP is a critical determinant of mechanosensation and serotonin (5-HT) release.[8-12] ATP is also known to be released from glial cells and may mediate signaling by nearby neurons.[13,14] A goal of our current research is to gain a better understanding of how purinergic signaling in the gut is altered in disease. For this work, direct detection of ATP *in vitro* is necessary to study the temporal dynamics of release and clearance. Electrochemical methods with small microelectrodes and microsensors are ideal for such measurements.[15-19] Unfortunately, ATP is electrochemically inactive meaning that its direct detection as an oxidation or reduction current is not possible.

Various analytical methods have been used for the detection of ATP. Many of these, however, provide information about static or equilibrium concentrations of the analyte and not on temporal changes in concentration, for example, near the sites of neurogenic release and action. For example, luciferase-based bioluminescence is considered the gold standard for in situ ATP detection even at sub-nanomolar concentrations.[20] There are techniques that can be used to measure physiologically relevant ATP concentrations including: spectrophotometry,[21] liquid chromatography,[22-25] fluorescence,[26,27] chemiluminescence,[28-30] bioluminescence[31,32] and electrochemical methods using potentiometric[33,34] and amperometric biosensors.[35-49] Of these, only the electrochemical biosensors would be useful for transient changes in ATP concentration *in vitro* or *in vivo* near the sites of release.

Reports have emerged in recent years on electrodes modified with aptamers for the selective detection of ATP and metabolites, as exemplified in these selected citations.[50-53] One aptamer-based electrochemical sensor was applied for the direct real-time detection of ATP released from cultured astrocyte cells.[50] The aptamer-based methods for ATP detection provide excellent detection figures of merit, but generally are not suitable for measuring rapid changes in analyte concentration. Amperometric ATP biosensors have been prepared and employed with a common design using hexokinase (Hex) and glucose oxidase (GOx) incorporated within a polymer matrix.[35,36,38,40,43-45] This dual enzyme biosensor reports changes in the ATP concentration indirectly via reduction of the glucose concentration in solution as the substrate reacts with ATP at Hex to form glucose 3-phosphate.[35,36,38,40,43-45] This reduces the H_2O_2 concentration at the electrode, which is detected as a decrease in the oxidation current at +0.85 V vs. Ag/ AgCl. The H_2O_2 is produced by GOx at a level that is directly proportional to the glucose concentration in solution. Glucose is added at a constant concentration in the measurement buffer when this type of biosensor is used.

Herein, the electrochemical behavior of an ATP biosensor with GOx and Hex immobilized within an electroactive poly(3,4-ethylenedioxythiophene) (PEDOT) polymer film on a "platinized" Pt microelectrode is reported. Amperometric detection of ATP, via the oxidation current for H_2O_2 at 0.85 V vs. Ag/AgCl, yielded the following figures of merit: a response time of 15±1 s, an experimental detection limit (S/N=3) of 10.0± 0.2 μmol L^{-1} and a sensitivity of 100–500 mA M^{-1} cm^{-2}. A unique feature of this ATP biosensor design is the fact that improved selectivity for ATP can be achieved by amperometric detection at 0.20 V vs. Ag/AgCl. The new science reported is the effective use of PEDOT for immobilizing the enzymes, the improved biosensor response stability when using a platinized Pt microelectrode, and the improved response selectivity with detection at -0.20 V.

3.2 Results

The indirect detection mechanism for ATP by the biosensor is shown in Figure 3.1. At 0.85 V vs. Ag/AgCl, ATP is indirectly detected based on the oxidation current for enzymatically produced H_2O_2. The glucose concentration in the Krebs buffer is constant (11 mmol L^{-1}) and this leads to a constant H_2O_2 oxidation current in the amperometric detection mode in the absence of ATP. When ATP is present, glucose is consumed along with ATP by Hex and this leads to a decrease in the glucose concentration near the electrode. The decreased glucose concentration at GOx sites leads to a reduction in the H_2O_2 produced and a lower oxidation current. The current decrease is proportional to the ATP concentration in solution.

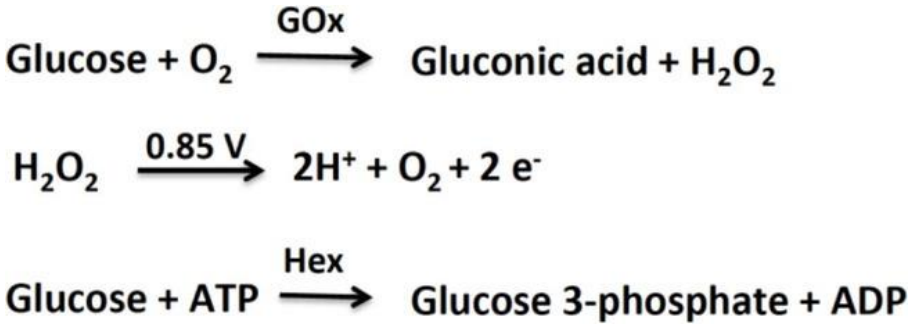

Figure 3.1. The enzymatic scheme and detection mechanism for ATP using the microelectrode biosensor poised at 0.85 V vs. Ag/AgCl.

The active dual enzyme layer was formed on the Pt microelectrode by potential cycling in a solution of GOx-Hex-EDOT in $TBABF_4$+DCM. Figure 3.2 shows a series of cyclic voltammograms recorded with increasing cycle number. There is a progressive increase in the oxidation current and charge on the forward (positive potential going) sweep and reduction current and charge on the reverse sweep as the polymer grows thicker on the electrode. The oxidized polymer has positive charges every few monomeric units along the polymeric backbone. The positively charged network acts as a conduit for electronic conduction. During synthesis, counter anions, or dopants, are transported into the conducting polymer to charge balance on the positively

charged sites. The growth of the conductive PEDOT film entraps the enzymes and also provides a conductive pathway to transport electrons from the enzyme sites to the electrode during detection at 0.85 V. ATP diffuses through pores and channels of the polymer to the active enzyme sites. The H_2O_2 produced internally in the PEDOT is presumably oxidized at exposed Pt sites at the base of the polymer layer.

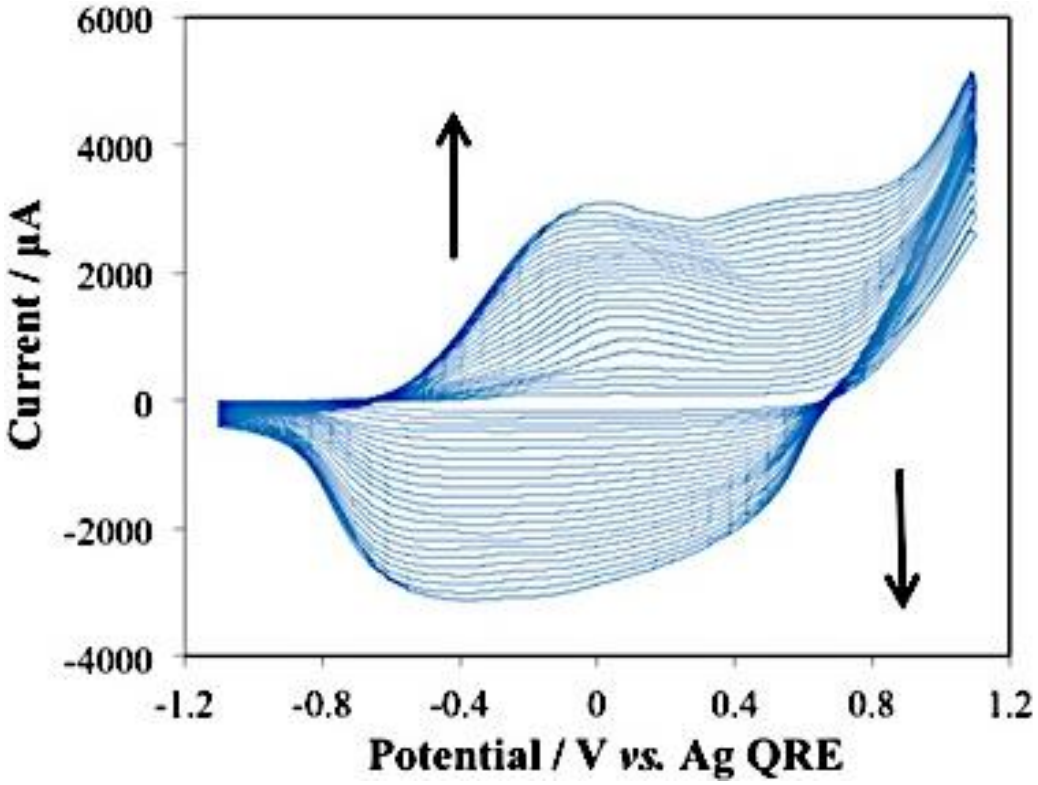

Figure 3.2. Cyclic voltammetry *i-E* curves recorded with increasing cycle number for a Pt microelectrode in 4.5 mol L^{-1} EDOT, 0.1 mol L^{-1} $TBABF_4$, 10 mg mL^{-1} GOx, and 40 mg mL^{-1} Hex in deoxygenated DCM. Cycling was performed at 50 mV s^{-1}. The arrows indicate the current increase with cycle number.

The progressive increase in voltammetric current and charge with cycle number reflects the growth of an electroactive PEDOT film.[54-60] The electropolymerization involves an electrogenerated EDOT cation radical as the reactive species. PEDOT formation then proceeds through a series of radical coupling reactions and electrochemical reoxidations.[58,60]

The PEDOT film morphology was studied by SEM. Characteristic electron micrographs are

presented in Figure 3.3 for a PEDOT-GOx-Hex polymer film deposited on a Pt microelectrode using 25 potential cycles. The lower magnification micrograph (a) reveals a granular polymer morphology across the surface. The polymer formed over all regions of the exposed wire as no uncoated areas were found. The higher magnification micrograph (b) reveals 1–2 μm diameter polymer aggregates that consist of 250–500 nm diameter rounded particles. Each aggregate is connected to others forming a 3D polymer network. Importantly, the micrograph reveals the presence of pores and channels between the aggregates through which ATP and glucose can presumably penetrate to reach the internal enzyme sites. This nanostructured "cauliflower-like" morphology is characteristic of a 3-D branched multi-globular polymer.

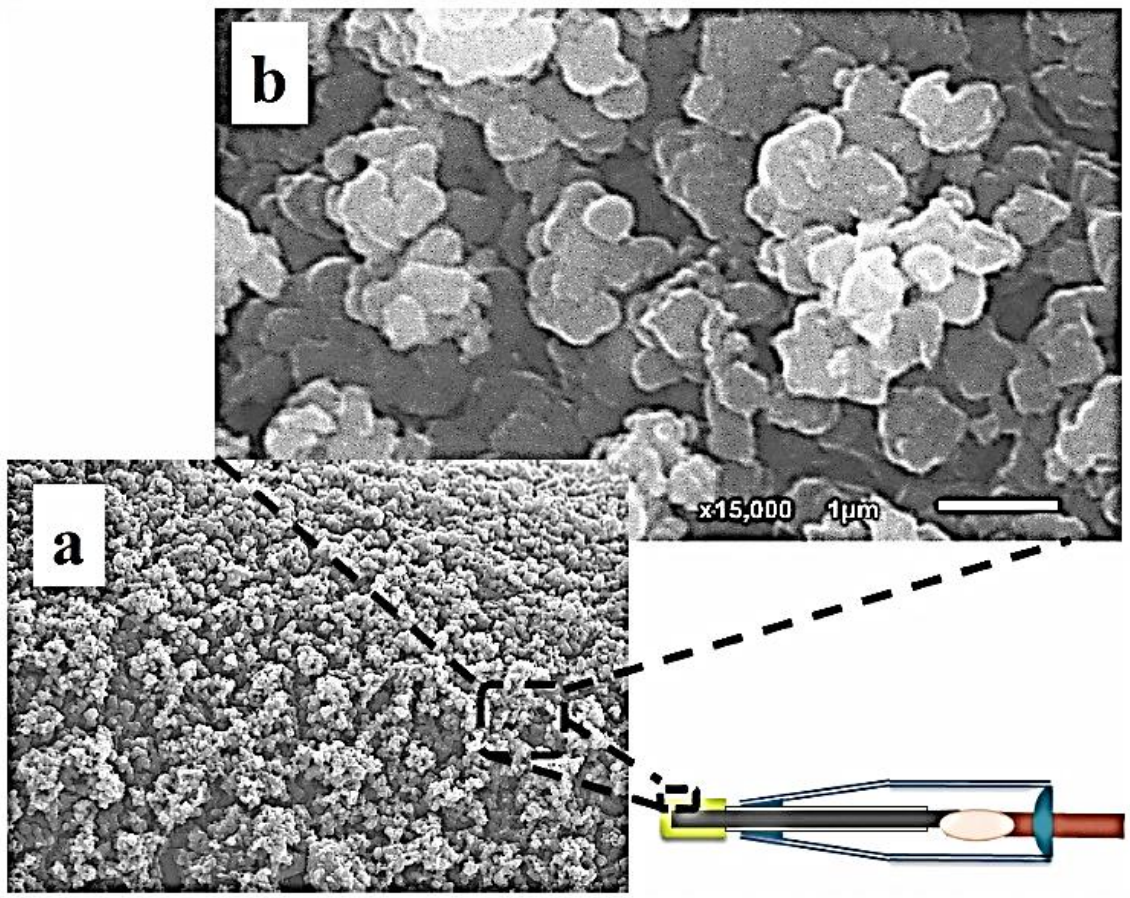

Figure 3.3. SEM micrographs of the PEDOT-GOx-Hex layer on a Pt microelectrode at (a) low and (b) high magnification. The polymer layer was formed using 25 potential cycles, as described in Figure 3.2.

Figure 3.4 shows cyclic voltammetric *i-E* curves for the biosensor in solutions of ATP in Krebs buffer, pH 7.4. Curves are shown for increasing ATP concentration from 0 to 100 μmol L^{-1}. The oxidation current at 0.85 V on the forward sweep decreases, as expected, with increasing ATP concentration (see Scheme 3.1). Glucose is consumed along with ATP at the Hex sites and this leads to a reduced concentration of glucose at the GOx sites. Therefore, there is less H_2O_2 produced in the vicinity of the Pt microelectrode to be oxidatively detected. At potentials positive of 1.1 V, there is a significant increase in the current that also trends in a decreasing manner with increasing ATP concentration. This current is associated with the overoxidation of the PEDOT[56,59,60] The overoxidation produces an increased number of charged states in the polymer backbone and results in the incorporation of carbon-oxygen functional groups along the polymer chains. This current decreases with increasing ATP concentration also due to a reduced concentration of produced H_2O_2. Even with the larger current, the signal-to-noise ratio was found to be better at the less positive detection potential of 0.85 V. Note that on the reverse sweep, the reduction current at −0.20 V also decreases with increasing ATP concentration. This current can also be used for ATP detection, as will be discussed below.

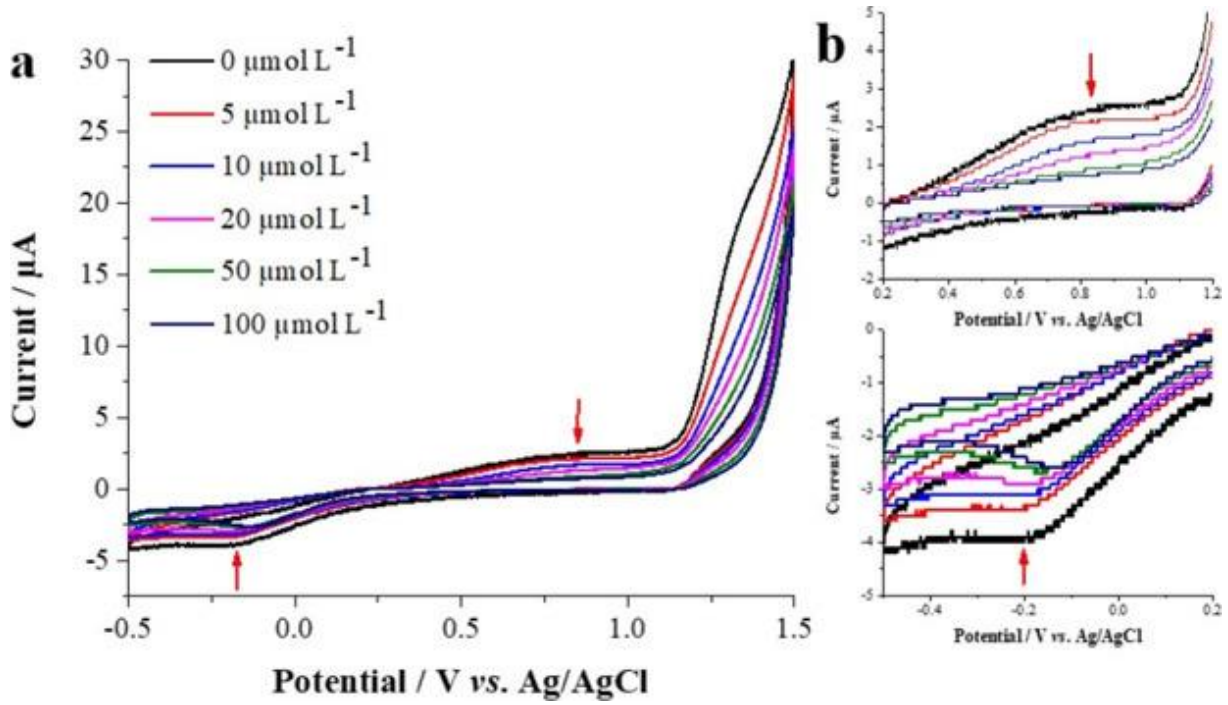

Figure 3.4. (a) Cyclic voltammetry *i-E* curves for the ATP biosensor in solutions of varying ATP concentration in Krebs buffer, pH 7.4. The scan rate was 100 mV s^{-1} with the 10^{th} scan presented for each concentration measured. The curves reveal that ATP detection can be accomplished using either the oxidation current 0.85 V or the reduction current at −0.20 V, as indicated by arrows. The PEDOT-GOx-Hex film was formed on the Pt wire using 100 cycles. (b) Shows expanded views of the voltametric i-E curves in the 0.85 and −0.20 V potential regions.

ATP detection was performed using continuous amperometry with the biosensor poised at 0.85 V vs. Ag/AgCl. The current was recorded in response to serial additions of 10 µmol L^{-1}, 20 µmol L^{-1}, and 50 µmol L^{-1} ATP, prepared from a 5 mmol L^{-1} ATP stock solution, to 10 mL of stirred Krebs buffer solution. As seen in Figure 3.5, the current decreases proportionally with increasing ATP concentration. The arrows indicate the point where the stock solution addition was made. The lowest detectable concentration in this detection mode was 10.0±0.2 µmol L^{-1} (S/N=3) with a 15±1 s response time. The response time is defined as the time required to reach 90 % of the maximum current response. The data were not smoothed in anyway. The fluctuations in current on the diffusion-limited current plateaus resulted from the magnetic stirrer.

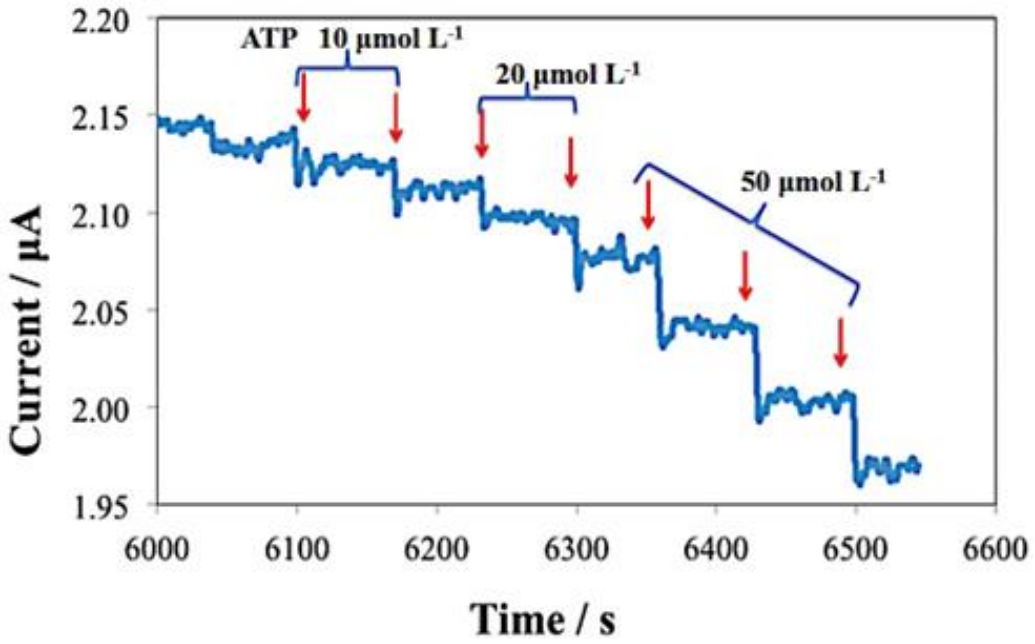

Figure 3.5. Continuous amperometry *i-t* curves for an ATP biosensor at 0.85 V vs. Ag/AgCl during serial additions of 10 µmol L^{-1}, 20 µmol L^{-1}, and 50 µmol L^{-1} ATP to stirred Krebs buffer, pH 7.4. The PEDOT-GOx-Hex film was formed on the Pt wire using 100 cycles. The solution concentration of ATP after each serial addition is shown in the figure.

The biosensor response reproducibility was assessed based on the current measured at 0.85 V for repeat additions of 20 µmol L^{-1} ATP to a stirred Krebs buffer solution. The reproducibility was assessed in this experiment using five biosensors prepared in an identical manner. The relative standard deviation (RSD) of the current response was 6.5 %. This indicates that the ATP biosensor, freshly prepared, provides acceptable reproducibility.

The response variability for a single biosensor was also assessed using 20 repeat additions of 20 µmol L^{-1} ATP into a stirred Krebs buffer solution at pH 7.4. Figure 3.6a shows amperometric current traces at 0.85 V for sequential additions of ATP. The response variability for this particular biosensor was unusually high with an RSD of 14.6 %. Generally, though, the short-term response variability of a single biosensor was less than 10 % for 10–20 additions. For example, another biosensor prepared using 50 PEDOT electropolymerization cycles produced a current response of 17.8±0.7 nA for nine serial additions of 20 µM ATP added to 10 mL of room temperature,

magnetically stirred Krebs buffer pH 7.4 (~20 μL from a 10 mM ATP stock solution). This is an RSD of 3.7 %, indicating good reproducibility. Figure 3.6b shows a typical linear response curve for a single biosensor. Response linearity is observed from at least 10 to 200 μmol L^{-1} (R^2=0.9985). Single measurements at each concentration are presented.

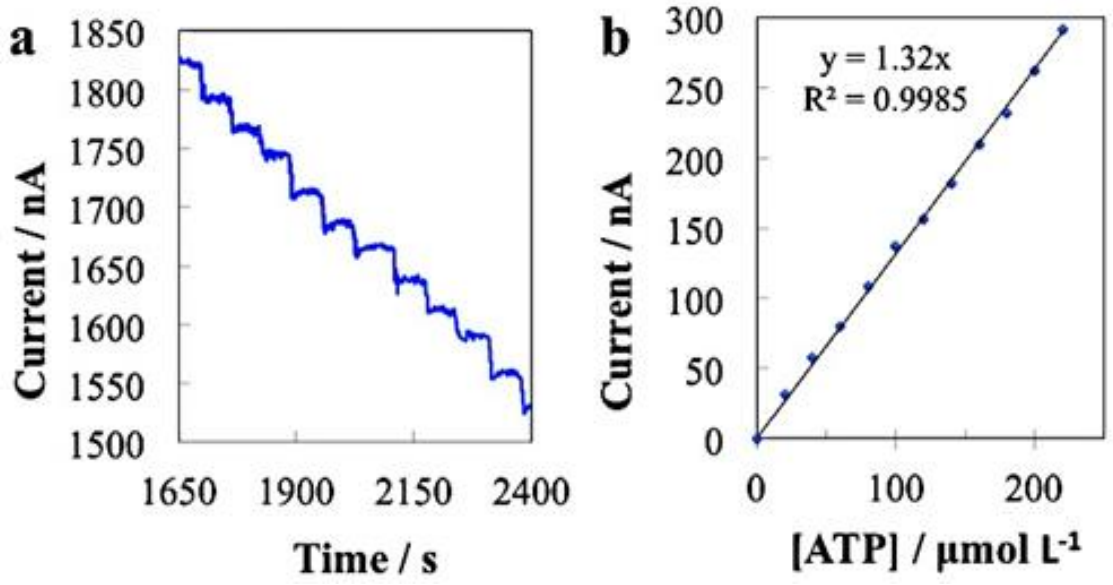

Figure 3.6. (a) Reproducibility of a single ATP biosensor as depicted by the amperometric current response for 11 of 20 sequential additions of 20 μmol L^{-1} ATP to a stirred Krebs buffer solution at pH 7.4. (b) A response curve generated using the same biosensor for different concentrations of ATP. Detection was made at 0.85 V vs. Ag/AgCl. The PEDOT-GOx-Hex film was formed on the Pt wire using 100 potential cycles.

The biosensor response stability and shelf-life were evaluated. Measurements using the biosensor prepared with the PEDOT-GOx-Hex film on a smooth Pt wire using 100 cycles between −1.1 and 1.1 V vs. Ag QRE revealed poor response stability over 1–3 day period after preparation when stored in a refrigerator in a humid headspace above a phosphate buffer solution, pH 7.4. For example, the oxidation current at 0.85 V decreased by 50 % generally within one day of preparation and storage. This poor response stability was observed with multiple biosensors. Adhesion of the polymer film to the smooth Pt wire appeared to be a cause for the response loss as fragments of the polymer layer, and presumably the enzymes, detached in solution during the testing. To improve

the polymer adhesion, the smooth Pt wire was roughened by platinization in 1 $mmol^{-1}$ potassium hexachloroplatinate (K_2PtCl_6) dissolved 0.1 mol L^{-1} $HClO_4$.[61-65] The platinization was accomplished by potential cycling between 0.3 and 1.2 V vs. Ag/AgCl. The platinization was performed prior to electrochemically depositing the PEDOT/GOx/Hex sensing film. Figure 3.7 shows SEM micrographs (all at 10,000x magnification) of the Pt wire before and after platinization with different potential cycle numbers. There are debris or dust particles visible at isolated spots, but otherwise the Pt wire is smooth at this magnification (a). The electrodeposited Pt nanoparticles are evident in the micrographs for the different cycle numbers (b-e). At low cycle number (10 cycles), spherical nanometer particles *ca*. 50 to 200 nm in diameter decorate the surface (b). The metal coverage increases, and the particles grow larger in size with increasing cycle number (40 cycles) (c). The particles coalesce forming aggregates, some spherical and some more elongated in shape, with increasing cycle number (80 cycles) (d). The particle size is *ca*. 250 nm after 40 cycles (c) and *ca*. 750 nm after 80 cycles (d). After 160 cycles (e), a full and thick layer of the metal is formed making the surface morphology appear relatively smooth at this magnification. Optimal deposition was determined to be 40 cycles.

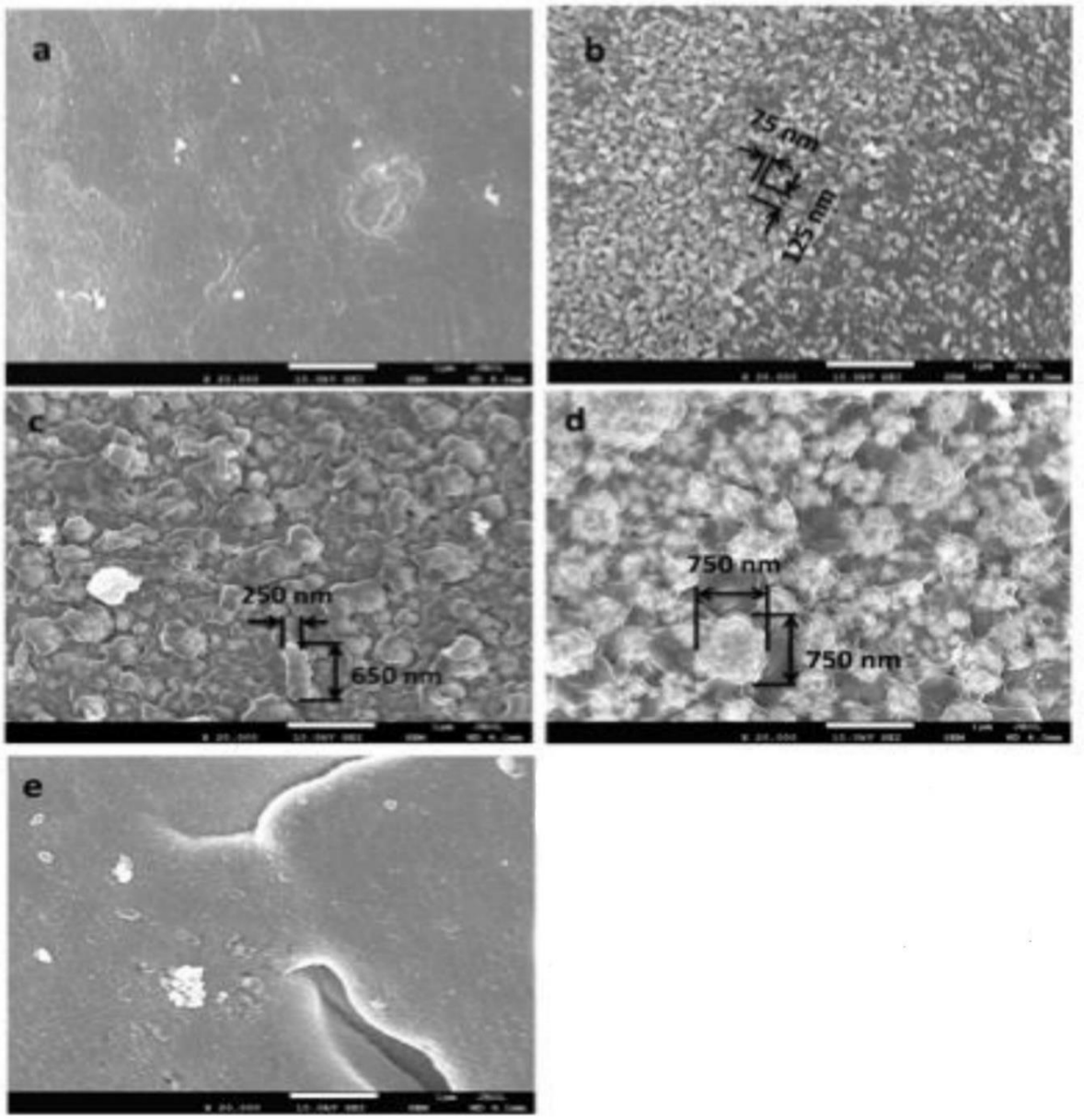

Figure 3.7. Scanning electron micrographs of a Pt wire and platinized-Pt wire, all at a magnification of 10,000x. (a) Before and (b) after platinization with 10 potential cycles. The micrographs in (c-e) show the Pt wire after platinization using (c) 40, (d) 80, and (e) 160 potential cycles. Energy-dispersive x-ray analysis confirmed the nanoparticles to be Pt.

Experiments were performed to learn if improved adhesion of the polymer film could be achieved by platinizing the surface. The roughness increase should improve the physical interlocking of the PEDOT polymer with the electrode surface, thereby improving the adhesion. Figure 3.8a presents cyclic voltammograms for the Pt wire before and after platinization (40 cycles).

Cyclic voltammetry *i-E* curves in 0.5 mol L^{-1} H_2SO_4 reveal a significant increase in the surface area of exposed metal after platinization, as expected. The charge for hydrogen adsorption and desorption (0.1 to −0.2 V), Pt oxide formation (0.9 V) and Pt oxide reduction (0.5 V) are all increased after platinization.[61-65] Figure 3.8b reveals the biosensor response stability is significantly improved after the platinization. The ATP biosensor formed on the platinized wire lost only 40 % of its initial response after one week and less than 10 % after three days. This compares with over 80 % signal loss within 3 days for the biosensor formed on the smooth Pt wire. In fact, for the platinized biosensor, the response stabilized at 60 % of the initial response even after 7 days. In between tests, all biosensors were stored at 4 °C in a sealed glass vial in the presence of 0.1 mol L^{-1} phosphate buffer solution, pH 7.4. The biosensor tip was not immersed in the buffer but rather was suspended in a humid headspace 2–4 mm above the liquid phase. Optimization experiments revealed this is the best storage condition for the biosensor. The improved stability is consistent with what has been reported for an ATP biosensor using GOx and Hex incorporated within a sol-gel membrane.[66]

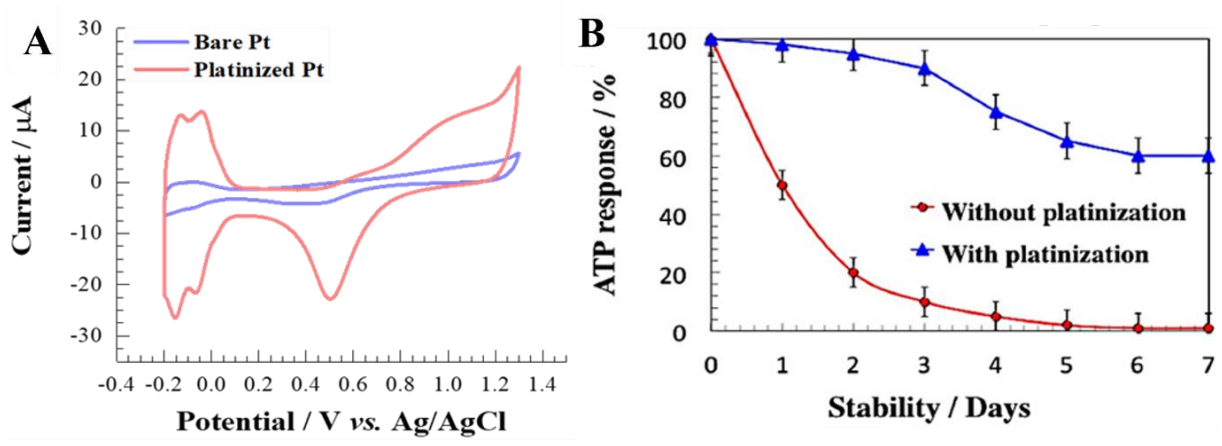

Figure 3.8. (A) Cyclic voltammetry i-E curves for a 50 µm diameter Pt wire in 0.5 mol L^{-1} H_2SO_4 before and after platinization using 40 potential cycles. Scan rate was 0.1 V s^{-1}. The hydrogen desorption charge for the Pt wire was 2.7 and 37.5 µC before and after the platinization, respectively. (B) Plots of the response stability over time for ATP biosensors prepared on an unmodified Pt wire and a Pt wire platinized using 40 cycles. The PEDOT-GOx-Hex film was

Figure 3.8. (cont'd)

formed on the Pt wire using 100 potential cycles. The sensor response was recorded at 0.85 V using 20 μmol L^{-1} additions of ATP to continuously stirred Krebs buffer. Data are presented as mean ± std. dev. for n=3 biosensors.

The selectivity of the biosensor was evaluated against other oxidizable interferents.[67,68] One of our target applications for the biosensor is the *in vitro* measurement of ATP release from sympathetic nerves supplying blood vessels. Sympathetic nerves release both ATP and norepinephrine (NE) with both functioning as vasoconstrictors to regulate vascular tone.[1-4,16] Therefore, for this application, it is important to know if the biosensor responds to NE. Figure 3.8A shows that the oxidation current at 0.85 V and the reduction current at −0.20 V decrease proportionally with the ATP concentration. Figure 3.8B shows a decrease in the current at −0.20 V for four repeat injections of 20 μmol L^{-1} ATP, −23±9 nA. There is little oxidation current at this potential for repeat additions of 20 μmol L^{-1} norepinephrine (NE). This shows that ATP can be selectively detected at this potential in the presence of NE. In contrast, Figure 3.8C shows a reproducible decrease in the current for four repeat additions of 20 μmol L^{-1} ATP, −23±5 nA. However, a significant oxidation current for 20 μmol L^{-1} NE is seen at this potential, 150±10 nA. Clearly, ATP cannot be selectively detected in the presence of NE at this positive potential.

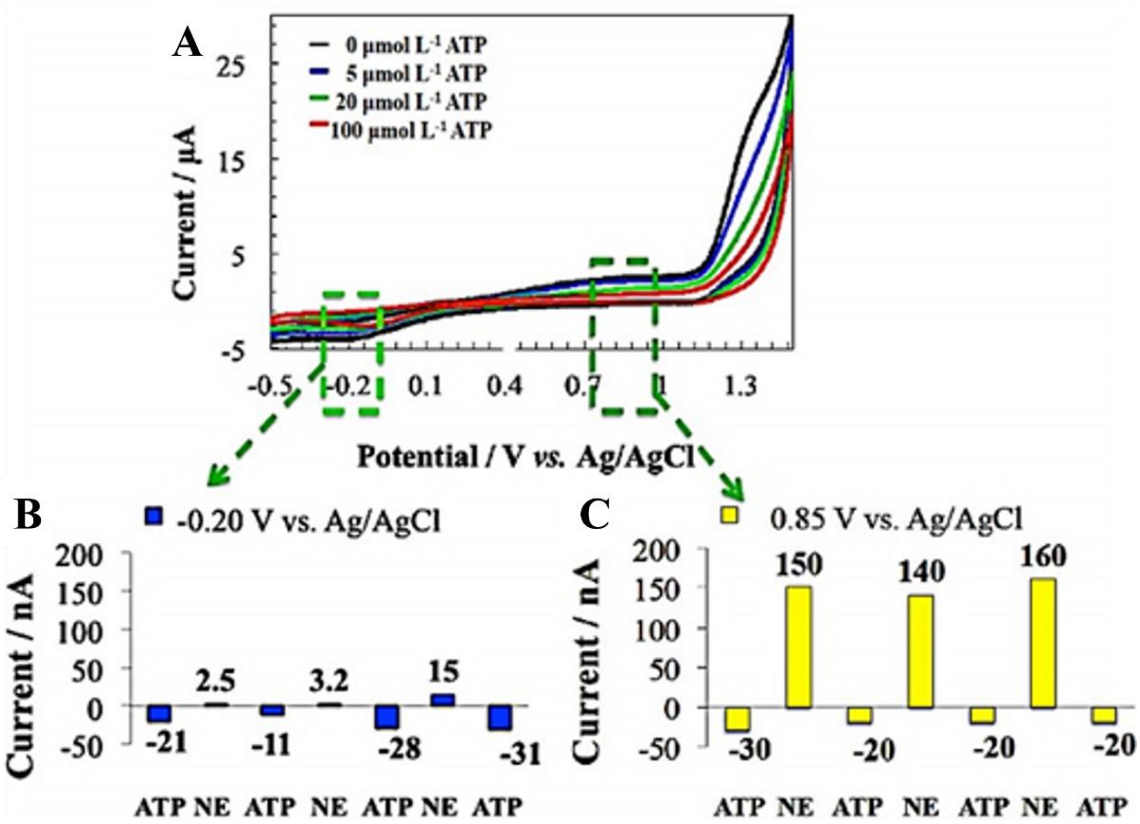

Figure 3.9. (A) Cyclic voltammetry i-E curves for the PEDOT/GOx/Hex biosensor in different concentrations of ATP in Krebs buffer, pH 7.4. Amperometric current magnitudes are presented for alternating additions of 20 µmol L^{-1} ATP and 20 µmol L^{-1} norepinephrine (NE) in stirred Krebs buffer with the biosensor poised at (B) 0.85 and (C) −0.20 V. The electrode was platinized using 40 potential cycles at 50 mV s^{-1}. The PEDOT-GOx-Hex film was formed on the Pt wire using 100 potential cycles.

The NE oxidation is occurring at the conducting polymer/solution interface or at exposed Pt sites within the polymer. Other oxidizable bioanalytes (*e. g.*, catechol and indole amines, uric acid, ascorbic acid) were also tested with robust oxidation currents measured for all at 0.85 V (data not shown). Therefore, the biosensor operated at 0.85 V is not selective for ATP in the presence of the oxidizable bioanalytes. Detection of ATP at −0.20 V occurs by the redox reaction proposed in Figure 3.10. At this potential, the cathodic current passed is due to the reduction of the oxidized conducting polymer. However, when ATP is present, the H_2O_2 that is produced at the GOx sites can reoxidize the polymer back to the conducting state and this leads to added cathodic current—a sort of catalytic current.

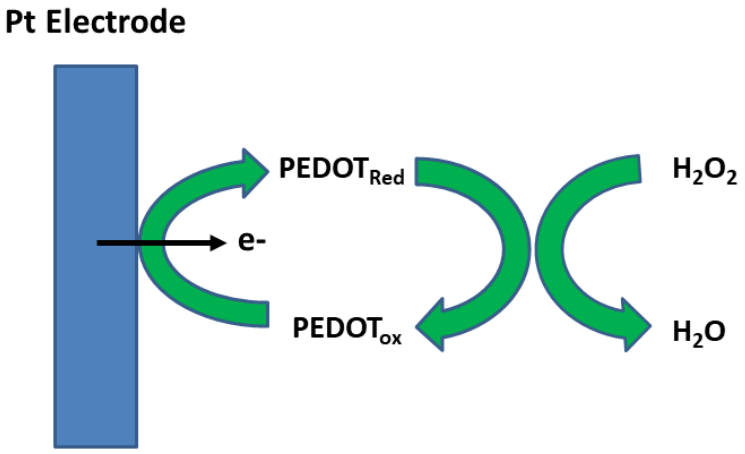

Figure 3.10. Electrochemical reaction scheme for the detection of ATP (i. e., H_2O_2 produced at GOx sites) at −0.20 V using the PEDOT/GOx/Hex biosensor.

The selectivity of the biosensor at −0.20 V vs. Ag/AgCl was evaluated against multiple potential electroactive interferents: 10 μmol L^{-1} uric acid (UA), 10 μmol L^{-1} ascorbic acid (AA), 2 μmol L^{-1} serotonin (5-HT) and 2 μmol L^{-1} NE. The results are presented in Figure 3.11. It can be seen that there are large negative currents for the ATP additions. There is, however, minimal current response for any of the added interferents as all are oxidizable, but not at this detection potential. A reproducible negative current of about 8 nA is observed for the two injections of 60 μmol L^{-1} ATP, before and after exposure of the biosensor to the interferents.

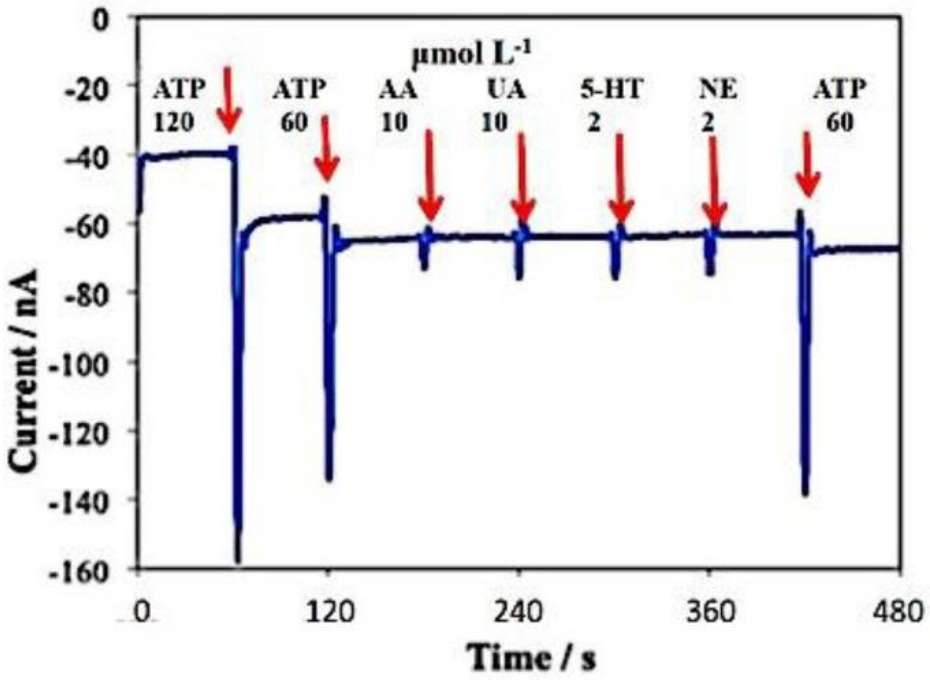

Figure 3.11. Selectivity of the PEDOT/GOx/Hex biosensor for ATP (120 and 60 µmol L^{-1}) in the presence of added interferents: 10 µmol L^{-1} UA, 10 µmol L^{-1} AA, 2 µmol L^{-1} 5-HT and 2 µmol L^{-1} NE. Detection was made at −0.20 V vs. Ag/AgCl in stirred Krebs buffer, pH 7.4, at room temperature. The electrode was platinized for 40 cycles at 0.05 V s^{-1}. The PEDOT-GOx-Hex film was formed on the Pt wire using 100 potential cycles.

The ATP biosensor response linear dynamic range and sensitivity were evaluated and compared at 0.85, 1.1 (overoxidation of the PEDOT), and −0.20 V. Only one biosensor was used in these studies with replicate measurements made at each concentration. At each potential, the current response was recorded as a function of the ATP concentration in stirred Krebs buffer under natural aeration conditions and O_2 saturation. The O_2 saturation was achieved by sparging the buffer solution with oxygen gas for 30 min prior to the measurements. The representative response curves are presented in Figure 3.12. The overoxidation at 1.1 V produces a larger current response than is recorded at 0.85 V, but it is also associated with a larger level of background noise. The sensitivity at 1.1 V is about 3× higher under natural aeration conditions and 2x higher under O_2 saturation than the sensitivity of the measurement at 0.85 V. Importantly, the sensitivity at −0.20 V is similar to that at 0.85 V under both natural aeration and O_2 saturation. In all cases, good response linearity

was observed from 20–100 μmol L^{-1}. The higher sensitivity at all potentials for O_2 saturated solutions is due to a greater concentration of dissolved O_2 than is present under natural aeration. Dissolved O_2 is essential for the production of H_2O_2 at GOx sites (see Figure 3.1).

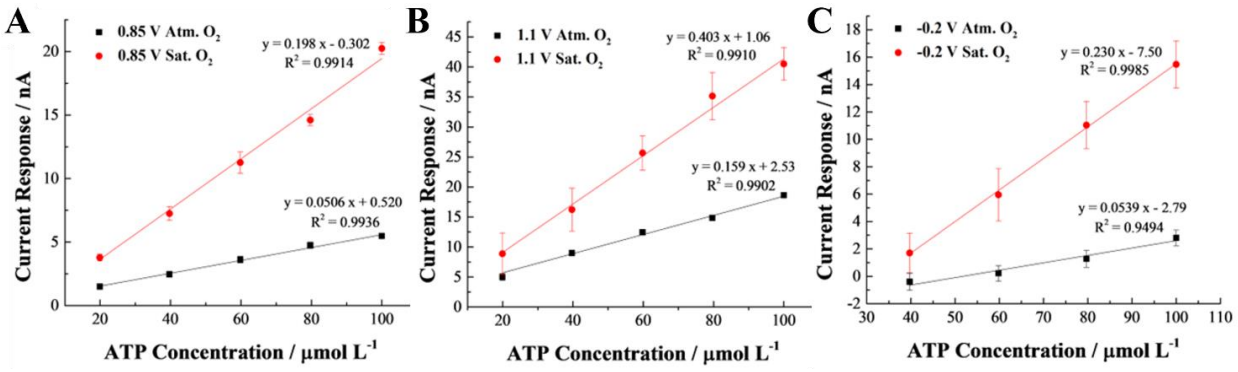

Figure 3.12. Assessment of the response sensitivity of the same ATP biosensor at three different detection potentials (A) 0.85, (B) 1.1 and (C) −0.20 V. Reference: Ag/AgCl. Measurements were recorded from 20–100 or 40–100 μmol L^{-1}. The response curves were generated under conditions of natural aeration and O_2 saturation. Values are reported as mean ± std. dev. for an 80 s average of the current at each ATP concentration. Error bars for the black curves in a and b are within the size of the marker. The electrode was platinized for 20 cycles at 0.05 V s^{-1} and electrocoating with the PEDOT-GOx-Hex polymer film was performed between −0.4 to 1.4 V vs Ag QRE at 50 mV s^{-1} for 50 cycles.

One issue of concern with the PEDOT/GOx/Hex biosensor is the exposure of the enzymes to the organic solvent, DCM that is used as the solvent for dissolving the EDOT monomer and electropolymerizing the PEDOT layer. The concern is enzyme deactivation in the organic solvent. Control experiments were performed to determine if exposure of the enzymes to DCM produces any deactivation, presumably by denaturation. In these experiments, an ATP biosensor was prepared according to the design of Patel *et al.*[40] This design incorporates GOx and Hex into a polyphenol film formed in aqueous solution. The response of the biosensor was first tested against 40 μmol L^{-1} ATP and 40 μmol L^{-1} glucose. The results are presented in Figure 3.13. Three successive additions of ATP to the stirred Krebs buffer solution produced reproducible decreased currents of *ca*. 60 nA. This measurement assessed the activity of both GOx and Hex. Then, a solution of just 40 μmol L^{-1} glucose was added to check the activity of GOx. A decreased current

of *ca*. 20 nA was measured. The biosensor was then immersed in DCM for 50 min as this replicated the immersion time in the solvent when forming the PEDOT layer. It can be seen that current change for 40 μmol L^{-1} ATP decreased by 75 % to *ca*. 15 nA, while the response to glucose decreased by only about 20 % to *ca*. 15 nA. These results indicate that the Hex activity is significantly more affected by the organic solvent than is GOx activity. It is supposed this is the reason our current version of the biosensor is not able to achieve lower detection limits, as are other ATP biosensors reported in the literature. To address this problem, efforts are underway to form the PEDOT layer from an aqueous monomer solution.

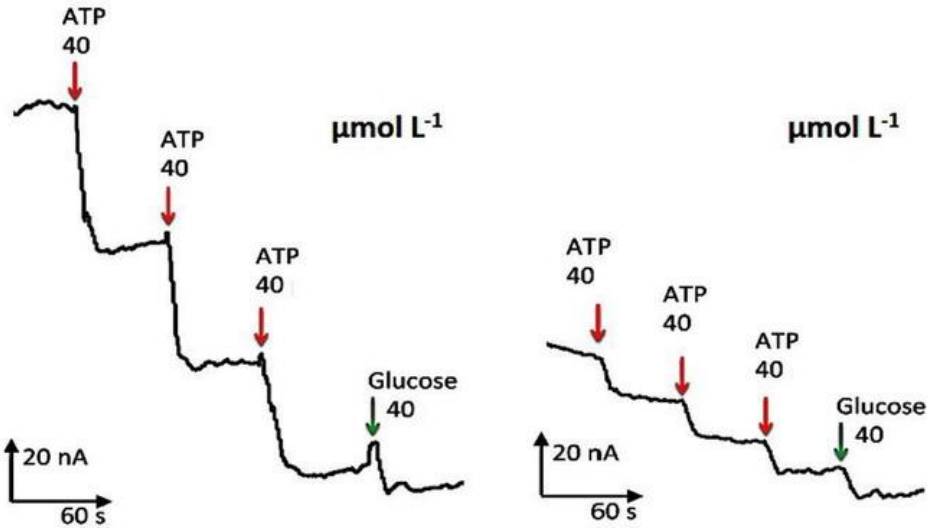

Figure 3.13. Amperometric current responses for ATP and glucose at a biosensor prepared by incorporating GOx and Hex into a polyphenol film in aqueous solution.[40] The biosensor was poised at 0.85 V for the additions of ATP and glucose in stirred Krebs buffer before (left) and after (right) a 50-min immersion in dichloromethane. The electrode was platinized for 40 cycles at 0.05 V s^{-1}. The biosensor was prepared by immersing the Pt wire in a solution containing 50 mmol L^{-1} phenol, 40 mg mL^{-1} Hex and 10 mg mL^{-1} GOx for 10 min. This was followed by poising the electrode at 0 V for 20 s followed by a step to +0.9 V for 10 min, and then back to 0 V for 20 s to form the polyphenol layer with the entrapped enzymes.

3.3 Discussion

The results demonstrate the PEDOT/GOx/Hex biosensor responds to ATP indirectly by either oxidizing the enzymatically produced H_2O_2 at 0.85 V, or by reduction of conducting polymer

sites at −0.20 V that are reoxidized by the H_2O_2. In absence of ATP, a constant amount of H_2O_2 is produced near the electrode when the concentration of glucose present in Krebs buffer is held constant. As ATP is introduced into the solution, glucose is consumed alongside ATP by the Hex enzymatic reaction. This reduces the glucose concentration at the GOx sites within the polymer and decreases the current associated with the oxidation of H_2O_2 formed locally.

One aspect of the new science reported herein is the improved longer-term response stability of the biosensor layer on a Pt microelectrode roughened by platinization. The rougher surface apparently leads to better polymer layer adhesion due to greater physical interlocking between the polymer layer and electrode. Stable biosensor responses of 90 % of the original signal over three days of storage and a stable 60 % of the original signal after seven days of storage were observed.

The second aspect of the new science is the significantly improved selectivity of the biosensor for ATP when operated at −0.20 V vs. Ag/AgCl. Various oxidizable interferences that would be present in the *in vitro* measurements planned for the biosensor do not contribute to the current response at the negative potential of −0.20 V as they do at 0.85 V. This is a very important finding and is made possible by the use of the conducting polymer PEDOT. The linear dynamic range, sensitivity and reproducibility of the biosensor response in pure solutions of ATP are similar at the two detection potentials, while the response selectivity is dramatically improved at the negative detection potential.

A limitation of the current biosensor design is the fact that the experimentally determined limit of detection (S/N=3) is *ca*. 10 μmol L^{-1}, or slightly lower. This LOD is higher than what is envisioned being needed for the planned ATP measurements *in vitro*. For such measurements, an LOD of 0.1 to 1 μmol L^{-1} is needed based on past work. Additionally, the LOD obtained with the biosensor is not as low as several of the other ATP biosensor designs reported on in the literature

(see Table 3.1). A reason for this is the utilization of DCM as the solvent for the PEDOT electropolymerization step. The control data reported above indicate that the activity of Hex is particularly reduced by contact with the solvent. Use of an organic solvent presumably denatures the enzyme in solution and diminishes the activity. Ongoing work is focused on forming the PEDOT/GOx/Hex active layer from an aqueous solution. This should provide for more efficient enzyme loading and better preservation of enzyme activity during the immobilization procedure.

Enzymatic System	Sensor Details	Response Time (R_t) and Response Sensitivity (S)	Linear Range	Stability	Reference
GOx & Hex	Modified O_2 electrode; enzymes immobilized on PE membrane	R_t=120 s	0.25–2.0 mM	Not addressed	35
	Pt electrode; Glutaralde-hyde-BSA immobilization	R_t=120-180 s	50–500 μM	30 % after 7 days	36
	Pt disk, 1 mm diam.; Enzymes entrapped in polymer	R_t=5-80 s S=730 mA M^{-1} cm^{-2}	10–200 nM	40 % after 14 days	37
	Pt disk, 25 μm diam.; Enzymes entrapped in polymer	R_t=150 ms S=65 mA M^{-1} cm^{2}	0.2–1 μM		
	Glassy carbon, 3 mm diam.; Enzymes entrapped in sol-gel membrane	R_t=15 s S=6 mA M^{-1} cm^{-2}	0.5–20 μM	65 % after 22 days	66
	Pt disk, 50 μm diam.; Enzymes entrapped in a polyphenol film	R_t=40-50 s S=1650 mA M^{-1} cm^{-2}	0.25–4 μM	75 % after 7 days	40
Gk & G3Pox	Pt/Ir wire, 25–100 μm diam.; Enzymes entrapped in sol-gel membrane	R_t<10 s S=250 mA M^{-1} cm^{-2}	0.2–50 μM	Not addressed	38
GOx & Hex	Platinized Pt wire, 50 μm diam; Enzymes polymerized in PEDOT film (−0.20 V vs. Ag/AgCl detection)	R_t=15±1 s S=100–500 mA M^{-1} cm^{-2}	10–200 μM	60 % after 7 days	This work

Table 3.1. Detection figures of merit for other enzyme-based amperometric biosensors for ATP reported on in the literature. Legend: GOx=glucose oxidase; Hex=hexokinase; Gk=glycerol kinase; G3Pox=glycerol-3-phosphate oxidase; PE=polyethylene; BSA=bovine serum albumin; PEDOT=polyethylenedioxythiophene.

3.4 Conclusions

This paper reports on a new ATP biosensor design that consists of glucose oxidase and

hexokinase enzymes immobilized within the electroactive polymer polyethylenedioxythiophene (PEDOT) on the surface of a platinized Pt microelectrode. The biosensor can be used to detect ATP indirectly based on the oxidation current for H_2O_2 produced at the glucose oxidase sites. Platinizing the Pt microelectrode to increase the surface roughness produced improved polymer adhesion over what was achieved with the smooth Pt. This led to improved biosensor stability during storage with greater than 90 % of the initial response maintained after 3 days and 60 % after 7 days. Another important advance is the improved biosensor selectivity in the amperometric detection mode at −0.20 V vs. Ag/AgCl, a potential at which oxidizable interferences do not contribute to the current response. The current measured at these potential results from the reduction of PEDOT sites reoxidized by locally produced H_2O_2. The linear dynamic range (10–200 μmol L^{-1}), sensitivity (100–500 mA/M-cm^2), response time (15±1 s) and detection limit of 10.0±0.2 μmol L^{-1} for ATP were similar at the more selective −0.20 V and more interference prone at the 0.85 V detection potential.

Reprinted (adapted) with permission from:

Peteu, S. F.; Russell, S. A.; Galligan, J. J.; Swain, G. M. An Electrochemical ATP Biosensor with Enzymes Entrapped within a PEDOT Film. *Electroanalysis* **2020**, *33*(2), 495-505.

REFERENCES

1. Sangsiri, S.; Xu, H.; Fernandes, R.; Fink, G. D.; Lujan, H. L.; DiCarlo, S. E.; Galligan, J. J. Spinal Cord Injury Alters Purinergic Neurotransmission to Mesenteric Arteries in Rats. *Am. J. Physiol. Heart Circ. Physiol.* **2019**, *318*(2), H223-H237

2. Burnstock, G. Purinergic Signaling in the Cardiovascular System. *Circ. Res.* **2017**, *120*(1), 207-228.

3. Demel, S. L.; Dong, H.; Swain, G. M.; Galligan, J. J. Antioxidant Treatment Restores Prejunctional Regulation of Purinergic Transmission in Mesenteric Arteries of Deoxycorticosterone Acetate-Salt Hypertensive Rats. *Neuroscience* **2010**, *168*(2), 335-345.

4. Sangsiri, S.; Dong, H.; Swain, G. M.; Galligan, J. J.; Xu, H. Impaired Function of Prejunctional Adenosine A1 Receptors Expressed by Perivascular Sympathetic Nerves in DOCA-Salt Hypertensive Rats. *J. Pharmacol. Exp. Ther.* **2013**, *345*(1), 32-40.

5. Belai, A.; Burnstock, G. Evidence for Coexistence of ATP And Nitric Oxide in Non-Adrenergic, Non-Cholinergic (NANC) Inhibitory Neurones in the Rat Ileum, Colon and Anococcygeus Muscle. *Cell Tissue Res.* **1994**, *278*(1), 197-200.

6. Burnstock, G. Physiology and Pathophysiology of Purinergic Neurotransmission. *Physiol. Rev*. **2007**, *87*, 659-797.

7. Burnstock, G. Introduction to Purinergic Signaling. *Methods Mol. Biol.* **2020**, *2041*, 1-15.

8. Burnstock, G. The Journey to Establish Purinergic Signaling in the Gut. *Neurogastroenterol. Motil.* **2008**, *20*, 8-19.

9. Christofi, F. L.; Kim, M.; Wunderlich, J. E.; Xue, J.; Suntres, Z.; Cardounel, A.; Jave, N. H.; Yu, J. G.; Grants, I.; Cooke, H. J. Endogenous Adenosine Differentially Modulates 5-Hydroxytryptamine Release From a Human Enterochromaffin Cell Model. *Gastroenterol.* **2004**, *127*(1), 188-202.

10. Cooke, H. J.; Wunderlich, J.; Christofi, F. L. "The Force Be with You": ATP in Gut Mechanosensory Transduction. *News Physiol. Sci.* **2003**, *18*(2), 43-49.

11. Fields, R. D.; Burnstock, G. Purinergic Signaling in Neuron–Glia Interactions. *Nat. Rev. Neurosci.* **2006**, ***7***, 423-436.

12. Patel, B. A. Mucosal Adenosine Triphosphate Mediates Serotonin Release from Ileal But Not Colonic Guinea Pig Enterochromaffin Cells. *Neurogastroenterol. Motil.* **2014**, *26*(2), 237-246.

13. Abbracchio, M. P.; Burnstock, G.; Verkhratsky, A.; Zimmermann, H. Purinergic Signalling in the Nervous System: An Overview. *Trends Neurosci.* **2009**, *32*(1), P19-29.

14. Brown, I. A.; McClain, J. L.; Waters, R. E.; Patel, B. A.; Gulbransen, B. D. Enteric Glia

Mediate Neuron Death in Colitis Through Purinergic Pathways That Require Connexin-43 and Nitric Oxide. *Cell. Mol. Gastroenterol. Hepatol.* **2016**, *2*(1), 77-91.

15. Patel, B. A. Electroanalytical Approaches to Study Signaling Mechanisms in the Gastrointestinal Tract. *Neurogastroenterol Motil.* **2011**, *23*(7), 595-605.

16. Park, J.; Quaiserová-Mocko, V.; Patel, B. A.; Novotný, M.; Liu, A.; Bian, X.; Galligan, J. J.; Swain, G. M. Diamond Microelectrodes For *In Vitro* Electroanalytical Measurements: Current Status and Remaining Challenges. *Analyst* **2008**, *133*, 17-14.

17. Wu, F.; Yu, P.; Mao, L. Analytical and Quantitative in Vivo Monitoring of Brain Neurochemistry by Electrochemical and Imaging Approaches. *ACS Omega.* **2018**, *3*(10), 13267-13274.

18. Bucher, E. S.; Wightman, R. M. Electrochemical Analysis of Neurotransmitters. *Annu. Rev. Anal. Chem.* **2015**, *8*, 239-261.

19. Mellander, L.; Cans, A. S.; Ewing, A. G. Electrochemical Probes for Detection and Analysis of Exocytosis and Vesicles. *Chem Phys Chem.* **2010**, *11*(13), 2756-2763.

20. McCapra, F. Potential Applications of Bioluminescence and Chemiluminescence in Biosensors. In: *Biosensors. Fundamentals and Applications;* Oxford Univ. Press, New York; 1987, pp. 617– 663.

21. Bergmeier, H. U. *Methods of Enzymatic Analysis;* VCH Publishers, Weinheim; 1984.

22. Manfredi, G.; Wang, L.; Gajewski, C. D.; Matttiazzi, M. Measurements of ATP in Mammalian Cells. *Methods* **2002**, *26*(4), 317-326.

23. Sudo, J. I.; Terui, J.; Ivase, H.; Kakuno, K. Assay of ATPase and Na,K-ATPase Activity Using High-Performance Liquid Chromatographic Determination of ADP Derived from ATP. *J. Chromatogr. B* **2000**, *744*(1), 19-23.

24. Deng, Q.; Kauri, L. M.; Qian, W. J.; Dahlgren, G. M.; Kennedy, R. T. Microscale Determination of Purines in Tissue Samples by Capillary Liquid Chromatography with Electrochemical Detection. *Analyst* **2003**, *128*, 1013-1018.

25. Lwin, A.; Patel, B. A. High Performance Liquid Chromatography Method for the Detection of Released Purinergic and Biogenic Amine Signaling Molecules from In Vitro Ileum Tissue. *J Sep Sci.* **2010**, *33*(11), 1538-1545.

26. Foy, G. P.; Pacey, G. E. Determination of ATP Using Chelation-Enhanced Fluorescence. *Talanta* **1996**, *43*(2), 225-232.

27. Hou, F.; Wang, X.; Jiang, C. Determination of ATP as a Fluorescence Probe with Europium(III)-Doxycycline. *Anal. Sci.* **2005**, *21*(3), 231-234.

28. Zhang, S.; Yan, Y.; Bi, S. Design of Molecular Beacons as Signaling Probes for Adenosine

Triphosphate Detection in Cancer Cells Based on Chemiluminescence Resonance Energy Transfer. *Anal. Chem.* **2009**, *81*(21), 8695-8701.

29. Wang, J.; Jiang, Y.; Zhou, C.; Fang, X. Aptamer-Based ATP Assay Using a Luminescent Light Switching Complex. *Anal. Chem.* **2005**, *77*(11), 3542-3546.

30. Pérez-Ruiz, T.; Martinez-Lozano, C.; Thomas, V.; Martin, J. Determination of ATP Via the Photochemical Generation of Hydrogen Peroxide Using Flow Injection Luminol Chemiluminescence Detection. *Anal. Bioanal. Chem.* **2003**, *377*, 189-194.

31. Qiu, J.; Zhou, Y.; Chen, H. Lin, J. M. Immunomagnetic Separation and Rapid Detection of Bacteria Using Bioluminescence and Microfluidics. *Talanta* **2009**, *79*(3), 787-795.

32. Kamidate, T.; Yanashita, K.; Tani, H.; Ishida, A.; Notani, M. Firefly Bioluminescent Assay of ATP in the Presence of ATP Extractant by Using Liposomes. *Anal. Chem.* **2006**, *78*(1), 337-342.

33. Karube, I.; Tamiya, E.; Gotoh, M.; Kagawa, Y. A Microsensor for Adenosine-5'-Triphosphate pH-Sensitive Field Effect Transistor. *Anal. Chim. Acta* **1986**, *187*, 287-291.

34. Migita, S.; Ozasa, K.; Tanaka, T.; Haruyama, T. Enzyme-based Field-Effect Transistor for Adenosine Triphosphate (ATP) Sensing. *Anal. Sci.* **2007**, *23*, 45-48.

35. Scheller, F.; Pfeiffer, D. Glucose Oxidase—Hexokinase Bienzyme Electrode Sensor for Adenosine Triphosphate. *Anal. Chim. Acta* **1980**, *117*, 383-386.

36. Compagnone, D.; Guilbault, G. G. Glucose Oxidase/Hexokinase Electrode for the Determination of ATP. *Anal. Chim. Acta.* **1997**, *340*(1-3), 109-113.

37. Kueng, A.; Kranz, C.; Mizaikoff, B. Amperometric ATP Biosensor Based on Polymer Entrapped Enzymes. *Biosens. Bioelectron.* **2004**, *19*(10), 1301-1307.

38. Llaudet, E.; Hatz, S.; Droniou, M.; Dale, N. Microelectrode Biosensor for Real-Time Measurement of ATP in Biological Tissue. *Anal. Chem.* **2005**, *77*(10), 3267-3273.

39. Soldatkin, O. O.; Schuvailo, O. M.; Marinesco, S.; Cespuglio, R.; Soldatkin, A. P. Microbiosensor Based on Glucose Oxidase and Hexokinase Co-Immobilised on Platinum Microelectrode for Selective ATP Detection. *Talanta* **2009**, *78*(3), 1023-1028.

40. Patel, B. A.; Rogers, M.; Wieder, T.; O'Hare, D.; Boutelle, M. G. ATP Microelectrode Biosensor for Stable Long-Term *In Vitro* Monitoring From Gastrointestinal Tissue. *Biosens. Bioelectron.* **2011**, *26*(6), 2890-2896.

41. Hecht, E.; Liedert, A.; Ignatius, A.; Mizaikoff, B.; Kranz, C. Local Detection of Mechanically Induced ATP Release from Bone Cells with ATP Microbiosensors. *Biosens. Bioelectron.* **2013**, *44*, 27-33.

42. Palygin, O.; Levchenko, V.; Ilatovskaya, D. V.; Pavlov, T. S.; Ryan, R. P.; Cowley Jr., A.

W.; Staruschenko, A. Real-Time Electrochemical Detection of ATP and H_2O_2 Release in Freshly Isolated Kidneys. *Am. J. Physiol. Renal Physiol.* **2013**, *305*(1), F134-F141.

43. Kucherenko, I.; Didukh, D. Y.; Soldatkin, O. O.; Soldatkin, A. P. Amperometric Biosensor System for Simultaneous Determination of Adenosine-5′-Triphosphate and Glucose. *Anal. Chem.* **2014**, *86*(11), 5455-5462.

44. Lalo, U.; Palygin, O.; Rasooli-Nejad, S.; Andrew, J.; Haydon, P. G.; Pankratov, Y. Exocytosis of ATP From Astrocytes Modulates Phasic and Tonic Inhibition in the Neocortex. *PLoS Biol.* **2014**, *12*(4), e1001747.

45. Kucherenko, I. S.; Soldatkin, O. O.; Lagarde, F.; Jeffezic-Renault, N.; Dzyadevych, S. V.; Soldatkin, A. P. Determination of Total Creatine Kinase Activity in Blood Serum Using an Amperometric Biosensor Based on Glucose Oxidase and Hexokinase. *Talanta* **2015**, *144*, 604-611.

46. Park, J. H.; Byun, J. Y.; Shim, W. B.; Kim, S. U.; Kim, M. G. High-Sensitivity Detection of ATP Using a Localized Surface Plasmon Resonance (LSPR) Sensor and Split Aptamers. *Biosens. Bioelectron.* **2015**, *73*, 26-31.

47. Yu, P.; He, X. L.; Mao, L. Q. Dual Recognition Unit Strategy Improves the Specificity of the Adenosine Triphosphate (ATP) Aptamer Biosensor for Cerebral ATP Assay. *Anal. Chem.* **2015**, *87*(2), 1373-1380.

48. Zhang, Q.; Qiu, H.; Tang, F.; Tao, Y.; Guan, B.; Li, X.; Yang, W. Aptamer-based Dry-reagent Strip Biosensor for Detection of Small Molecule ATP. *Chem. Lett.* **2016**, *45*, 289-290.

49. Palygin, O.; Evans, L. C.; Cowley Jr., A. W.; Staruschenko, A. Acute In Vivo Analysis of ATP Release in Rat Kidneys in Response to Changes of Renal Perfusion Pressure. *J. Am. Heart Assoc.* **2017**, *6*(9), e006658.

50. Santos-Cancel, M.; Simpson, L. W.; Leach, J. B.; White, R. J. Direct, Real-Time Detection of Adenosine Triphosphate Release from Astrocytes in Three-Dimensional Culture Using an Integrated Electrochemical Aptamer-Based Sensor. *ACS Chem. Neurosci.* **2019**, *10*(4), 2070.

51. Jiang, Y. A.; Wu, W. J.; Ji, W. L.; Wei, H.; Mao, L. Q. Aptamer Superstructure-Based Electrochemical Biosensor for Sensitive Detection of ATP in Rat Brain with *In Vivo* Microdialysis. *Analyst* **2019**, *144*, 1711-1717.

52. Suaebah, E.; Seshimo, Y.; Shibata, M.; Kono, S.; Hasegawa, M.; Kawarada, H. Aptamer Strategy for ATP Detection on Nanocrystalline Diamond Functionalized by a Nitrogen and Hydrogen Radical Beam System. *J. Appl. Phys.* **2017**, *121*, 044506.

53. Yu, P.; He, X. L.; Zhang, L.; Mao, L. Q. Dual Recognition Unit Strategy Improves the Specificity of the Adenosine Triphosphate (ATP) Aptamer Biosensor for Cerebral ATP Assay. *Anal. Chem.* **2015**, *87*(2), 1373-1380.

54. Peteu, S. F.; Whitman, B. W.; Swain, G. M.; Galligan, J. J. Electrochemical Detection of Peroxynitrite Using Hemin–PEDOT Functionalized Boron-Doped Diamond Microelectrode. *Analyst* **2016**, *141*, 1796-1806.

55. Peteu, S. F.; Bose, T.; Bayachou, M. Polymerized Hemin as an Electrocatalytic Platform for Peroxynitrite's Oxidation and Detection. *Anal. Chim. Acta* **2013**, *780*, 81-88.

56. Zanardi, G.; Terzi, F.; Seeber, R. Polythiophenes and Polythiophene-Based Composites in Amperometric Sensing. *Anal. Bioanal. Chem.* **2013**, *405*, 509-531.

57. Peteu, S. F.; Peiris, P.; Gebremichael, E.; Bayachou, M. Nanostructured Poly(3,4-Ethylenedioxythiophene)–Metalloporphyrin Films: Improved Catalytic Detection of Peroxynitrite. *Biosens. Bioelectron.* **2010**, *25*(8), 1914-1921.

58. Roncali, J. Electrogenerated Functional Conjugated Polymers as Advanced Electrode Materials. *J. Mater. Chem.* **1999**, *9*, 1875-1893.

59. Zykwinska, A.; Domagala, W.; Pilawa, B.; Lapkowski, M. Electrochemical Overoxidation of Poly(3,4-Ethylenedioxythiophene)—PEDOT Studied by Means of In Situ ESR Spectroelectrochemistry. *Electrochim. Acta* **2005**, *50*(7-8), 1625-1633.

60. Hui, Y.; Bian, C.; Wang, J.; Tong, J.; Xia, S. Comparison of Two Types of Overoxidized PEDOT Films and Their Application in Sensor Fabrication. *Sensors* **2017**, *17*(3), 628.

61. Kim, C. S.; Oh, S. M. Enzyme Sensors Prepared by Electrodeposition on Platinized Platinum Electrodes. *Electrochim. Acta* **1996**, *41*(15), 2433-2439.

62. Losada, J.; Armada, M. P. G. A Glucose Amperometric Sensor Based on Covalent Immobilization of Glucose Oxidase in Poly-2-Aminoaniline Film Via Chloranil on Platinized Platinum Electrode. *Electroanal.* **1997**, *9*(18), 1416-1421.

63. Li, Q. S.; Ye, B. C.; Liu, B. X.; Zhong, J. J. Improvement of the Performance of H_2O_2 Oxidation at Low Working Potential by Incorporating TTF-TCNQ Into a Platinum Wire Electrode For Glucose Determination. *Biosens. Bioelectron.* **1999**, *14*(3), 327-334.

64. Vidal, J. C.; Garcia, E.; Castillo, J. R. Development of a Platinized and Ferrocene-Mediated Cholesterol Amperometric Biosensor Based on Electropolymerization of Polypyrrole in a Flow System. *Anal. Sci.* **2002**, *18*, 537-542.

65. Reyes De Corcuera, J. I.; Cavalieri, R. P.; Powers, J. R. Improved Platinization Conditions Produce a 60-Fold Increase in Sensitivity of Amperometric Biosensors Using Glucose Oxidase Immobilized in Poly-*o*-Phenylenediamine. *J. Electroanal. Chem.* **2005**, *575*(2), 229-241.

66. Liu, S.; Sun, Y. Co-Immobilization of Glucose Oxidase and Hexokinase on Silicate Hybrid Sol–Gel Membrane for Glucose and ATP Detections. *Biosens. Bioelectron.* **2007**, *22*(6), 905-911.

67. Molaakbari, E.; Mostafavi, A.; Beitollahi, H. First Electrochemical Report for Simultaneous Determination of Norepinephrine, Tyrosine and Nicotine Using a Nanostructure Based Sensor. *Electroanal.* **2014**, *26*(10), 2252-2260.

68. Chen, W.; Lin, X.; Luo, H.; Huang, L. Electrocatalytic Oxidation and Determination of Norepinephrine at Poly(Cresol Red) Modified Glassy Carbon Electrode. *Electroanalysis* **2005**, *17*(11), 941-945.

CHAPTER 4. *IN VITRO* MONITORING OF NITRIC OXIDE RELEASE IN THE MOUSE COLON USING A BORON-DOPED DIAMOND MICROELECTRODE MODIFIED WITH PLATINUM NANOPARTICLES AND NAFION

4.1 Introduction

Boron-doped diamond (BDD) has made a significant impact on the field of electrochemical analysis owing to its many outstanding properties including (i) low and stable background current that is generally pH-independent due to the relative absence of ionizable surface carbon–oxygen functional groups, (ii) stable film morphology and microstructure, (iii) resistance to molecular adsorption and biofouling, and (iv) relatively rapid electron-transfer kinetics for multiple redox systems in aqueous,[1-3] organic,[4,5] and ionic liquid[6] electrolyte media. BDD has found great utility in the field of neurochemical analysis, proving to be a suitable material for *in vitro* and *in vivo* measurements in the peripheral and central nervous systems.[7,8] Our group has demonstrated that BDD microelectrodes provide a reproducible, stable, and sufficiently sensitive oxidation current response *in vitro* for norepinephrine released from sympathetic nerves innervating the arteries and veins of rats[9,10] and serotonin[11-13] and nitric oxide[14] released in the mucosa and myenteric plexus of the small intestine and colon of guinea pigs, rats, and mice. The ability to stably detect serotonin released in the gut using BDD microelectrodes is noteworthy as this redox system is a notorious carbon electrode biofouler.[15]

In the present paper, we expand on the application of BDD microelectrodes in neuroanalytical chemistry and report on their use to measure nitric oxide (NO) release from myenteric ganglia in the mouse colon *in vitro*. NO is known for being a highly reactive, toxic gas, that quickly reacts in air to form nitrogen oxides.[16] Within the biological system, however, NO plays an important role in cellular metabolism and has been linked to numerous physiological processes including blood pressure control, regulation of vascular tone, neurotransmission, bronchodilatation,

antibacterial and anti-tumor processes, and learning and memory.[17-19] NO detection has been a research topic for many years, and a number of analytical techniques have been used, such as spectroscopy,[20] chemiluminescence,[21] chromatography,[22] electrophoresis,[23,24] and electrochemical methods.[14,25-27] Electrochemical techniques, specifically those that employ microelectrode sensors for direct electrochemical detection of NO, offer sufficient spatiotemporal resolution for the detection of transient concentration changes *in vitro* and *in vivo* near sites of release.

By incorporating noble metals, such as platinum, into the BDD microelectrode design and implementing a permselective polymer, one can improve the sensitivity and selectivity of electrochemical NO detection. Sensor modification with platinum nanoparticles was chosen specifically for its modest electrocatalytic action toward NO oxidation and poisoning resistance against many chemical compounds.[28,29] The selectively permeable Nafion ionomer was used to overcoat the modified BDD substrate. The sulfonate groups along Nafion's backbone give the polymer acidic characteristics, allowing protons to be easily transported through the polymer film while electrostatically repelling negatively charged species.[30-32] This effectively blocks interferents, such as nitrite and nitrate, from reaching the electrode surface, which are stable byproducts produced from NO metabolism. These species can be problematic in the electrochemical NO detection as they can accumulate in solution following repeated NO production [33,34] and are also why measurement of nitrite and nitrate is often used as an indirect measure of NO release.[23,35,36]

We describe herein the preparation and characterization of a BDD microelectrode modified with platinum nanoparticles and a Nafion layer (Nafion/Pt/BDD) that exhibits selectivity and sensitivity for NO oxidation, and apply these sensors *in vitro* to measure the electrically stimulated release of NO from myenteric ganglia in the mouse colon. We end the discussion by going over preliminary data for NO detection evoked using optogenetics and the selective excitation of

nitrergic neurons in a transgenic mouse model.

4.2 Results and Discussion

Scanning electron microscopy and Raman spectroscopy were used to characterize the diamond film morphology and microstructure. Figure 4.1 presents scanning electron micrographs taken of the BDD microelectrodes at low and high magnification. The micrographs reveal the nanocrystalline morphology of the film that completely covers the conically shaped Pt wire substrate. The radius at the tip of the cone is 5-10 μm. The diamond film consists of faceted crystallites or grains of diamond that are hundreds of nanometers in diameter. Figure 4.2 presents a typical Raman spectrum of the BDD film as well as a series of Raman spectra collected along a line profile across the film. The spectrum consists of a single sharp line at 1332 cm^{-1}, which is the first-order phonon mode for diamond. The spectral features are reflective of a boron-doping level in the low 1020 cm^{-3} range: sufficiently electrically conducting for the electrochemical measurements. There is weak scattering intensity centered at 1580 cm^{-1}, which arises from sp^2 carbon impurity likely at the interface between the Pt and BDD overlayer. The scattering cross-section for sp^2-bonded carbon (graphite) is *ca.* 50x larger than the cross section for diamond, so Raman spectroscopy is particularly sensitive to any sp^2-bonded carbon. The adventitious impurity, since we suppose it exists at the interface, does not contribute significantly to the electrochemical behavior of the BDD microelectrodes.

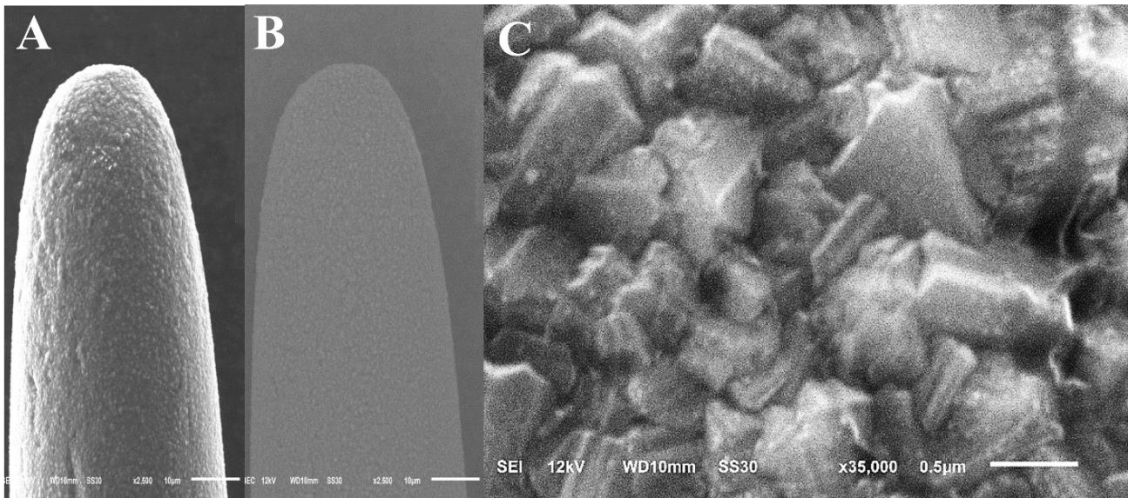

Figure 4.1. Scanning electron micrograph (secondary electron image) (A) showing the tip of a conically shaped BDD microelectrode in the secondary electron imaging mode and (B) the corresponding backscattered electron image (scale bar is 10 µm). Scanning electron micrograph (secondary electron image) (C) showing the nanocrystalline morphology of the BDD film with nanometer sized grains or faceted crystallites and the individual grain boundaries (scale bar is 0.5 µm).

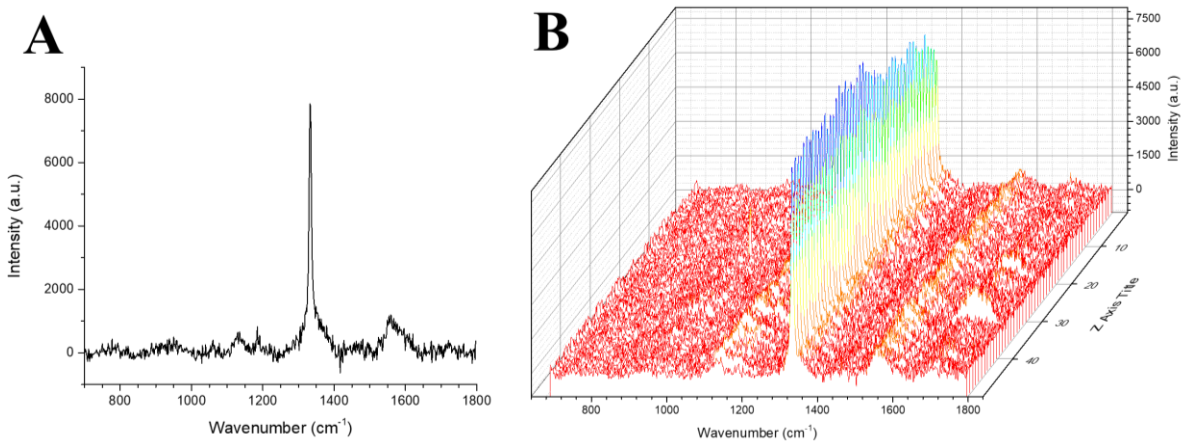

Figure 4.2. Raman spectrum of a BDD microelectrode (A) showing a sharp, narrow diamond phonon line around 1332 cm-1, suggesting good film quality and relatively few defects. Weak scattering near 1580 cm-1 indicates a small level of sp2- bonded carbon impurity. Waterfall plot (B) showing Raman spectra recorded along a 50 µm line profile of the diamond film (1 acquisition per 1 µm). The results indicate the film quality is uniform across the film.

Figure 4.3 presents the BDD microelectrode sensor design. The corresponding scanning electron micrographs reveal the change in surface texture before and after Pt nanoparticle formation and Nafion film application. The top micrograph reveals the conically shaped microelectrode tip

and the boron-doped nanocrystalline diamond film morphology before being overcoated with a layer of Pt nanoparticles potentiodynamically for 10 cycles at 0.01 V s^{-1} using a 2 mmol L^{-1} K_2PtCl_6 in 0.5 mol L^{-1} H_2SO_4. The middle micrograph shows an even coverage of the Pt nanoparticles that range from 80 to 2000 nm in diameter. Nafion was then dip-coated over the metalized surface from a solution containing 2.5% (w/v) Nafion and dried overnight at 55 °C. From the bottom micrograph, clustered deposits of Nafion can be seen which form small channels/openings that are about 5–15 nm wide. This sort of clustering of ion-exchange sites through electrostatic interaction is very typical of ion-containing polymers.[37] This sort of random clustering of spherical domains is likely a condition of the polymer film's dry state during imaging, as hydrated films tend to have a more interconnected, channel-type network.[38]

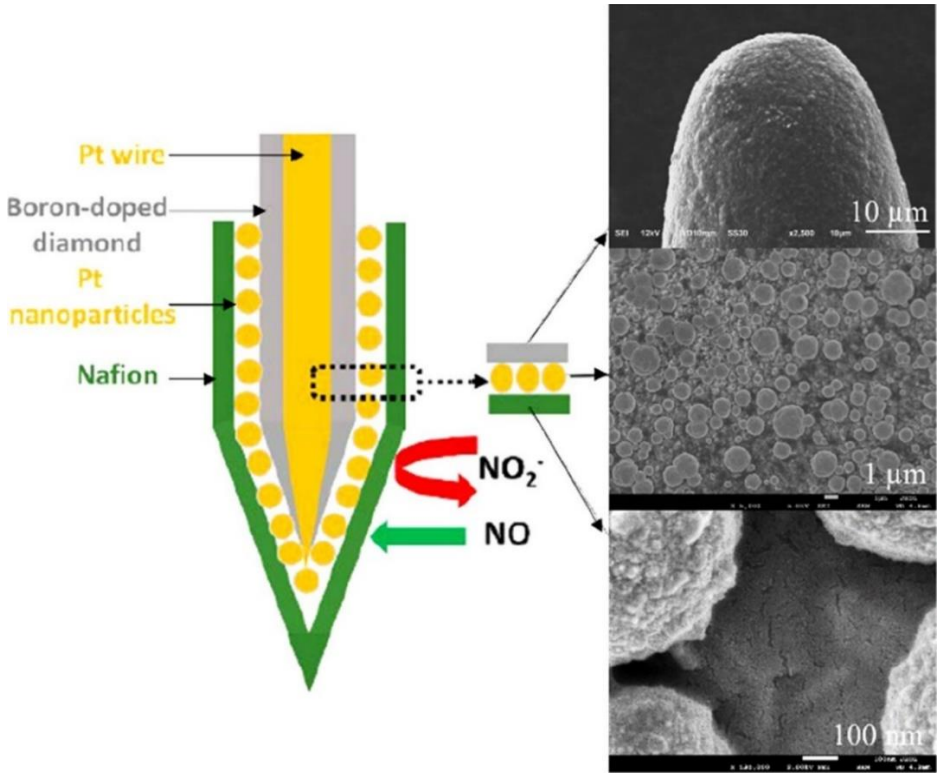

Figure 4.3. Schematic of the Nafion/Pt/BDD microelectrode sensor design. The etched 76 µm diam Pt wire is overcoated with a layer of boron-doped nanocrystalline diamond (top right), electrodeposited with Pt nanoparticles (10 cycles) (middle right), and dip-coated from a colloidal Nafion solution (2.5 w/v %) (bottom right).

Despite the advantages BDD electrodes offer, electron-transfer kinetics for NO oxidation are somewhat sluggish. This necessitates the use of relatively high positive potentials for detection (≥1.0 V *vs* Ag/AgCl), making the electrode susceptible to electroactive interferents. As electrochemical oxidation of NO occurs on Pt at slightly less positive potentials, the BDD electrode was decorated with Pt nanoparticles as a first step in electrode modification. The optimization experiments were performed using the BDD disk macroelectrode to determine the optimal K_2PtCl_6 concentration, scan rate, and cycle number. 4.4A shows a series of CV *i*–*E* curves (10 cycles presented) for a BDD microelectrode recorded between −0.2 and 1.3 V with the initial scan in the negative direction starting at 1.0 V. The voltammetric traces show the initial nucleation of Pt particles on the first scan as cathodic current commences just negative of 0.1 V. With subsequent scans, however, Pt particles nucleate and grow from these initial nucleation sites at less negative potentials increasing the amount of metal exposed.[39] We previously reported on the nucleation and growth of Pt nanoparticles on BDD electrodes.[39,40] As a consequence of this particle growth, the peak currents and charge for hydrogen adsorption and desorption between 0.1 and −0.2 V on the exposed Pt grow in magnitude with increasing cycle number. With increasing scans, the curves evolve into a shape characteristic of polycrystalline Pt. The voltammetric profile of the electrode substrate in H_2SO_4 before and after platinization can be seen in 4.4B. Before platinization, the CV for the BDD microelectrode is featureless and the current is low. There is a small cathodic current increase just negative of −0.2 V, which is attributed to H_2 evolution at exposed Pt of the underlying substrate. After platinization, a significant increase in voltammetric current and well-defined features for Pt are evident: hydrogen adsorption and desorption from 0.2 to −0.25 V, Pt oxide formation from 0.5 to 1.0 V, and Pt oxide reduction from 0.8 to 0.3 V.

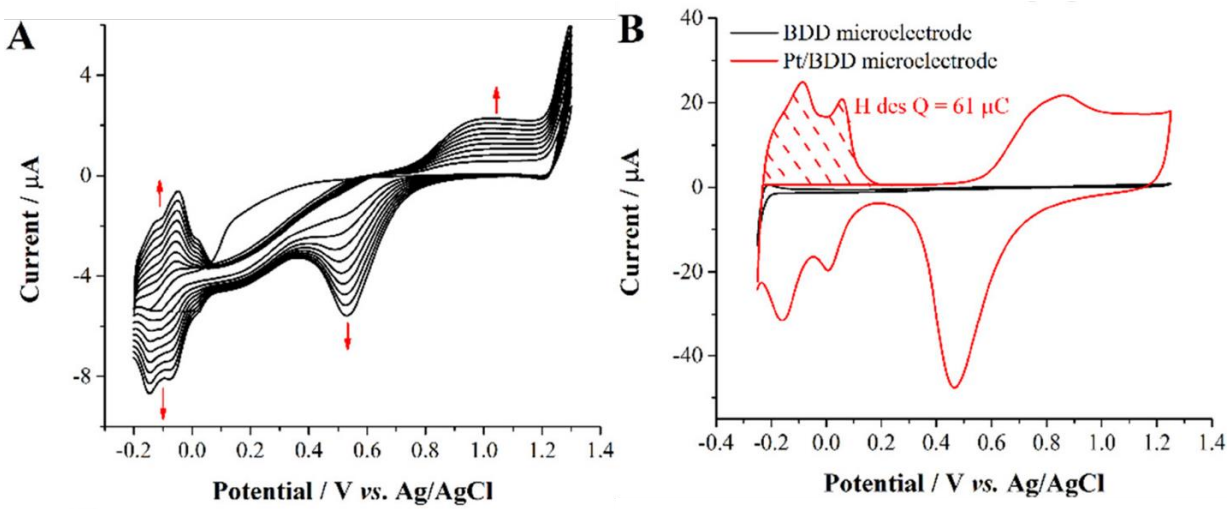

Figure 4.4. (A) Cyclic voltammetric (CV) *i–E* curves for a BDD microelectrode in 2.0 mmol L^{-1} K_2PtCl_6 dissolved in 0.5 mol L^{-1} H_2SO_4 at a scan rate of 0.01 V s^{-1}. Ten potential cycles are shown with the arrows indicating the current increase with Pt nanoparticle nucleation and growth. (B) CV for a BDD microelectrode before (black) and after (red) platinization (as in (A)) in 0.5 mol L^{-1} H_2SO_4 at a scan rate of 0.1 V s^{-1}. The hydrogen desorption charge (H des Q) is 61 μC.

The electrodeposition parameters affect the Pt nucleation and growth process, hence the number of particles formed and their size distribution across the surface. Experiments were performed using a BDD macroelectrode to optimize the Pt nanoparticle size and coverage as well as the electrochemically active surface area (ECSA) as a function of the K_2PtCl_6 solution concentration, cyclic voltammetric scan rate, and cycle number. Sample micrographs showing some of the results of this optimization can be seen in Figure 4.5. The optimized conditions for voltammetrically forming the Pt adlayers were determined to be 10 potential cycles between −0.2 and 1.3 V *vs* Ag/AgCl in 2.0 mmol L^{-1} K_2PtCl_6 dissolved in 0.5 mol L^{-1} H_2SO_4 at a scan rate of 0.01 V s^{-1}. These parameters were used to modify the BDD microelectrodes reported below. These conditions produced, for the BDD macroelectrode, a nominal particle size of 308 ± 107 nm, a particle density of 1.2×10^6 cm^{-2}, a Pt loading of 7.6 μg cm^{-2}, and an electrochemically active Pt surface area (ECSA) of 2.2 cm^{-2}.

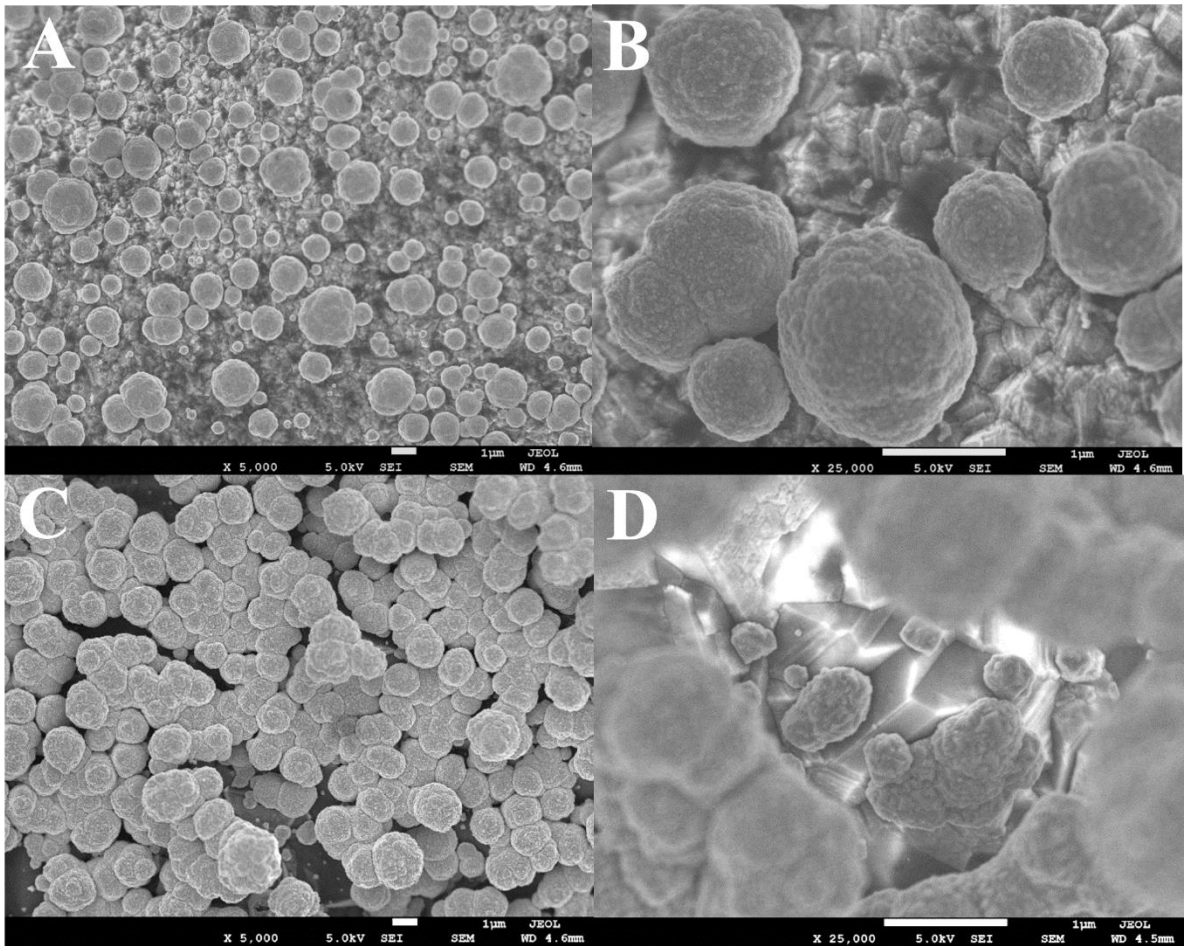

Figure 4.5. SEM micrographs of the Pt nanoparticles on a BDD microelectrode surface formed potentiodynamically using ten potential cycles at (A) low and (B) high magnification. Uniform coverage of the Pt particles across the substrate can be seen with minimal coalescence. SEM micrographs showing the distribution and morphology of Pt nanoparticles formed using twenty-five potential cycles at (C) low and (D) high magnification, which show extensive particle coalescence and very little exposure of the underlying diamond substrate The scale bars are 1 μm in all micrographs. The Pt nanoparticles were formed using 2.0 mmol L-1 K_2PtCl_6 in 0.5 mol L^{-1} H_2SO_4 at 0.01 V s^{-1}.

A potential interferent in the oxidative detection of NO *in vitro* is the nitrite anion. Nitrite is a stable byproduct of NO metabolism that has traditionally been viewed as an acute biomarker of NO flux and formation in biological systems.[35,36,41] The anion undergoes oxidation at potentials near those at which NO is detected. To discriminate against nitrite, the Pt/BDD thin-film electrode was overcoated with a film of Nafion. This ionomer contains negatively charged sulfonate groups within the pores that serve to electrostatically repel anionic species from reaching the underlying

electrode and being detected. A drop-casting method was used for film formation on the Pt/BDD macroelectrode, which involved placing a specific volume of the colloidal polymer solution on the electrode surface and allowing the solvent to evaporate for a fixed time at a controlled temperature. The drying time and temperature can affect polymer morphology and proton conductivity and, therefore, can impact selectivity and other recording properties.[26,42] Electrochemical measurement data revealed that Nafion films formed on Pt/BDD using 50 µL of 2.5% (w/v) Nafion and dried overnight at 55 °C offer the best nitrite anion rejection (current reduction > 95%). It should be noted that the Nafion film decreases the ECSA of the Pt/BDD electrode. Figure 4.6 shows cyclic voltammetric *i–E* curves for a Pt/BDD macroelectrode with and without a Nafion film in 0.5 mol L^{-1} H_2SO_4. A reduction in the voltammetric charge is observed with the polymer coating. When the concentration or volume of Nafion used during drop casting was increased, the polymer thickness increased, which lengthened the electrode's response time for NO oxidation.

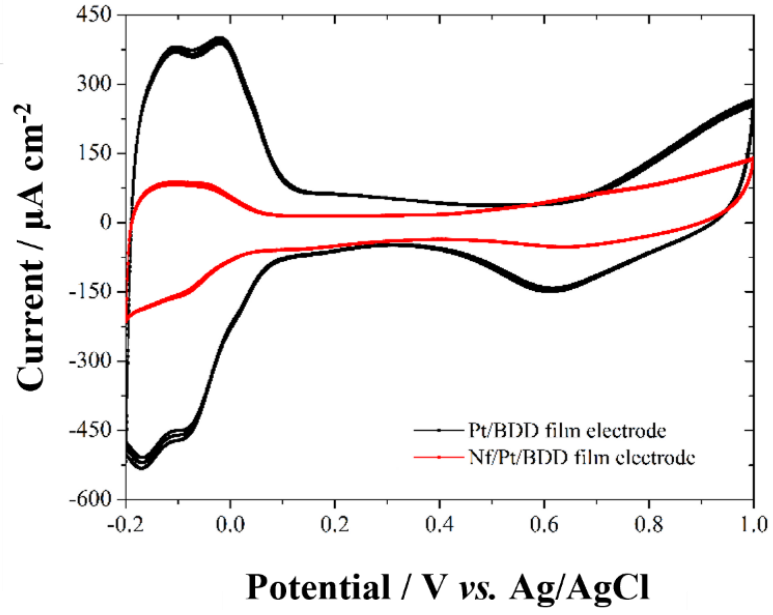

Figure 4.6. Cyclic voltammetric *i-E* curves for a Pt/BDD macroelectrode before and after Nafion film application in 0.5 mol L^{-1} H_2SO_4 at 0.05 V s^{-1}. The Pt adlayer on both electrodes was deposited using ten potential cycles in 2.0 mmol L^{-1} K_2PtCl_6 dissolved in 0.5 mol L^{-1} H_2SO_4 at a scan rate of 0.01 V s^{-1}. The polymer layer was formed by drop casting 50 µL of a 2.5 wt.% colloidal Nafion solution and drying for 90 min (rather than overnight) at 55°C.

The Nafion film was applied to the BDD microelectrodes by dip coating from a solution containing 2.5 or 5.0% (w/v) Nafion and drying overnight at 55 °C in the laboratory ambient air. Using the 2.5% colloidal Nafion solution, two dip coats produced no more nitrite rejection than a single dip coat ($p = 0.780$); therefore, only a single dip coat was used. Similar to the macroelectrode experiments, use of a 2.5 *vs* 5.0% colloidal Nafion solution for dip coating did not offer a significant nitrite sensitivity reduction ($p = 0.706$). The effect of humidity during the drying of the Nafion film on the NO and nitrite oxidation currents was also examined. After dip coating the Pt/BDD microelectrodes once in a 2.5% (w/v) Nafion solution, the electrodes were dried overnight at 55 °C in the ambient or in a humidified environment. The latter was achieved by suspending the microelectrode ~1 cm above water in a parafilm-sealed glass vial. NO and nitrite oxidation current responses were examined using CA with the Nafion/Pt/BDD microelectrode polarized at 0.8 V *vs* Ag/AgCl and sequentially adding DEA-NONOate to generate NO or sodium nitrite stock to 10 mL of magnetically stirred and nitrogen blanketed 0.1 mol L^{-1} PB pH 7.4. The response curves are presented in Figure 4.7. There was a significant increase ($p = 0.034$) in NO sensitivity for films dried in a humid environment compared to laboratory ambient air. The Nafion/Pt/BDD microelectrodes dried in the absence of moisture showed very little change in NO response after film application (average decrease of 9.2%) while Nafion/Pt/BDD microelectrodes dried under humid conditions showed an increase in NO sensitivity, approximately 38%. Although these particular sensors showed differing baseline sensitivities for nitrite, the sensors that were dried in a humid environment exhibited a much greater nitrite response rejection (average decrease of 63%) compared to dry films (average decrease of 31%).

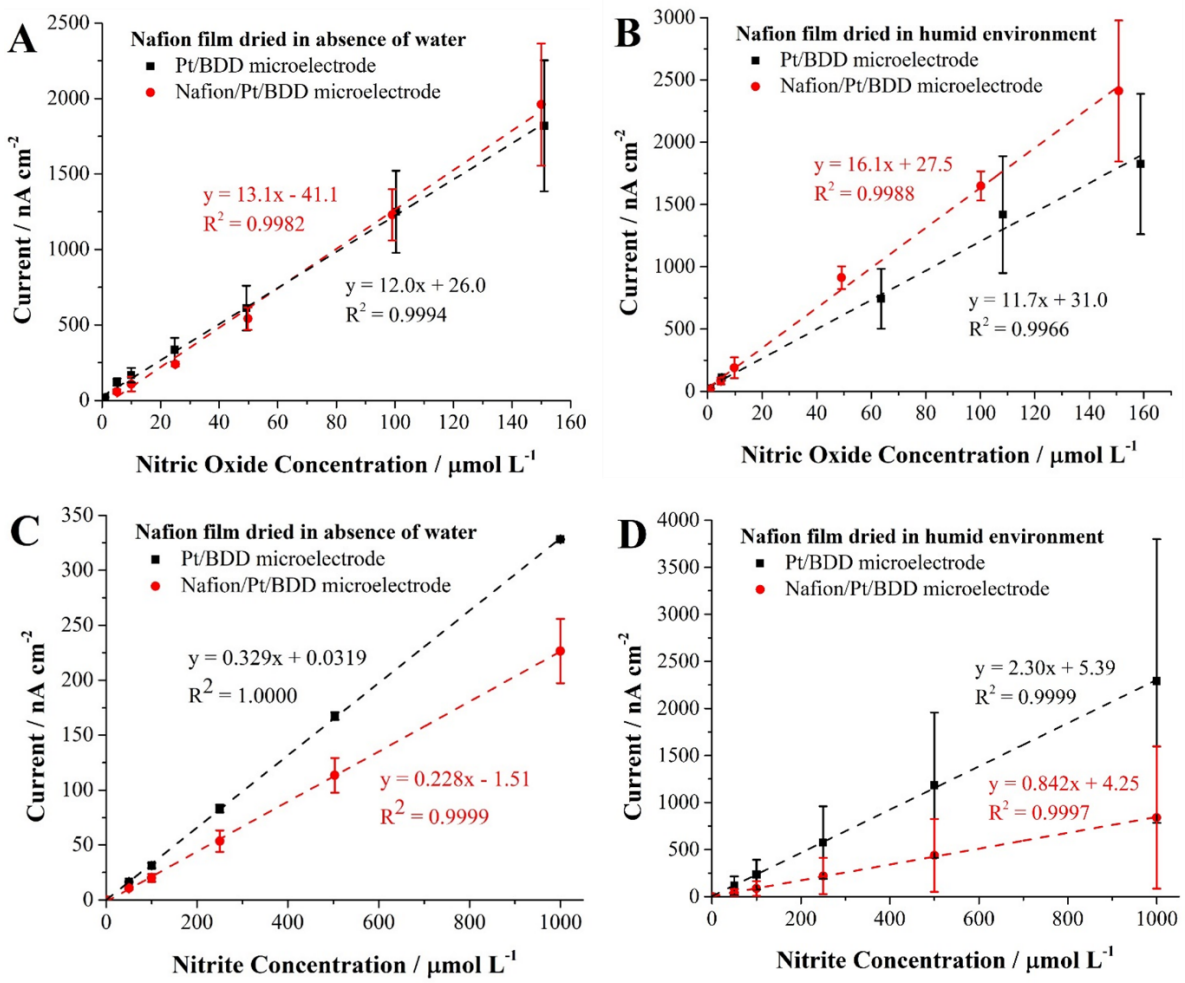

Figure 4.7. Response curves generated using continuous amperometry (detection potential of 0.8 V vs. Ag/AgCl) for Nafion/Pt/BDD microelectrodes in response to increasing NO concentrations from a 50 mmol L-1 DEA-NONOate stock solution and increasing concentrations of nitrite from a 100 mmol L-1 sodium nitrite stock solution. Data are presented for BDD microelectrodes with and without a Nafion layer formed by dip coating (1x) in a 2.5% Nafion solution. Plots reflect the mean ± std. dev. current response for n=3 electrodes normalized to the electrochemically active surface area. Panel (A) shows the response to NO oxidation before and after coating the Nafion film and drying overnight at 55℃ in the absence of moisture. Panel (B) shows another response to NO for three separate sensors that were instead dried overnight suspended ~1 cm over water in a parafilm sealed vial at 55 ℃. Panel (C) shows the response to nitrite for the same electrodes dried in panel A before and after the Nafion coating was applied and dried in the absence of moisture. Panel (D) shows the response to nitrite for the same electrodes displayed in panel (B) before and after drying the Nafion film in a humid environment.

Unlike microelectrode sensors, a considerable decrease in NO sensitivity (decrease of 25%) after application of the Nafion film was observed for the Nafion/Pt/BDD macroelectrodes (see Table 4.1). This is likely a consequence of the drop-casting deposition used, which yields a

thicker, less permeable polymer film compared to the simple dip coat applied to the microelectrode sensors. Interestingly, Nafion films that were dried in a humid environment offered better rejection of nitrite as well as a significant increase in sensitivity toward NO oxidation. It is known that Nafion morphology and ionic conduction are dependent on how hydrated the polymer is.[38] This ionomer contains segregated domains of fluorocarbon and sulfonate sites with the negatively charged sulfonate sites being highly hydrophilic. These hydrophilic regions self-assemble to form an extended network of hydrated pores and channels.[32] As the accessibility to these sulfonate sites limits the ion-exchange capacity,[30] hydration could also affect the extent of repulsion of negatively charged interferents. With respect to the increase in NO sensitivity with the hydrated films, the positive influence of Nafion on NO detection has been reported elsewhere.[31,43] A possible explanation of this phenomenon was offered by Brown et al.,[31] which is that Nafion may stabilize NO^+ formed following oxidation and consequently prevent the formation of oxidation products like nitrite and nitrate, which can adsorb to the electrode surface and decrease NO sensitivity. Thus, it would seem that Nafion films dried in the absence of moisture are not as permselective to the transport of small molecules. The Nafion/Pt/BDD microelectrodes were optimally prepared by dip coating once in 2.5% (w/v) Nafion, dried at 55 °C overnight in a humid environment, and stored suspended ~1 cm above water in a parafilm-sealed vial to maintain film hydration before and between *in vitro* measurements.

Figures of merit	**Pt/BDD**	**Nafion/Pt/BDD**
Sensitivity (μA μM^{-1})	1.16	0.87
Limit of detection (μmol L^{-1})	2.07	1.75
Limit of quantification (μmol L^{-1})	6.90	5.83
Linear range (μmol L^{-1})	0-50	0 -10
Reproducibility (RSD for 99 μmol L^{-1} NO)	3.22%	3.28%

Table 4.1. Values are presented a single set of measurements with each electrode. Sensitivity was determined from the slope of the response curves generated from linear sweep voltammetric currents. The theoretical limit of detection and limit of quantitation are defined at the lowest

Table 4.1. (cont'd)

concentration of NO that yields a S/N ≥3 and S/N ≥10, respectively. Reproducibility was determined from the relative standard deviation (RSD) of the current response to repeat additions of 99 μmol L^{-1} NO.

Optimally prepared Nafion/Pt/BDD microelectrodes were tested in standard solutions of NO and nitrite prior to use *in vitro*. Figure 4.8 shows LSV *i–E* curves for a microelectrode in response to increasing concentration of DEA-NONOate generated NO from 0 to 200 μmol L^{-1} and 1 mmol L^{-1} nitrite. The supporting electrolyte was deoxygenated 0.1 mol L^{-1} phosphate buffer (PB) pH 7.4 and the scan rate was 0.01 V s^{-1}. As the potential is swept from 0.2 to 1.2 V, the oxidation of NO onset is at ~0.5 V. This current then rises and reaches a maximum at ~0.8 V, as the rate of the electrochemical reaction becomes mass transport limited. In addition to this current, the current for water oxidation commences at 1.0 V (see curve for 0 μmol L^{-1} NO). The oxidation current at 0.8 V increases with increasing NO concentration. The oxidation of nitrite occurs at potentials positive of 0.8 V. Therefore, detection of NO at 0.8 V affords maximum oxidation current for NO and a minimal contribution from nitrite oxidation. Even with the Nafion layer, some current for nitrite oxidation is still observed even though the current for 1 mmol L^{-1} nitrite is less than the current for only 200 μmol L^{-1} NO. Both careful control of the potential used for amperometric detection and incorporation of the Nafion film serve to mitigate the influence of nitrite on the measured NO oxidation current.

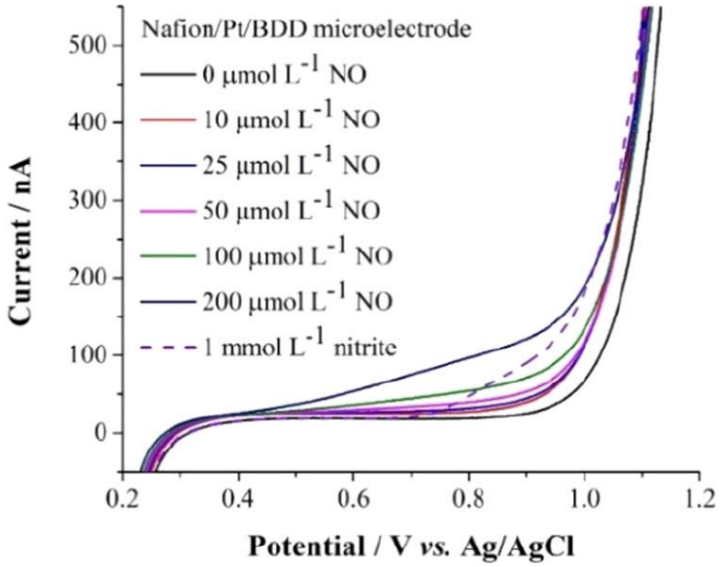

Figure 4.8. Linear sweep voltammetric (LSV) *i–E* curves showing the response of a Nafion/Pt/BDD microelectrode to increasing concentrations of DEA-NONOate generated NO from 0 to 200 µmol L^{-1}. The microelectrode response to 1 mmol L^{-1} nitrite is also presented for comparison (note the higher concentration of nitrite compared to NO). The Nafion film was applied through a single dip coat from a 2.5% (w/v) colloidal Nafion solution dried overnight at 55 °C in a humid environment. The electrolyte was deoxygenated 0.1 mol L^{-1} PB pH 7.4, and the scan rate was 0.01 V s^{-1}.

The effect of the Nafion layer on the NO and nitrite oxidation was investigated using the Nafion/Pt/BDD disk macroelectrode and LSV. Representative data are presented in Figure 4.9. The voltammetric *i–E* curves show the current response for increasing concentrations of NO in 0.1 mol L^{-1} PB pH 7.2 before (Figure 4.9A) and after (Figure 4.9B) Nafion film application. The oxidation peak potential for NO was *ca*. 0.85 V for both electrodes and the peak oxidation current increased proportionally with NO concentration from 1 to 100 µmol L^{-1}. However, the peak current was reduced by about 50% for the Nafion-coated electrode. Figure 4.9C shows the selectivity of the Nafion/Pt/BDD macroelectrode in a solution of 1 mmol L^{-1} nitrite and 0.1 mol L^{-1} PB pH 7.2 after adding with 99 µmol L^{-1} NO. The presence of 1 mmol L^{-1} nitrite has little to no effect on the oxidation of 99 µmol L^{-1} NO demonstrating that Nafion provides good rejection against nitrite oxidation. A key difference between the voltammetric curves obtained with the Nafion/Pt/BDD macroelectrodes *vs* the microelectrodes is the presence of pseudo-steady current for the latter. A

more time-independent flux of NO is achieved at the smaller dimensioned BDD microelectrode.

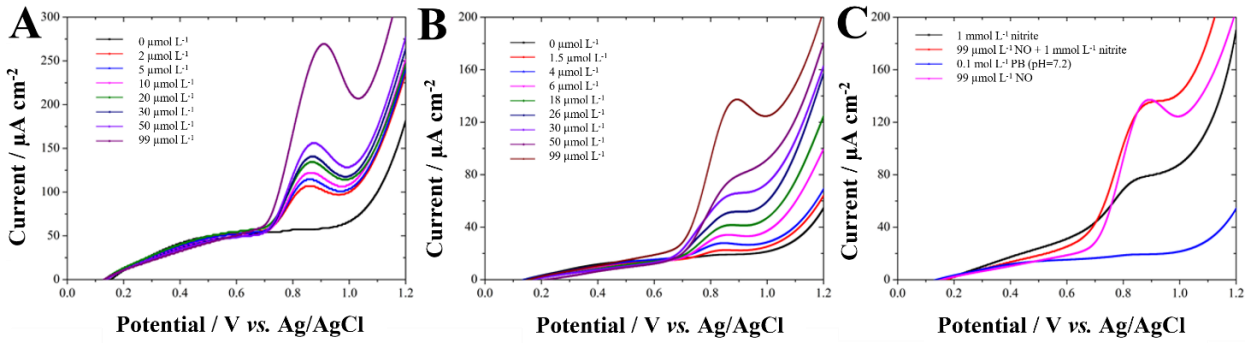

Figure 4.9. Linear sweep voltammetric *i-E* curves for a Pt/BDD macroelectrode (A) before and (B) after Nafion film addition with increasing concentrations of NO in 0.1 mol L^{-1} phosphate buffer (PB) pH = 7.2. Comparison of linear sweep voltammetric curves for (C) PB only (blue), 99 µmol L^{-1} NO in PB pH 7.2 (pink), 1.0 mmol L-1 nitrite in PB pH 7.2 (black), and 99 µmol L^{-1} NO and 1 mmol L^{-1} nitrite in PB pH 7.2 (red). The scan rate was 0.01 V s-1. The Pt adlayer was formed using 10 potential cycles in 2.0 mmol L-1 K_2PtCl_6 dissolved in 0.5 mol L^{-1} H_2SO_4 at a scan rate of 0.01 V s^{-1}. The polymer layer was formed by drop casting 50 µL of a 2.5 wt.% colloidal Nafion solution and drying overnight at 55 ºC.

The Nafion/Pt/BDD microelectrode electrochemical response was also evaluated using CA, as this electrochemical technique offers better temporal resolution for measuring neurotransmitter release and is the technique used for the *in vitro* measurements discussed below. Figure 4.10 shows *i–t* curves for two Pt/BDD microelectrodes, with and without a Nafion film, in response to increasing concentrations of DEA-NONOate generated (A) NO and (B) nitrite. As DEA-NONOate decomposition is a time-dependent reaction, there is a delay in response between the addition of the DEA-NONOate stock solution and the maximum current response. It typically took no longer than 300 s for the maximum NO concentration to be reached. The solution concentration was maintained by careful blanketing of the electrochemical cell with N_2 and airtight addition of the stock solution through a gas-tight syringe. The corresponding response curves generated from the CA data are presented as insets. The oxidation potential was poised at 0.8 V *vs* Ag/AgCl in both measurements. There is only a small decrease in NO sensitivity with the Nafion film (4% decrease); however, the Nafion film decreased the nitrite sensitivity significantly by 81%.

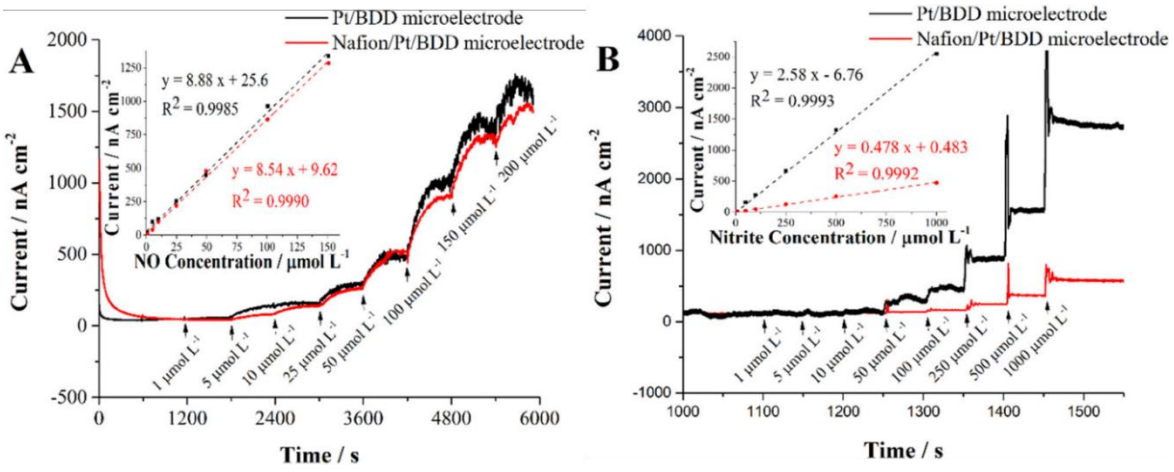

Figure 4.10. Continuous amperometric (CA) *i–t* traces for Pt/BDD microelectrodes with and without a Nafion coating for (A) NO and (B) nitrite. The detection potential used was 0.8 V vs Ag/AgCl. The supporting electrolyte solution was 0.1 mol L^{-1} PB pH 7.4. Curve A was smoothed using four-point boxcar averaging, and Curve B was filtered using a 0.3 Hz low-pass filter. The Nafion/Pt/BDD microelectrode was dip-coated using a 2.5% colloidal Nafion solution and dried overnight at 55 °C in a humid environment.

The reproducibility of the Nafion/Pt/BDD microelectrodes for NO oxidation current was determined using CA. Figure 4.11 presents the response of a microelectrode to repeat additions of 20 µmol L^{-1} NO generated from the decomposition of DEA-NONOate. For a single sensor, five repeat additions produced a response reproducibility of 5.9% RSD. The average response to 20 µmol L^{-1} NO for n = 3 sensors was 186 ± 5 nA cm^{-2}, or an RSD of 2.5%.

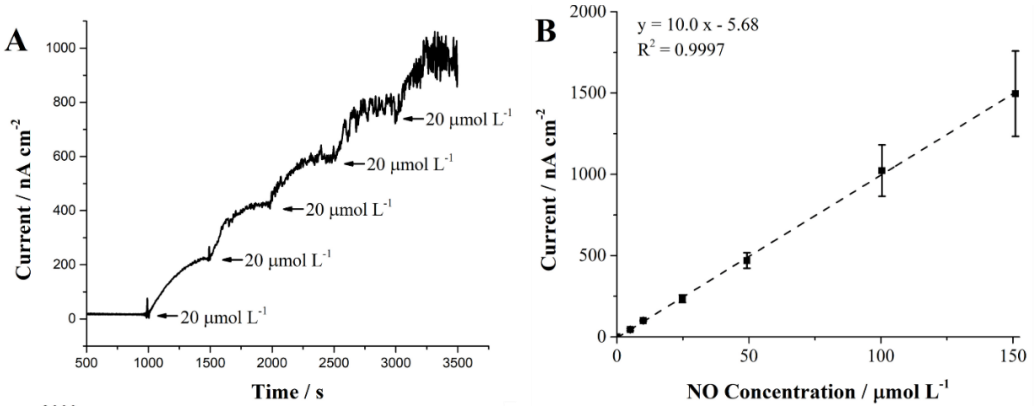

Figure 4.11. (A) Continuous amperometric (CA) *i-t* curve (0.125 Hz low pass filter) for a Nafion/Pt/BDD microelectrode in response to repeat 20 µmol L^{-1} additions of NO generated using DEA-NONOate. The reproducibility for five injections was 5.9 % RSD. (B) Calibration curve for NO oxidation current using CA and n=3 Nafion/Pt/BDD microelectrodes prepared using a 2.5 % (w/v) colloidal Nafion solution to dip coat. The detection potential used was 0.8 V vs Ag/AgCl.

Table 4.2 presents the detection figures of merit for NO determined using Pt/BDD and Nafion/Pt/BDD microelectrodes. Table 4.1 shows the detection figures of merit for the Nafion/Pt/BDD macroelectrode NO sensors for comparison. Detection was performed using CA with DEA-NONOate as the source of generated NO. The theoretical LOD and LOQ were calculated from the ratio of 3 and 10 times the standard deviation of the blank (40 points) and the slope of the response curve. The sensitivity was 16.7 ± 2.7 mA M^{-1} cm^{-2} (n = 3 electrodes) for the Nafion/Pt/BDD microelectrodes. There was a slight increase in sensitivity for NO (approximately 37%) with the application of the Nafion film, which was dried in a humid environment. After Nafion application, the LOD decreased from 1.1 to 0.5 μmol L^{-1}, the LOQ decreased from 3.7 to 1.5 μmol L^{-1}, and the LDR narrowed slightly. As the LOD and LOQ for the Nafion/Pt/BDD microelectrodes are within the concentrations that exist in the biological system, it is suitable to apply these electrodes *in vitro*. Although it was determined that the Nafion film stability for the Nafion/Pt/BDD macroelectrodes was 77.3% after 7 days, the lifetime of the Nafion films was examined by determining the Nafion/Pt/BDD microelectrode's response to nitrite following consecutive *in vitro* measurements. There was minimal change to nitrite response after 3 days of use *in vitro*. However, after 4 days of use, the sensitivity to nitrite increased significantly, suggesting that the Nafion coating needs to be renewed at this point.

Figure of merit	**Pt/BDD**	**Nafion/Pt/BDD**
Sensitivity (mA $M^{-1}cm^{-2}$)	12.2 ± 2.7	16.7 ± 2.7
Limit of detection (μmol L^{-1})	1.1 ± 0.4	0.5 ± 0.1
Limit of quantification (μmol L^{-1})	3.7 ± 1.2	1.5 ± 0.5
Linear range (μmol L^{-1})	1.1- 150	0.5-130

Table 4.2. Detection Figures of Merit for NO Oxidation at the Pt/BDD and Nafion/Pt/BDD Microelectrodes Using CA. Values are average ± standard deviation for n = 3 electrodes of each type. Sensitivity was determined from the slope of the response curves generated from CA measurements at 0.8 V vs Ag/AgCl. Theoretical LOD and LOQ values are defined as 3s/S and 10s/S, where s is the standard deviation of the blank and S is the slope of the response curve.

Intestinal motility, or the coordinated contraction and relaxation of muscle cells used to

propel food content in the gut, is regulated primarily through the release of acetylcholine from excitatory motor neurons and NO and adenosine triphosphate (ATP), or a similar purine, from inhibitory motor neurons.[44,45] NO acts as an inhibitory neuromuscular transmitter mediating the relaxation response during the peristaltic reflex.[45,46] Nitrergic enteric neurons are particularly susceptible to neuropathy in digestive disorders,[47] making the measurement of real-time release and clearance of NO a valuable tool in studying how nitrergic signaling is altered in a diseased state. NO was detected from myenteric ganglia of the mouse large intestine using CA and transmural electrical stimulation. 4.12 shows representative CA *i–t* traces for an increasing number of electrical stimuli (80 V, 10 Hz, 0.5 ms pulse duration) delivered across two Ag/AgCl wires placed parallel to a circular muscle tissue preparation. As expected, the NO oxidation current measured with the Nafion/Pt/BDD microelectrode at 0.8 V *vs* Ag/AgCl increased with increasing pulse number as the concentration of extracellular NO increases. This current reaches a peak response after three pulses, plateaus, and then slightly decreases with increasing pulse number. The plateau in response is likely due to the complete depolarization of nNOS neurons and peak enzyme activation. The small decrease in oxidation current is possibly due to an insufficient recovery time between stimulations. Experiments were also performed with the nNOS antagonist, l-NNA (100 μmol L^{-1}), and the sodium channel blocker TTX (0.5 μmol L^{-1}) in the perfusate. The drugs were continuously perfused over the tissue for 10 min before repeating the electrical stimulations. There is no oxidation current detected in the presence of TTX or l-NNA at any of the pulse numbers. This indicates the oxidation current has an action potential-dependent neurogenic origin and that the current is primarily due to NO oxidation originating from the action of nNOS.

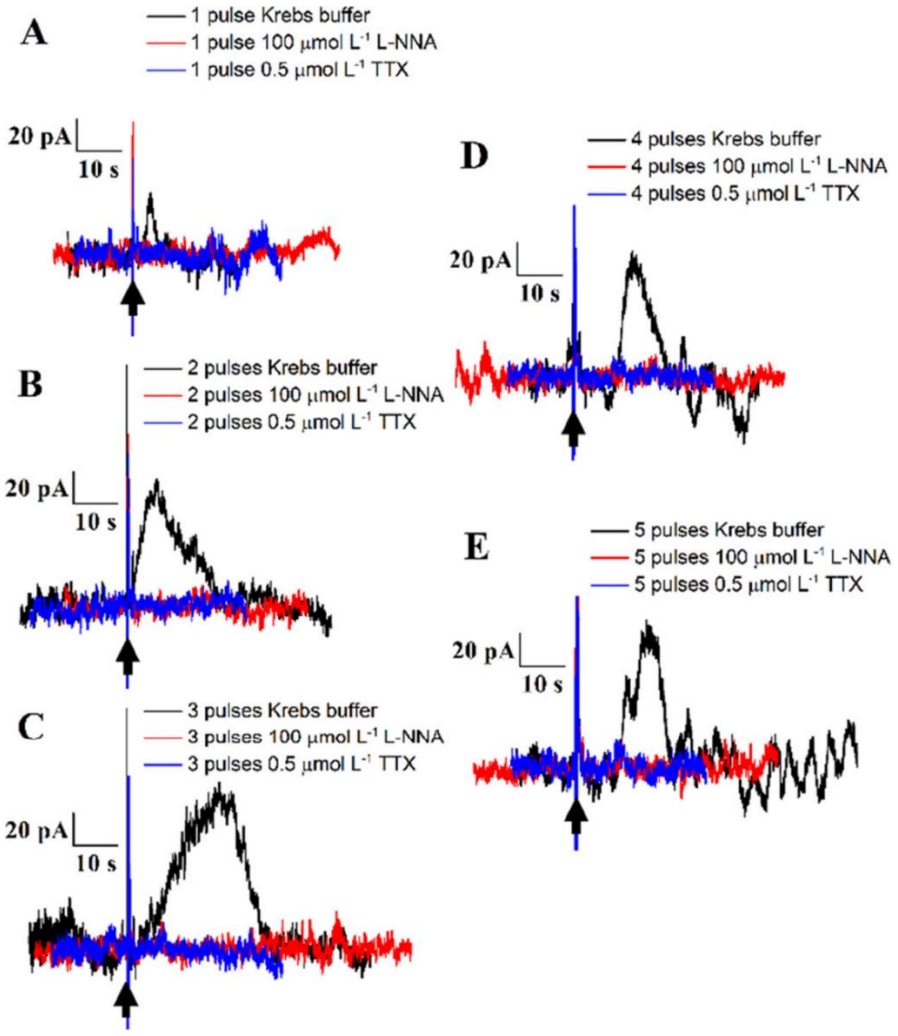

Figure 4.12. (A–E) CA *i–t* recordings of NO oxidation current at a Nafion/Pt/BDD microelectrode evoked by electrical stimuli (A–E) as a function of pulse number (1–5). The arrow marks the onset of the stimulation. Oxidation current responses were measured in a circular muscle preparation from a male mouse in the presence and absence of the nNOS inhibitor, 100 μmol L^{-1}l-NNA, and the sodium channel blocker, 0.5 μmol L^{-1} TTX. The microelectrode was polarized at 0.8 V vs Ag/AgCl. The perfusate was Krebs buffer pH 7.4 at 36–37 °C. The *i–t* curves were passed through a 10 Hz low-pass filter for smoothing.

Figure 4.13 shows a compilation of data (mean ± standard error of the mean (SEM)) for the NO oxidation current recorded using a single Nafion/Pt/BDD microelectrode in the absence and presence of l-NNA or TTX for male (n = 6) and female (n = 6) mice as a function of pulse number. The microelectrode used responded stably for weeks, as is typical of BDD microelectrodes used in the gut. For the male mice, the nNOS inhibitor abolished ~88% of the current response and the

sodium channel blocker abolished ~96% of the current response. For the female mice, the nNOS inhibitor abolished ~91% of the current response and the sodium channel blocker abolished ~90% of the current response. It is interesting to note that the mean NO oxidation current for the female WT mice is decreased compared to the male mice. However, a post hoc test following two-way ANOVA revealed that these differences are not statistically significant. Regardless, this observation was somewhat surprising as other studies have shown that female rats show higher overall NO production in the gut compared to male rats.[48,49] It is possible that results from those studies may be attributed to NO production through the inducible nitric oxide synthase (iNOS) isoform, which is localized to the intestinal mucosa and associated with cytokine upregulation.[50] On the other hand, there is possible clinical evidence for disrupted nitrergic signaling in females as well as the prevalence of chronic constipation, gastroparesis, and irritable bowel syndrome[51] suggesting a sex difference may be possible. Regardless, these results present strong support for the proper inclusion of both sexes with future studies regarding nitrergic signaling.

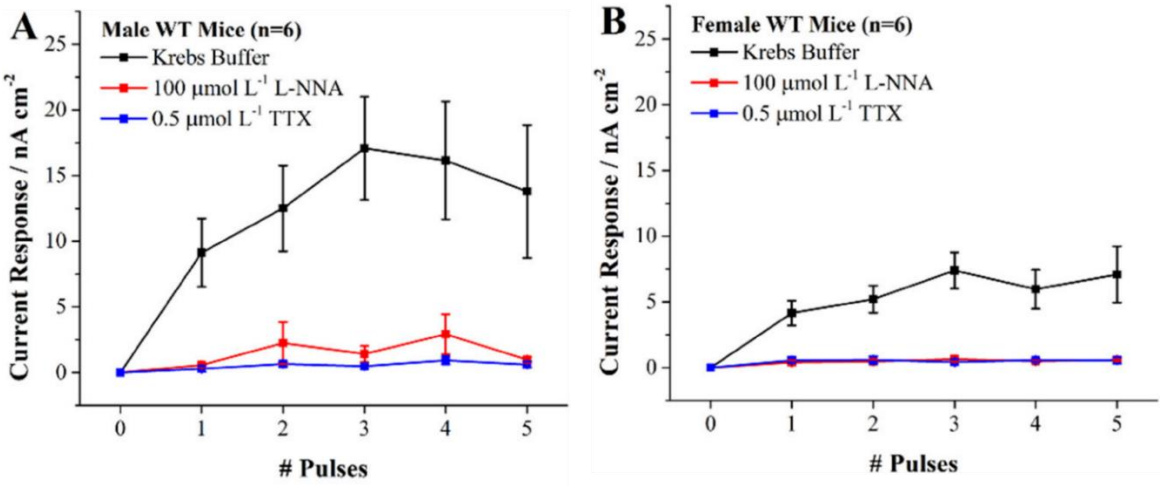

Figure 4.13. Mean ± SEM peak current responses for a single sensor normalized to its electrochemically active area for n = 6 male mice (A) and n = 6 female mice (B) in response to the number of electrical stimuli delivered in the presence and absence of nNOS inhibitor l-NNA and sodium channel blocker TTX. Experimental conditions were the same as those in Figure 5.

A calibration curve was generated by perfusing DEA-NONOate concentrations through the

flow bath at 36–37 °C and is presented in Figure 4.14. The peak current response seen in the figure for three pulses corresponds to a concentration of approximately 448 ± 102 nmol L^{-1} for the male mice and 193 ± 36 nmol L^{-1} for the female mice. These concentrations are within range of what has been measured from male guinea pig ileum using a BDD microelectrode and CA. These measurements approximated a maximum nicotine-evoked concentration of 46 nmol L^{-1} NO from longitudinal muscle myenteric plexus and 124 nmol L^{-1} NO from circular muscle without the myenteric plexus attached.[14]

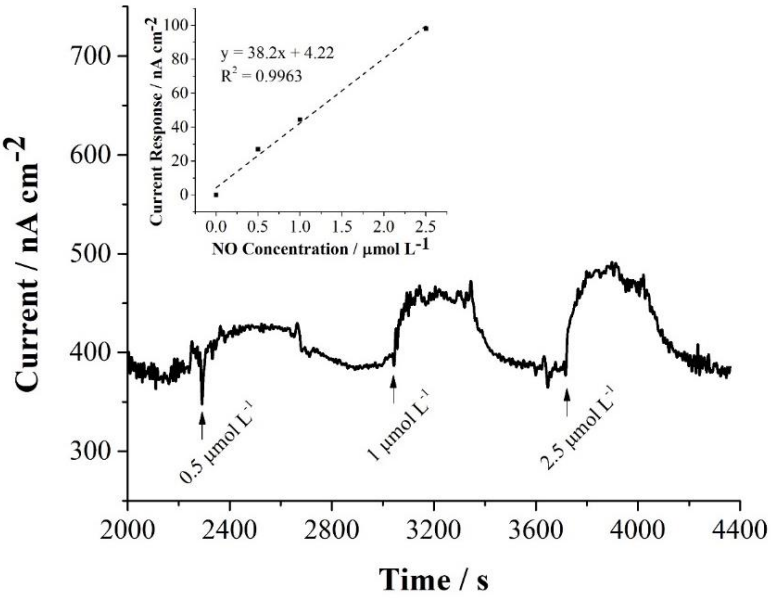

Figure 4.14. A sampling of CA *i-t* recordings with a Nafion/Pt/BDD microelectrode in the recording chamber to different concentrations of NO generated from the NO donor DEA-NONOate that was added to perfusing Krebs buffer pH 7.4. The bath temperature was 36-37 ℃ and the buffer flow rate was 4 mL min^{-1}. The inset shows the corresponding response curve normalized to the electrode's Pt electrochemically active area (ECSA).

Our group is using optogenetics to better understand the neural network in the myenteric plexus and how nerve fibers project to the muscle layers in the gastrointestinal wall to control intestinal motility patterns.[52] Optogenetics is a neuromodulation technique that utilizes light to selectively activate neurons. By genetically implanting light-sensitive ion channels into specific neurons of interest, this technique allows one to selectively probe the activity of specific neuron

subtypes within complex neural circuits. Using the Cre/Lox recombinase system, transgenic mice were bred such that the light-sensitive ion channel, channelrhodopsin-2 (ChR2), tagged with yellow fluorescence protein (eYFP), was expressed in NOS-containing neurons. These cells can then be selectively excited using short pulses of blue light (470 nm) to induce a conformation change in ChR2 causing an influx of Na^{+} and Ca^{+2} ions, depolarization, and neurotransmitter release. Figure 4.15 shows preliminary data in which NO release was recorded in response to blue light stimulation (BLS) with a Nafion/Pt/BDD microelectrode polarized at 0.8 V *vs* Ag/AgCl. Short pulses (10 Hz, 20 ms pulse duration) of blue light (470 nm) were delivered using a light-emitting diode (LED) positioned ~100 μm from the electrode tip. There is an increase in the current response from (Figure 4.15A) 1 to (Figure 4.15B) 3 blue light pulses delivered. The current response is similar between (Figure 4.15B) 3 and (Figure 4.15C) 5 pulses; however, the response diminishes at (Figure 4.15D) 7 pulses. NO is produced on demand when intracellular Ca^{+2} is elevated. The decrease in current with the higher pulse number is likely linked to the depletion of intracellular Ca^{+2} with the higher pulse number. It should also be noted that at 3 and 5 pulses, the current returns to a level below the baseline. At longer times not seen here, the current does eventually return to baseline. It is possible that the change in baseline observed is due to a local ionic concentration change at the electrode–solution interface. It is our goal to apply NO and ATP biosensors, which have been prepared and described elsewhere[53] to determine whether nitrergic neurons also store and release ATP along with NO.

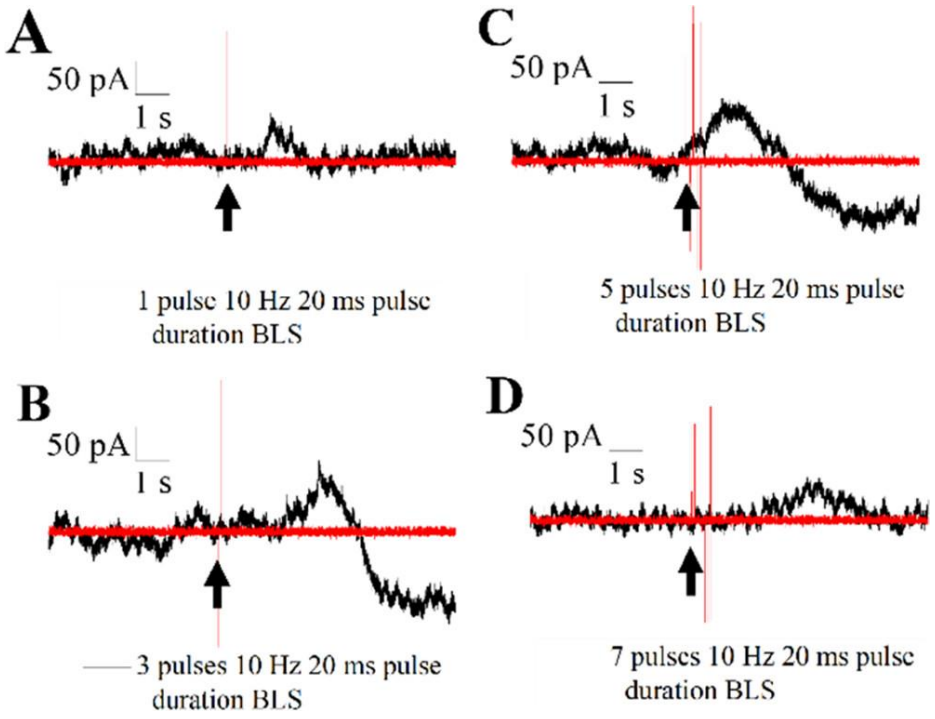

Figure 4.15. CA *i–t* curves recording NO oxidation current with a Nafion/Pt/BDD microelectrode as a function of increasing number of blue light pulses delivered to a circular muscle preparation from the large intestine of a transgenic mouse. The arrow marks the onset of the stimulation, which is identified through the red trace. Stimulations were performed at 10 Hz with a 20 ms pulse duration. Detection of NO was performed at 0.8 V vs Ag/AgCl. The perfusate was Krebs buffer pH 7.4 at 36–37 °C. The current data were smoothed using a 10 Hz low pass filter.

4.3 Conclusions

Real-time detection of NO has been historically difficult due to NO's short half-life and low effective concentration *in vivo*. A Nafion/Pt/BDD microelectrode was developed with sufficient sensitivity and selectivity for NO oxidation *in vitro* in the gut. We showed that neurogenic NO release from myenteric ganglia in the mouse colon can be successfully measured electrochemically using a Nafion/Pt/BDD microelectrode. Male mice released more NO than female mice, based on oxidation current magnitudes, in a pulse-dependent manner. NO oxidation currents were largely abolished in the presence of the sodium channel blocker, tetrodotoxin, and the nNOS antagonist, *N*-nitro-l-arginine. The Nafion/Pt/BDD microelectrodes provided good sensitivity, reproducibility, rejection of nitrite, and stability in the *in vitro* environment. There are a few analytical techniques

that can be used to detect real-time concentration changes near sites of neurotransmitter release. The work presented here shows the sensors are useful for studying the dynamics of NO released in the GI tract. Furthermore, we introduced a new tool and some preliminary data for a novel means of studying neurotransmitter release from specific subsets of neurons using optogenetics. It is our hope that results from these future studies will fill a much-needed knowledge gap in the functional underpinnings of myenteric plexus circuitry and how that circuitry modulates motor reflex.

Reprinted (adapted) with permission from:

Henderson, S.; Bhardwaj, K.; Perugachi, V.; Espinoza-Montero, P.; Galligan, J. J.; Swain, G. M. *In Vitro* Monitoring of Nitric Oxide Release in the Mouse Colon Using a Boron-Doped Diamond Microelectrode Modified with Platinum Nanoparticles and Nafion. *Anal. Chem.* **2023**, *95*(2), 1027-1037.

REFERENCES

1. Wang, S.; Swope, V. M.; Butler, J. E.; Feygelson, T.; Swain, G. M. The Structural and Electrochemical Properties of Boron-Doped Nanocrystalline Diamond Thin-Film Electrodes Grown from Ar-Rich and H_2-Rich Source Gases. *Diam. Relat. Mater*. **2009**, *18*(4), 669-677.

2. Macpherson, J. V. A Practical Guide to Using Boron Doped Diamond in Electrochemical Research. *Phys. Chem. Chem. Phys*. **2015**, *17*, 2935-2949.

3. Jarošová, R.; De Sousa Bezerra, P. M.; Munson, C.; Swain, G. M. Assessment of Heterogeneous Electron-Transfer Rate Constants for Soluble Redox Analytes at Tetrahedral Amorphous Carbon, Boron-Doped Diamond, and Glassy Carbon Electrodes. *Phys. Status Solidi A* **2016**, *213*(8), 2087-2098.

4. Pastor-Moreno, G.; Riley, D. J. Electrochemical Studies of Moderately Boron Doped Polycrystalline Diamond in Non-Aqueous Solvent. *Electrochim. Acta* **2002**, *47*(16), 2589-2595.

5. Haymond, S.; Babcock, G. T.; Swain, G. M. *Electroanal.* Electron Transfer Kinetics of Ferrocene at Microcrystalline Boron-Doped Diamond Electrodes: Effect of Solvent and Electrolyte. **2003**, *15*(4), 249-253.

6. Jarošová, R.; Bhardwaj, K.; Swain, G. M. Temperature Dependence of the Heterogeneous Electron-Transfer Rate Constant for Ferrocene Carboxylic Acid in Room Temperature Ionic Liquids at Microstructurally Distinct Carbon Electrodes. *J. Electroanal. Chem.* **2020**, 875, 114744.

7. Dong, H.; Wang, S.; Galligan, J. J.; Swain G. M. Boron-Doped Diamond Nano/Microelectrodes for Bio-Sensing and *In Vitro* Measurements. *Front. Biosci.* **2011**, *3*(2), 518-540.

8. Purcell, E. K.; Becker, M. F.; Guo, Y.; Hara, S. A; Ludwig, K. A.; McKinney, C. J.; Monroe, E. M.; Rechenberg, R.; Rusinek, C. A.; Saxena, A.; Siegenthaler, J. R.; Sortwell, C. E.; Thompson, C. H.; Trevathan, J. K.; Witt, S.; Li, W. Next-Generation Diamond Electrodes for Neurochemical Sensing: Challenges and Opportunities. *Micromachines* **2021**, *12*(2), 128-155.

9. Park, J.; Galligan, J. J.; Fink, G. D.; Swain, G. M. In Vitro Continuous Amperometry with a Diamond Microelectrode Coupled with Video Microscopy for Simultaneously Monitoring Endogenous Norepinephrine and Its Effect on the Contractile Response of a Rat Mesenteric Artery. *Anal. Chem.* **2006**, *78*(19), 6756-6764.

10. Park, J.; Quaiserová-Mocko, V.; Pecková, K.; Galligan, J. J.; Fink, G. D.; Swain, G. M. Fabrication, Characterization, and Application of a Diamond Microelectrode for Electrochemical Measurement of Norepinephrine Release from the Sympathetic Nervous System. *Diam. Relat. Mater*. **2006**, *15*(4-8), 761-772.

11. Patel B. A.; Bian, X.; Quaiserová-Mocko, V.; Galligan, J. J.; Swain, G. M. *In Vitro* Continuous Amperometric Monitoring of 5-Hydroxytryptamine Release from Enterochromaffin Cells of the Guinea Pig Ileum. *Analyst* **2007**, *132*(1), 41-47.

12. Galligan, J. J.; Patel, B. A.; Schneider, S. P.; Wang, H.; Zhao, H.; Novotny, M.; Bian, X.; Kabeer, R.; Fried, D.; Swain, G. M. Visceral Hypersensitivity in Female But Not in Male Serotonin Transporter Knockout Rats. *Neurogastroenterol. Motil*. **2013**, *25*(6), e373-e381.

13. France, M.; Skorich, E.; Kadrofske, M.; Swain, G. M.; Galligan, J. J. Sex-Related Differences in Small Intestinal Transit and Serotonin Dynamics in High-Fat-Diet-Induced Obesity in Mice. *Exp. Physiol*. **2016**, *101*(1), 81-89.

14. Patel, B. A.; Galligan, J. J.; Swain, G. M.; Bian, X. Electrochemical Monitoring of Nitric Oxide Released by Myenteric Neurons of the Guinea Pig Ileum. *Neurogastroenterol. Motil.* **2008**, *20*(11), 1243-1250.

15. Güell, A. G.; Meadows, K. E.; Unwin, P. R.; Macpherson, J. V. Trace Voltammetric Detection of Serotonin at Carbon Electrodes: Comparison of Glassy Carbon, Boron Doped Diamond and Carbon Nanotube Network Electrodes. *Phys. Chem. Chem. Phys*. **2010**, *12*, 10108-10114.

16. Ford, P.C.; Miranda, K.M. The Solution Chemistry of Nitric Oxide and Other Reactive Nitrogen Species. *Nitric Oxide*. **2020**, *103*, 31-46.

17. Moncada, S.; Higgs, A. The L-Arginine-Nitric Oxide Pathway. *N. Engl. J. Med*. **1993**, *329*(27), 2002–2012.

18. Wink, D. A.; Mitchell, J. B. Chemical Biology of Nitric Oxide: Insights into Regulatory, Cytotoxic, and Cytoprotective Mechanisms of Nitric Oxide. *Free Radic. Biol. Med*. **1998**, *25*(98), 434–456.

19. Dröge, W. Free Radicals in the Physiological Control of Cell Function. *Physiol. Rev*. **2002**, *82*(1), 47–95.

20. Hogg, N. Detection of Nitric Oxide by Electron Paramagnetic Resonance Spectroscopy. *Free Radic. Biol. Med*. **2010**, *49*(2), 122-129.

21. Bates, J. N. Nitric Oxide Measurement by Chemiluminescence Detection. *Neuroprotocols* **1992**, 1(2), 141-149.

22. Everett, S. A.; Denis, M. F.; Tozer, G. M.; Prise, V. M.; Wardman, P.; Stratford, M. R. L. Nitric Oxide in Biological Fluids: Analysis of Nitrite and Nitrate by High-Performance Ion Chromatography. *J. Chromatog. A* **1995**, *706*(1-2), 437-442.

23. Kikura-Hanajiri, R.; Martin, R. S.; Lunte, S. M. Indirect Measurement of Nitric Oxide Production by Monitoring Nitrate and Nitrite Using Microchip Capillary Electrophoresis with Electrochemical Detection. *Anal. Chem*. **2002**, *74*(24), 6370-6377.

24. Caruso, G.; Fresta, C. G.; Siegel, J. M.; Wijesinghe, M. B.; Lunte, S. M. Microchip Electrophoresis with Laser-Induced Fluorescence Detection for the Determination of the Ratio of Nitric Oxide to Superoxide Production in Macrophages During Inflammation *Anal. Bioanal. Chem.* **2017**, *409*, 4529-4538.

25. Wink, D.A.; Christodoulou, D.; Ho, M.; Krishna, M. C.; Cook, J. A.; Haut, H.; Randolph, J. K.; Sullivan, M.; Coia, G.; Murray, R.; Meyer, T. A Discussion of Electrochemical Techniques for the Detection of Nitric Oxide. *Methods* **1995**, *7*(1), 71-77.

26. Ferreira, N. R.; Ledo, A.; Frade, J. G.; Gerhardt, G. A.; Laranjinha, J.; Barbosa, R. M. Electrochemical Measurement of Endogenously Produced Nitric Oxide in Brain Slices Using Nafion/*o*-Phenylenediamine Modified Carbon Fiber Microelectrodes. *Anal. Chim. Acta* **2005**, *535*(1-2), 1-7.

27. Li, Y.; Sella, C.; Lemaître, F.; Guille-Collignon, M.; Thouin, L; Amatore, C. Electrochemical Detection of Nitric Oxide and Peroxynitrite Anion in Microchannels at Highly Sensitive Platinum-Black Coated Electrodes. Application to ROS and RNS Mixtures prior to Biological Investigations. *Electrochim. Acta* **2014**, *144*, 111-118.

28. Allen, B. W.; Piantadosi, C. A.; Coury, L. A. Electrode Materials for Nitric Oxide Detection. *Nitric Oxide* **2000**, *4*(1), 75–84.

29. Luo, X.; Morrin, A.; Killard, A. J.; Smyth, M. R. Application of Nanoparticles in Electrochemical Sensors and Biosensors. *Electroanalysis* **2006**, *18*(4), 319–326.

30. Chen, T. Y.; Leddy, J. Ion Exchange Capacity of Nafion and Nafion Composites *Langmuir* **2000**, *16*(6), 2866–2871.

31. Brown, F. O.; Finnerty, N. J.; Lowry, L. P. Nitric Oxide Monitoring in Brain Extracellular Fluid: Characterisation of Nafion-Modified Pt Electrodes In Vitro and In Vivo. *Analyst* **2009**, *134*(10), 2012-2020.

32. Stenina, I.; Golubenko, D.; Nikonenko, V.; Yaroslavtsev, A. Selectivity of Transport Processes in Ion-Exchange Membranes: Relationship with the Structure and Methods for Its Improvement. *Int. J. Mol. Sci.* **2020**, *21*(15), 5517-5550.

33. Kelm, M. Nitric Oxide Metabolism and Breakdown. *Biochim. Biophys. Acta Bioenerg.* **1999**, *1411*(2–3), 273–289.

34. Amatore, C.; Arbault, S.; Bouret, Y.; Cauli, B.; Guille, M.; Rancillac, A.; Rossier, J. Nitric Oxide Release during Evoked Neuronal Activity in Cerebellum Slices: Detection with Platinized Carbon-Fiber Microelectrodes. *ChemPhysChem* **2006**, *7*(1), 181-187.

35. Salter, M.; Duffy, C.; Garthwaite, J.; Strijbos, P. J. L. M. Ex Vivo Measurement of Brain Tissue Nitrite and Nitrate Accurately Reflects Nitric Oxide Synthase Activity In Vivo. *J. Neurochem.* **1996**, *66*(4), 1683-1690.

36. Tsikas, D. Analysis of Nitrite and Nitrate in Biological Fluids by Assays Based on the Griess

Reaction: Appraisal of the Griess Reaction in the L-Arginine/Nitric Oxide Area of Research. *J. Chromatogr. B* **2007**, *851*(1-2), 51-70.

37. Gierke, T. D.; Munn, G. E.; Wilson, F. C. The Morphology in Nafion* Perfluorinated Membrane Products, as Determined by Wide- and Small- Angle X-Ray Studies. *J. Polym. Sci.* **1981**, *19*(11), 1687-1704.

38. Allen, F. I.; Comolli, L. R.; Kusoglu, A.; Modestino, M. A.; Minor, A. M.; Weber, A. Z. Morphology of Hydrated As-Cast Nafion Revealed through Cryo Electron Tomography. *ACS Macro Lett*. **2015**, *4*(1), 1-5.

39. Bennett, J. A., Swain, G. M. Investigating the Nucleation and Growth of Electrodeposited Pt on Polycrystalline Diamond Electrodes. *J. Electrochem. Soc.* **2010**, *157*(8), F89-F95.

40. Bennett, J. A.; Show, Y.; Wang, S.; Swain, G. M. Pulsed Galvanostatic Deposition of Pt Particles on Microcrystalline and Nanocrystalline Diamond Thin-Film Electrodes: I. Characterization of As-Deposited Metal/Diamond Surfaces. *J. Electrochem. Soc.* **2005**, *152*(5), E184-E192.

41. Gladwin, M. T.; Schechter, A. N.; Kim-Shapiro, D. B.; Patel, R. P.; Hogg, N.; Shiva, S.; Cannon III, R. O.; Kelm, M.; Wink, D. A.; Espey, M. G.; Oldfield, E. H.; Pluta, R. M.; Freeman, B. A.; Lancaster, J. R.; Feelisch, M.; Lundberg, J. O. The Emerging Biology of the Nitrite Anion. *Nat. Chem. Biol*. **2005**, *1*(6), 308–314.

42. Gerhardt, G. A..; Hoffman, A. F. Effects of Recording Media Composition on the Responses of Nafion-Coated Carbon Fiber Microelectrodes Measured Using High-Speed Chronoamperometry. *J. Neurosci. Methods* **2001**, *109*(1), 13-21.

43. Diab, N.; Schuhmann, W. Electropolymerized Manganese Porphyrin/Polypyrrole Films as Catalytic Surfaces for the Oxidation of Nitric Oxide. *Electrochim. Acta* **2001**, *47*(1-2), 265-273.

44. Burnstock, G. Purinergic Signalling in the Gastrointestinal Tract and Related Organs in Health and Disease. *Purinergic Signal.* **2014**, *10*, 3–50.

45. Gallego, D.; Mañé, N.; Gil, V.; Martínez-Cutilles, M.; Jiménez, M. Mechanisms Responsible for Neuromuscular Relaxation in the Gastrointestinal Tract. *Rev. Esp. Enferm. Dig.* **2016**, *108*(11), 721-731.

46. Bornstein, J. C.; Costa, M.; Grider, J. R. Enteric Motor and Interneuronal Circuits Controlling Motility. *Neurogastroenterol. Motil.* **2004**, *16*(s1), 34-38.

47. Bódi, N.; Szalai, Z.; Bagyánszki. Nitrergic Enteric Neurons in Health and Disease—Focus on Animal Models. *Int. J. Mol. Sci.* **2019**, *20*(8), 2003-2012.

48. Ba, Z. F.; Yokoyama, Y.; Toth, B.; Rue III, L. W.; Bland, K. I.; Chaudry, I. H. Gender Differences in Small Intestinal Endothelial FunctionL Inhibitory Role of Androgen. *Am. J. Physiol. Gastrointest. Liver Physiol.* **2004**, *286*, G452-G457.

49. Homma, H.; Hoy, E.; Xu, D. Z.; Lu, Q.; Feinman, R.; Deitch, E. A. The Female Intestine is More Resistant than the Male Intestine to Gut Injury and Inflammation when Subjected to Conditions Associated with Shock States. *Am. J. Physiol. Gastrointest. Liver Physiol.* **2005**, *288*, G466-G472.

50. Morin, M. J.; Karr, S. M.; Faris, R. A.; Gruppuso, P. A. Developmental Variability in Expression and Regulation of Inducible Nitric Oxide Synthase in Rat Intestine. *Am. J. Physiol. Gastrointest. Liver Physiol.* **2001**, *281*, G552-G559.

51. Gonzales, Z.; Loganathan, P.; Sarosiek, I.; McCallum, R. W. Gender-Related Differences in Gastroparesis. *Am. J. Med. Sci.* **2020**, *360*(5), 474-483.

52. Perez-Medina, A. L.; Galligan, J. J. Optogenetic Analysis of Neuromuscular Transmission in the Colon of ChAT-ChR2-YFP BAC Transgenic Mice. *Am. J. Physiol. Gastrointest. Liver Physiol*. **2019**, *317*, G569 –G579.

53. Peteu, S. F.; Russell, S. A.; Galligan, J. J.; Swain, G. M. An Electrochemical ATP Biosensor with Enzymes Entrapped within a PEDOT Film. *Electroanalysis* **2021**, *33*(2), 495-505.

CHAPTER 5. *EX VIVO* ELECTROCHEMICAL MONITORING OF CHOLINERGIC SIGNALING IN THE MOUSE COLON USING AN ENZYME-BASED BIOSENSOR

5.1 Introduction

Alzheimer's disease (AD) is the most common cause of dementia and is hallmarked by the presence of extracellular amyloid beta (Aβ) plaques and intracellular Tau protein tangles.[1] Age is the number one risk factor for developing late-onset AD, though genetics and family history also play a role. For example, those carrying one or two copies of the e4 form of the APOE gene have about a 3-fold and 8- to 12-fold greater risk, respectively, of developing AD compared to those who have two copies of the e3 form of the gene. Having the e4 form of the gene though does not guarantee AD development.[2] Due to the complexity of the disease and lack of animal models that fully mimic disease progression in humans, the early-stage pathogenesis of AD remains unclear. Although there are many hypotheses surrounding the pathogenesis of AD (i.e., Aβ hypothesis, Tau protein hypothesis, neuroinflammation hypothesis, etc.), it is well-established that cholinergic signaling plays a vital role. The cholinergic hypothesis suggests that dysfunction of acetylcholine (ACh) containing neurons in the brain contributes to the cognitive decline in those with advanced AD.[3] The cholinergic abnormalities that manifest in aged humans and AD patients include alterations in choline (Ch) transport, ACh release, and nicotinic and muscarinic receptor expression.[3] Most current approved therapies for AD target the cholinergic system such as acetylcholinesterase (AChE) inhibitors like donepezil, rivastigmine, and galantamine. These drugs help slow (but not prevent) cognitive decline in patients with mild to moderate dementia.[4,5] The cholinergic hypothesis has been around for 40+ years, and—though not without flaws—portrays a convincing role of cholinergic dysfunction in AD progression.[6,7] ACh is a common neurotransmitter found in both the central and peripheral nervous systems that plays a critical role in cognition, learning, memory, and neural plasticity.[8-10] Within the periphery, ACh is the primary excitatory

neurotransmitter in the enteric nervous system (ENS), mediating smooth muscle contraction to aid in peristaltic propulsion of food content through the gastrointestinal (GI) tract.[11]

The focus on neurodegenerative disease is typically dominated by the study of central nervous system (CNS) dysfunction, but there has been an increasing number of studies that indicate the involvement of the gut in early-stage AD pathology. For example, enteric AD-related protein deposition, changes in neuromuscular transmission, impaired gut function, and gut dysbiosis have been found in various AD rodent models, in some cases before full brain pathology occurs.[12-15] Cholinergic neuron loss in the brain is a prominent feature in AD pathology,[5] though it is unclear whether cholinergic signaling is also affected in the ENS in AD. One study in which Aβ was injected into the GI tract of a general purpose strain of ICR mice found that Aβ became internalized into cholinergic neurons in the myenteric plexus.[16] The loss of cholinergic neurons in the ileum of APP/PS1 transgenic mice has been reported[12] as well as decreased AChE activity in the small intestine of 5xFAD mice[14] and reduced neurogenic cholinergic contractions in the colon of SAMP8 mice.[13] Cholinergic signaling is critical for regulation of GI motility. Mice with conditionally deleted choline acetyltransferase (ChAT), the enzyme responsible for ACh synthesis, in neural crest-derived enteric neurons experienced dysmotility, significantly decreased colonic transit, and intestinal dysbiosis.[17] Our group is interested in using electrochemical and pharmacological tools to determine if cholinergic signaling is impaired in the ENS in AD like it is in the CNS.

Electrochemical tools have long been a useful tool in neurochemical analysis. Voltammetric and amperometric techniques which employ microelectrode or nanoelectrode sensors offer a means to detect the real time release of electroactive signaling molecules like dopamine (DA) and serotonin (5-HT) nears sites of release. However, it is often the case that the neurotransmitter of interest, such as ACh, is not electroactive and cannot be electrochemically detected. In cases such

as this, enzymatic biosensors are often employed. Enzyme-based sensors rely on the formation of electroactive products, commonly H_2O_2, to detect these non-electroactive species. Construction of enzyme-based sensors for ACh typically involves the cross-linking of AChE and choline oxidase (ChOx) with bovine serum albumin (BSA) using glutaraldehyde on a solid support. Using this reaction scheme, ACh is hydrolyzed in the presence of AChE to produce Ch, which can then be oxidized in the presence of ChOx to produce H_2O_2 which is oxidized at the electrode interface. Cross-linking is typically done using moderate concentrations of glutaraldehyde to prevent excessive cross-linking, which can impact the enzyme's catalytic activity.[18-20] Other methods of enzyme immobilization include physical entrapment within a three-dimensional matrix such as a polymer or sol-gel, adsorption through electrostatic interaction, covalent coupling directly to a solid support, or affinity bonds between functional groups on the solid support and affinity tags within a protein sequence.[21-23] Although there are advantages and disadvantages to each method, cross-linking is typically the method of choice in construction of ACh/Ch biosensors.[19,20,24-27] Some researchers compared enzyme immobilization through cross-linking the AChE/ChOx enzyme film on a polypyrrole-polyvinylsulpfonate modified Pt electrode vs entrapping the enzymes within the polymer film.[19] The authors found that biosensors prepared using cross-linking with glutaraldehyde and BSA demonstrated a higher affinity of the enzymes toward the electrode substrate and better operational stability.[19] Other researchers have used a self-assembly of gold nanoparticles along with AChE bound on the surface of a multi-walled carbon nanotube(MWCNT)/ChOx/sol-gel modified Pt electrode for ACh detecion.[28] Pyrolytic graphite electrodes have also been modified with MWCNTs and zinc oxide nanoparticles before depositing the dual-enzyme layer and capping the electrode with a cationic poly(diallyldimethyl ammonium chloride) polymer film to prevent enzyme leaching for Ch and ACh biosensors.[27] These sensors showed excellent enzyme bioactivity as well

as improved electrocatalytic activity from the MWCNTs toward H_2O_2.[27]

Use of metal and metal oxide nanostructures (nanoparticles, nanotubes, nanorods, nanosheets, etc.) have a history of being incorporated into biosensor design and can either be co-immobilized with the enzymes or incorporated into the electrode surface.[29,30] These nanomaterials function to increase the electrochemically active surface area (ECSA), enhance the rate of electron transfer, catalyze specific chemical reactions, improve enzyme stability, or impart desired electrostatic properties during enzyme-immobilization and biosensing.[29,30] Pt metal is unique in its ability to catalyze the decomposition of H_2O_2.[29] Although unmodified Pt microelectrodes possess catalytic activity toward H_2O_2 oxidation, the incorporation of Pt nanoparticles dramatically increases the usable surface area and consequently the number of electrocatalytic sites.[29] Incorporation of Pt nanoparticles on the transducer surface has also show to improve long-term stability of electrodes, improve the signal to noise ratio, and increase enzyme loading.[31-33]

Another important consideration to make in the preparation of electrochemical biosensors is selectivity. Non-conducting polymers of phenylenediamine (PD) are commonly used to enhance selectivity by allowing small molecules like H_2O_2 to permeate through the polymer while restricting permeability of larger molecules such as ascorbic acid (AA).[34,36,37] Thin films of this polymer with rapid response times can easily be electropolymerized in aqueous solution either before and after enzyme immobilization from the following PD isomers: *o*-phenylenediamine (*o*PD), *m*-phenylenediamine (*m*PD), and *p*-phenylenediamin (*p*PD).[24-26,34,35] Films generated from the *m*PD monomer offer the best permselectivity for H_2O_2 over AA[34,37] and have been commonly utilized in ACh/Ch biosensor construction.[24-26,35]

In this paper, we report on the use of an electrochemical biosensor and continuous amperometry (CA) to study the real-time release of ACh from myenteric ganglia in the mouse

colon. We have previously developed a modified boron-doped diamond microelectrode to electrochemically monitor nitric oxide release from the mouse colon.[38] For this work, we prepared enzyme-based ACh/Ch biosensors based on literature[24] to measure cholinergic signaling from the mouse colon in male and female wild type mice. This work is foundational for the planned use of the biosensor to study cholinergic signaling in mouse models of AD. These sensors consist of a platinized-Pt microelectrode electrodeposited with a permselective p*m*PD nonconductive polymer film and coated with a multienzyme film containing AChE and ChOx. ACh and Ch are detected through the enzymatic production of H_2O_2 from the reduction of the co-factor O_2, which is electrochemically oxidized.

5.2 Results and Discussion

The general design of the ACh/Ch biosensor is seen in Figure 5.1. The microelectrode, which reveals an elliptical area of platinized-Pt, is insulated with non-conductive epoxy. Following electrodeposition of the p*m*PD film, a multi-enzyme film was applied to the polymer-modified electrode. As ACh is not electrochemically active, ACh is indirectly measured through the oxidation of enzymatically produced H_2O_2. Briefly, ACh is hydrolyzed in the presence of AChE to produce Ch. In turn, Ch is then oxidized in the presence of the second enzyme, ChOx, to produce two moles of H_2O_2 using the co-factor, O_2. The H_2O_2 diffuses through the porous p*m*PD film to be oxidized at the platinized-Pt interface, generating a current response that is directly proportional to ACh concentration. The sensor also responds to Ch via the second enzymatic reaction only.

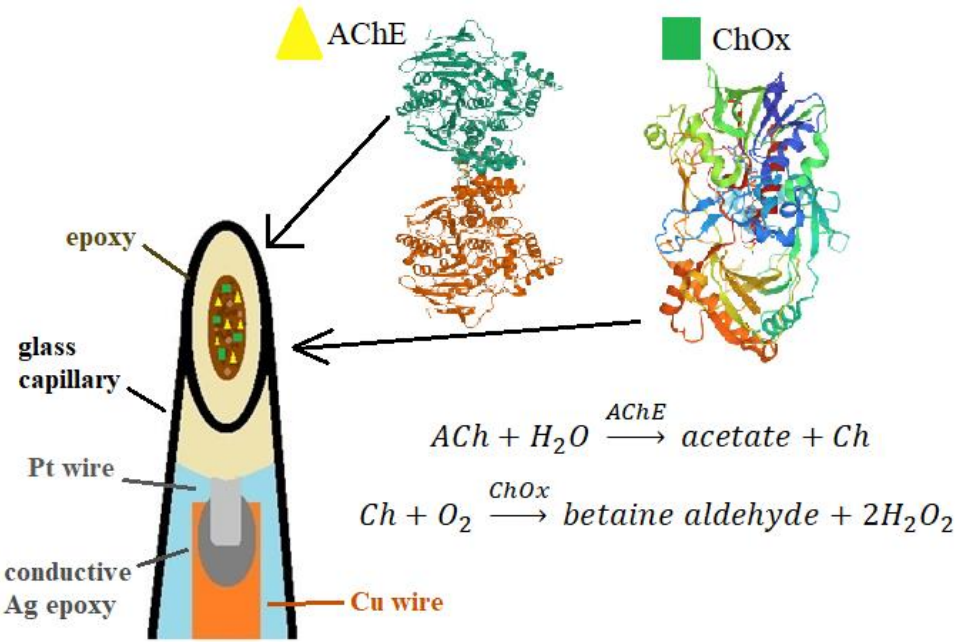

Figure 5.1. ACh/Ch electrochemical biosensor design and reaction scheme. Image created using protein structures from the RCSB PDB (rcsb.org) of PDB ID 1EEA[39] and 2JBV.[40]

To enhance the electrochemically active area of the electrode and to "roughen" the substrate for better enzyme adhesion, Pt nanoparticles were electrodeposited onto the microelectrodes prior to p*m*PD electrodeposition and enzyme immobilization. Cyclic voltammograms showing the electrodeposition of Pt nanoparticles and the change in ECSA before and after electrodeposition can be seen in Figure 5.2. In Figure 5.2A, one can see the reduction of Pt(IV) to Pt metal on the first potential sweep with an increase in cathodic current starting at ~0.05 V, initiating nucleation. With increasing cycle number there is an increase is oxidation current at ~1.0 V for Pt-oxide formation, an increase in cathodic current at ~0.6 V for Pt-oxide reduction, and an increase in voltammetric current between 0.1 to -0.2 for hydrogen adsorption and desorption as more Pt nanoparticles form and grow out from those nucleation sites. In Figure 5.2B, the same electrode is potential cycled in 0.5 mol L^{-1} H_2SO_4 before and after electrodeposition. A significant increase in the ECSA of the electrode is evident, with a hydrogen desorption charge increase from 21.0 nC to 559 nC, producing a roughness factor of 37.

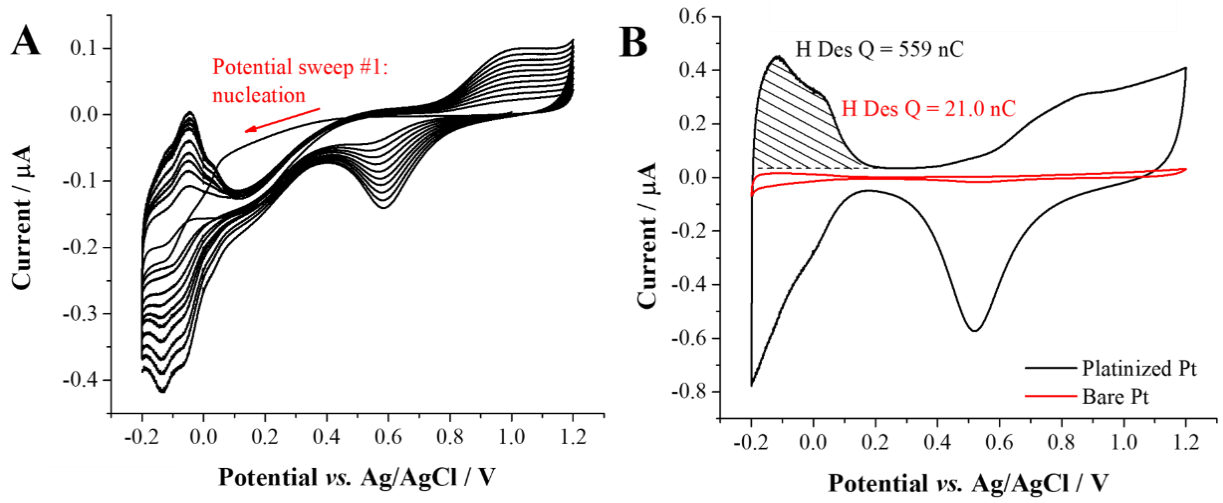

Figure 5.2. Cyclic voltammogram showing the electrodeposition of Pt nanoparticles by potential cycling a deoxygenated 2 mmol L^{-1} K_2PtCl_6 solution from -0.2 to 1.2 V at 10 mV s^{-1} for 10 cycles with the first cathodic sweep starting at 1.0 V (A). Cyclic voltammogram showing the same electrode shown in (A) before and after electrodeposition in 0.5 mol L^{-1} sulfuric acid (B). The last of 8 cycles is shown at 50 mV s^{-1}.

The p*m*PD films were prepared by potential cycling the platinized-Pt microelectrodes in a solution containing 5 mM *m*PD monomer in 0.1 mol L^{-1} phosphate buffer (PB), pH 7.4. A sample cyclic voltammogram illustrating this process can be seen in Figure 5.3. As potential is swept from 0.2 to 1.0 V, there is a large oxidation peak that occurs around 0.6 V in which the *m*PD monomer is oxidized to produce a radical cation. These radical cations are very reactive and couple with one another to produce dimers which are more easily oxidized due to more extensive π electron delocalization increasing the electron density around the redox sites.[37,41] As those dimers become oxidized, the chain length grows and the branched p*m*PD film forms.[41] The oxidation charge for this peak is 186 nC. With increasing cycle number, this oxidation peak disappears as the self-passivating p*m*PD film insulates the electrode and prevents further monomer oxidation, forming a thin uniform coating across the electrode substrate. The scan rate (10, 25, and 50 mV s^{-1}) and cycle number (10, 20, 30, and 40 cycles) were optimized for sufficient H_2O_2 permeability and optimal selectivity against electroactive interferents ascorbic acid (AA), dopamine (DA), norepinephrine

(NE), and serotonin (5-HT). The lower scan rates offered a tighter network of polymer and better rejection of electroactive interferents through size exclusion, but restricted H_2O_2 permeability. Therefore, 25 mV s^{-1} was selected as a compromise between electrode sensitivity toward enzymatically produced H_2O_2 and selectivity. Increasing the number of cycles at this scan rate had little effect on H_2O_2 permeability but a significant effect on the degree of electroactive interferent blockage, therefore 40 cycles was determined to be optimal for ACh sensor preparation

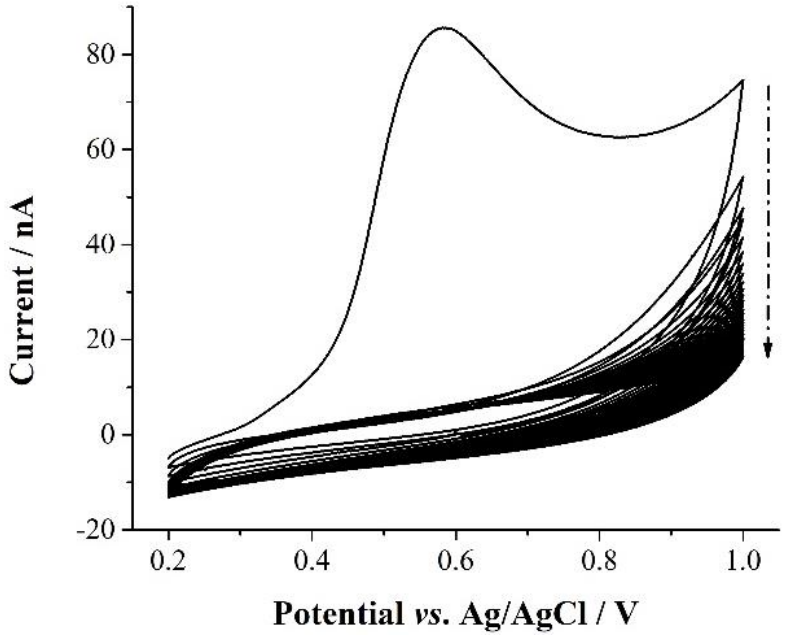

Figure 5.3. Cyclic voltammogram showing the electrodeposition of the pmPD films prepared by potential cycling the platinized-Pt microelectrodes in a solution containing 5 mM mPD monomer in 0.1 mol L^{-1} PB, pH 7.4. A large oxidation peak for mPD oxidation at ~0.6 V is evident that disappears with increasing cycle number as the self-passivating pmPD coats the entirety of electrode. The oxidation charge for this peak is 186 nC.

Following p*m*PD electrodeposition, 1 µL of a multienzyme solution consisting of equal parts of 200 U mL^{-1} ChOx, 400 U mL^{-1} AChE, 10% (w/v) BSA for enzyme stabilization, and 0.75% (v/v) glutaraldehyde was deposited onto the modified electrodes and dried for 2 hours at room temperature before storing immersed in 0.1 mol L^{-1} PB, pH 7.4, at 4°C. The volume (0.5, 1, 2, and 3 µL) of this multienzyme solution was optimized for peak response to ACh. Increasing the

solution volume from 0.5 to 1 µL produced a thicker multienzyme film with better coverage of the modified Pt substrate and consequently a significant enhancement in sensitivity toward ACh. However, solution volumes past 1 µL increases the multienzyme film thickness to the extent that enzymatically produced H_2O_2 can no longer diffuse effectively to the Pt substrate, and we see a greater variability in sensor-to-sensor response. Therefore, 1 µL was selected as the optimal solution volume for the multienzyme layer.

Prior to p*m*PD electrodeposition, Pt microelectrodes were roughened by electrodepositing Pt nanoparticles using cyclic voltammetry (CV) in a 2 mmol L^{-1} K_2PtCl_6 solution. This modification not only enhanced the sensitivity of the biosensors, but it also improved batch reproducibility (see Figure 5.4). One can see the change in the microelectrode's morphology at each step of the electrode fabrication process in Figure 5.5, which presents scanning electron microscopy (SEM) micrographs in the secondary electron image mode. A bare Pt substrate can be seen in Figure 5.5A. The surface is relatively smooth with exception of long striations produced from mechanical abrasion while grinding. Figure 5.5B shows the platinized-Pt substrate, which exhibits a highly roughened surface decorated by small and large Pt nanoparticles. Figure 5.5C shows the same platinized-Pt microelectrode at a lower magnification, revealing the Pt nanoparticle coverage conforming with the ridges in the Pt substrate. Figure 5.5D shows a platinized-Pt microelectrode coated with the p*m*PD polymer film. One can see a thin film that bridges the Pt nanoparticles together, but it is difficult to discern the polymer morphology.

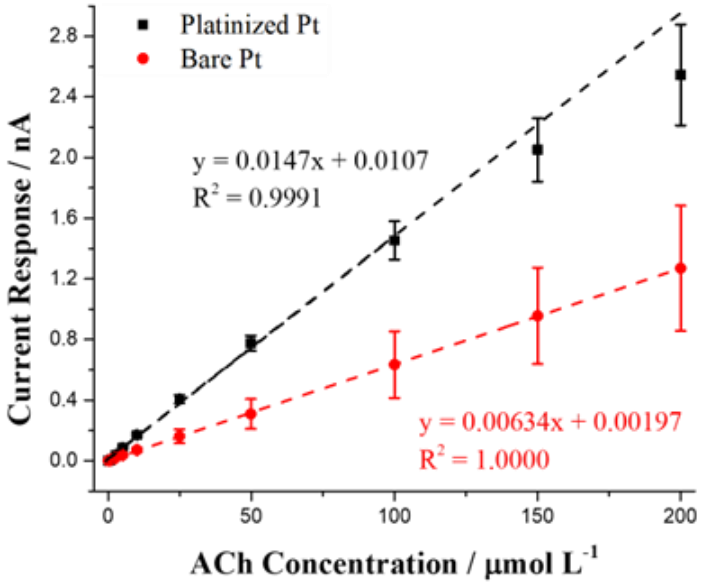

Figure 5.4. Response curves showing the change in sensitivity when preparing biosensors using bare Pt microelectrodes and platinized-Pt microelectrodes prior to pmPD polymer coating and pipetting 1 µL of the multi-enzyme solution on the modified electrodes. The sensitivity toward ACh approximately doubles, likely attributed to the increase in electrochemically active area of the platinized electrodes. More interestingly, the batch reproducibility decreased from 33% to 6.1% by platinizing the electrodes prior to enzyme immobilization. This improvement in reproducibility is likely due to better adhesion of the cross-linked enzymes to the electrode substrate.

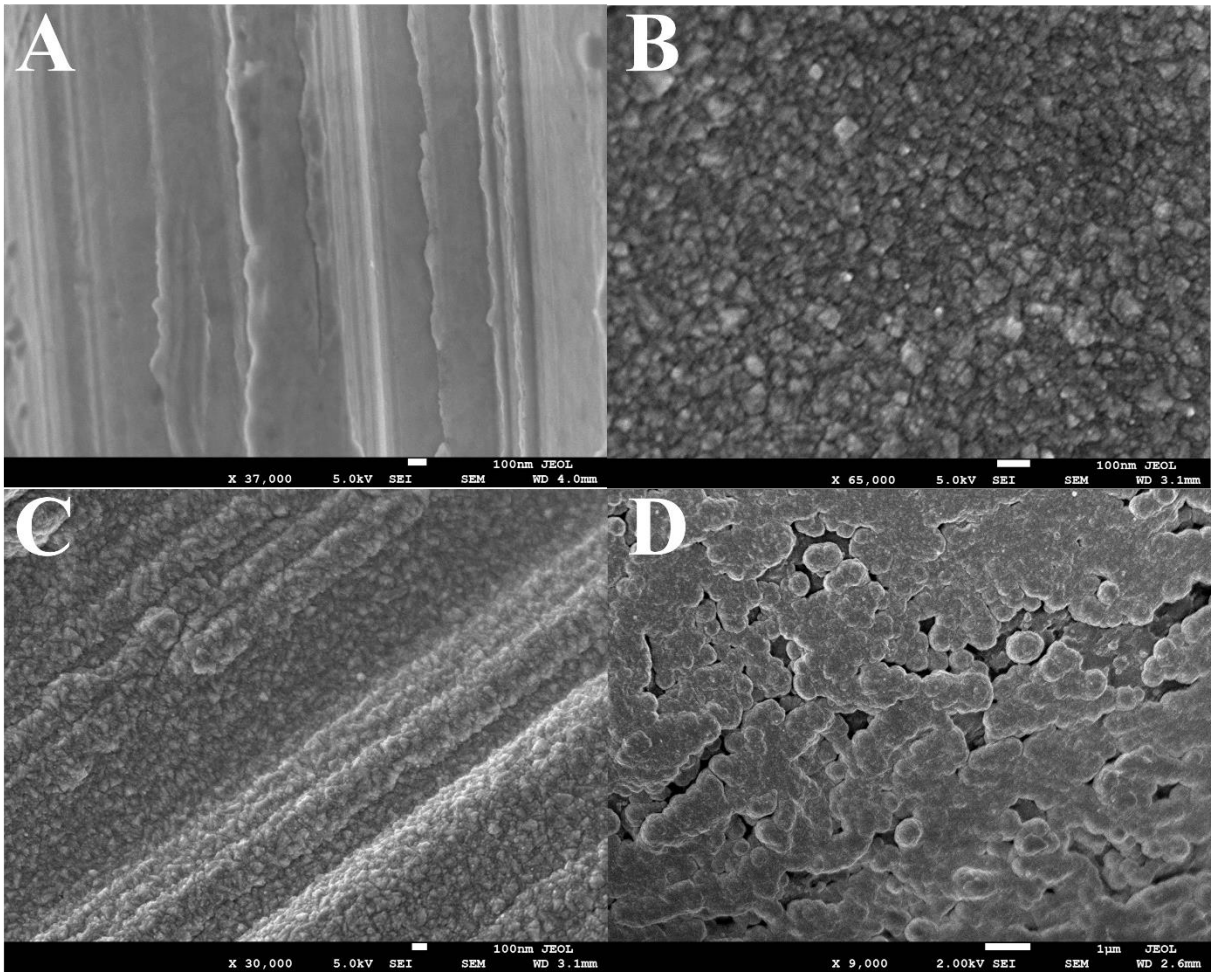

Figure 5.5. Secondary electron images using SEM revealing the change in morphology and microstructure of the Pt microelectrodes as they are platinized and coated in pmPD. Micrograph (A) shows a bare Pt microelectrode, which is relatively featureless with exception of long striations generated from mechanical abrasion during the grinding process. Micrographs (B) and (C) reveal the platinized-Pt microelectrodes, which display a highly roughened microelectrode surface with Pt nanoparticles that conform with the striations in the Pt metal. Micrograph (D) shows a platinized-Pt microelectrode coated in a pmPD film. The film molds around the Pt nanoparticles, forming polymer bridges from nanoparticle to nanoparticle.

To better visualize the films and discriminate between polymer coating and Pt, a bare Pt wire (80 µm diam.) was partially coated in *pm*PD by immersion into a deoxygenated 5 mmol L^{-1} *m*PD in 0.1 mol L^{-1} PB, pH 7.4, solution and scanning from 0.2 to 1.0 V at 25 mV s^{-1} for 40 cycles. Figure 5.6 presents the SEM micrographs of this p*m*PD film. In Figure 5.6A, one can delineate the polymer-coated and uncoated regions of the Pt wire. In Figure 5.6B, a higher magnification micrograph of the p*m*PD coating reveals good polymer coverage that conforms to any roughness

features on the native Pt wire. In Figure 5.7A, a cross section of the p*m*PD coated Pt wire is seen in which a blade was used to cut through the electrode post-polymerization. The polymer film detached and flaked off the surface at the cut edge. These pieces of delaminated polymer reveal a film thickness of ~50 nm, which is slightly higher than what has been reported in literature[34,36,37] The polymer accumulates in roughened regions of the Pt substrate to form large and small clusters of p*m*PD in these areas. Figure 5.7B reveals a larger p*m*PD cluster revealing small pores and channels that span across the polymer. This is typical of p*m*PD films, which tend to have a very porous morphology that allows small molecules, like H_2O_2, to partition in and diffuse through while rejecting larger molecules, like AA, DA, norepinephrine (NE), and 5-HT from reaching the underlying substrate.[34,36,37,42] Figure 5.7C reveals a small cluster of p*m*PD, which shows a distinct spherical morphology.

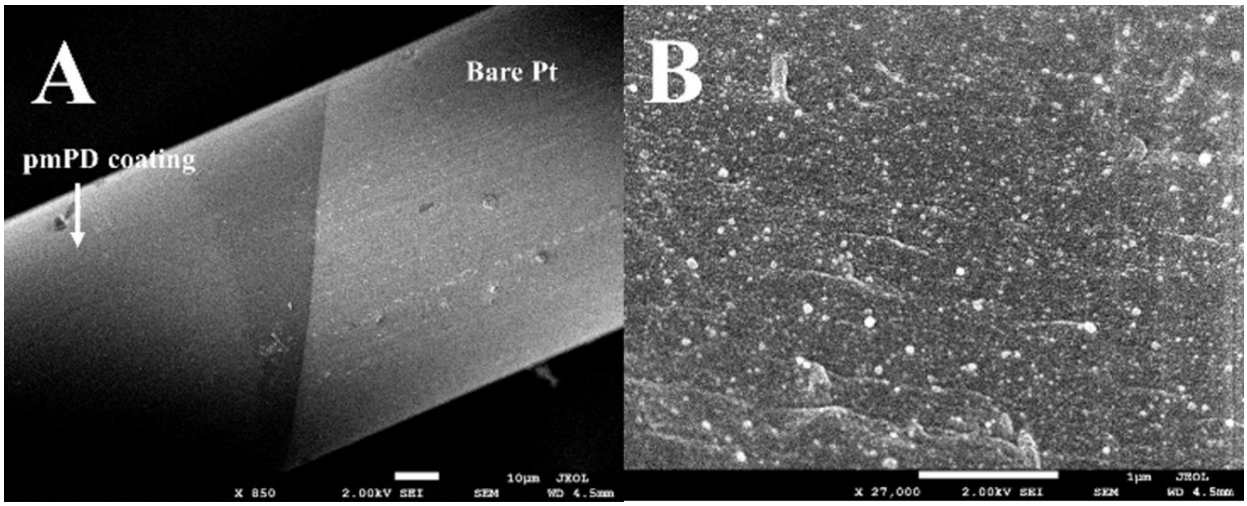

Figure 5.6. Secondary electron micrographs of a length of Pt wire (80 µm diam.) that was partially coated with pmPD. Micrograph A shows the boundary between the coated and uncoated regions of the wire and micrograph B shows a more magnified region of the pmPD coated wire, which indicates good coverage of the polymer over the Pt substrate.

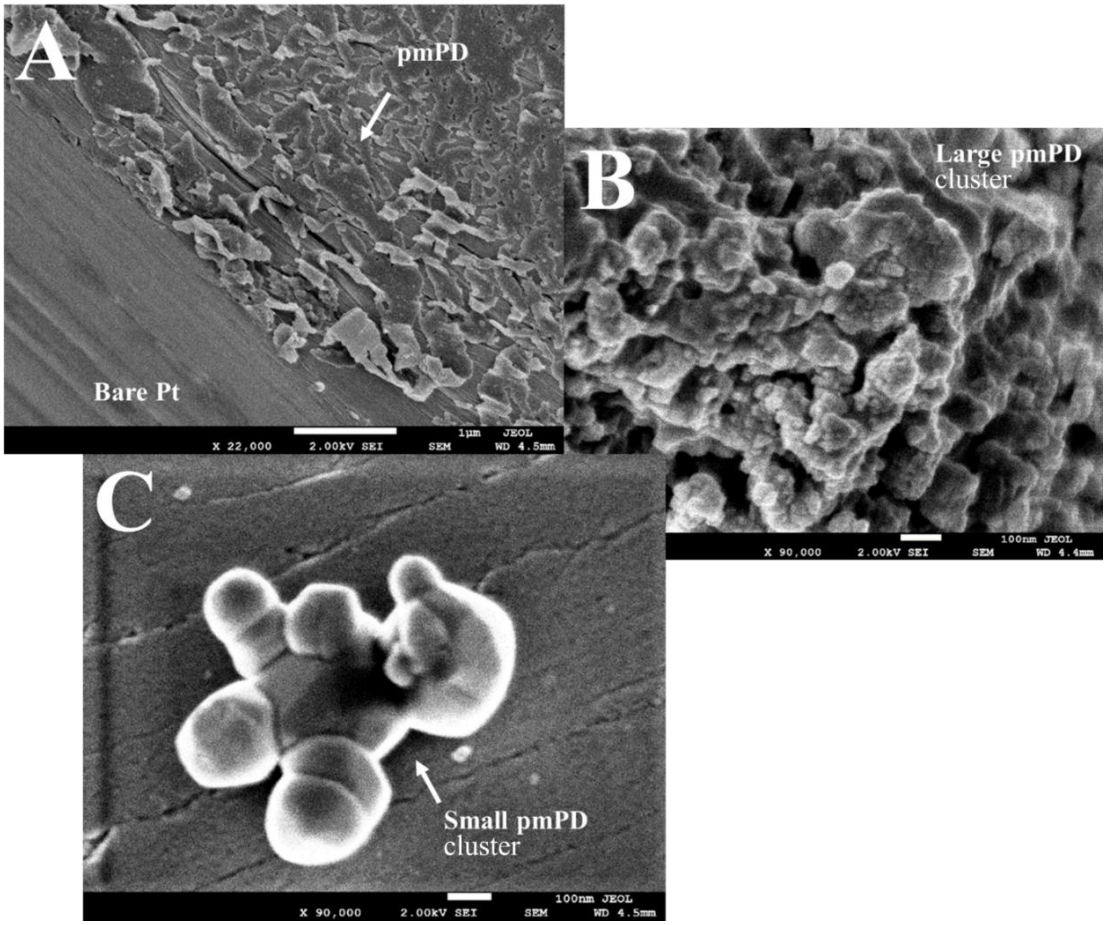

Figure 5.7. Secondary electron images using SEM of a cross sectional area of the pmPD coated Pt wire (80 µm diam.) revealing the relative thickness of the pmPD layers as the polymer film peels back in flakes where the razer blade made contact with the wire (A). The approximate thickness of the film was ~50 nm. The polymer tends to adhere and accumulate on defect sites on the Pt to form large and small clusters of pmPD. A relatively large cluster (B) shows small pores and channels that range from 20-85 nm in diameter across the film surface. A small cluster (C) reveals a distinct spherical morphology for the polymer.

To determine the detection potential to be used for the amperometric experiments, linear sweep voltammetry (LSV) was used to determine the oxidation potential of enzymatically generated H_2O_2. Figure 5.8A shows voltammograms for increasing concentration of ACh added to 10 mL of Krebs buffer, pH 7.4, with the potential being swept from 0.2 to 1.0 V. The scan rate used was 10 mV s^{-1}. One can see the onset of oxidation at ~0.4 V and significant increase in voltammetric current with increasing ACh concentration at ~0.7 V. At this potential, the current is at its maximum and mass transport limited. In data not shown, an experiment was conducted to evaluate if mass

transport for this process was diffusion-limited. A series of cyclic voltammograms were collected as a function of scan rate in response to 1 mmol L^{-1} H_2O_2. It was revealed that the peak oxidation current increases linearly with scan rate opposed to scan rate$^{1/2}$. This suggests that adsorption of H_2O_2 is occurring during electrochemical oxidation. The likely explanation for this is that H_2O_2 adsorbs to Pt-oxide formation sites, electron transfer occurs between the Pt-oxide/adsorbed H_2O_2 complex consequently reducing those surface sites, and those binding sites then become electrochemically regenerated, giving rise to the observed current response.[43,44] For multiple ACh/Ch biosensors, E_p^{ox} was 0.67 ± 0.05 V (n=5). Based on the voltammetric data, a detection potential of 0.75 V was selected for the CA experiments. Figure 5.8B shows an example amperometric *i-t* curve in which a biosensor was polarized at 0.75 V, and increasing concentration of ACh was added every 100 s to 10 mL of magnetically stirred Krebs buffer at room temperature. The biosensor responds rapidly in the amperometric detection mode to the ACh additions, producing an increase in oxidation current that responds linearly from 0.5 to 200 µmol L^{-1}, as is evident in the response curve inset.

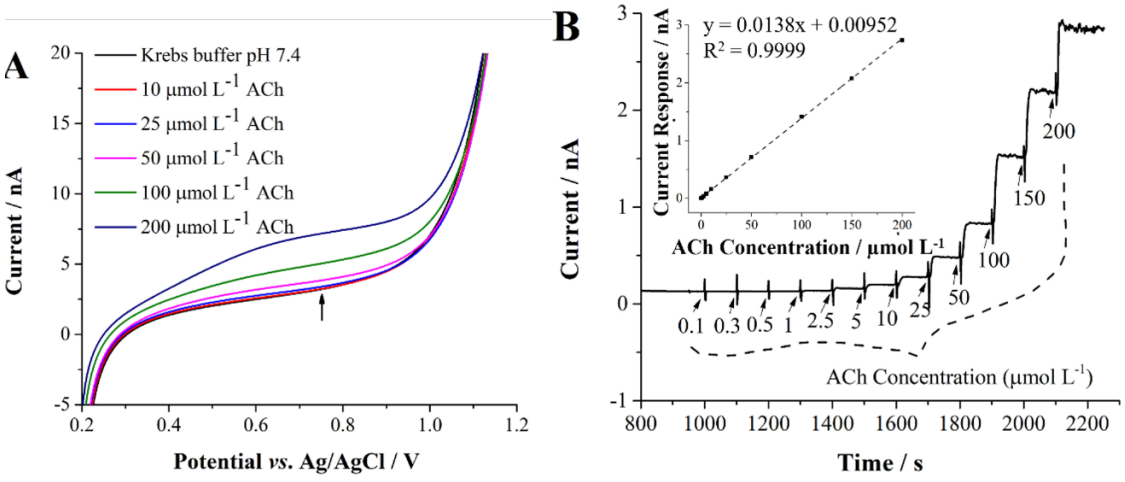

Figure 5.8. (A) Linear sweep voltammetric i-E curves showing the response to increasing concentrations of ACh added to Krebs buffer, pH 7.4. The scan rate was 10 mV s^{-1}. Amperometric i-t curve (B) showing an oxidation current that increases proportionally with increasing ACh concentration added to 10 mL of magnetically stirred Krebs buffer, pH 7.4. The detection potential was 0.75 V vs. Ag/AgCl.

Based on the detection scheme in Figure 1, the biosensor responds to both Ch and ACh. It is possible to detect ACh only if preparing two separate sensors: one with AChE and ChOx immobilized and the other with ChOx only immobilized. By employing both sensors in the sensing media and subtracting the ChOx-only response, changes in basal levels of ACh can be determined.[24] Although, this can become difficult in practice due to variability in electrode fabrication. Some researchers have overcome this by producing mass-fabricated microelectrode arrays which are much more uniform in design and manufacture.[26] However, these recording sites are 100 µm from one another, limiting spatial resolution.[26] Due to the nature of our measurements and their dependence of electrode position on current response, it is not possible to employ a similar electrode for our measurements. As ACh is rapidly hydrolyzed into Ch by AChE following synaptic release, *ex vivo* measurements are a combination of ACh and Ch release and a tool for measuring cholinergic neuronal function rather than isolating the ACh response specifically. Figure 5.9 shows example *i-t* curves showing the difference in sensor response to Ch vs. ACh (A) and how the response to equimolar additions of ACh compares to equimolar additions of the electroactive interferents AA, DA, NE, and 5-HT (B). In both curves, the electrode was polarized at 0.75 V vs. Ag/AgCl and the electrolyte was 10 mL of magnetically stirred Krebs buffer, pH 7.4. The current responses to Ch and ACh are nearly identical for n=3 sensors ($p=0.76$), as is the response time ($p=0.99$), suggesting that the conversion of ACh to Ch occurs rapidly. The biosensor responds reproducibly to both Ch and ACh with repeat 10 µmol L^{-1} additions of each with a RSD of 4.7% for Ch and 0.7% for ACh for n=5 additions. One can see that although the biosensor responds reproducibility to ACh, there is little to no response to the equimolar additions of AA, DA, NE, and 5-HT. This indicates excellent selectivity toward ACh and Ch, making the biosensor useful for measuring cholinergic signaling in complex media.

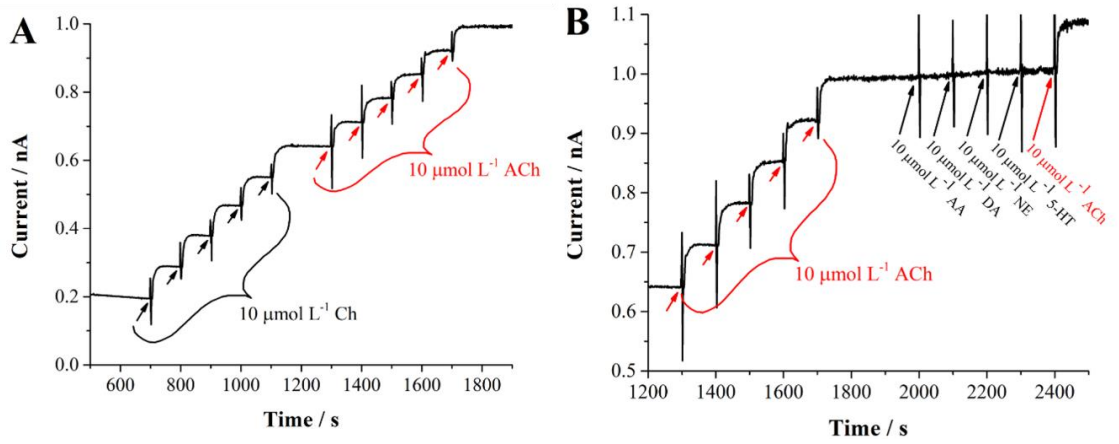

Figure 5.9. Amperometric i-t curves (A) showing the respective responses to equimolar additions of Ch and ACh added to 10 mL of magnetically stirred Krebs buffer, pH 7.4. The detection potential was 0.75 V vs. Ag/AgCl. A second amperometric i-t curve (B) showing the response to equimolar additions of ACh followed by equimolar additions of electroactive interferents AA, DA, NE, and 5-HT. The last addition returns to ACh. Both measurements were made at room temperature.

Table 5.1 summarizes the detection figures of merit calculated for the biosensors to ACh from CA measurements made at room temperature. The sensitivity is normalized to the geometric area of the microelectrode. The response time was defined as the time it took for the current response to 50 µmol L^{-1} ACh to rise from 5% to 90% of its maximum steady state response. The response time is competitive with other ACh/Ch biosensors, which are typically ≥8 s,[18,19,27,28] but slower than other biosensors utilizing p*m*PD, which are typically ≤1 s.[24-26] This is likely because our pmPD films appear to be thicker than what is typically observed in literature, which is 10-35 nm.[34,36,37] Although there seems to be little effect on sensitivity, our thicker p*m*PD films (~50 nm) are likely slowing response time .The reproducibility was determined by calculating the RSD of the slope of the response curves within a single batch of biosensors (n=3). The selectivity ratio for AA, DA, NE, and 5-HT was determined from the current response to ACh normalized to the current response of each interferent. The lifetime of the biosensors was assessed by preparing a batch of biosensors and using CA to determine the current response from 0.5 to 100 µmol L^{-1} ACh at room temperature immediately after biosensor preparation, after 7 days of storage, and after 14 days of

storage. The electrodes were stored immersed in 0.1 mol L^{-1} PB, pH 7.4, in the refrigerator at 4°C between measurements. The average biosensor response for n=3 sensors was recorded. The respective response curves can be seen in Figure 5.10. Over a two-week period, there was no change in sensitivity for the three biosensors. Therefore, for *ex vivo* measurements, the sensors were used within two weeks of preparation.

Sensitivity (mA mol^{-1} L cm^{-2})	190 ± 10
LOD (µmol L^{-1})	0.8 ± 0.3
LOQ (µmol L^{-1})	2.9 ± 1.0
Linear Dynamic Range (µmol L^{-1})	3 - 130
Response Time (s)	2 ± 1
Reproducibility	6.1% RSD
Selectivity $\left(\frac{I_{ACh}}{I_{interferent}}\right)$	125 ± 1 (AA), 60 ± 1 (DA), 24 ± 1 (NE), 50 ± 1 (5-HT)
Lifetime	≥ 2 weeks

Table 5.1. Detection Figures of Merit for ACh. Values are average ± standard deviation (SD) for n=3 electrodes for measurements conducted at room temperature (25°C). Limit of detection (LOD) is defined as S/N ≥3 and limit of quantification (LOQ) is defined as S/N ≥10.

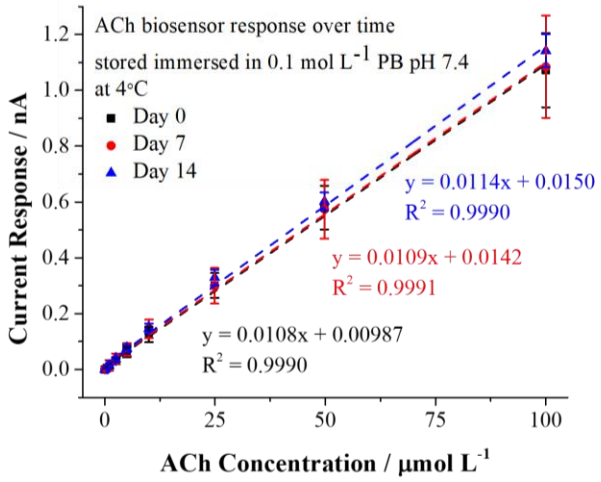

Figure 5.10. Response curves showing the amperometric current response to 0.5 to 100 µmol L^{-1} ACh added to 10 mL of magnetically stirred Krebs buffer, pH 7.4, at room temperature for n=3 biosensors. The detection potential was 0.75 V vs Ag/AgCl. The average current response ± standard deviation was determined immediately after sensor preparation, after 7 days of storage, and after 14 days of storage. The sensors were stored immersed in 0.1 mol L^{-1} PB, pH 7.4, at 4°C between measurements. There is no loss in sensitivity to ACh over the two week period, therefore sensors used for ex vivo measurements were used within two weeks of preparation.

To prepare for *ex vivo* measurements, the effects of oxygenation and physiological

temperature were evaluated. Similar to the experimental set up used for the tissue measurements, Krebs buffer, pH 7.4, was perfused through a recording chamber at 4 mL min^{-1} while the working electrode was positioned at the center of the chamber using a micromanipulator. The electrode was polarized at 0.75 V vs. Ag/AgCl and the background current allowed to stabilize. Using standard solutions, 1, 3, 5, and 10 µmol L^{-1} ACh were perfused through the recording chamber with a brief rinse period between each concentration. For a single biosensor, these measurements were performed at room temperature (25°C), after bubbling O_2 gas into the buffer for 20 min prior to and during the measurement, and at physiological temperature (37°C) with oxygenation. The data can be seen in Figure 5.11. There is not a significant difference in the response after oxygenation, indicating that atmospheric O_2 provides a sufficient concentration of the cofactor needed for Ch oxidation in the enzymatic reactions. Unsurprisingly, increasing the temperature nearly doubled the sensitivity of the sensor.

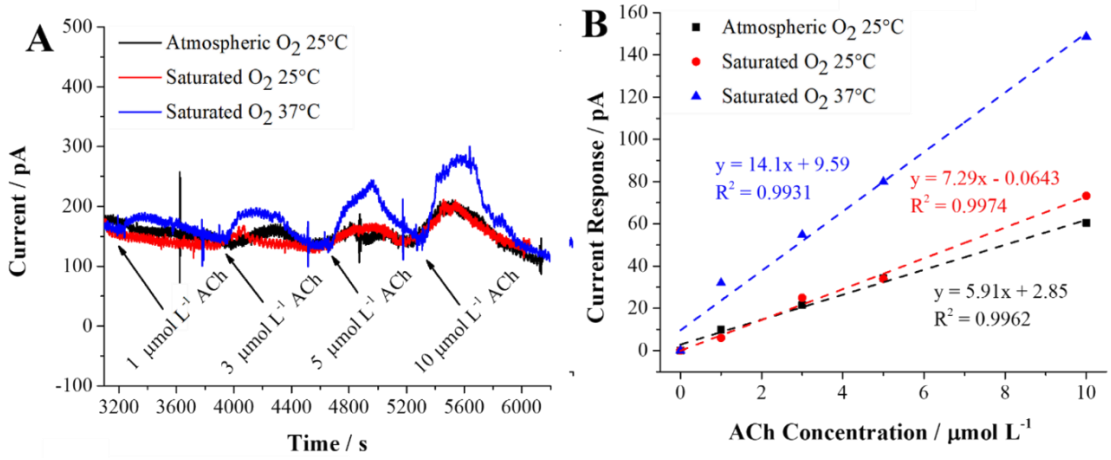

Figure 5.11. Amperometric *i-t* traces (A) showing the biosensor's response to increasing concentration of ACh added to Krebs buffer pH 7.4, which is continuously perfused through a recording chamber at 4 mL min^{-1}. A brief rinse period with buffer was performed between additions. The detection potential was 0.75 V vs Ag/AgCl. The respective response curves can be seen in (B), where the black trace shows the current response at room temperature (25°C), the red trace shows the current response at room temperature but after saturating the buffer with O_2, and the blue trace shows the current response after oxygenating the buffer and increasing the temperature to physiological temperature (37°C).

To account for sensor-to-sensor variability during the *ex vivo* measurements, a calibration was performed prior to each tissue measurement in the flow bath. A sample *i-t* curve and its corresponding response curve can be seen in Figure 5.12 in which warmed (36-37°C) Krebs buffer, pH 7.4, was perfused through a recording chamber at 4 mL min^{-1}. The electrode was polarized at 0.75 V vs. Ag/AgCl and increasing concentrations of ACh were perfused through the chamber after the background current stabilized. A rinse was performed following the final ACh concentration, and restoration of baseline current was achieved. The sensitivity from these calibrations was used to estimate the peak concentration of ACh/Ch detected in the extracellular solution around the biosensor after electrical stimulation of nearby myenteric ganglia in the mouse colon. Compared to the measurements conducted at room temperature, the LOD decreased to 0.3 ± 0.2 µmol L^{-1} and the sensitivity increased to 360 ± 60 mA mol^{-1} L cm^{-2} for n=6 sensors at physiological temperature.

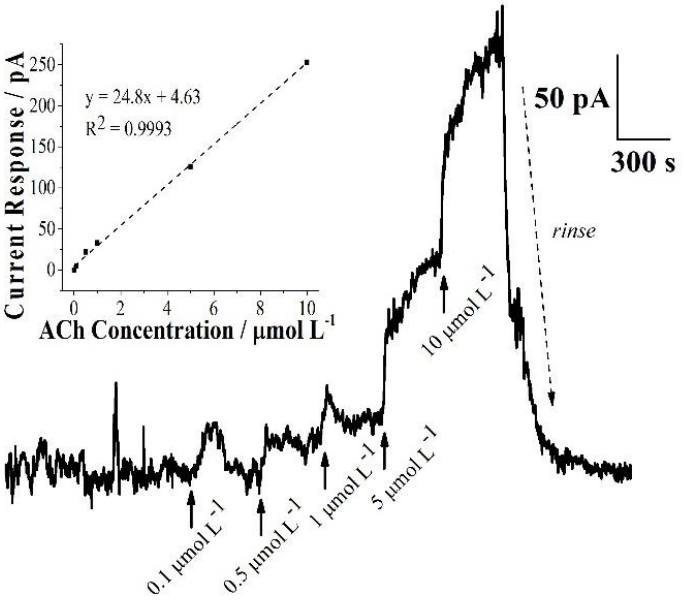

Figure 5.12. Continuous amperometric *i-t* curve and corresponding response curve (inset) showing a calibration of a single biosensor using standard ACh solutions prior to an ex vivo measurement. The detection potential was 0.75 V vs. Ag/AgCl and the electrolyte was Krebs buffer, pH 7.4, perfused at 4 mL min^{-1} at 37°C. The current was smoothed by a 10 Hz lowpass filter.

To determine how many times a single biosensor could be used for *ex vivo* measurements, a calibration was performed using a biosensor over four consecutive days, running a full tissue

measurement after each calibration. These data can be seen in Figure 5.13. There is little loss in sensitivity between days 1 and 2, less than 5%. However, after day 3, the sensitivity decreases by 30% and by day 4 it decreases by 57%. This gradual decline with prolonged use *ex vivo* is not that surprising as proteins in the tissue can progressively adsorb to the electrode surface, fouling the substrate. Therefore, individual biosensors were not used for more than two *ex vivo* measurements. For experiments in which two animals were tested within the same day, the same sensor was used, but with a brief second calibration performed in response to 1 µmol L^{-1} ACh additions to ensure that the same current response was achieved.

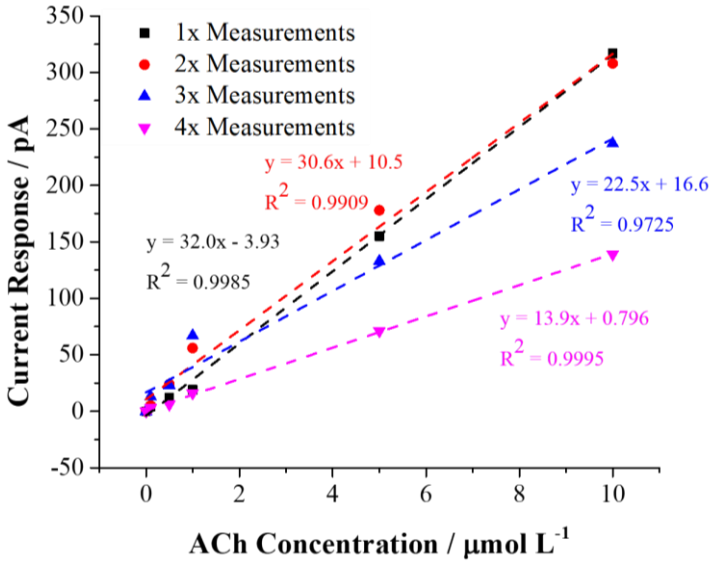

Figure 5.13. Response curves generated when calibrating a single biosensor after four consecutive ex vivo measurements over the course of four days. The response plots the current response to 0.1, 0.5, 1, 5, and 10 µmol L^{-1} ACh perfused through the recording chamber at 4 mL min^{-1} at 37°C. The sensor was polarized at 0.75 V vs Ag/AgCl. There is little loss in sensitivity between days 1 and 2, less than 5%. However, after day 3, the sensitivity decreased by 30% and by day 4 it decreased by 57%. Considering these findings, individual sensors were used for no more than two tissue measurements to avoid significant loss in sensitivity.

For *ex vivo* measurements, the number of electrical stimuli delivered to the tissue was gradually increased and the corresponding current response was recorded. The measured current response results from a combination of synaptic ACh release and ACh which has been hydrolyzed

into Ch by AChE in the extracellular space. Due to time limitations, replicate stimulations were not performed for each set of electrical stimuli, but we did verify that identical stimulations produced identical current responses. This data is presented in Figure 5.14. Figure 5.15 shows a sample response for a single male and female mouse in which the tissue is stimulated for 10, 20, 30, 40, and 50 pulses at 10 Hz, 80 V, 0.5 ms pulse duration. Stimulations were performed every 5-10 min, allowing sufficient time for vesicular restoration to occur[45,46] The *i-t* traces are normalized to each electrode's calibration to display the extracellular ACh/Ch concentration with respect to time. A slight increase in peak ACh/Ch concentration can be seen from 10 to 40 pulses. From 40 to 50 pulses the peak concentration is the same, but the peak broadens, indicating that at 40 pulses the peak rate of release is obtained, but greater number of stimuli prolongs this release. The mean ± standard error of mean (SEM) peak concentrations as well as the integrated area of each peak can be seen in Figure 5.16. Overall, with exception of the mean comparison between 10 and 40 and 10 and 50 pulses for the peak ACh/Ch concentration for the male mice, there is not a significant increase in peak concentration or area with increasing number of electrical stimulation pulses. This suggests that these electrical stimulation conditions elicit a peak neurotransmitter release from cholinergic enteric neurons. A current response was unable to be recorded using fewer than 10 electrical stimuli, as these concentrations are likely below the LOD (0.3 ± 0.2 μmol L^{-1} at physiological temperature) of the sensor. The peak concentrations of ACh/Ch detected are identical between the male and female mice. Likewise, there is not a significant sex-difference when comparing the respective areas of the peaks. The peak ACh/Ch concentration for the male mice was 600 ± 47 nmol L^{-1} at 50 pulses and the peak concentration for the female mice was 626 ± 197 nmol L^{-1} at 30 pulses. Due to the absence of similar studies in the gut, our results cannot be compared directly with any literature data. The amount of ACh/Ch detected will depend on the distance of the

microelectrode from the release sites and the number of cholinergic neurons in the vicinity of the microelectrode, offset by the rate of clearance. ACh concentration in the brain extracellular fluid is in the low nanomolar range[47,48] Naturally, electrically stimulated tissue would elicit a higher local ACh concentration. For example, in an *ex vivo* experiment, electrically stimulated mouse brain slices elicited an ACh concentration of 0.41 ± 0.05 µmol L^{-1}.[49] In another study, KCl and nicotine were used to stimulate ACh release from the prefrontal cortex in rats *in vivo.* Low micromolar levels of ACh were detected using a microelectrode array.[25] It is generally accepted that synaptically released ACh can reach a peak millimolar concentration at the neuromuscular junction, however this concentration decays rapidly due to diffusion, reuptake, metabolism, and receptor binding.[50] Unless using nanoelectrodes, it is not possible to probe the synaptic cleft where ACh concentration is at its peak. Rather we are measuring a small fraction of ACh or Ch which has been formed through the metabolism of ACh that diffuses away from multiple cholinergic release sites. This suggests our measurements, which are in the submicromolar range, could possibly be a reasonable estimate.

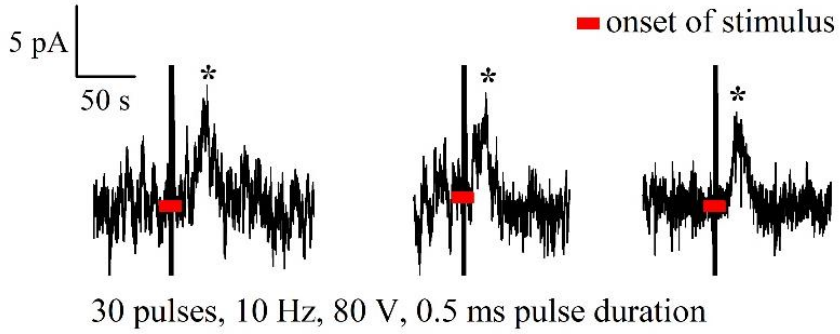

Figure 5.14. Sample *ex vivo* amperometric measurement in which three consecutive stimulations were made, all at 30 pulses, 10 Hz, 80 V, 0.5 ms pulse duration. The red bar represents the onset of the electrical stimulus. The detection potential used was 0.75 V vs Ag/AgCl. The responses to the three stimulations are similar with an average current response of 6.6 ± 1.1 pA. Due to time constraints, replicate stimulations were not performed for each measurement. Instead, the tissue was stimulated for 10, 20, 30, 40, and 50 pulses to generate a pulse number response curve.

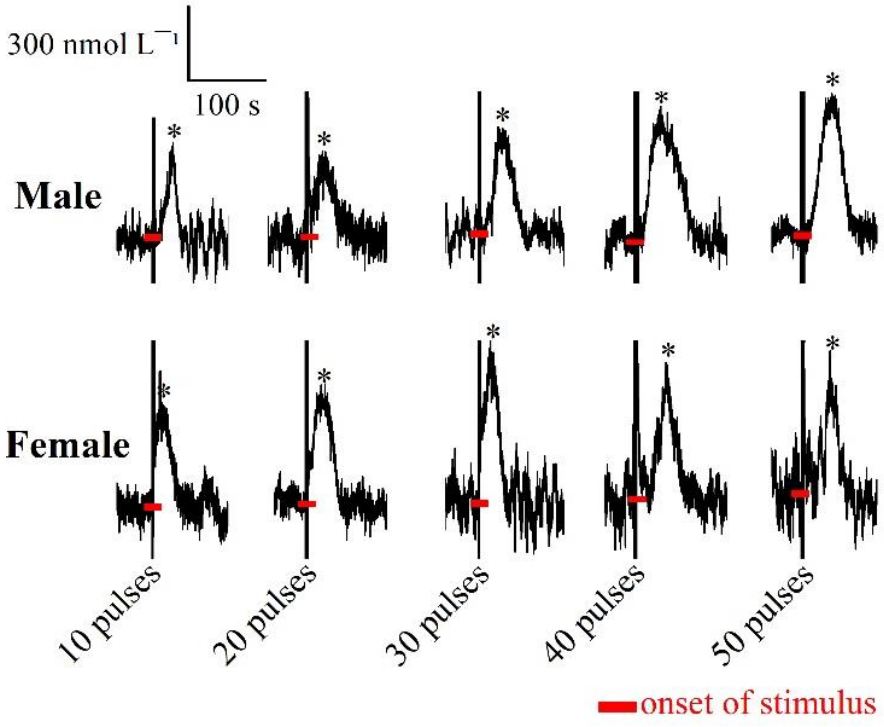

Figure 5.15. *Ex vivo* continuous amperometric responses generated by normalizing the i-t curves to their respective calibrated sensitivities showing the change in extracellular concentration of ACh/Ch following 10, 20, 30, 40, and 50 electrical stimuli at 10 Hz, 80 V, 0.5 ms pulse duration. The red bars indicate the onset of the stimulus. The detection potential was 0.75 V vs. Ag/AgCl. Data was filtered through a 10 Hz lowpass filter.

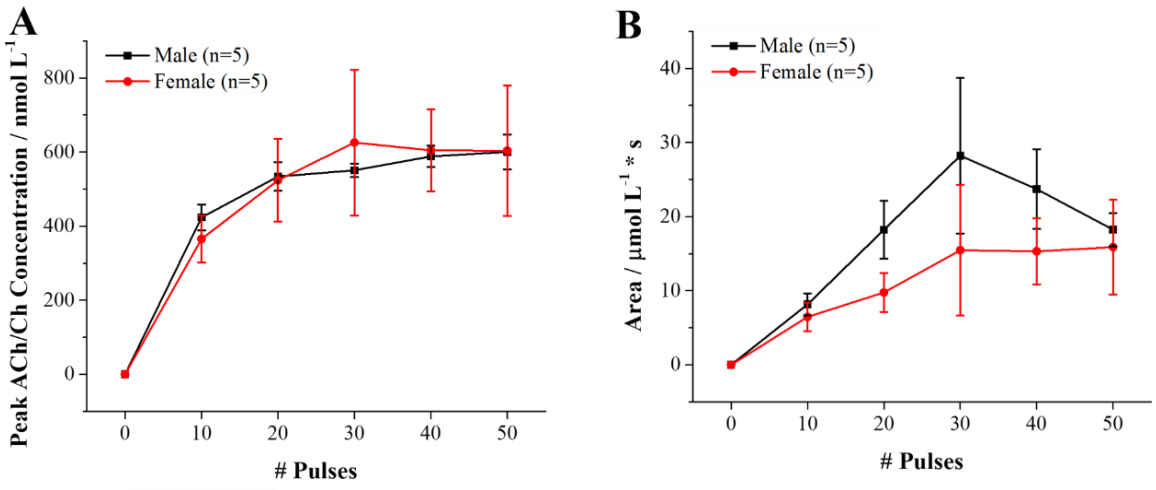

Figure 5.16. (A) Extracellular concentrations of ACh/Ch evoked with a tissue stimulation of 10-50 pulses at 10 Hz, 80 V, 0.5 ms pulse duration and the corresponding integrated areas of the current responses (B). Data are presented as mean ± SEM for n=5 male and n=5 female mice.

In cholinergic neurons ACh is synthesized by ChAT using Ch and acetyl-CoA. When ACh

is released across a chemical synapse, it acts on nicotinic or muscarinic receptors or, conversely, the actions of ACh are terminated by AChE, and ACh is hydrolyzed into Ch and acetate for reuptake and recycling.[46] By inhibiting AChE with a drug like neostigmine, one can increase the time that ACh resides in the extracellular solution, consequently increasing the area of our measured current response and confirming the source of oxidation current is in some part due to ACh.

Example continuous amperometric *i-t* traces showing the general pharmacological scheme that was followed for the *ex vivo* electrochemical measurements using a single 50 pulse stimulation can be seen in Figure 5.17. After completing the electrical stimulations, the tissue was perfused with 0.3 μmol L^{-1} TTX and the stimulations were repeated. After perfusing TTX, there is some electrical noise ~100 s downstream of the stimulation. However, one can see that the current response, which previously manifests as a sharp spike immediately following the electrical stimuli, is nearly abolished after perfusing the sodium channel blocker. This indicates that the current response is of neurogenic origin and release occurs via an action potential dependent process. Next, the tissue was rinsed with buffer and a single stimulation was repeated to verify that the TTX was rinsed out and the original current response was restored. Lastly, the tissue was perfused with 10 μmol L^{-1} neostigmine, an AChE inhibitor. This drug prevents the breakdown of ACh from occurring, resulting in an increase in half-life of ACh in the synaptic cleft. This extension in time that ACh sits in the extracellular space should hypothetically prolong the action of ACh and consequently increase the local concentration of ACh and delay the breakdown into Ch, resulting in an amperometric peak with a greater area than before drug perfusion.

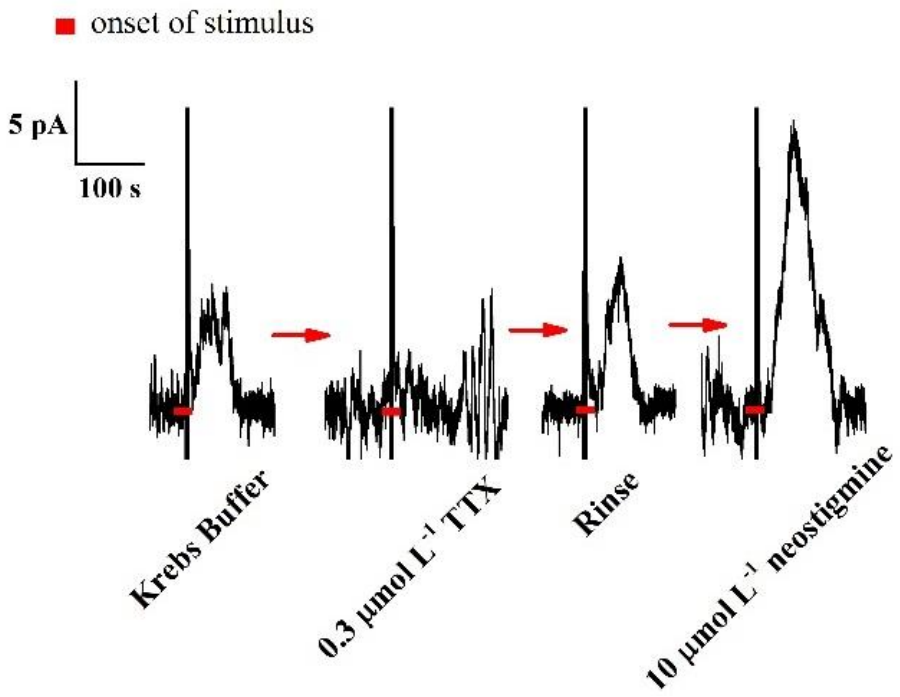

Figure 5.17. Sample continuous amperometric i-t curves showing the pharmacological sequence followed during ex vivo measurements. A single stimulation is shown in which 50 electrical stimuli at 10 Hz, 80 V, and 0.5 ms pulse duration are delivered to the tissue preparation. The red bars indicate the onset of the stimulus. The detection potential was 0.75 V vs. Ag/AgCl. Data was filtered through a 10 Hz lowpass filter.

A summary of the drug responses for the male and female mice is presented in Figure 5.18, in which the area of the oxidation peak following the 50 pulse electrical stimulation is compared before and after drug application. The response is essentially abolished in the presence of TTX. The response can be seen to be completely restored after rinsing TTX out. Overall, there is only a slight, far from significant, increase in response after perfusing neostigmine, but the response was variable not only from animal to animal, but also within the same animal. For example, in most cases only the first stimulation performed after perfusing the drug resulted in an enhanced ACh response, whereas repeated stimulations were often dramatically reduced. It is possible that the concentration of the AChE inhibitor was not high enough to see the desired response or that these observations are the result of some controversial effects of AChE inhibitors. For example, it has been found that the exaggerated concentration of ACh in the extracellular space could activate inhibitory

autoreceptors on the cholinergic neurons, therefore reducing the cholinergic neurons response to electrical stimulation.[48] However, the more likely explanation is that the bulk of the measured response is from Ch formed from the hydrolysis of ACh rather than ACh itself. When using analytical techniques such as microdialysis, measured concentrations of ACh vs Ch are overwhelmingly dominated by Ch[47] with extracellular ratios of ACh:Ch being about 1:12.[51] On the other hand, when using techniques like electrochemical detection with rapid response time, ratios of ACh:Ch can be as close as 1:1.[24-26] However, these sensors exhibit response times ≤1 s, so it is likely that our current sensor design does not respond fast enough to capture ACh concentration before being converted over to Ch. This is something that could be improved upon by implementing thinner films of p*m*PD, which provide a less tortuous path for H_2O_2 to diffuse through.

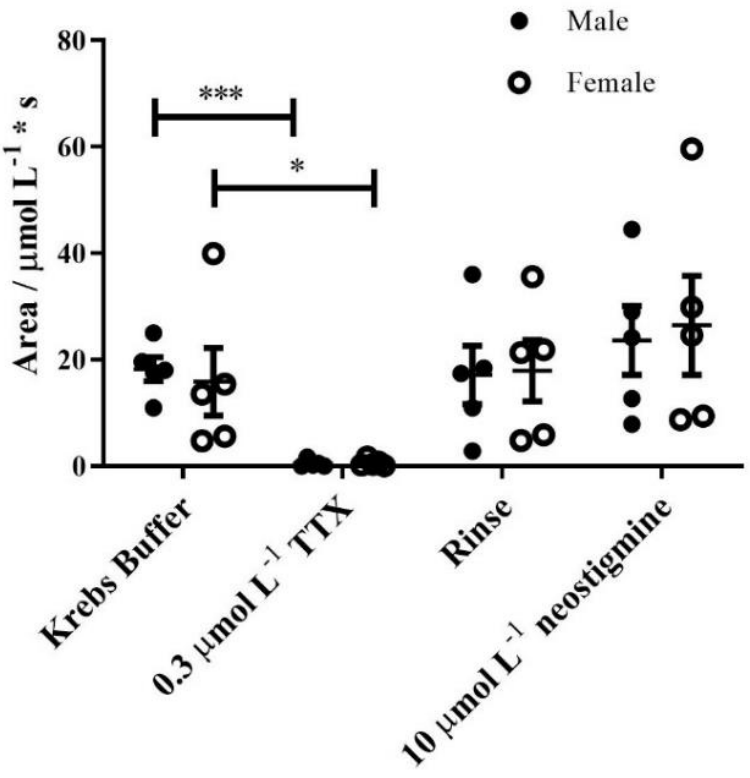

Figure 5.18. The mean ± SEM integrated peak area normalized to each biosensor's calibrated sensitivity for the amperometric responses to 50 pulses electrical stimuli at 10 Hz, 80 V, 0.5 ms pulse duration for male (n=5) and female (n=5) control mice in the presence and absence of 0.3 µmol L^{-1} TTX and 10 µmol L^{-1} neostigmine. *p≤0.05, ***p≤0.001.

5.3 Conclusions

ACh/Ch biosensors, which are selective against AA, DA, NE, and 5-HT, were successfully prepared and applied to measure electrically stimulated ACh release from myenteric ganglia in the mouse colon. We estimated a measured peak ACh/Ch concentration of 600 ± 47 nmol L^{-1} for the male mice and 626 ± 197 nmol L^{-1} for the female mice. The current responses were abolished in the presence of sodium channel blocker TTX suggesting that the measured current response is neurogenic in origin. The current response was elevated slightly in the presence of AChE inhibitor neostigmine, suggesting that the bulk of current response measured is from Ch which has been formed through the hydrolysis of ACh rather than ACh itself. This is one of the limitations of this sensor design, which is the inability to differentiate between ACh and Ch unless utilizing two separate sensors. This can be problematic, as ACh is rapidly hydrolyzed following synaptic release to Ch by AChE. Regardless, these sensors provide a useful tool for measuring cholinergic signaling that can be applied *ex vivo*. We plan on using these sensors to measure ACh/Ch release in an APP/PS1 mouse model of AD to determine if cholinergic signaling is also affected in the ENS of AD.

Reprinted (adapted) with permission from:

Henderson, S.; Strait, M.; Fernandes, R.; Xu, H.; Galligan, J.; Swain, G. *Ex Vivo* Electrochemical Monitoring of Cholinergic Signaling in the Mouse Colon Using an Enzyme-Based Biosensor. *ACS Chem. Neurosci.* In press.

REFERENCES

1. DeTure, M. A.; Dickson, D. W. The Neuropathological Diagnosis of Alzheimer's Disease. *Mol. Neurodegen*. **2019**, *14*(1), 32.

2. Alzheimer's Association. 2023 Alzheimer's Disease Facts and Figures. *Alzheimer's Dement*. **2023**, *19*(4).

3. Terry Jr., A. V.; Buccafusco, J. J. The Cholinergic Hypothesis of Age and Alzheimer's Disease-Related Cognitive Deficits: Recent Challenges and Their Implications for Novel Drug Development. *J. Pharmacol. Exp. Ther*. **2003**, *306*(3), 821-827.

4. Ferreira-Vieira, T. H.; Guimaraes, I. M.; Silva, F. R.; Ribeiro, F. M. Alzheimer's Disease: Targeting the Cholinergic System. *Curr. Neuropharmacol*. **2016**, *14*(1), 101-115.

5. Hampel, H.; *et al*. The cholinergic system in the pathophysiology and treatment of Alzheimer's disease. *Brain* **2018**, *141*(7), 1917–1933.

6. Bartus, R. T.; Dean, R. L.; Beer, B.; Lippa, A. S. The Cholinergic Hypothesis of Geriatric Memory Dysfunction. *Science* **1982**, *217*(4558), 408-417.

7. Contestabile, A. The History of the Cholinergic Hypothesis. *Behav. Brain Res*. **2011**, *221*(2), 334-340.

8. Hasselmo, M. E. The Role of Acetylcholine in Learning and Memory. *Curr. Opin. Neurobiol*. **2006**, *16*(6), 710-715.

9. Drever, B. D.; Riedel, G.; Platt, B. The Cholinergic System and Hippocampal Plasticity. *Behav. Brain Res.* **2011**, *221*(2), 505-514.

10. Maurer, S. V.; Williams, C. L. The Cholinergic System Modulates Memory and Hippocampal Plasticity via Its Interactions with Non-Neuronal Cells. *Front. Immunol*. **2017**, *8*, 1489.

11. Furness, J. B.; Types of Neurons in the Enteric Nervous System. *J. Auton. Nerv. Syst*. **2000**, *81*(1-3), 87-96.

12. Han, X.; Tang, S.; Dong, L.; Song, L.; Dong, Y.; Wang, Y.; Du, Y. Loss of Nitrergic and Cholinergic Neurons in the Enterc Nervous System of APP/PS1 Transgenic Mouse Model. *Neurosci. Lett*. **2017**, *646*, 59-65.

13. Pellegrini, C.; Daniele, S.; Antonioli, L.; Benvenuti, L.; D'Antongiovanni, V.; Piccarducci, R.; Pietrobono, D.; Citi, V.; Piragine, E.; Flori, L.; Ippolito, C.; Segnani, C.; Palazon-Riquelme, P.; Lopez-Castejon, G.; Martelli, A.; Colucci, R.; Bernardini, N.; Trincavelli, M. L.; Calderone, V.; Martini, C.; Blandizzi, C.; Fornai, M. Prodromal Intestinal Events in Alzheimer's Disease (AD): Colonic Dysmotility and Inflammation Are Associated with Enteric AD-Related Protein Deposition. *Int. J. Mol. Sci.* **2020**, *21*(10), 3523.

14. Stoye, N. M.; dos Santos Guilherme, M.; Endres, K. Alzheimer's Disease in the Gut—Major Changes in the Gut of 5xFAD Model Mice with ApoA1 as Potential Key Player. *FASEB J.* **2020**, *34*(9), 11883-11899.

15. Menden, A.; Hall, D.; Hahn-Townsend, C.; Broedlow, C. A.; Joshi, U.; Pearson, A.; Crawford, F.; Evans, J. E.; Klatt, N.; Crynen, S.; Mullan, M.; Ait-Ghezala, G. *Sci. Rep*. **2022**, *12*, 4797.

16. Sun, Y.; Sommerville, N. R.; Liu, J. Y. H.; Ngan, M. P.; Poon, D.; Ponomarev, E. D.; Lu, Z.; Kung, J. S. C.; Rudd, J. A. Intra-Gastrointestinal Amyloid-β1–42 Oligomers Perturb Enteric Function and Induce Alzheimer's Disease Pathology. *J. Physiol*. **2020**, *598*(19), 4209-4223.

17. Johnson, C. D.; Barlow-Anacker, A. J.; Pierre, J. F.; Touw, K.; Erikson, C. S.; Furness, J. B.; Epstein, M. L.; Gosain, A. Deletion of Choline Acetyltransferase in Enteric Neurons Results in Postnatal Intestinal Dysmotility and Dysbiosis. *FASEB J*. **2018**, *32*(9), 4744-4752.

18. Xin, Q.; Wightman, R. M. Enzyme Modified Amperometric Sensors for Choline and Acetylcholine with Tetrathiafulvalene Tetracyanoquinodimethane as the Electron-Transfer Mediatior. *Anal. Chim. Acta* **1997**, *341*(1), 43-51.

19. Aynacı, E.; Yasar, A.; Arslan, F. An Amperometric Biosensor for Acetylcholine Determination Prepared From Acetylcholinesterase-Choline Oxidase Immobilized in Polypyrrole-Polyvinylsulphonate Film. *Sens. Actuators B: Chem*. **2014**, *202*(31), 1028-1036.

20. Barbosa, O.; Ortiz, C.; Berenguer-Murcia, A.; Torres, R.; Rodrigues, R. C.; Fernandez-Lafuente, R. Glutaraldehyde in Bio-Catalysts Design: A Useful Crosslinker and a Versatile Tool in Enzyme Immobilization. *RSC Adv.* **2014**, *4*(4), 1583-1600.

21. Sassolas, A.; Blum, L. J.; Leca-Bouvier, B. D. Immobilization Strategies to Develop Enzymatic Biosensors. *Biotechnol. Adv.* **2012**, *30*, 489-511.

22. Nguyen, H. H.; Kim, M. An Overview of Techniques in Enzyme Immobilization. *Appl. Sci. Converg. Technol.* **2017**, *26*(6), 157-163.

23. Patel, B. A. Electrochemical Biosensors. In *Electrochemistry for Bioanalysis*; Patel, B., Eds.; Elsevier: Amsterdam, 2020, pp 267-284.

24. Mitchell, K. M. Acetylcholine and Choline Amperometric Enzyme Sensors Characterized in Vitro and in Vivo. *Anal. Chem.* **2004**, *76*(4), 1098-1106.

25. Bruno, J. P.; Gash, C.; Martin, B.; Zmarowski, A.; Pomerleau, F.; Burmeister, J.; Huettl, P.; Gerhardt, G. A. Second-By-Second Measurement of Acetylcholine Release in Prefrontal Cortex. *Eur. J. Neurosci*. **2006**, *24*, 2749-2757.

26. Burmeister, J. J.; Pomerleau, F.; Huettl, P.; Gash, C. R.; Werner, C. E.; Bruno, J. P.;

Gerhardt, G. A. Ceramic-Based Multisite Microelectrode Arrays for Simultaneous Measures of Choline and Acetylcholine in CNS. *Biosens. Bioelectron.* **2008**, *23*(9), 1382-1389.

27. Zhang, L.; Chen, J.; Wang, Y.; Yu, L.; Wang, J.; Peng, H.; Zhu, J. Improved Enzyme Immobilization for Enhanced Bioelectrocatalytic Activity of Choline Sensor and Acetylcholine Sensor. *Sens. Actuators B: Chem.* **2014**, *193*(31), 2014.

28. Hou, S.; Ou, Z.; Chen, Q.; Wu, B. Amperometric Acetylcholine Biosensor Based On Self-Assembly of Gold Nanopariticles and Acetylcholinesterase on the Sol-Gel/Multi-Walled Carbon Nanotubes/Choline Oxidase Composite-Modified Platinum Electrode. *Biosens. Bioelectron.* **2012**, *33*(1), 44-49.

29. Kucherenko, I. S.; Soldatkin, O. O.; Kucherenko, D. Y.; Soldatkina, O. V.; Dzyadevych, S. V. Advances in Nanomaterial Application in Enzyme-Based Electrochemical Biosensors: A Review. *Nanoscale Adv.* **2019**, *1*, 4560-4577.

30. Nunes, D.; Pimentel, A.; Gonçalves, A.; Pereira, S.; Branquinho, R.; Barbquinha, P.; Fortunato, E.; Martins, R. Metal Oxide Nanostructures for Sensor Applications. *Semicond. Sci. Technol.* **2019**, *34*(4), 043001.

31. Kim, C. S.; Oh, S. M. Enzyme Sensors Prepared by Electrodeposition on Platinized Platinum Electrodes. *Electrochim. Acta* **1996**, *41*(15), 2433-2439.

32. Reyes De Corcuera, J. I.; Cavalieri, R. P.; Powers, J. R. Improved Platinization Conditions Produce a 60-Fold Increase in Sensitivity of Amperometric Biosensors Using Glucose Oxidase Immobilized in Poly-*o*-phenylenediamine. *J. Electroanal. Chem.* **2005**, *575*(2), 229-241.

33. Li, Y.; Sella, C.; Lemaître, F.; Collignon, M. G.; Thouin, L.; Amatore, C. Highly Sensitive Platinum-Black Coated Platinum Electrodes for Electrochemical Detection of Hydrogen Peroxide and Nitrite in Microchannel. *Electroanalysis* **2013**, *25*(4), 895-902.

34. Killoran, S. J.; O'Neill, R. D. Characterization of Permselective Coatings Electrosynthesized on Pt–Ir From the Three Phenylenediamine Isomers for Biosensor Applications. *Electrochim. Acta* **2008**, *53*(24), 7303-7312.

35. Kucherenko, D. Y.; Siediuko, D. V.; Knyzhnykova, D. V.; Soldatkin, O. O.; Soldatkin, A. P. Development of Amperometric Biosensor for Choline Determination. *Biopolym. Cell* **2016**, *32*(3), 229-234.

36. Murphy, L. J. Reduction of Interference Response at a Hydrogen Peroxide Detecting Electrode Using Electropolymerized Films of Substituted Naphthalenes. *Anal. Chem.* **1998**, *70*(14), 2928-2935.

37. Dai, Y. Q.; Zhou, D. M.; Shiu, K. Permeability and Permselectivity of Polyphenylenediamine Films Synthesized at a Palladium Disk Electrode. *Electrochim. Acta* **2006**, *52*, 297-303.

38. Henderson, S.; Bhardwaj, K.; Perugachi, V.; Espinoza-Montero, P.; Galligan, J. J.; Swain, G. M. *In Vitro* Monitoring of Nitric Oxide Release in the Mouse Colon Using a Boron-Doped Diamond Microelectrode Modified with Platinum Nanoparticles and Nafion. *Anal. Chem.* **2023**, *95*(2), 1027-1037.

39. Raves, M. L.; Giles, G.; Schrag, J. D.; Schmid, M. F.; Phillips Jr., G. N.; Chiu, W.; Howard, A. J.; Silman, I.; Sussman, J. L. Quaternary Structure of Tetrameric Acetylcholinesterase. In *Structure and Function of Cholinesterases and Related Proteins*, eds.; Springer, 1998; pp 351-356.

40. Quaye, O.; Lountos, G. T.; Fan, A. M. O.; Gadda, G. Role of Glu312 in Binding and Positioning of the Substrate for the Hydride Transfer Reaction in Choline Oxidase. *Biochem.* **2008**, *47*(1), 243-256.

41. Kennedy, B.; Glidle, A.; Cunnane, V. J. A Study of the Oxidation and Polymerisation of Meta Substituted Phenol and Aniline Derivatives. *J. Electroanal. Chem.* **2007**, *608*, 22-30.

42. Zhou, H.; Chen, H.; Luo, S.; Chen, J.; Wei, W.; Kuang, Y. Preparation and Bioelectrochemical Responses of the Poly*(m*-Phenylenediamine) Glucose Oxidase Electrode. *Sens. Actuators B Chem.* **2004**, *101*(1-2), 224-230.

43. Johnston, D. A.; Cardosi, M. F.; Vaughan, D. H. The Electrochemsitry of Hydrogen Peroxide on Evaporated Gold/Palladium Composite Electrodes, Manufacture and Electrochemical Characterization. *Electroanalysis* **1995**, *7*(6), 520-526.

44. Hall, S. M.; Khudaish, E. A.; Hart, A. L. Electrochemical Oxidation of Hydrogen Peroxide at Platinum Electrodes. Part 1. An Adsorption-Controlled Mechanism. *Electrochim. Acta* **1998**, *43*(5-6), 579-588.

45. Stevens, C. F.; Wesseling, J. F. Activity-Dependent Modulation of the Rate at which Synaptic Vesicles Become Available to Undergo Exocytosis. *Neuron* **1998**, *21*(2), 415-424.

46. Harrington, A. M.; Hutson, J. M.; Southwell, B. R. Cholinergic Neurotransmission and Muscarinic Receptors in the Enteric Nervous System. *Prog. Histochem. Cytochem.* **2010**, *44*(4), 173-202.

47. Uutela, P.; Reinilä, R.; Piepponen, P.; Ketola, R. A.; Kostiainen, R. Analysis of Acetylcholine and Choline in Microdialysis Samples by Liquid Chromatography/Tandem Mass Spectrometry. *Rapid Commun. Mass Spectrom.* **2005**, *19*(20), 2950-2956.

48. Nirogi, R.; Mudigonda, K.; Kandikere, V.; Ponnamaneni, R. Quantification of Acetylcholine, an Essential Neurotransmitter, in Brain Microdialysis Samples by Liquid Chromatography Mass Spectrometry. *Biomed. Chromatogr.* **2010**, *24*, 39-48.

49. Asri, R.; O'Neill, J. C.; Patel, K. A.; Siletti, K. A.; Rice, M. E. Detecion of Evoked Acetylcholine Release in Mouse Brain Slices. *Analyst* **2016**, *141*(23), 6415.

50. Scimemi, A.; Beato, M. Determining the Neurotransmitter Concentration Profile at Active

Synapses. *Mol. Neurobiol.* **2009**, *40*(3), 289-306.

51. Köppen, A.; Klein, J.; Schmidt, B. H.; Ver Der Staay, F.-J.; Löffelholz, K. Effects of Nicotinamide on Central Cholinergic Transmission and on Spatial Learning in Rats. *Pharmacol. Biochem. Behav.* **1996**, *53*(4), 783-790.

CHAPTER 6. EXAMINATION OF ENTERIC NEUROPATHY IN ALZHEIMER'S DISEASE AND AMYLOIDOSIS IN THE GUT

6.1 Introduction

Alzheimer's disease (AD) is a progressive neurodegenerative disease classically characterized by the presence of amyloid-β (Aβ) plaques and neurofibrillary tangles. AD is associated with memory loss, short attention span, inability to learn new things, and a progressive decline in cognition.[1] AD is considered the most common cause of dementia in the elderly. However, individuals suffering with AD also exhibit peripheral nervous system symptoms of which gut dysbiosis and constipation stand out.[2-4] Several hypotheses have proposed mechanisms to explain the gut-brain connection in AD with a focus on gut microbiome composition, disturbances in gut permeability, and systemic inflammation.[2,5-7] The gut-brain connection has been linked to several neurodegenerative diseases in central nervous system (CNS).[8] For example, the contribution of gut-brain connection in Parkinson's disease has been well documented, where α-synuclein neuronal aggregation is associated with GI dysmotility and dopaminergic neuronal degeneration in brain.[9-11] Unlike Parkinson's disease, studies of GI dysmotility in AD are limited.

It is well established that the activity of amyloid precursor protein (APP) and Aβ accumulation are highly associated with AD pathology in the CNS causing cholinergic neurodegeneration of the basal forebrain.[12] APP, from which Aβ is derived, is also expressed in the enteric nervous system (ENS).[13] The presence of Aβ accumulation in the gut and stool has been reported in patients with neuropathologically confirmed AD.[14-18] The ENS controls GI motility, secretion, and blood flow through coordinated interactions between networks of interneurons, motorneurons, and sensory neurons that populate the GI tract from the esophagus to the anus.[19] Disruption in neurotransmission, particularly in the ENS could contribute to GI dysfunction in AD. In some animal models of AD, Aβ accumulation in the ENS causes increased inflammation,

GI dysmotility, and loss of enteric neurons,[15,20-23] including nitrergic and cholinergic neurons,[24] prior to the development of severe cognitive deficits. However, the fundamental effects of disruptions in enteric neuromuscular transmission, specifically in myenteric neurons in AD associated GI dysmotility, is still unknown.

There are over 200 transgenic animal models that have been developed to mimic the progressive pathology of familial AD (https://www.alzforum.org/research-models/alzheimers-disease). The 5xFAD mouse is a widely used Aβ pathogenic model whereby Aβ accumulation in the brain occurs as early as 2 months of age. In addition, neuronal loss in the CNS occurs at 3 months, and cognitive impairment is observed at 5 months of age.[25,26] Literature has reported that 5xFAD mice also present minor GI dysmotility,[22,27] changes in enteric neuronal structure,[27] altered colonic gene expressions and calcium homeostasis, increased enteric neuronal viability,[22] and GI dysbiosis.[28] Another model commonly utilized in AD research is the APP/PS1 double transgenic mouse model. These mice start to develop Aβ plaques by 6 months of age which increase up to 12 months of age[29,30] Neuronal loss adjacent to these plaques occurs between 8 to 10 months[31] Memory impairments start as early as 6 months of age while spatial learning becomes impaired by 12 months[32,33] These mice have also shown overexpression of Aβ and phosphorylated Tau protein in myenteric neurons, intestinal dysfunction, inflammation, and increased intestinal permeability[24,34-36]

Currently, there are no studies *directly* supporting that Aβ accumulation occurs in enteric ganglia in the myenteric plexus of AD mice and if Aβ accumulation disrupts myenteric neuromuscular transmission causing GI dysmotility. Because myenteric neurons control GI motility, we determined the expression of Aβ in the brain and colonic myenteric plexus from male and female 5xFAD and wild-type (WT) mice by using immunostaining and an ELISA assay at

26 weeks of age. We also assessed colonic transit in vivo; propulsive motility and GI smooth muscle contractions *ex vivo,* electrochemical detection of colonic nitric oxide (NO) release; and changes in myenteric neuromuscular transmission using smooth muscle intracellular electrophysiological recordings. In later work, we performed similar studies using male and female APP/PS1 mice. Although cholinergic neurodegeneration of the basal forebrain is a major contributor in AD brain pathology,[12] we studied both cholinergic and nitrergic neuromuscular transmission since the loss of both enteric cholinergic and nitrergic neurons has been also reported in animal models of AD.[24] We report on preliminary immunostaining for Aβ and the electrochemical detection of colonic NO using a modified boron-doped diamond (BDD) microelectrode and ACh/Ch using an enzyme-based biosensor to determine if nitrergic or cholinergic neuromuscular signaling is altered in APP/PS1 mice.

Part A: 5XFAD MICE DO NOT HAVE MYENTERIC AMYLOIDOSIS, DYSREGULATION OF NEUROMUSCULAR TRANSMISSION OR GASTROINTESTINAL DYSMOTILITY

6.2A Results

In the beginning of this study (~9 weeks old), all male 5xFAD mice had a lower body weight when compared with aged-matched WT mice, but this difference was not observed in female 5xFAD vs WT mice (Figure 6.1A). The lower body weight persisted in male 5xFAD mice (Figure 1A) until 25 weeks of age. The lower body weight in male 5xFAD mice was not associated with lower food intake, since male 5xFAD mice had similar food intake compared with WT mice (Figure 6.1B). All 5xFAD mice did not show significant decline in body weight and food intake until 25 weeks of age.

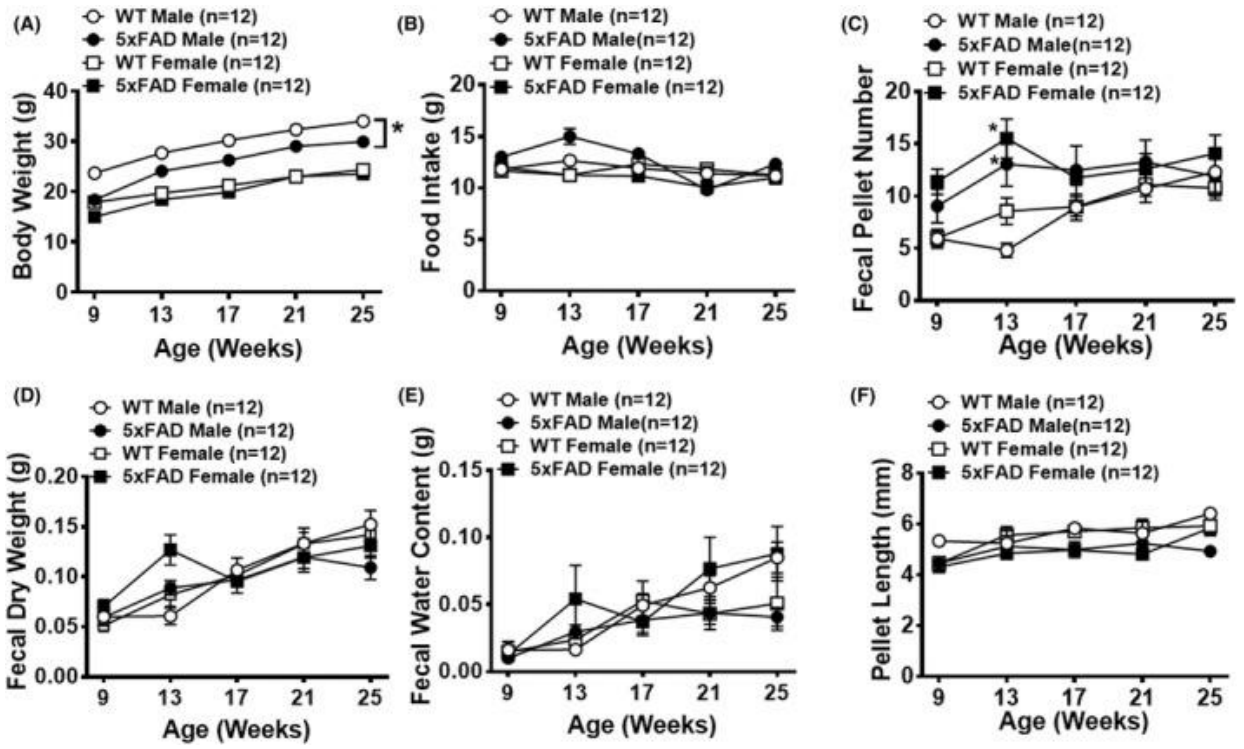

Figure 6.1. Measurements of body weight (A), food intake (B), fecal pellet number (C), fecal dry weight (D), fecal water content (E), and pellet length (F) in WT and 5xFAD male and female mice from Weeks 9–25. Data are presented as mean ± SE, *$p < 0.05$. 5xFAD male mice showed lower body weight than WT mice persistently. All 5xFAD mice show increased pellet number than WT mice in Week 13 only. Data are presented as mean ± SE, *$p < 0.05$, 5xFAD vs WT.

Fecal pellet number, dry weight, fecal water content, and pellet length in all mice are shown in Figure 6.1C–F. In both male and female 5xFAD mice, we observed a very transient increase in fecal pellet number compared with WT mice at the early stages of age progression (Figure 6.1C). Overall, compared with the WT mice, all 5xFAD mice did not show significant changes in fecal pellet dry weight (Figure 6.1D), water content (Figure 6.1E), and pellet length (Figure 6.F) during the age progression study.

Myogenic contractions in the duodenum, ileum, proximal and distal colon were induced by using the muscarinic cholinergic agonist, bethanechol (0.1–30 μmol L^{-1}, Figure 6.2). Overall, there were no significant changes in concentration-dependent post-junctional cholinergic muscular reactivity in 5xFAD mice across the four regions of the GI tract (Figure 6.2A–D). Only female

5xFAD mice showed an increased colonic reactivity at very high concentration of bethanechol compared with WT mice (Figure 6.2D).

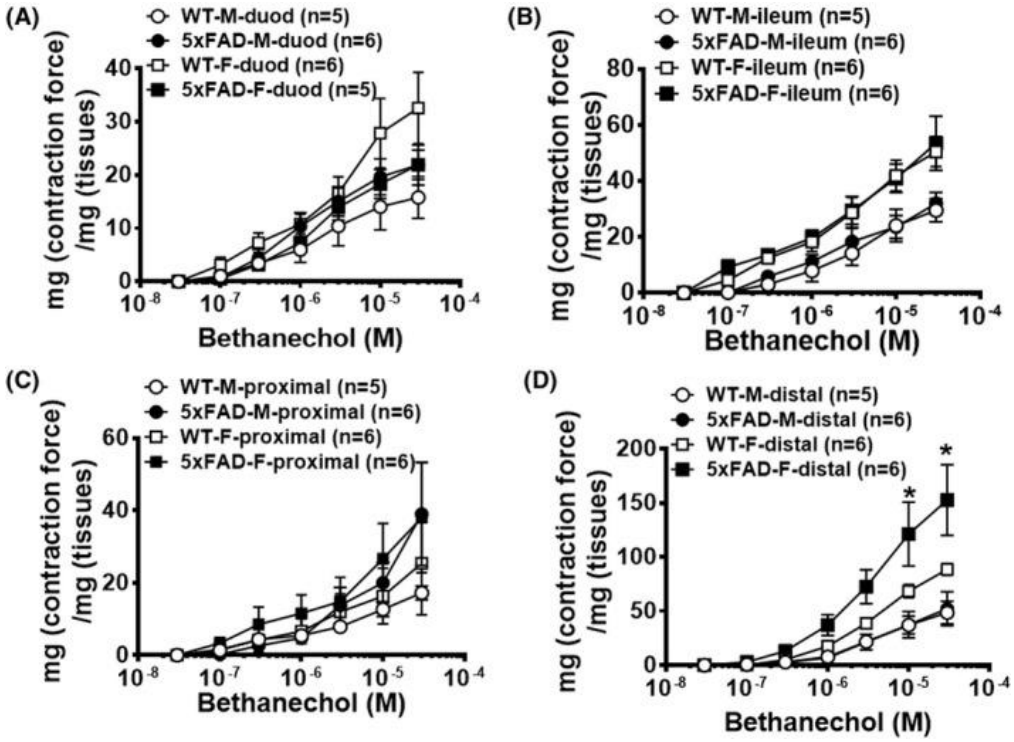

Figure 6.2. Concentration response curves for bethanechol in small intestinal and colonic longitudinal smooth muscle from WT and 5xFAD male and female mice. Bethanechol induced contractions in the (A) duodenum, (B) ileum, (C) proximal colon, and (D) distal colon. Bethanechol-induced contraction force was converted to mg (force)/mg (tissue weight). Data are mean ± SE; * $p < 0.05$, 5xFAD vs WT.

Next, we measured muscle contractions induced by electrical stimulation at frequencies of 0.5, 1, 3, 5, and 10 Hz (Figure 6.3). There were no significant differences in frequency response curves in the four regions of the GI tract between WT and 5xFAD mice (Figure 6.3). TTX ($0.3\ \mu mol\ L^{-1}$) was used to block neurogenic neuromuscular transmission via nerve stimulation. After TTX treatment, frequency response curves for nerve stimulation were significantly reduced in all tissues and there were no significant differences between WT and 5xFAD male or female mice. Overall, there were no changes in excitatory neuromuscular transmission in 5xFAD mice.

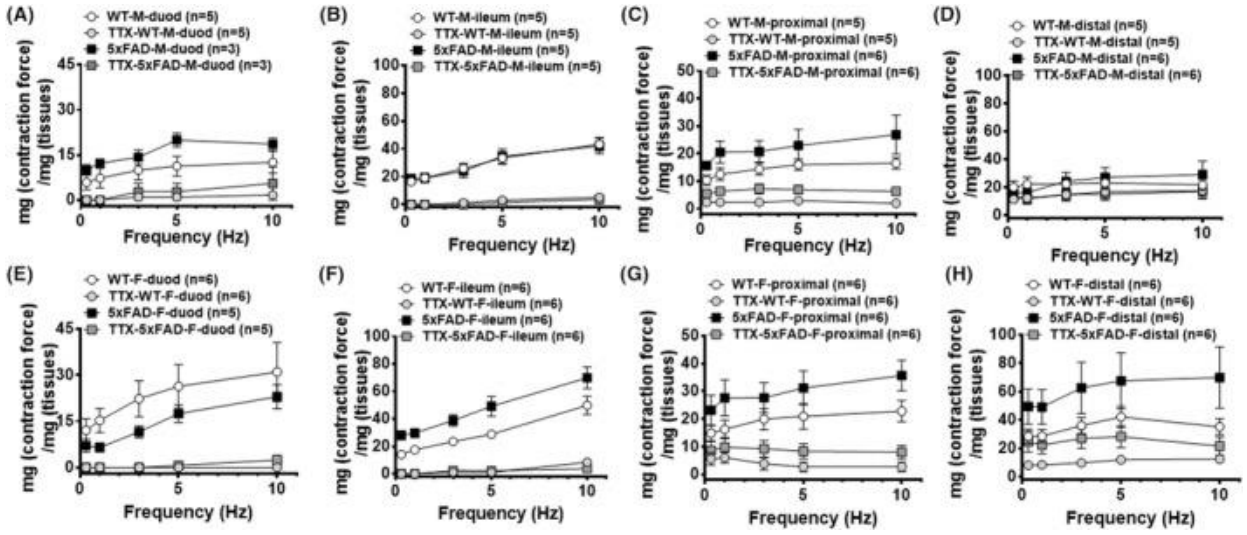

Figure 6.3. Frequency responses curves for electrical nerve stimulation in small intestinal and colonic longitudinal smooth muscle from WT and 5xFAD male and female mice, before and after application of TTX (0.3 μmol L^{-1}). Longitudinal smooth muscle contractions were recorded after electrical stimulation in male mice using the (A) duodenum, (B) ileum, (C) proximal colon, and (D) distal colon; and in female mice using the (E) duodenum, (F) ileum, (G) proximal colon, and (H) distal colon. Contraction force was converted to mg (force)/mg (tissue weight). Data are presented as mean ± SE.

Colonic propulsion was evaluated by measurement of the CMMC (Figure 6.4). Compared with male WT mice, male 5xFAD mice showed an increase in total number of CMMCs with shorter durations in between each CMMC (Figure 6.4A,B) but without changes in propagation speed (Figure 6.4C). However, female mice had similar measurements and there were no significant changes in colonic propulsion in female 5xFAD and WT mice (Figure 6.4A–C).

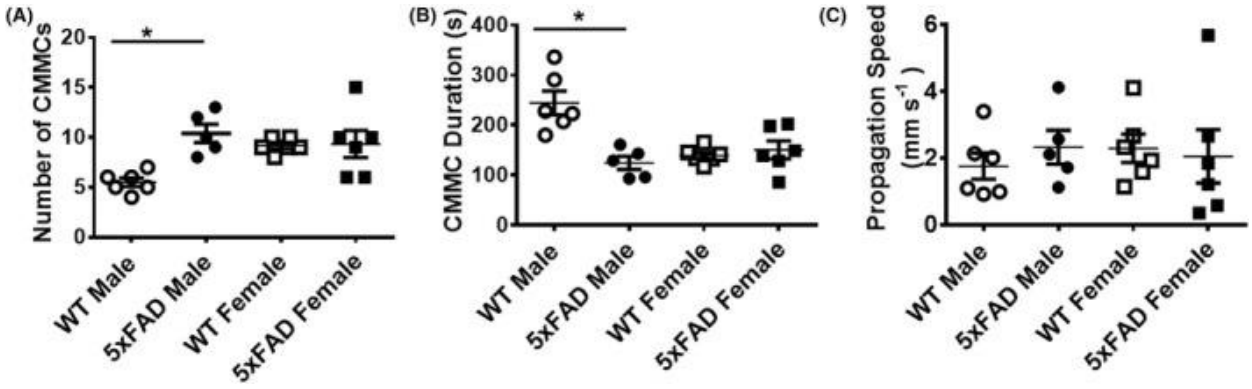

Figure 6.4. Colonic migrating motor complexes (CMMCs) recorded from the colon of WT and 5xFAD male and female mice. (A), Total number of CMMCs; (B), CMMC duration; and (C),

Figure 6.4. (cont'd)

CMMC propagation speed were measured. 5xFAD male mice showed increases in number of CMMC and decreased CMMC duration than WT mice, but there were no significant changes in propagation speed. Data are presented as mean ± SE, *$p < 0.05$, 5xFAD vs WT.

Using 5xFAD mice, we also explored whether there was dysfunction at the colonic neuromuscular junction. IJPs were recorded from colonic circular smooth muscle cells (Figure 6.5). IJPs consist of a fast purinergic hyperpolarization of membrane potential followed by a slower nitrergic hyperpolarization before the membrane potential returns to baseline (~-45 mV) (Figure 6.5A). Using train durations of 100–300 ms, we did not observe significant differences in IJP amplitude in 5xFAD mice vs. WT mice (Figure 6.5B–D). When the purinergic component of the IJP was blocked by MRS2179 (10 μmol L^{-1}, a P2Y1 receptor inhibitor), IJP amplitudes were significantly reduced in all mice, the nitrergic component of the IJP (leftover of IJP from purinergic blockade) was also similar in 5xFAD and WT mice (Figure 6.5B–D). Overall, there were no significant changes in colonic inhibitory neurotransmission in all 5xFAD mice.

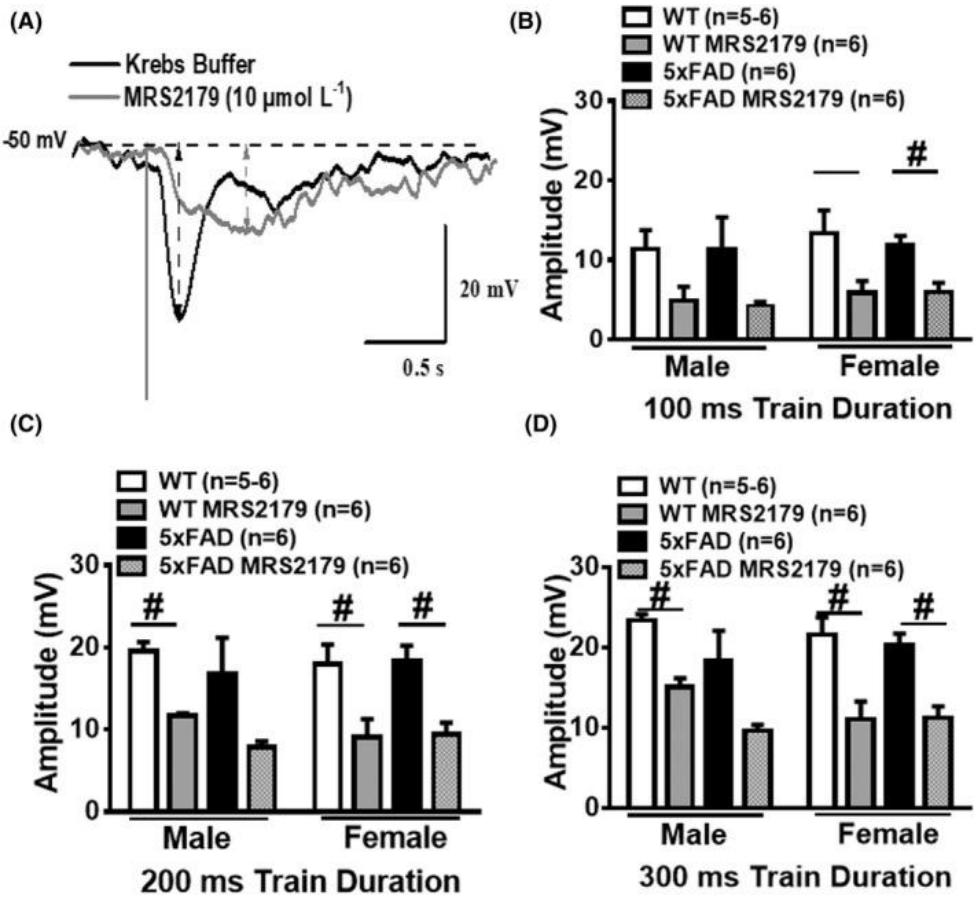

Figure 6.5. Inhibitory junction potentials (IJP) in the colon from WT and 5xFAD male and female mice. (A), Representative IJP recording from colonic circular smooth muscle of a WT mouse with or without MRS2179, a P2Y1 antagonist at 300 ms stimulation duration. Black arrow indicates the IJP amplitude measurement with Krebs buffer, gray arrow indicates the IJP measurement after MRS2179 application. (B)–(D), measurements of IJP at 100 ms, 200 ms, and 300 ms stimulation duration. 5xFAD male and female mice do not show significant differences in IJP amplitude (mV) at 100 ms, 200 ms, and 300 ms duration compared with WT mice. MRS2179 significantly decreased IJP amplitude but no significant differences were seen between WT and 5xFAD mice. Data are presented as mean ± SE, #$p < 0.05$, control vs MRS2179.

Inhibitory neurotransmission plays a key role in control of colonic motility, and loss of nitrergic myenteric neurons in AβPP/PS1 AD mice has been reported previously. [24] We determined colonic myenteric nitrergic neuronal function directly by measuring electrically stimulated NO release from myenteric ganglia using amperometry. NO oxidation current response curves were similar in 5xFAD vs WT in male and female mice, although all female mice had a smaller peak current than male mice (Figure 6.6A–C). A post-hoc test following two-way ANOVA revealed that

these sex differences were only statistically significant for the 5xFAD mice at 3 pulses. In addition, peak oxidation currents were nearly completely inhibited by L-NNA (NOS inhibitor) and TTX in all mice, demonstrating that the responses were neurogenic NO release from myenteric ganglia (Figure 6.7A–E). Overall, we did not observe significant changes in colonic nitrergic inhibitory neurotransmission in 5xFAD mice compared with WT mice.

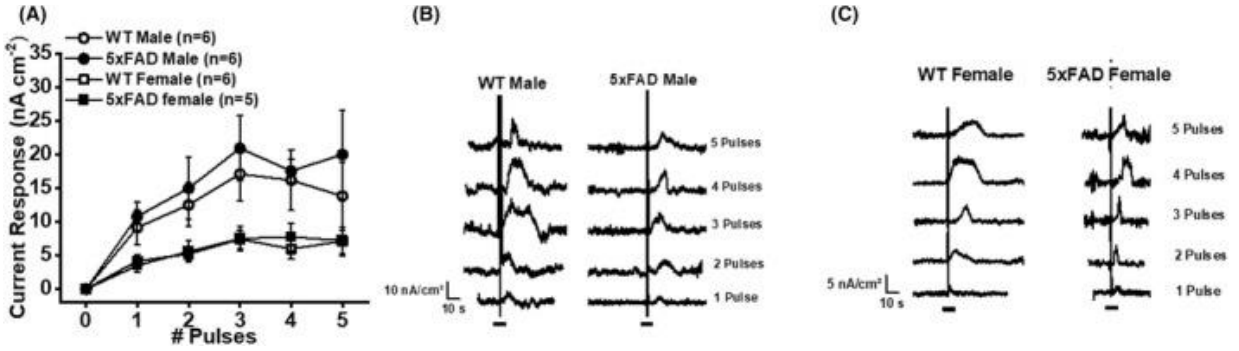

Figure 6.6. Detection of NO release from colonic myenteric ganglia in WT and 5xFAD male and female mice using continuous amperometry. NO release was directly measured using transmural electrical stimulation and continuous amperometry. A frequency-response curve was generated by plotting the peak current response normalized to the electrode's electrochemically active area against the number of electrical stimuli delivered. (A) Peak NO current responses curves from male and female mice. (B) and (C), Representative current-time recordings from male and female mice. Increasing the number of stimuli caused increased current until a peak response is observed at 3 pulses. This response then plateaus and decreases slightly with increasing number of stimuli. The black bar indicates the onset of stimulation and the corresponding stimulation artifact. Data are presented as mean ± SE.

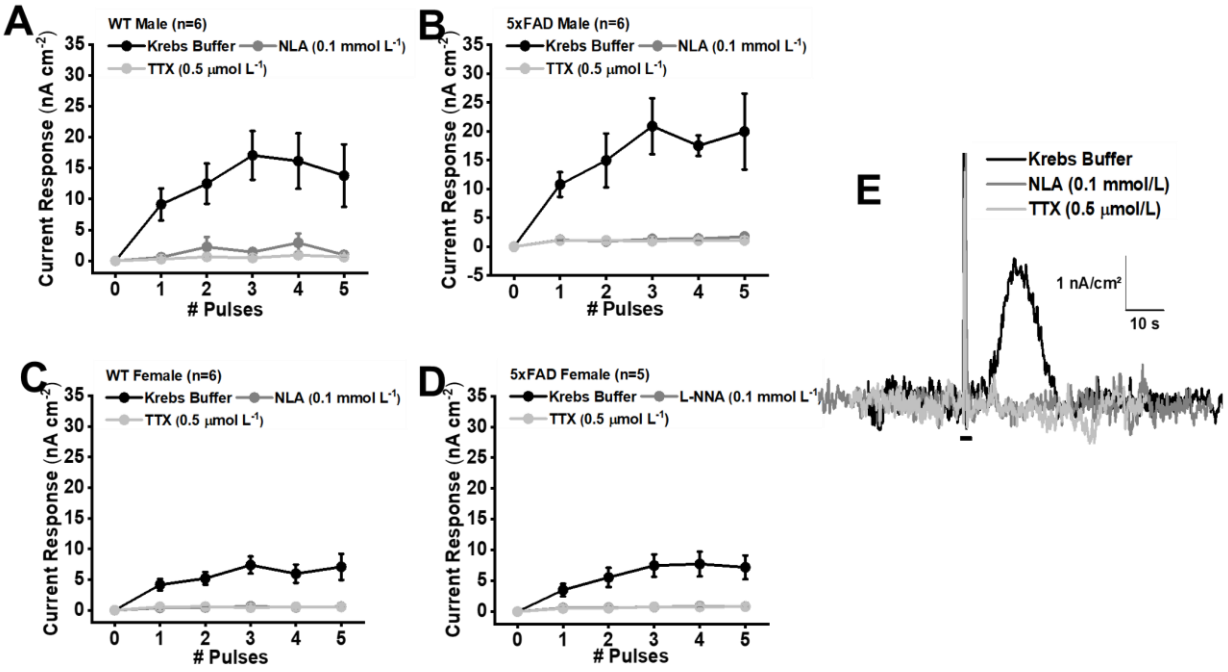

Figure 6.7. Confirmation of myenteric neurogenic NO release in WT and 5xFAD male and female mice. NO release was measured from colonic segment from a A) WT male; B) 5xFAD male, C) WT female, and D) 5xFAD female mice using continuous amperometry before and after TTX and LNA treatment. In the presence of TTX, the current is inhibited by ~92%, confirming that the measured response is neural. Similarly, NLA treatment reduced the current response by ~90% verifying the nitrergic neuronal responses. E), A sample i-t curve showing the recording from WT female mouse. Following 3 pulses of electrical stimulation (see black bar), a spike in current is observed correlating with the release of NO on the rise of the curve followed by clearance from the extracellular space with the descending phase. The current was almost completely diminished after TTX and NLA applications. Data are presented as mean ± SE.

We used two anti-Aβ antibodies with different epitopes in our study, from ThermoFisher and Cell Signaling. The ThermoFisher antibody (71–5800) is a 30 amino acid synthetic polyclonal peptide derived from the full length (1–43 amino acid) Aβ peptide (https://www.thermofisher.com/antibody/product/beta-Amyloid-Antibody-Polyclonal/71-5800). All 5xFAD mice at 6 months of age showed strong Aβ immunoclusters in whole brain slices, without visible immunoclusters in the brain of WT mice (Figure 6.8). However, we did not detect any visible positive Aβ immune staining in the colonic myenteric plexus (CMP) in whole mount tissue preparations (Figure 6.8, whole), or in colonic coronal and transverse sections from all 5xFAD mice (Figure 6.8, section). The Cell Signaling antibody detects several isoforms of Aβ (Aβ-

37, −38, −39, −40, and − 42) (https://www.cellsignal.com/products/primary-antibodies/b-amyloid-d54d2-xp-rabbit-mab/8243). With the Cell Signaling antibody, our data were similar to the ThermoFisher antibody results, where the antibody detected very strong Aβ-immunoclusters in the brain from all 5xFAD mice. However, we could not detect any visible positive Aβ immune staining in the myenteric plexus from these mice too (data not shown). More specifically, the expression of insoluble $A\beta_{42}$ (by ELISA assay) in the brains from 5xFAD mice was significantly increased when compared with brains from WT mice, $A\beta_{42}$ expression was undetectable in brains from WT mice and the ileum and clone tissues from all 5xFAD mice (Figure 6.9).

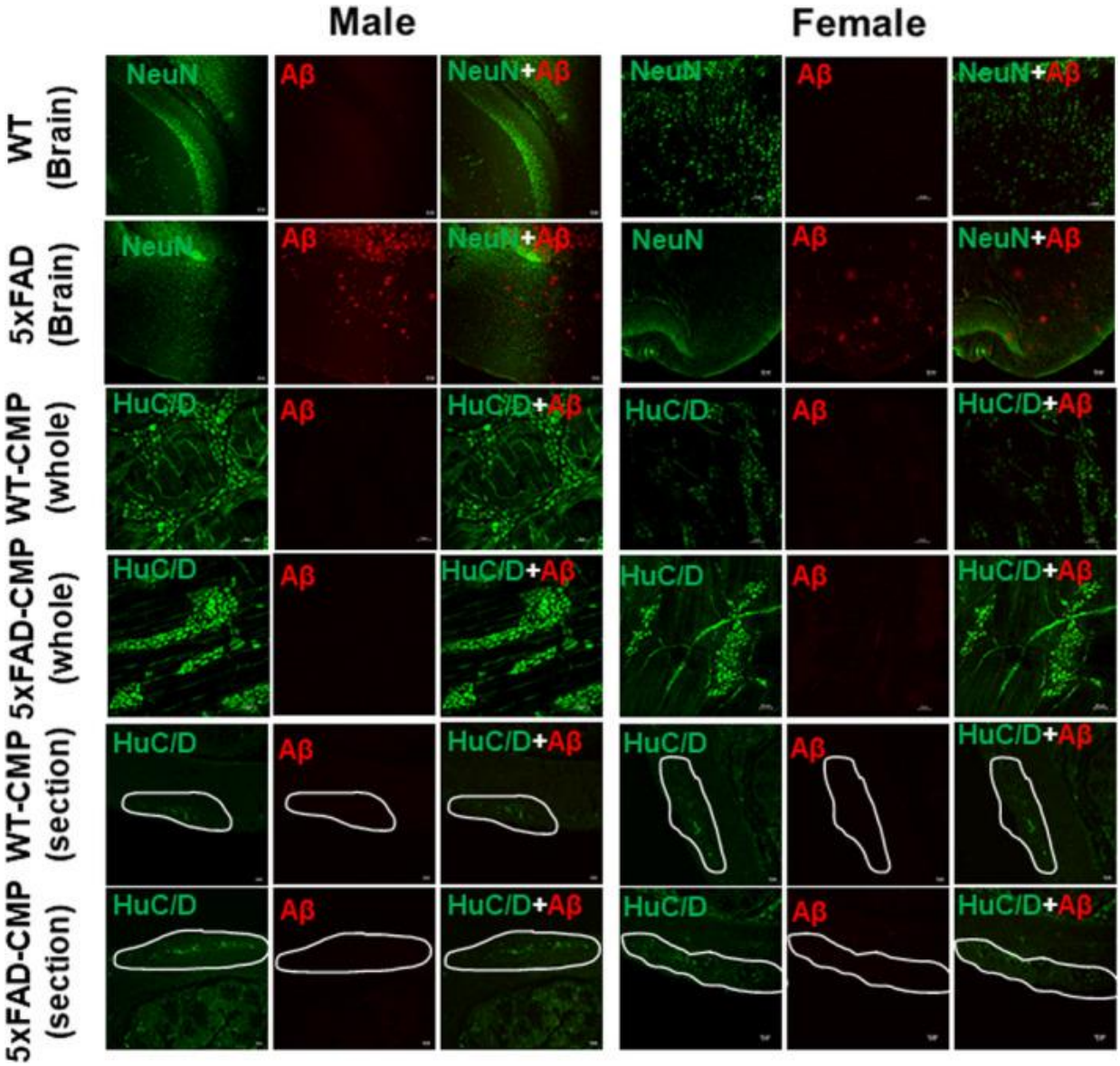

Figure 6.8. Detection of Aβ expression in parasagittal cortex sections and colonic myenteric ganglia in WT and 5xFAD male and female mice. Row one and two, representative images from brain sections; row three to six, representative images from colonic circular myenteric plexus (CMP); row three and four, representative images from whole tissue preparations (whole); row five and six, colonic cross sections (section). Circle markers indicate the colonic myenteric ganglia area between circular and longitudinal smooth muscle layers. NeuN (green), a neuronal nuclear protein marker antibody, indicates the neurons in brain slices; HuC/D (green), a neuronal nuclear protein marker antibody, indicates ENS neurons in GI; Aβ (red), anti-Aβ antibody from ThermoFisher, indicates the expression of Aβ in brain and myenteric ganglia. Confocal images were acquired at 10x and 20x. n = 6 in each group of mice.

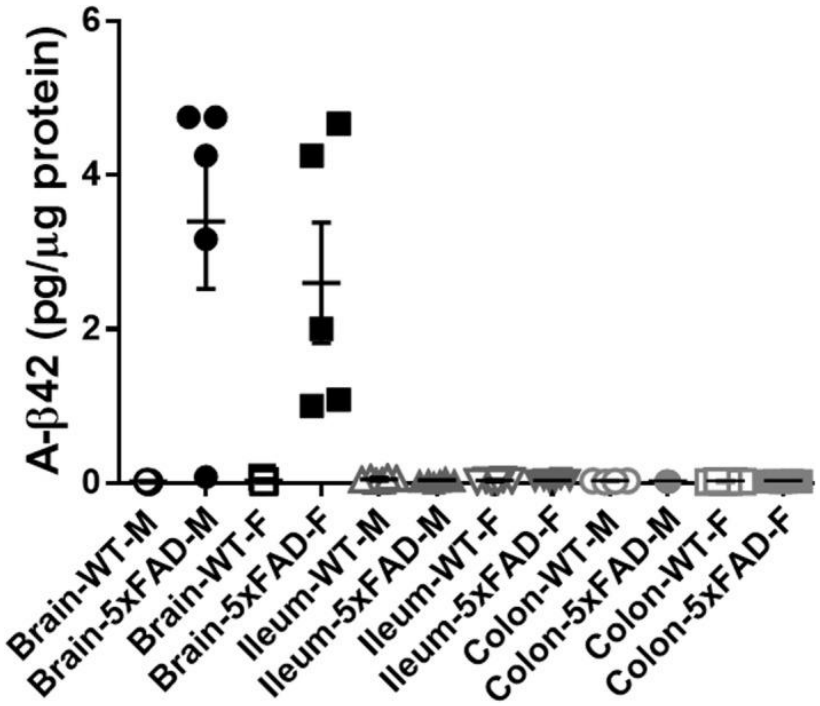

Figure 6.9. Aβ-42 expression in tissues from WT and 5xFAD male and female mice. ELISA assay was used to determine expression of Aβ42 from the brain, ileum, and colon tissues from these mice. Expression of Aβ42 in the ileum and colon from all 5xFAD mice was undetectable (n = 4–6 in each group).

6.3A Discussion

Patients with neuropathologically confirmed AD also exhibit peripheral nervous system symptoms such as gut dysbiosis and constipation.[2-4] In AD patients, Aβ accumulation in the gut wall and stool have been reported,[14-18] which strongly supports the contribution of amyloidosis in GI dysmotility of AD patients. Some mouse models of AD also revealed amyloidosis in the GI wall and moderation of GI dysmotility, alterations of microbiome composition, disturbances in gut permeability, changes GI structure and systemic inflammation.[15,20-23,27] However, Aβ accumulation associated with enteric neuronal dysfunction, specifically myenteric neurons in GI dysmotility, has not been studied mechanistically, even though Aβ accumulation was directly detected by positive immune staining in the myenteric ganglia in AD mouse models of AβPP/PS1 (APPswe, PSNE1dE9)[15] and TgCRND8.[23] These two studies directly showed that amyloidosis

occurred in the myenteric ganglia. Our goal was to identify a novel mechanism for myenteric neuronal dysfunction in GI dysmotility of AD. We used an APP overexpression mouse model that produces robust levels of Aβ and $A\beta_{42}$ leading to synaptic dysfunction and neuronal cell death in the brain causing cognitive deficits. The 5xFAD mouse model is one of the most popular models used in AD studies. These mice show rapidly accumulating and robust intraneuronal $A\beta_{42}$ levels as early as 1.5 months of age.[25] $A\beta_{42}$ favors formation of insoluble fibrils in AD and has a strong genetic link to early-onset familial AD. However, reported GI dysmotility in 5xFAD mice was very limited, [22,27] 5xFAD mice had *only* either a shorter colonic propulsion in ex-vivo[22] or a shorter transition time in vivo at age of 21 and 40 weeks[27] in previous reports. These authors did not provide any other studies supporting if 5xFAD mice showed the signs of constipation (a shorter colonic propulsion with less fecal pellet output), or the diarrhea (a shorter transition time with more fecal pellet output) et al, these experiments may be more physiologically relevant in measurement of mouse GI function. Although we did not perform similar experiments as reported by these authors, we have included multiple in vivo and ex vivo studies, which are more comprehensive in assessing GI function. Overall GI function should not be assessed using only one experiment in animal models.

In addition, amyloidosis associated GI dysfunction in 5xFAD mice cannot be concluded without the support of amyloidosis in ENS. In previous studies in 5xFAD mice, [22,27] the authors did not provide any direct evidence showing the occurrence of amyloidosis in GI from 5xFAD mice. More importantly, the authors have analyzed the expression of the most common AD-linked genes in different regions of the GI tract, but overall they did not find significant changes in these gene expressions in 5xFAD mice compared with WT mice, even until at 40 weeks of age.[27] In their studies, even the expression of APP and PSEN1/2 genes in entire GI tract were very comparable

between 5xFAD vs WT mice,[27] these data against that overexpressions of APP/PSEN gene have been employed in GI from 5xFAD mice, but the data are strongly supporting our observations that 5xFAD mice do not have amyloidosis in colonic ENS, since 5xFAD mice should be with the overexpression of three APP and two PSEN1 genes.

It has been also reported that there were changes in enteric neuronal structure/function and altered cellular viability in enteric neurons in 5xFAD mice.[22,27] However, these authors determined the neuronal variability, structure/function and other biomarkes in cultured enteric neurons, not the primary enteric neurons. They also used recombinant human Aβ to induce neuronal amyloidosis. Therefore, the results from these studies are incomparable with our studies. Although 5xFAD mice were also used to study GI dysbiosis,[28] however, there was no *direct* evidence supporting the amyloidosis in myenteric ganglia in these mice too.

In our studies, at the age of 6 months, 5xFAD mice have developed some cognitive impairments in behavioral tests (we did not include the data in this submission). In clinical relevance, the appearance of GI symptoms is much earlier than the symptoms of cognitive impairment in AD patients.[14-18] We expected that the development of enteric amyloidosis will be earlier than in brain. Gene expressional studies[27] also did not support that extending the time point will increase the chance of Aβ expression in GI tract, because of lacking the changes of AD-linked gene expression in GI tract from 5xFAD mice even at age of 40 weeks.

Taken together, we believe that the amyloidosis associated myenteric neuronal dysfunction in GI dysmotility has not been reported in 5xFAD AD model. When we attempted to recapture amyloidosis in the colonic myenteric ganglia, we did not find visible Aβ immunostaining in colonic myenteric ganglia in 5xFAD mice at 26 weeks of age. Aβ immunoclusters were visualized in brain slices from all 5xFAD mice, indicating that the experimental timeline is sufficient to develop

amyloidosis in these mice. To confirm our observations, we used two anti-Aβ antibodies with different ectopic sequences from different companies. The results were very similar in both antibodies, 5xFAD mice did not show any visible Aβ accumulation in myenteric ganglia. In addition, Aβ42, an insoluble Aβ isoform, was also undetectable in the ileum and colon but was detected in brain tissues from 5xFAD mice using an ELISA assay. This study did not support amyloidosis in the GI wall in 5xFAD mice as well, as has been reported in other studies.[20,22] Likewise, we did not observe significant GI dysmotility or colonic myenteric neuronal dysfunction in 5xFAD mice too. GI motility was broadly evaluated through GI transit in vivo (fecal pellet output), GI neuromuscular contractility ex vivo, and also the contribution of colonic myenteric neuromuscular transmission. None of these studies support the presence of myenteric dysfunction associated GI dysmotility in 5xFAD mice. Although 5xFAD male mice showed an increase in total number of CMMCs with shorter durations in between each CMMC, but without changes in propagation speed. These mice did not have any significant GI dysmotility in vivo, as we did not detect any signs of decline in body weight and food intake, constipation, or diarrhea from these mice. In addition, we did not detect the presence of nitrergic neurodegeneration in colonic myenteric ganglia.

APP, a precursor to Aβ, is expressed in the ENS.[14-17] Therefore, we anticipated an accelerated drive toward intraneuronal $A\beta_{42}$ generation throughout the ENS. However, amyloidosis was absent in myenteric ganglia in 5xFAD mice. Amyloidosis in myenteric ganglia was detected directly in other AD animal models such as the AβPP/PS1 (APPswe, PSNE1dE9)[15] and TgCRND8[23] models. We cannot completely explain why the amyloidosis is absent in the ENS of 5xFAD mice, but the model facilitates studies of amyloidosis phenotypes in CNS. Recently, we used similar anti-Aβ antibodies and identified amyloidosis in colonic myenteric ganglia from

AβPP/PS1 (APPswe, PSNE1dE9) mice, which indicates that amyloidosis in the ENS depends on the animal model of AD, and amyloidosis in the ENS is technically detectable, and the antibodies used in the current study are efficient to detect amyloidosis in GI too. 5xFAD mice overexpress five human mutated genes and use the Thy1 transgene cassette as a promoter,[25] but AβPP/PS1 and TgCRND8 models overexpress only two or three human mutated genes and use the prion transgene cassette as a promoter.[37-39] It is well known that the prion promotor is more efficient for gene transfer, and gives the highest level of transgene expression in contrast to other promotors.[40] In addition, neurons in the ENS and CNS are derived from different embryonic precursors (i.e., neural crest vs neural tube),[41] and these neurons do not share similar molecular signaling pathways in neuronal development.[42] Therefore, the absence of amyloidosis phenotype in the ENS is not surprising. These data also indicate that the 5xFAD mouse model may not be suitable for studies of amyloidosis-associated myenteric neuronal dysfunction and GI dysmotility in AD. Other animal models, such as the AβPP/PS1 mouse, may be appropriate for this study. We have to be aware that all AD animal models are developed to mimic the amyloidosis and tau pathology in CNS. Currently, there is no reliable AD animal model to specifically show the amyloidosis and tau pathology in ENS.

Finally, we emphasize that we only determined the amyloidosis phenotypes in colonic myenteric ganglia in these 5xFAD mice. We did not examine amyloidosis in other GI areas. Therefore, we cannot exclude amyloidosis-associated alterations of the microbiome, mucosal permeability, gene expression, and inflammatory markers in the GI tract of these mice, as these alterations have been reported by other investigators.[22,27,28]

6.4A Conclusions

In conclusion, although 5xFAD mouse model is reliable for studies of the role of

amyloidosis in CNS pathology, 5xFAD mice may be inadequate to study amyloidosis in the ENS and GI dysmotility in AD. This model lacks amyloidosis in myenteric ganglia and associated GI dysmotility. Further work using animal models with promoters that target enteric specific neurons are needed to elucidate the gut-brain connection in AD.

Reprinted (adapted) with permission from:

Yelleswarapu, N. K.; Masino, M.; Henderson, S.; Fernandes, R.; Swain, G.; Galligan, J. J.; Xu, H. 5xFAD Mice Do Not Have Myenteric Amyloidosis, Dysregulation of Neuromuscular Transmission or Gastrointestinal Dysmotility. *Neurogastroenterol. Motil.* **2022**, *34*, e14439.

PART B: EXAMINATION OF NITERGIC AND CHOLINERGIC SIGNALING IN APP/PS1 MOUSE MODEL USING ELECTROCHEMICAL DETECTION

6.2B Results

As we previously determined that the 5xFAD mouse model for AD did not show myenteric dysfunction or associated GI dysmotility likely because amyloidosis was absent in the ENS, we wanted to verify that the new APP/PS1 transgenic mouse model selected showed myenteric amyloidosis before further testing. Early immunostaining of a single female hemizygote (Hz) mouse and a single female noncarrier (NC) control can be seen in Figure 6.10. Staining for Aβ accumulation was performed in the brain, colon, and small intestine of these mice. One can see numerous Aβ immunoclusters in the brain, small intestine, and colon of the Hz mice while immunoactivity for Aβ is completely absent in the NC control. This suggests that this model should be suitable for studies of the effects of myenteric amyloidosis on GI function and motor activity.

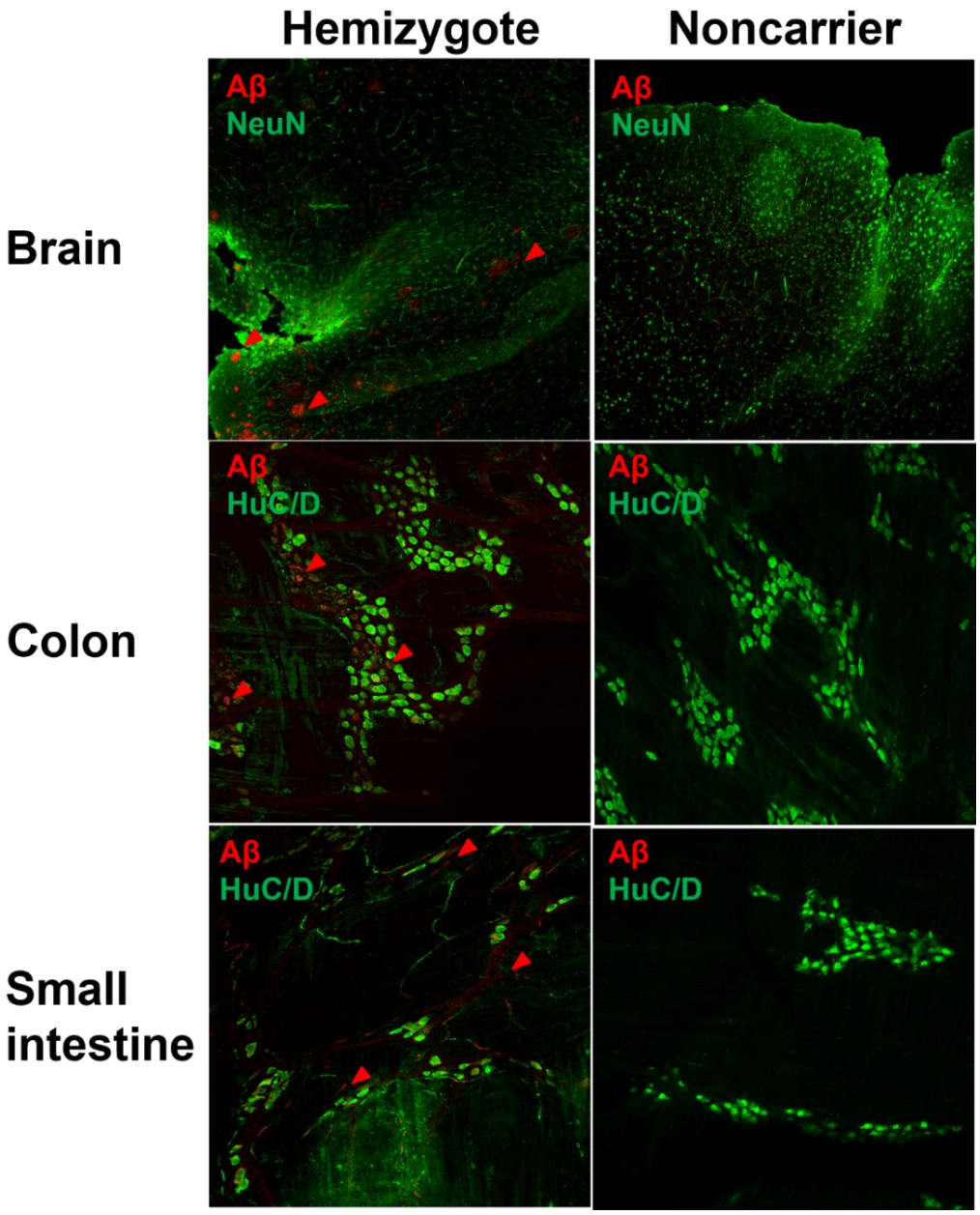

Figure 6.10. Detection of Aβ (red) expression in the parasagittal cortex in the brain and myenteric ganglia in the colon and small intestine from a single noncarrier (NC) female mouse and single hemizygote (Hz) female mouse. Immunostaining performed by Marlene Massino from the Neuroscience Program at MSU. Red arrows indicate areas of Aβ expression. NeuN (green) acts as a neuronal nuclear protein marker antibody, visualizing the neurons in brain slices while HuC/D (green) acts as a neuronal nuclear protein marker antibody, visualizing enteric neurons in intestine. Confocal images were acquired at 10x (brain) and 20x (small intestine and colon).

NO is a gaseous neuromuscular signaling molecule released from inhibitory motor neurons in the myenteric plexus to help mediate smooth muscle relaxation during peristalsis.[43,44] NO plays

a critical role in regulating GI motility. Nitrergic enteric neurons are particularly vulnerable to neuropathy in GI diseases,[45] making altered NO release a common cause of intestinal dysfunction. We examined colonic myenteric nitrergic function by directly measuring NO release from mouse myenteric ganglia using electrical stimulation and continuous amperometry. Sample amperometric *i-t* curves (Figure 6.11) can be seen as well as a summary of the oxidation current responses and their integrated peak areas (Figure 6.12). The peak oxidation current increases with increasing number of electrical stimuli delivered until it reaches a maximum response at 3 pulses. After this point the current response levels off. The integrated peak area follows a similar pattern, only the peak oxidation current response is reached at 4 pulses. There is no significant change between the Hz mice and the NC controls for both the male and female mice, however there are significant sex differences for both the NC and Hz mice. A significant decrease in peak current response was found for the female Hz mice compared to the male Hz mice at 3, 4, and 5 pulses. Likewise, there is a significant decrease in peak area for these mice at 4 pulses. A significant decrease for the female NC mice compared to the male NC mice was also observed at 4 and 5 pulses. Using previously conducted calibrations, the peak current responses correlate to a peak NO concentration of 239 ± 46 nmol L^{-1} for the male NC mice, 381 ± 136 nmol L^{-1} for the male Hz mice, 95 ± 20 nmol L^{-1} for the female NC mice, and 83 ± 11 nmol L^{-1} for the female Hz mice.

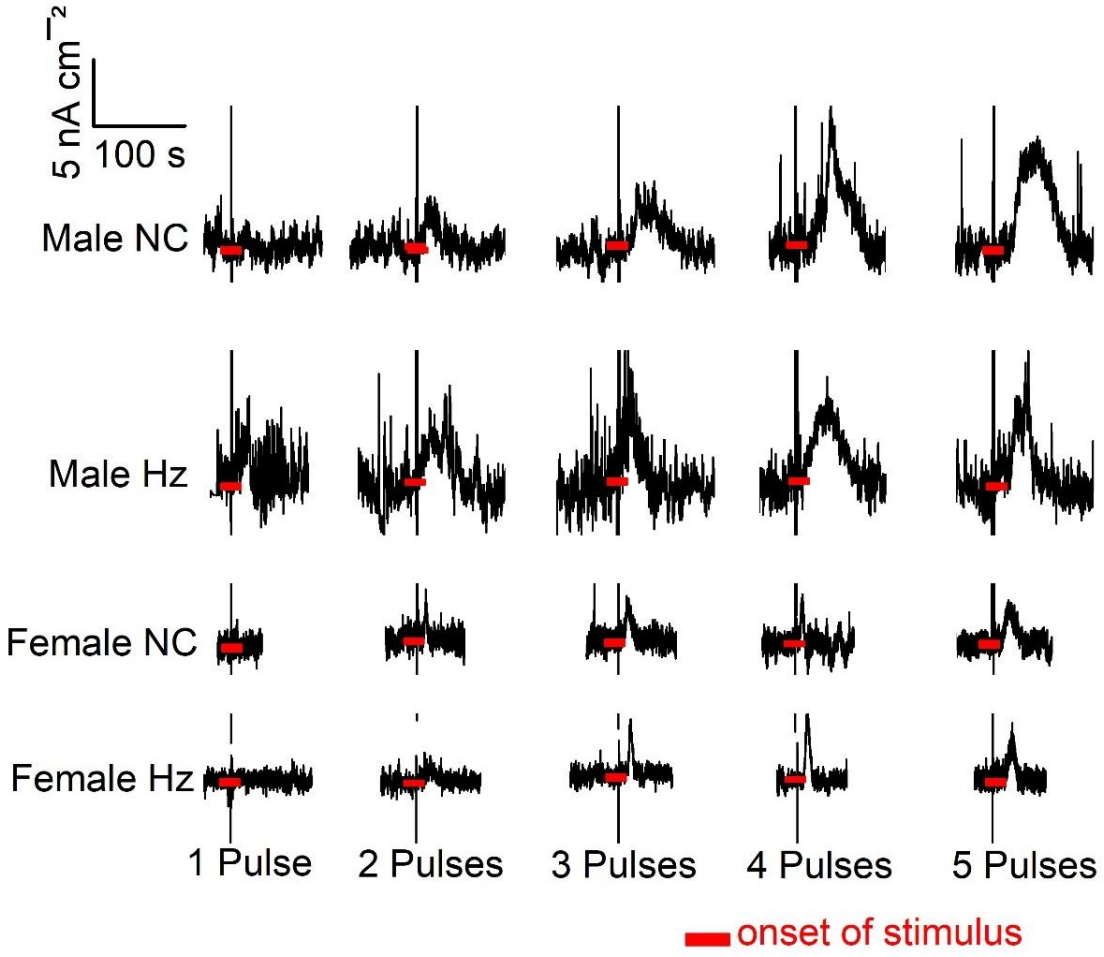

Figure 6.11. Representative amperometric *i-t* traces showing NO release from colonic myenteric ganglia. The detection potential used was 0.8 V vs Ag/AgCl. Sample current responses (normalized to the microelectrode's electrochemically active surface area) are shown for a single male NC mouse, single male Hz mouse, single female NC mouse, and single female Hz mouse as a function of the number of electrical stimuli delivered. The red bar indicates the onset of the electrical stimulus and the corresponding stimulation artifact can be seen. The responses between the Hz and NC mice are nearly identical for both the male and female mice, however there is a significant reduction in current response between the male and female mice. The peak current response and integrated area under the curve were used to generate pulse number-response curves. Data was smoothed using a 10 Hz low pass filter.

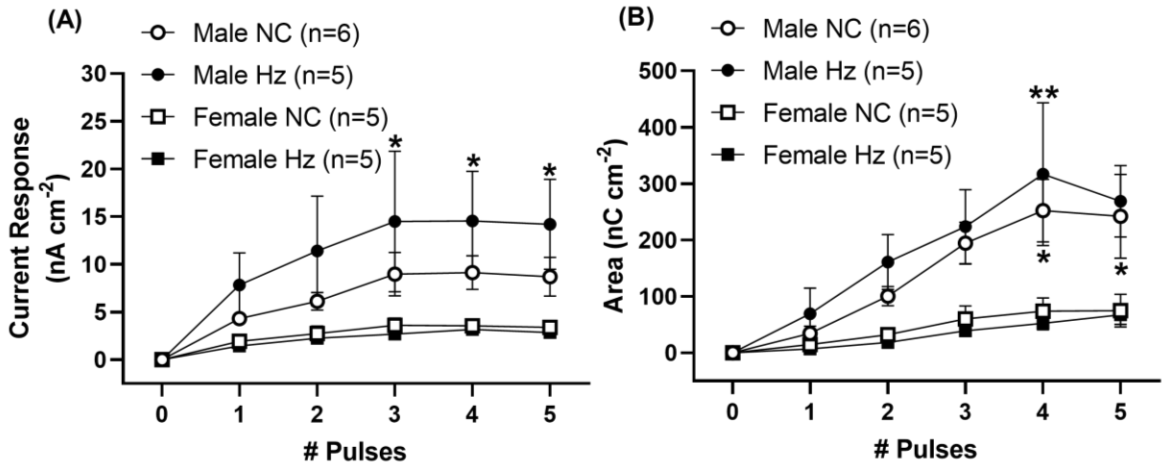

Figure 6.12. Detection of electrically stimulated NO from APP/PS1 mice. The mean ± SEM peak current response (A) and integrated area (B) are plotted in respect to the number of electrical stimuli delivered to the tissue. The responses are normalized to the microelectrode's electrochemically active surface area. The peak current response increases with increasing pulse number up to 3 pulses and plateaus after this point. The area of the current responses responds similarly, except a maximum is reached at about 4 pulses. There are no significant differences in peak current response or area between the Hz and NC mice for both the male and female mice. However, there is a significant decrease in peak current response for the female Hz mice compared to the male Hz mice at 3, 4, and 5 pulses. Likewise, there is a significant decrease in peak area for these mice at 4 pulses. A significant decrease for the female NC compared to the male NC mice was also observed at 4 and 5 pulses. Data was analyzed using two-way ANOVA followed by Bonferroni's post-hoc test. *$p<0.05$, **$p<0.01$.

To verify the source of oxidation current measured was due to NO release from myenteric nitrergic neurons, two pharmacological agents were used. Tetrodotoxin (TTX) is a sodium-channel blocker which prevents action potential propagation while L-Nitro-N-Arginine (L-NNA) is a nitric oxide synthase (NOS) inhibitor which competes for arginine binding sites of NOS, the rate limiting enzyme in on demand NO synthesis. Sample amperometric *i-t* traces showing the respective pharmacological sequence (Figure 6.13) can be seen as well as a summary of the drug effect responses for all mice (Figure 6.14). The current response was almost completely abolished in the presence of TTX and L-NNA, verifying that the measured current response was due to neurogenic NO release from nitrergic myenteric neurons. Statistically significant changes in current response were found before and after drug treatment with exception of the female Hz between the rinse and

L-NNA treatment, however the difference between the initial Krebs buffer stimulation and L-NNA was statistically significant ($p<0.05$).

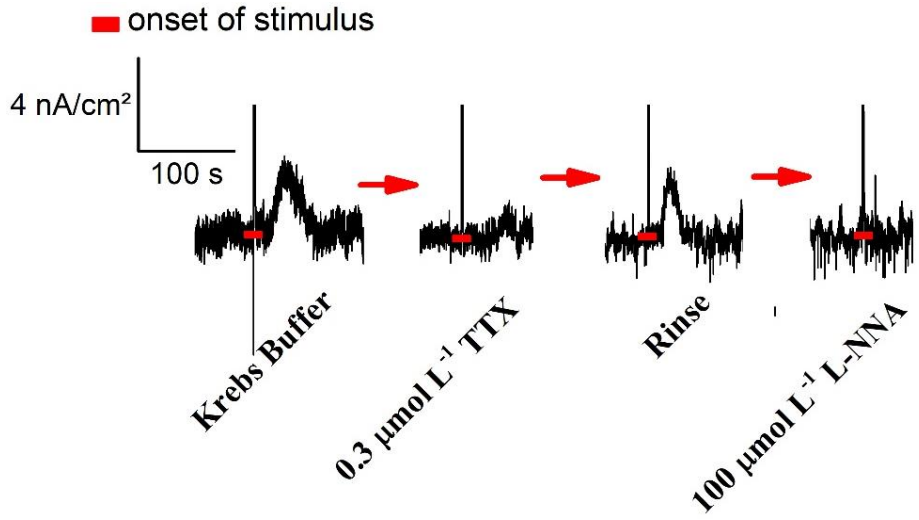

Figure 6.13. Representative amperometric *i-t* traces from a single mouse showing the drug sequence treatment used for NO measurements: the tissue was electrically stimulated using 1-5 pulses (80 V, 10 Hz, 0.5 ms pulse duration); perfused with 0.3 µmol L^{-1} TTX for 10 mins before repeating stimulations; rinsed with Krebs buffer pH 7.4 for 15 mins before repeating a single stimulation to verify restoration of oxidation current; and perfused with 100 µmol L^{-1} L-NNA for 10 mins before repeating stimulations. Data was smoothed using a 10 Hz low pass filter.

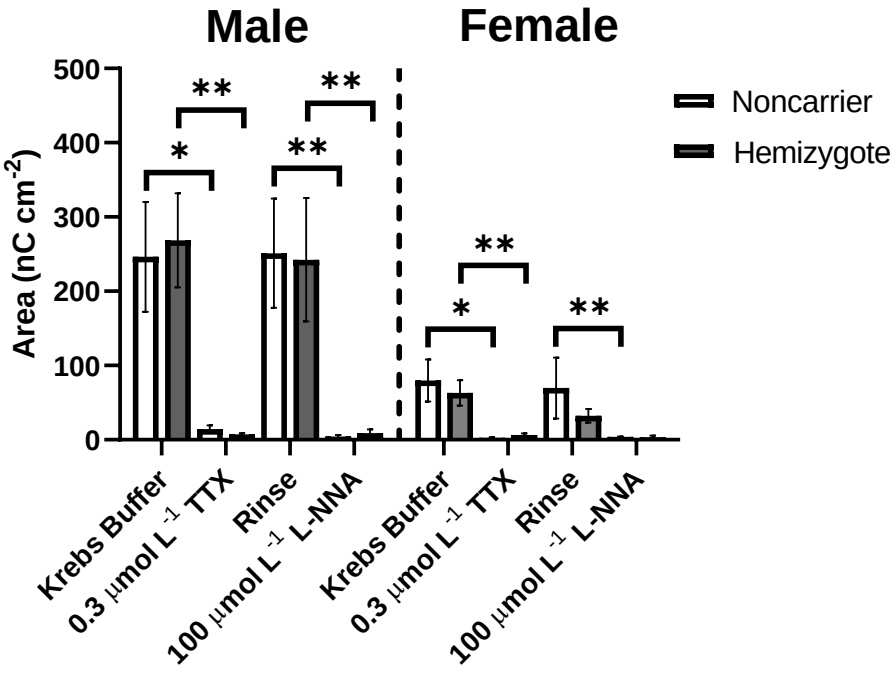

Figure 6.14. Summary of the drug effect responses for n=6 male NC mice, n=5 male Hz mice, n=5 female NC mice, and n=5 female Hz mice using the integrated area of the current response to 5

Figure 6.14. (cont'd)

pulses of electrical stimulation. Means between groups were compared using unpaired student's t-tests. The current response was almost completely abolished with the application of sodium channel blocker TTX and NOS inhibitor L-NNA, with the current response being nearly fully restored between drug application. This suggests that the measured oxidation current was due to neurogenic NO release from myenteric ganglia. *$p<0.05$, **$p<0.01$.

Cholinergic dysfunction has been well documented in the central nervous system, but whether that dysfunction extends to the ENS is less well known. We looked at myenteric cholinergic function by directly measuring ACh/Ch release from mouse myenteric ganglia using electrical stimulation and continuous amperometry. To account for sensor-to-sensor variability, individual electrodes were calibrated in the flow batch using 0.1, 0.5, 1, 5, and 10 μmol L^{-1} ACh. The corresponding response curves were used to normalize oxidation current responses to a ACh/Ch concentration. The biosensor responds with identical response times and sensitivity to both ACh and Ch. As synaptically released ACh is rapidly hydrolyzed in the presence of AChE in the extracellular space to Ch, the biosensor measures a combination of ACh and Ch as an indicator of cholinergic function rather than ACh itself. Sample amperometric *i-t* curves (Figure 6.15) normalized to the each biosensor's calibration to display extracellular ACh/Ch concentrations can be seen as well as a summary of these responses and their integrated peak areas (Figure 6.16). The peak ACh/Ch concentration increases from 10 to 30 pulses with no real change from 30 to 50 pulses. A similar pattern is observed with the integrated peak area. In general, there is not a significant increase in peak concentration or area with increasing number of electrical stimuli with the exception of the peak ACh/Ch concentration from 10 to 40 and 50 pulses for the male NC mice and from 10 to 50 pulses for the female Hz mice. As a current response was unable to be observed below 10 electrical stimuli pulses (where the differences likely would be significant), it is assumed that those concentrations are below that of the LOD of the sensor (0.3 ± 0.2 μmol L^{-1}). Responses among all mice are very similar with no significant differences between the Hz mice and the NC controls

nor the male and female mice. The peak ACh/Ch concentration recorded was 600 ± 47 nmol L^{-1} for the male NC mice, 485 ± 76 nmol L^{-1} for the male Hz mice, 626 ± 197 nmol L^{-1} for the female NC mice, and 607 ± 116 nmol L^{-1} for the female Hz mice.

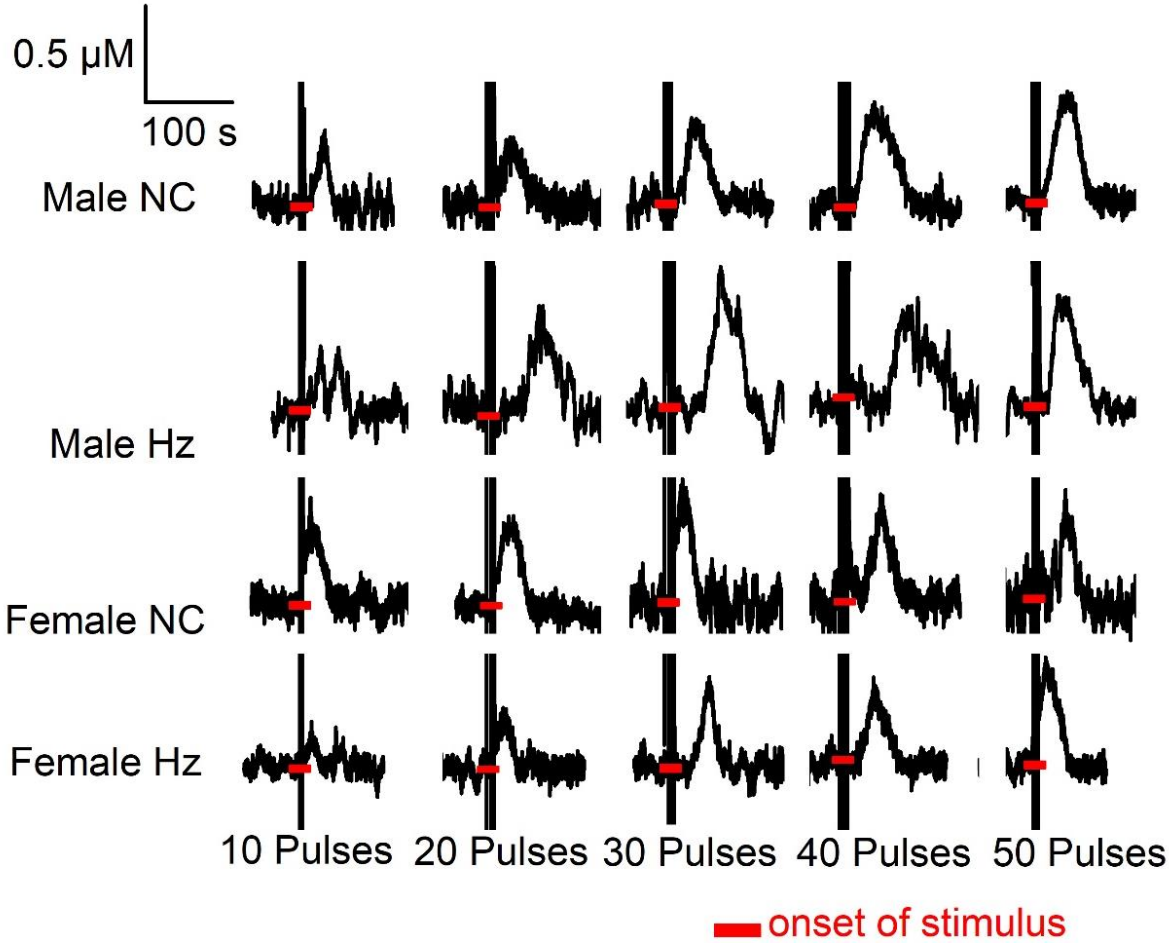

Figure 6.15. Representative *i-t* traces showing ACh/Ch release from colonic myenteric ganglia. Representative amperometric responses were generated by normalizing the ACh/Ch biosensor's current response to their respective calibrated sensitivities. The detection potential used was 0.75 V vs Ag/AgCl. Responses are shown for a single male NC mouse, single Hz mouse, single female NC mouse, and single female Hz mouse as a function of the number of electrical stimuli delivered. The red bar indicates the onset of the electrical stimulus and the corresponding stimulation artifact can be seen. The responses between the Hz and NC mice are nearly identical and there does not appear to be any sex differences. The peak ACh/Ch concentration and integrated area under the curve were used to generate pulse number-response curves. Data was smoothed using a 10 Hz low pass filter.

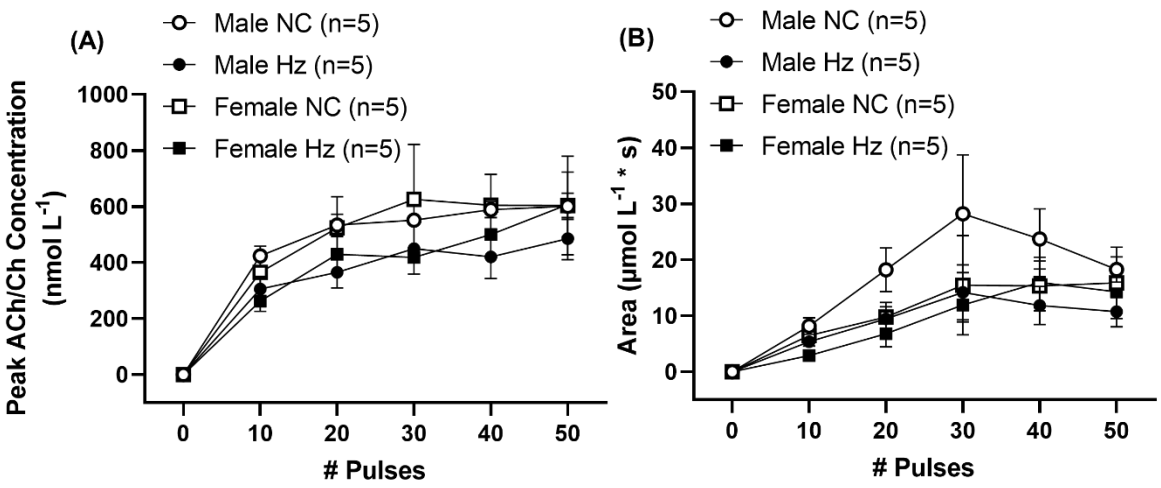

Figure 6.16. Detection of electrically stimulated ACh/Ch from APP/PS1 mice. The mean ± SEM peak concentration (A) and integrated area (B) are plotted in respect to the number of electrical stimuli delivered to the tissue. Both the peak concentration and integrated area increases with increasing pulse number from 10 to 30 pulses and plateaus after this point. There are no significant differences in peak current response or area between the Hz and NC mice nor between the male and female mice. Data was analyzed using two-way ANOVA.

To verify the source of oxidation current measured was due to ACh/Ch release from myenteric cholinergic neurons, two pharmacological agents were used. Tetrodotoxin (TTX) acts as a sodium-channel blocker to prevent action potential propagation while neostigmine acts as an AChE inhibitor to prevent the breakdown of ACh, consequently increasing the amount of time that ACh can reside in the extracellular space. This should hypothetically increase the integrated of our measured current response. Sample amperometric *i-t* traces showing the respective pharmacological sequence (Figure 6.17) can be seen as well as a summary of the drug effect responses for all mice (Figure 6.18). The current response was almost completely abolished in the presence of TTX with statistically significant decreases in current response for all mice, verifying that source of measured current was neuronal. The current response was almost completely restored after rinsing the TTX out, however only a minor increase (and not statistically significant) was observed with the neostigmine. This suggests that the bulk of the measured current response was from the turnover of ACh to Ch rather than ACh itself.

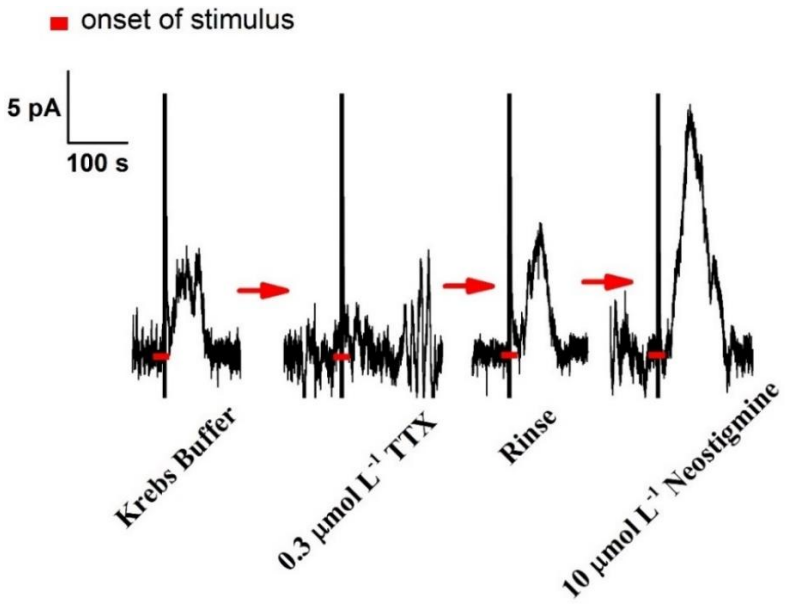

Figure 6.17. Representative amperometric *i-t* traces from a single mouse showing the drug sequence treatment used for ACh/Ch measurements. The tissue was electrically stimulated using 10-50 pulses (80 V, 10 Hz, 0.5 ms pulse duration); perfused with 0.3 µmol L^{-1} TTX for 10 mins before repeating stimulations; rinsed with Krebs buffer pH 7.4 for 15 mins before repeating a single stimulation to verify restoration of oxidation current; and perfused with 10 µmol L^{-1} neostigmine for 10 mins before repeating stimulations. Data was smoothed using a 10 Hz low pass filter.

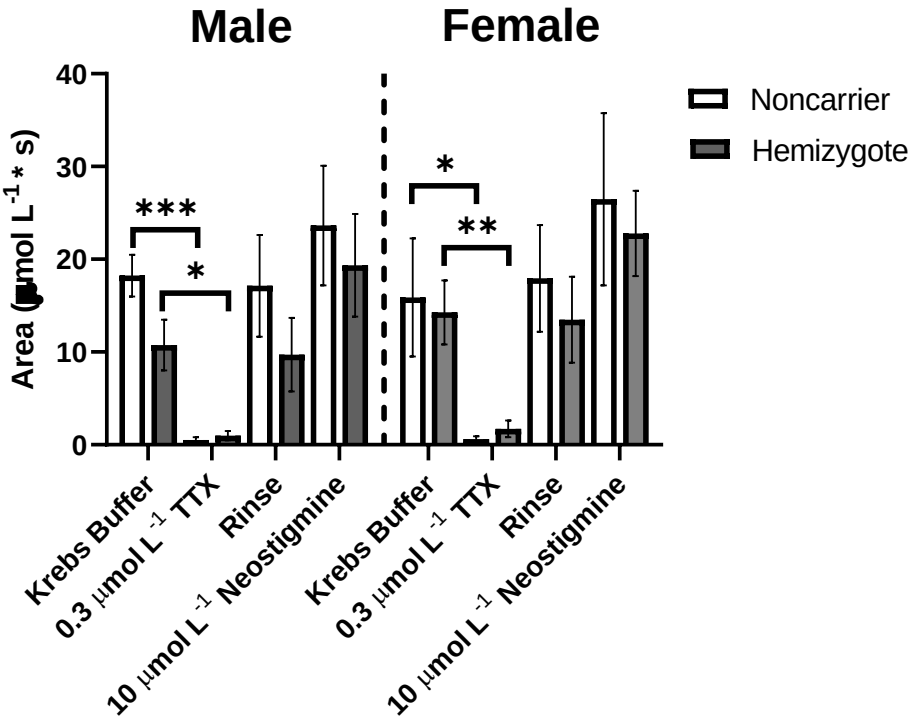

Figure 6.18. Summary of the drug effect responses for male NC mice, male Hz mice, female NC mice, and female Hz mice (n=5 for each group) using the integrated area of the normalized current

Figure 6.18. (cont'd)

response to 50 pulses of electrical stimulation. Means between groups were compared using unpaired student's t-tests. The current response was almost completely abolished with the application of sodium channel blocker TTX and the current response was restored between drug application. This suggests that the measured oxidation current was neural in source. The response increased slightly, but not significantly with application of the AChE inhibitor. This suggests that the bulk of measured current response is from Ch, which is formed through the rapid hydrolysis of synaptically released ACh, rather than ACh itself. *p<0.05, **p<0.01, ***p<0.001.

6.3B Discussion

Although some researchers found decreased expression of cholinergic and nitrergic neurons in APP/PS1 mice, others using the same model found no change in the proportion of cholinergic and nitrergic neurons.[34] We did not detect any significant differences between NO or ACh/Ch release between the Hz and NC controls. As amyloidosis has been well represented in this model in the brain, colon, and small intestine, we can conclude that neuromuscular signaling mediated by NO and ACh/Ch release in the colon is not impaired in the APP/PS1 mouse model of AD.

We did observe a significant decrease in NO release for the female mice compared to the male mice for both the NC and Hz mice. These results are interesting, as our results from electrophysiology data using 5xFAD mice does not suggest a change in inhibitory neuromuscular signaling among the sexes. These changes included a significant reduction in both the peak concentration of NO as well as the amount of NO being released. As sex-differences were not observed for the ACh/Ch measurements, these changes are likely due to a cause other than a simple difference in size or thickness in muscle layer between the sexes. In general, sex-differences in GI function are not uncommon. For example, there is increased prevalence of chronic constipation, gastroparesis, and irritable bowel syndrome in women compared to men.[46-48] These sex differences may be partly due to changes in serotonin signaling. Our group has previously found that female mice show increased extracellular 5-HT, increased 5-HIAA levels, and increased number of EC cells and whole tissue 5-HT in the small intestine.[49] These differences may also be due to altered

nitrergic signaling or changes in expression of NOS.

It has been established that estrogen affects nNOS regulation and colonic motility.[46,50] Decreased estradiol-17β levels can impair nitrergic mediated relaxation by reducing (6R)-tetrahydrobiopterin availability, which facilitates NOS dimerization during catalysis.[51] However, this contradicts our findings. Oxidative stress occurs when there is an imbalance in reactive oxygen species (ROS) and antioxidants to counteract these free radicals, the superoxide anion being the most abundant. Females generally have lower levels of oxidative stress compared to males,[52] however estrous cycles start to decline between 10 and 12 months in C57BL6 mice.[53] Estrogen has a neuroprotective effect on toxicity induced by oxidative stress.[54,55] Increases in ROS in aging is common, however female mice show a significantly greater increase in ROS with age compared to male mice.[56] NO can rapidly react with the superoxide anion to form peroxynitrite, a potent oxidant capable of overwhelming oxidative injury.[57] Because these studies were performed with older mice, it is possible that the decrease in NO is due to the rapid formation of peroxynitrite as a consequence of increased oxidative stress, quenching the NO response. This is only speculation, however, and further testing is needed to elucidate the cause of this sex difference.

6.4B Conclusions

Although we were able to detect Aβ accumulation in the APP/PS1 mouse model, proving it to be a more suitable model for studying ENS dysfunction in AD than the 5xFAD mouse model, we did not detect any significant differences in NO or ACh/Ch release. However, we did observe significant sex differences in NO release. Although further GI studies and immunostaining need to be conducted, it appears that both nitrergic and cholinergic neuromuscular signaling are not altered in the APP/PS1 mouse model of AD. Serotonin may be a more promising candidate is examining neurogenic dysfunction in the gut in AD. Although cholinergic signaling dysfunction in AD is a

major hallmark of the disease, impaired serotonergic signaling is another prominent neurochemical feature observed in AD. For example, decreases in total brain serotonin content as well as substantial loss of serotonin receptors in the amygdala, neocortex and hippocampus in post-mortem AD patients has been reported[58-60] Moreover, selective serotonin reuptake inhibitors (SSRIs) have been shown to relieve behavioral and cognitive impairments in AD patients,[61] making the serotonergic system a possible therapeutic target. There is abundant evidence of the role of serotonin within the microbiota-gut-brain axis in the development of AD.[62,63] The ECs which line the digestive tract make up the bulk of the body's total serotonin content (90-95%) whereas the brain only makes up 5-10%.[62,64] Insight as to whether serotonin overflow in the gut is altered in the APP/PS1 mouse model would be beneficial to the further elucidation of the role of enteric dysfunction in AD.

REFERENCES

1. DeTure, M. A.; Dickson, D. W. The Neuropathological Diagnosis of Alzheimer's Disease. *Mol Neurodegener*. **2019,** *14*(1), 32.

2. Kowalski, K.; Mulak, A. Brain-Gut-Microbiota Axis in Alzheimer's Disease. *J Neurogastroenterol. Motil*. **2019**, *25*(1), 48-60.

3. Zhang, T.; Han, Y. R.; Wang, J. Y.; Hou, D.; Deng, H.; Deng, Y. L.; Song, Z. Comparative Epidemiological Investigation of Alzheimer's Disease and Colorectal Cancer: The Possible Role of Gastrointestinal Conditions in the Pathogenesis Of AD. *Front. Aging Neurosci*. **2018**, *10*, 176.

4. Chen, C. L.; Liang, T. M.; Chen, H. H.; Lee, Y. Y.; Chuang, Y. C.; Chen, N. C. Constipation and its Associated Factors Among Patients With Dementia. *Int. J. Environ. Res. Public Health*. **2020**, *17*(23), 9006.

5. Hill, J. M.; Bhattacharjee, S.; Pogue, A. I.; Lukiw, W. J. The Gastrointestinal Tract Microbiome and Potential Link to Alzheimer's Disease. *Front. Neurol*. **2014**, *5*, 43.

6. Jiang, C.; Li, G.; Huang, P.; Liu, Z.; Zhao, B. The Gut Microbiota and Alzheimer's Disease. *J. Alzheimers Dis*. **2017**, *58*(1), 1-15.

7. Chen, C.; Ahn, E. H.; Kang, S. S.; Liu, X.; Alam, A.; Ye, K. Gut Dysbiosis Contributes to Amyloid Pathology, Associated With C/Ebpβ/AEP Signaling Activation in Alzheimer's Disease Mouse Model. *Sci. Adv*. **2020**, *6*(31), eaba0466.

8. Rao, M.; Gershon, M. D. The Bowel And Beyond: The Enteric Nervous System in Neurological Disorders. *Nat. Rev. Gastroenterol. Hepatol*. **2016**, *13*, 517-528.

9. Braak, H.; de Vos, R. A.; Bohl, J.; Del Tredici, K. Gastric Alpha-Synuclein Immunoreactive Inclusions in Meissner's and Auerbach's Plexuses in Cases Staged for Parkinson's Disease-Related Brain Pathology. *Neurosci. Lett*. **2006**, *396*(1), 67-72.

10. Kim, S.; Kwon, S. H.; Kam, T. I.; Panicker, N.; Karuppagounder, S. S.; Lee, S.; Lee, J. H.; Kim, W. R.; Kook, M.; Foss, C. A.; Shen, C.; Lee, H.; Kulkarni, S.; Pasricha, P. J.; Lee, G.; Pomper, M. G.; Dawson, V. L.; Dawson, T. M.; Ko, H. S. Transneuronal Propagation of Pathologic Alpha-Synuclein from the Gut to the Brain Models Parkinson's Disease. *Neuron* **2019**, *103*(4), 627-641.

11. Klingelhoefer, L.; Reichmann, H. Pathogenesis of Parkinson disease—The Gut–Brain Axis and Environmental Factors. *Nat. Rev. Neurol*. **2015**, *11*(11), 625-636.

12. Schliebs, R. Basal Forebrain Cholinergic Dysfunction in Alzheimer's Disease--Interrelationship with Beta-Amyloid, Inflammation and Neurotrophin Signaling. *Neurochem. Res*. **2005**, *30*(6-7), 895-908.

13. Wang, J.; Gu, B. J.; Masters, C. L.; Wang, Y. J. A Systemic View of Alzheimer Disease -

Insights from Amyloid-Beta Metabolism Beyond the Brain. *Nat. Rev. Neurol*. **2017**, *13*(10), 612-623.

14. Joachim, C. L.; Mori, H.; Selkoe, D. J. Amyloid Beta-Protein Deposition in Tissues Other Than Brain in Alzheimer's Disease. *Nature* **1989**, *341*, 226-230.

15. Puig, K. L.; Lutz, B. M.; Urquhart, S. A.; Rebel, A. A.; Zhou, X.; Manocha, G. D.; Sens, M.; Tuteja, A. K.; Foster, N. L.; Combs, C. K. Overexpression of Mutant Amyloid-Beta Protein Precursor and Presenilin 1 Modulates Enteric Nervous System. *J. Alzheimers Dis*. **2015**, *44*(4), 1263-1278.

16. Arai, H.; Lee, V. M.; Messinger, M. L.; Greenberg, B. D.; Lowery, D. E.; Trojanowski, J. Q. Expression Patterns of Beta-Amyloid Precursor Protein (Beta-APP) in Neural and Nonneural Human Tissues from Alzheimer's Disease and Control Subjects. *Ann. Neurol*. **1991**, *30*(5), 686-693.

17. Shankle, W. R.; Landing, B. H.; Ang, S. M.; Chui, H.; Villarreal-Engelhardt, G.; Zarow, C. Studies of the Enteric Nervous System in Alzheimer Disease and Other Dementias of the Elderly: Enteric Neurons in Alzheimer Disease. *Mod. Pathol*. **1993**, *6*(1), 10-14.

18. den Braber-Ymker, M.; Heijker, S.; Lammens, M.; Croockewit, S.; Nagtegaal, I. D. Intestinal Involvement in Amyloidosis is a Sequential Process. *Neurogastroenterol. Motil*. **2018**, *30*(12), e13469.

19. Furness, J. B.; Callaghan, B. P.; Rivera, L. R.; Cho, H. J. The Enteric Nervous System and Gastrointestinal Innervation: Integrated Local and Central Control. *Adv. Exp. Med. Biol*. **2014**, *817*, 39-71.

20. Pellegrini, C.; Daniele, S.; Antonioli, L.; Benvenuti, L.; D'Antongiovanni, V.; Piccarducci, R.; Pietrobono, D.; Citi, V.; Piragine, E.; Flori, L.; Ippolito, C.; Segnani, C.; Palazon-Riquelme, P.; Lopez-Castejon, G.; Martelli, A.; Colucci, R.; Bernardini, N.; Trincavelli, M. L.; Calderone, V.; Martini, C.; Blandizzi, C.; Fornai, M. Prodromal Intestinal Events in Alzheimer's Disease (AD): Colonic Dysmotility and Inflammation Are Associated with Enteric AD-Related Protein Deposition. *Int. J. Mol. Sci.* **2020**, *21*(10), 3523.

21. Sun, Y.; Sommerville, N. R.; Liu, J. Y. H.; Ngan, M. P.; Poon, D.; Ponomarev, E. D.; Lu, Z.; Kung, J. S. C.; Rudd, J. A. Intra-Gastrointestinal Amyloid-β1–42 Oligomers Perturb Enteric Function and Induce Alzheimer's Disease Pathology. *J. Physiol*. **2020**, *598*(19), 4209-4223.

22. Stoye, N. M.; dos Santos Guilherme, M.; Endres, K. Alzheimer's Disease in the Gut—Major Changes in the Gut of 5xFAD Model Mice with ApoA1 as Potential Key Player. *FASEB J.* **2020**, *34*(9), 11883-11899.

23. Semara, S.; Klotza, M.; Letiembreb, M.; Ginneken, C. V.; Braun, A.; Jost, V.; Bischof, M.; Lammers, W. J.; Liu, Y.; Fassbender, K.; Wyss-Coray, T.; Kirchhoff, F.; Schäfer, K. Changes of the Enteric Nervous System in Amyloid-B Protein Precursor Transgenic Mice Correlate With Disease Progression. *J. Alzheimers Dis*. **2013**, *36*(1), 7-20.

24. Han, X.; Tang, S.; Dong, L.; Song, L.; Dong, Y.; Wang, Y.; Du, Y. Loss of Nitrergic and Cholinergic Neurons in the Enterc Nervous System of APP/PS1 Transgenic Mouse Model. *Neurosci. Lett*. **2017**, *646*, 59-65.

25. Oakley, H.; Cole, S. L.; Logan, S.; Maus, E.; Shao, P.; Crat, J.; Guillozet-Bongaarts, A.; Ohno, M.; Disterhoft, J.; Van Eldik, L.; Berry, R.; Vassar, R. Intraneuronal β-Amyloid Aggregates, Neurodegeneration, and Neuron Loss in Transgenic Mice with Five Familial Alzheimer's Disease Mutations: Potential Factors in Amyloid Plaque Formation. *J. Neurosci*. **2006**, *26*(40), 10129-10140.

26. Ohno, M,; Chang, L.; Tseng, W.; Oakley, H.; Citron, M.; Klein, W. L.; Vassar, R.; Disterhoft, J. F. Temporal Memory Deficits in Alzheimer's Mouse Models: Rescue by Genetic Deletion of BACE1. *Eur. J. Neurosci*. **2006**, *23*(1), 251-260.

27. Nguyen, V. T. T.; Brücker, L.; Volz, A. K.; Baumgärtner, J. C.; dos Santos Guilherme, M.; Valeri, F.; May-Simera, H.; Endres, K. Primary Cilia Structure Is Prolonged in Enteric Neurons of 5xFAD Alzheimer's Disease Model Mice. *Int. J. Mol. Sci*. **2021**, *22*(24), 13564.

28. Valeri, F.; Dos Santos Guilherme, M.; He, F.; Stoye, N. M.; Schwiertz, A.; Endres, K. Impact of the Age of Cecal Material Transfer Donors on Alzheimer's Disease Pathology in 5xFAD Mice. *Microorganisms* **2021**, *9*(12), 2548.

29. Jankowsky, J. L.; Fadale, D. J.; Anderson, J.; Xu, G. M.; Gonzales, V.; Jenkins, N. A.; Copeland, N. G.; Lee, M. K.; Younkin, L. H.; Wagner, S. L.; Younkin, S. G.; Borchelt, D. R. Mutant Presenilins Specifically Elevate the Levels of the 42 Residue Beta-Amyloid Peptide *In Vivo*: Evidence for Augmentation of a 42-Specific Gamma Secretase. *Hum. Mol. Genet*. **2004**, *13*(2), 159-170.

30. Garcia-Alloza, M.; Robbins, E. M.; Zhang-Nunes, S. X.; Purcell, S. M.; Betensky, R. A.; Raju, S.; Prada, C.; Greenberg, S. M.; Bacskai, B. J.; Frosch, M. P. Characterization of Amyloid Deposition in the APPswe/PS1dE9 Mouse Model of Alzheimer Disease. *Neurobiol. Dis*. **2006**, *24*(3), 516-524.

31. Jackson, R. J.; Rudinskiy, N.; Herrmann, A. G.; Croft, S.; Kim, J. M.; Petrova, V.; Ramos-Rodriguez, J. J.; Pitstick, R.; Wegmann, S.; Garcia-Alloza, M.; Carlson, G. A.; Hyman, B. T.; Spires-Jones, T. L. Human Tau Increases Amyloid β Plaque Size But Not Amyloid β-Mediated Synapse Loss in a Novel Mouse Model of Alzheimer's Disease. *Eur. J. Neurosci*. **2016**, *44*(12), 3056-3066.

32. Kilgore, M.; Miller, C. A.; Fass, D. M.; Hennig, K. M.; Haggarty, S. J.; Sweatt, J. D.; Rumbaugh, G. Inhibitors of Class 1 Histone Deacetylases Reverse Contextual Memory Deficits in a Mouse Model of Alzheimer's Disease. *Neuropsychopharmacology*. **2010**, *35*(4), 870-880.

33. Lalonde, R.; Kim, H. D.; Maxwell, J. A.; Fukuchi, K. Exploratory Activity and Spatial Learning in 12-Month-Old APP(695)SWE/co+PS1/DeltaE9 Mice with Amyloid Plaques. *Neurosci. Lett*. **2005**, *390*(2), 87-92.

34. Feng, J.; Dong, L.; Zhang, J.; Han, X.; Tang, S.; Song, L.; Cong, L.; Wang, X.; Wang, Y.; Du, Y. Unique Expression Pattern of KIBRA in the Enteric Nervous System of APP/PS1 Mice. *Neurosci. Lett.* **2018**, *675*(14), 41-47.

35. Manocha, G. D.; Floden, A. M.; Miller, N. M.; Smith, A. J.; Nagamoto-Combs, K.; Saito, T.; Saido, T. C.; Combs, C. K. Temporal Progression of Alzheimer's Disease in Brains and Intestines of Transgenic Mice. *Neurobiol. Aging* **2019**, *81*, 166-176.

36. Chen, Y.; Fang, L.; Zhou, H.; Fan, Y.; Lin, L.; Li, J.; Xu, J.; Chen, Y.; Ma, Y.; Chen, Y. Gut Microbiome Alterations Precede Cerebral Amyloidosis and Microglial Pathology in a Mouse Model of Alzheimer's Disease. *Biomed Res. Int.* **2020**, *2020*, 8456596.

37. Chishti, M. A.; Yang, D. S.; Janus, C.; Phinney, A. L.; Horne, P.; Pearson, J.; Strome, R.; Zuker, N.; Loukides, J.; French, J.; Turner, S.; Lozza, G.; Grilli, M.; Kunicki, S.; Morissette, C.; Paquette, J.; Gervais, F.; Bergeron, C.; Fraser, P. E.; Carlson, G. A.; George-Hyslop, P. S.; Westaway, D. Early-Onset Amyloid Deposition and Cognitive Deficits in Transgenic Mice Expressing a Double Mutant Form of Amyloid Precursor Protein *695*. *J. Biol. Chem.* **2001**, *276*(24), 21562-21570.

38. Van Vickle, G. D.; Esh, C. L.; Kalback, W. M.; Patton, R. L.; Luehrs, D. C.; Kokjohn, T. A.; Fifield, F. G.; Fraser, P. E.; Westaway, D.; McLaurin, J.; Lopez, J.; Brune, D.; Newel, A. J.; Poston, M.; Beach, T. G.; Roher, A. E. TgCRND8 Amyloid Precursor Protein Transgenic Mice Exhibit An Altered Gamma-Secretase Processing And An Aggressive, Additive Amyloid Pathology Subject To Immunotherapeutic Modulation. *Biochemistry* **2007**, *46*(36), 10317-10327.

39. Jankowsky, J. L.; Slunt, H. H.; Ratovitski, T.; Jenkins, N. A.; Copeland, N. G.; Borchelt, D. R. Co-Expression of Multiple Transgenes in Mouse CNS: A Comparison of Strategies. *Biomol. Eng.* **2001**, *17*(6), 57-165.

40. Maskri, L.; Zhu, X.; Fritzen, S.; Kühn, K.; Ullmer, C.; Engels, P.; Andriske, M.; Stichel, C. C.; Lübbert, H. Influence of Different Promoters on the Expression Pattern of Mutated Human Alpha-Synuclein in Transgenic Mice. *Neurodegenerative Dis.* **2004**, *1*(6), 255-265.

41. Lake, J. I.; Heuckeroth, R. O. Enteric Nervous System Development: Migration, Differentiation, and Disease. *Am. J. Physiol. Gastrointest. Liver Physiol.* **2013**, *305*(1), G1-G24.

42. Rao, M.; Gershon, M. D. Enteric Nervous System Development: What Could Possibly Go Wrong? *Nat. Rev. Neurosci.* **2018**, *19*(9), 552-565.

43. Bornstein, J. C.; Costa, M.; Grider, J. R. Enteric Motor and Interneuronal Circuits Controlling Motility. *Neurogastroenterol. Motil.* **2004**, *16*(s1), 34-38.

44. Gallego, D.; Mañé, N.; Gil, V.; Martínez-Cutilles, M.; Jiménez, M. Mechanisms Responsible for Neuromuscular Relaxation in the Gastrointestinal Tract. *Rev. Esp. Enferm. Dig.* **2016**, *108*(11), 721-731.

45. Bódi, N.; Szalai, Z.; Bagyánszki. Nitrergic Enteric Neurons in Health and Disease—Focus on Animal Models. *Int. J. Mol. Sci.* **2019**, *20*(8), 2003-2012.

46. Gonzalez, Z.; Loganathan, P.; Sarosiek, I.; McCallum, R. W.; Gender-Related Differences in Gastroparesis. *AJMS* **2020**, *360*(5), 474-483.

47. Camilleri, M. Diagnosis and Treatment of Irritable Bowel Syndrome. *JAMA* **2021**, *325*(9), 865-877.

48. Banibakhsh, A.; Sidhu, D.; Khan, S.; Haime, H.; Foster, P. A. Sex Steroid Metabolism and Action in Colon Health and Disease. *J. Steroid Biochem. Mol. Biol.* **2023**, *233*, 106371.

49. France, M.; Skorich, E.; Kadrofske, M.; Swain, G. M.; Galligan, J. J. Sex-Related Differences in Small Intestinal Transit and Serotonin Dynamics in High-Fat-Diet-Induced Obesity in Mice. *Exp. Physiol.* **2016**, *101*(1), 81-89.

50. Li, Y.; Xu, J.; Jiang, F; Jiang, Z.; Liu, C.; Li, L.; Luo, Y.; Lu, R.; Mu, Y.; Liu, Y.; Xue, B. G Protein-Coupled Estrogen Receptor is Involved in Modulating Colonic Motor Function Via Nitric Oxide Release in C57BL/6 Female Mice. *Neurogastroenterol. Motil*. **2015**, *28*(3), 432-442.

51. Ravella, K.; Hendy, Al-Hendy, A.; Sharan, C.; Hale, A.B.; Channon, K. M.; Srinivasan, S.; Gangula, P. R. Chronic Estrogen Deficiency Causes Gastroparesis by Altering Neuronal Nitric Oxide Synthase Function. *Dig. Dis. Sci*. **2013**, *58*(6), 1507-1515.

52. Kander, M. C.; Cui, Y.; Liu, Z. Gender Difference in Oxidative Stress: A New Look at the Mechanisms for Cardiovascular Diseases. *J. Cell. Mol. Med*. **2017**, *21*(5),1024-1032.

53. Nelson, J. F.; Felicio, L. S.; Randall, P. K.; Sims, C.; Finch, C. E. A Longitudinal Study of Estrous Cyclicity in Aging C57BL/6J Mice: I. Cycle Frequency, Length and Vaginal Cytology. *Biol. Reprod.* **1982**, *27*(2), 327-339.

54. Green, P. S.; Simpkins, J. W. Neuroprotective Effects of Estrogens: Potential Mechanisms of Action. *Int. J. Dev. Neurosci.* **2000**, *18*(4-5), 347-358.

55. Petrovska, S.; Dejanova, B.; Jurisic, V. Estrogens: Mechanisms of Neuroprotective Effect. *J. Physiol. Biochem.* **2012**, *68*, 455-460.

56. Ali, S. S.; Xiong, C.; Lucero, J.; Behrens, M.; Dugan, L. L.; Quick, K. L. Gender Differences in Free Radical Homeostasis During Aging: Shorter-Lived Female C57BL6 Mice Have Increased Oxidative Stress. *Aging Cell* **2006**, *5*(6), 565-574.

57. Beckman, J. S.; Koppenol, W. H. Nitric Oxide, Superoxide, and Peroxynitrite: The Good, the Bad, and the Ugly. *Am. J. Phys. Cell Phys.* **1996**, *271*(5), C1424-C1437.

58. Aral, H.; Kosaka, K.; Iizuka, R. Changes of biogenic amines and their metabolites in postmortem brains from patients with Alzheimer-type dementia. *J. Neurochem.* **1984**, *43*(2), 388-393.

59. Palmer, A. M.; Wilcock, G. K.; Esiri, M. M.; Francis, P. T.; Bowen, D. M. Monoaminergic Innervation of the Frontal and Temporal Lobes in Alzheimer's Disease. *Brain Res.* **1987**, *401*(2), 231-238.

60. Cross, A. J.; Crow, T. J.; Ferrier, I. N.; Johnson, J. A.; Bloom, S. R.; Corsellis, J. A. N. Serotonin Receptor Changes in Dementia of the Alzheimer Type. *J. Neurochem.* **1984**, *43*(6), 1574-1581.

61. Rodríguez, J. J.; Noristani, H. N.; Verkhratsky, A. The Serotonergic System in Aging and Alzheimer's Disease. *Prog. Neurobiol.* **2012**, *99*(1), 15-41.

62. Aaldijk, E.; Vermeiren, Y. The Role of Serotonin Within the Microbiota-Gut-Brain Axis in the Development of Alzheimer's Disease: A Narrative Review. *Aging Res. Rev.* **2022**, *75*, 101556.

63. Cutuli, D.; Giacovazzo, G.; Decandia, D.; Coccurello, R. Alzheimer's Disease and Depression in the Elderly: A Trajectory Linking Gut Microbiota and Serotonin Signaling. *Front. Psychiatry* **2022**, *13*, 1010169.

64. Gershon, M. D. 5-Hydroxytryptamine (Serotonin) in the Gastrointestinal Tract. *Curr. Opin. Endocrinol. Diabetes Obes.* **2013**, *20*(1), 14-21.

CHAPTER 7. OPTOGENTIC ANALYSIS OF NITRIC OXIDE RELEASE FROM NOS-CHR2-YFP TRANSGENIC MICE

7.1 Introduction

A major obstacle with studying the neural circuitry in the enteric nervous system (ENS) is the inability to target subpopulations of neurons. Traditional studies such as those using electrophysiological or imaging techniques can be quite rudimentary due to the heterogeneity of neuronal populations in the gut and could benefit from a more selective approach. Optogenetics is a neuromodulation technique that utilizes light to manipulate neuronal activity by genetically implanting light-sensitive ion channels into cells of interest. This method is particularly advantageous in neuroanalytical studies because it allows one to selectively probe the activity of specific neuron types within complex neural circuits.[1] Channelrhodopsin-2 (ChR2) is a naturally occurring light-gated cation channel that has been heavily utilized in neuroscience owed to its fast on/off kinetics of photo-induced cell depolarization.[1] ChR2 consists of a seven transmembrane helix protein with a covalently bound retinal chromophore.[2] In the ground state, this retinal chromophore exists in an all-trans state and then isomerizes to 13-*cis* retinal after absorbing blue light (470 nm).[3,4] This opens the ion channel enabling the influx of Na^+, K^+, and Ca^{2+} cations into the neuron. A schematic of this ion channel is given in Figure 7.1. By linking a neuron-specific promoter to the ChR2 gene, one can selectively activate this ion channel in specific neurons rather than activating all neurons and nerve fibers, as is done with electrical stimulation.

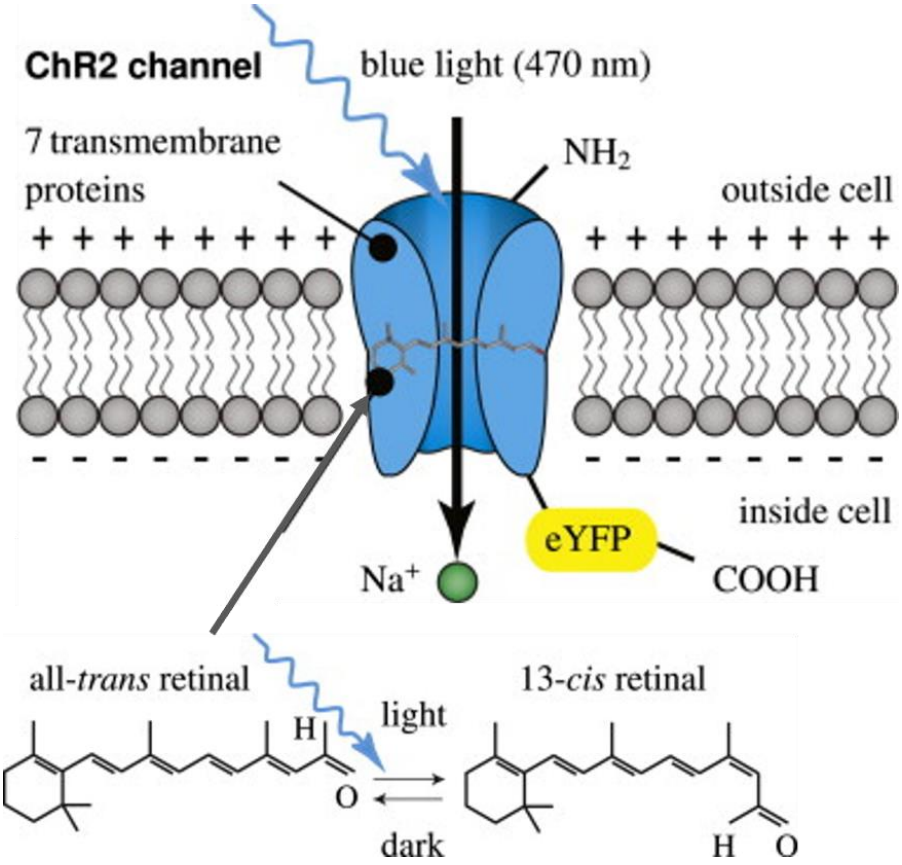

Figure 7.1. Schematic of the ChR2 cation channel. When blue light (470 nm) strikes the ion channel, the covalently bound retinal chromophore isomerizes to 13-cis retinal, consequently opening the ion channel and allowing for an influx of cations. Reproduced from Ref[4] with permission from Elsevier.

To conduct studies utilizing optogenetics, cells of interest must be genetically modified to express light-sensitive opsins by linking a neuron-specific promoter to the ChR2 gene.[5] ChR2 regulates membrane potential and must be highly expressed on the cell membrane of excitable cells due to its low single-channel conductance.[5] This can be achieved by delivering high copy numbers of transgene to cells through viral vector injection into the host animal, or conversely transgenic animals can be bred together.[1,5] In this first approach using a single transgenic animal line, a defined promoter that is active in specific cell types, such as choline acetyl transferase (ChAT) or nitric oxide synthase (NOS), is directly assembled with the transgene of interest (ChR2) and this DNA cassette is incorporated into the animal through pronuclear injection.[5] Alternatively, "gene

trapping," transgenic vectors based on bacterial artificial chromosomes (BACs), site specific transgenesis, or the knock-in approach can also be used.[5] A description of these approaches can be read from Figure 7.2.

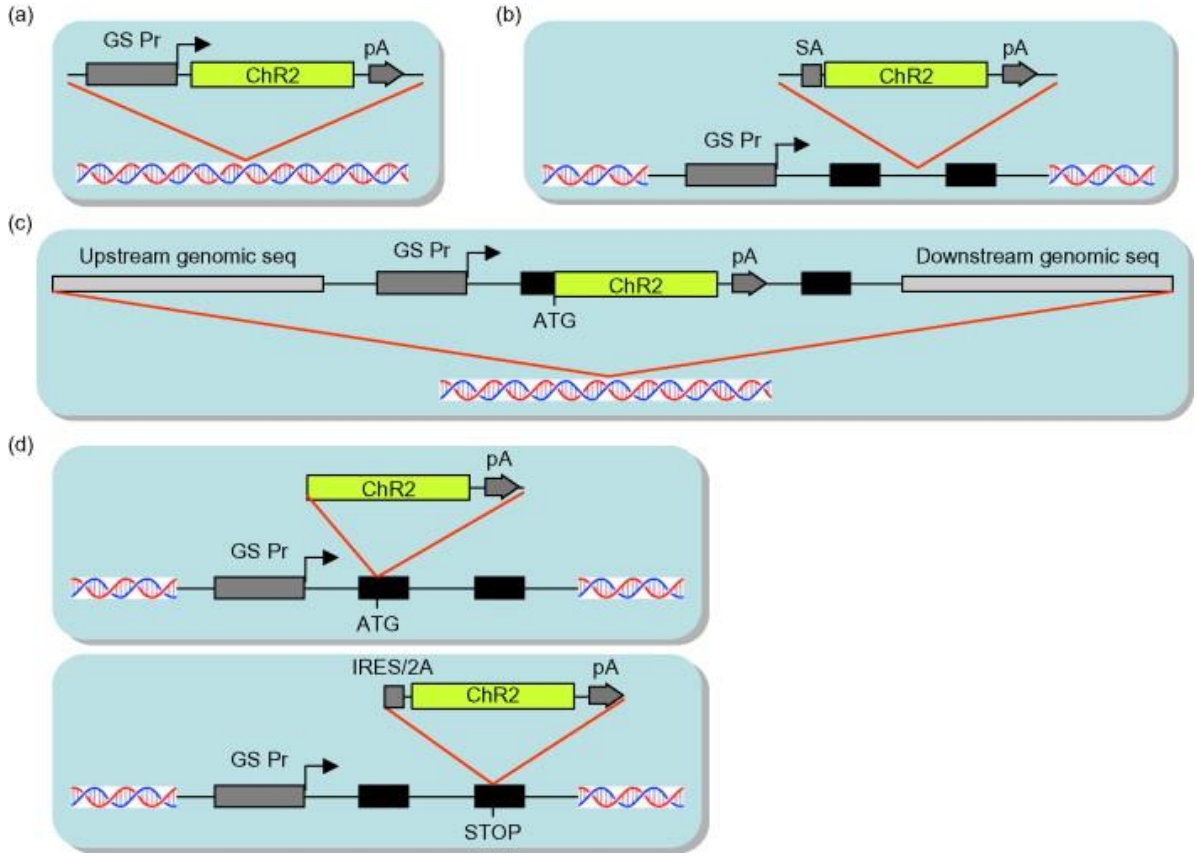

Figure 7.2. Summary of the single transgenic approaches for expressing ChR2. (a) An expression cassette containing a gene-specific promoter (GS Pr) and polyadenylation (pA) sequence is integrated into the genome. Polyadenylation occurs when a pA tail is added to an RNA transcript, which is part of a process that is necessary for mature messenger RNA formation for translation. (b) A "gene trap" approach is used in which the ChR2 transgene expression is determined by a "trapped" nearby endogenous promoter, and a DNA cassette containing this promoterless transgene, an RNA splice acceptor site (SA), and a pA sequence are randomly integrated into the genome. (c) Transgenic vectors based on BACs in which the ChR2 transgene is inserted into the ATG translation start site of the endogenous gene in a BAC clone, and this clone is then randomly integrated into the genome. The upstream and downstream genomic sequences of the BAC flank the specific promoter-linked transgene, which helps increase the probability of cell type-specific transgene expression. (d) A knock-in approach is used in which the transgene is inserted into either the target gene's ATG start codon for direct expression or at the STOP codon using an IRES or 2A sequence to place the transgene at the 3′end of the endogenous gene. This approach targets the transgene to the desired gene by homologous recombination. Reproduced from Ref[5] with permission from Elsevier.

Alternatively, the more flexible and customizable binary approach can be used for transgene expression in which two separate mouse lines are bred: the driver line and the reporter line. The driver line is generated using one of the aforementioned single transgenic approaches and expresses a master control "driver" gene from a desired gene-specific promoter while the reporter line carries the desired transgene in a cassette, the expression of which is controlled by the driver gene.[5] More commonly, the driver gene is a site-specific recombinase, such as the Cre protein, although transcriptional activators can also be used as the driver.[5] The Cre protein mediates recombination between two loxP sites within DNA of the reporter gene, which results in the deletion of the STOP cassette located between the promoter and transgene, leading to activation of transgene expression.[5] The most commonly utilized locus for generating the Cre-dependent reporter line is the *Gt(ROSA)26Sor* (*Rosa26*) locus.[5] A schematic summarizing this approach can be seen in Figure 7.3.

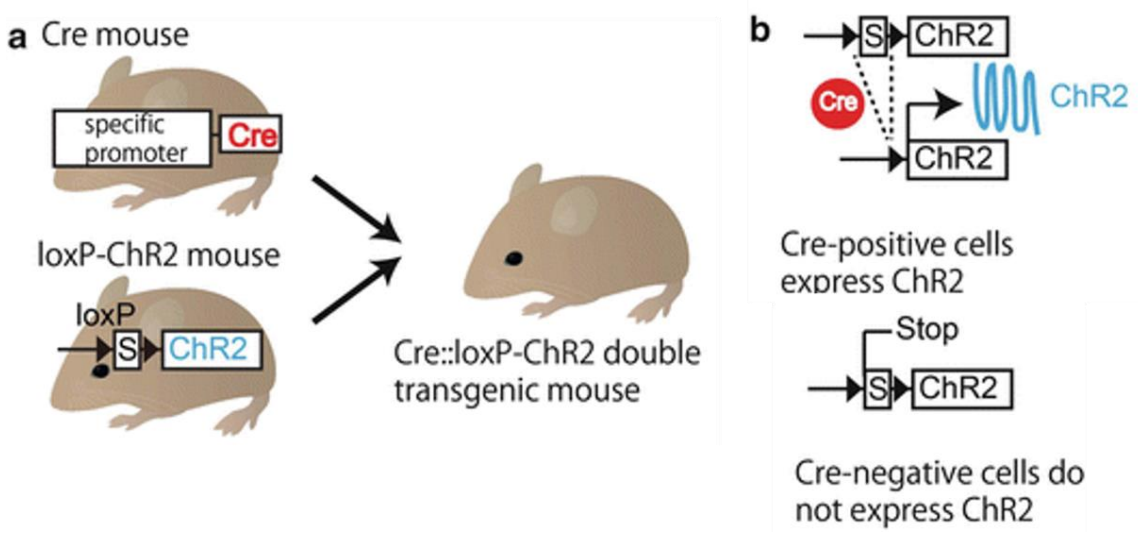

Figure 7.3. Summary of the Cre-loxP system. (a) Driver mice which express Cre recombinase under control of a site-specific promoter are bred with reporter mice which carry a ubiquitous promoter-loxP-STOP-loxP-ChR2 cassette, producing a double transgenic mouse. (b) This results in the deletion of the STOP cassette located between the promoter and transgene, leading to ChR2 expression under a ubiquitous promoter only in Cre recombinant enzyme-expressing cells while cells that do not express Cre recombinase do not express ChR2. Reproduced from Ref[6] with permission from Springer Nature.

One issue with using Cre driver lines is that the promoters utilized are rarely limited to a single population of cells and can be active in several regions with similar or sometimes different types of cells.[5] To overcome this, there are strategies that can be implemented. For example, a cell type-specific promoter can be used rather than a ubiquitous promoter, two different drivers that are expressed in overlapping cell populations can create a "double reporter" line with dual STOP cassettes, or alternatively a single driver can be delivered virally in a region-specific manner to prevent ubiquitous expression of the transgene.[5]

There has been work done in our group examining optogenetic control of excitatory and inhibitory motor function using electrophysiology,[7] although there has been no work utilizing electrochemical detection alongside blue light stimulation (BLS). By measuring nitric oxide (NO) release from NOS containing neurons using optogenetic stimulation, we can paint a more complete picture of the neurocircuitry that controls inhibitory motor function in the ENS. Additionally, if able to measure both ATP and NO release from NOS containing neurons using electrochemical sensors, this could provide direct evidence of a single or multiple populations of inhibitory motor neurons that release NO and a purine.

For this work, the Cre/lox recombinase system was used to express ChR2-eYFP in NOS containing neurons by cross breeding homozygous female B6;129S-Gt(ROSA)$^{26Sortm32(CAG-COP4*H134R/EYFP)Hze}$/J mice (ROSA) (Jackson Laboratories; Stock No: 012569) with homozygous male B6.129-NOS1$^{tm1(cre)Mgmj}$/J mice (Nos1^{cre}), which express Cre-recombinase in the neuronal nitric oxide synthase (nNOS) locus (Jackson Laboratory Stock no. 017526). The resulting offspring have the STOP cassette deleted in the Cre-expressing tissue and consequently express the ChR2(H134R)-EYFP fusion protein (which is immunoreactive by eYFP fluorescence) in NOS containing neurons. Excitable cells can then be activated using short pulses of blue light (470 nm)

and NO release can be measured using continuous amperometry (CA) and electrochemical detection with sensors sensitive and selective for NO oxidation.

7.2 Results

BLS parameters were selected based on similar electrophysiological studies performed in the GI tract previously by our group. In these studies, intracellular microelectrodes were used to impale circular muscle smooth muscle cells, and membrane potential changes following electrical or BLS were recorded from mice expressing ChR2/eYFP in cholinergic neurons. After stimulation, there is a sudden influx of cations or anions depending on which receptors on the smooth muscle cell are activated. If the membrane potential becomes more positive (increasing the probability of action potential generation), an excitatory junction potential (EJP) is generated. EJPs are associated with the activation of excitatory motor neurons and smooth muscle contraction. If the membrane potential becomes more negative (decreases the probability of action potential generation), an inhibitory junction potential (IJP) is generated. IJPs are associated with the activation of inhibitory motor neurons and smooth muscle relaxation. In these experiments, increasing the light pulse duration from 1 to 10 ms resulted in a dramatic increase in peak amplitude of IJPs recorded from circular muscle cells in the distal colon while a significant increase in IJP area under the curve (AUC) of the potential *vs.* time curves was only found from 1 to 5 ms pulse duration.[7] A pulse duration of 20 ms was found to produce a maximum amplitude IJP response with a plateaued AUC, therefore 20 ms was used for further studies as well as our work.[7]

For our studies, we utilized Nafion/Pt/BDD microelectrodes used in prior work to detect electrically stimulated NO release from mouse myenteric ganglia *in vitro* to detect NO release from $NOS1^{cre}$/ROSA mice, which express ChR2/enhanced yellow fluorescence protein (eYFP) in nitrergic neurons. We used BLS alongside electrical stimulation to measure NO release from (i)

nerves of the mouse colon circular muscle and (ii) ganglia in the myenteric plexus with nerve fibers that project to the longitudinal muscle layer to directly compare electrical vs. BLS within the same tissue preparations. We used a similar experimental set up as used in previous experiments, including the fabrication of the Nafion/Pt/BDD microelectrodes. This is described in extensive detail in Chapter 4. The exception was the placement of the blue light LED. A picture of the setup used for these experiments can be seen in Figure 7.4. The LED was positioned such that a concentrated field of blue light was focused where the Nafion/Pt/BDD microelectrode contacted the tissue. We found that the closer the LED is positioned to the tissue preparation, the greater the current response when stimulating with short pulses of blue light. However, if the LED was positioned too closely, a large stimulation artifact was observed. By positioning the LED approximately 100 μm above the tissue, an optimal current response was achieved with a minimal stimulation artifact. To prevent accidental photobleaching of the ion channel, an opaque black trash bag was placed over the experimental setup to block outside light. For most experiments, circular muscle tissue preparations from ~1 cm segments of the colon were used in which the circular muscle layer was exposed by peeling the mucosa and submucosa gut layers and pinning the preparation flat in a Sylgard-lined recording chamber. In some experiments, after removing the mucosa and submucosa, the tissue preparation was flipped and small strips of serosa were peeled off, which also removed longitudinal muscle. Then using a low-power microscope with a fluorescence attachment, ganglia in the myenteric nerve plexus were visualized using a YFP filter to determine where to position the Nafion/Pt/BDD recording microelectrode.

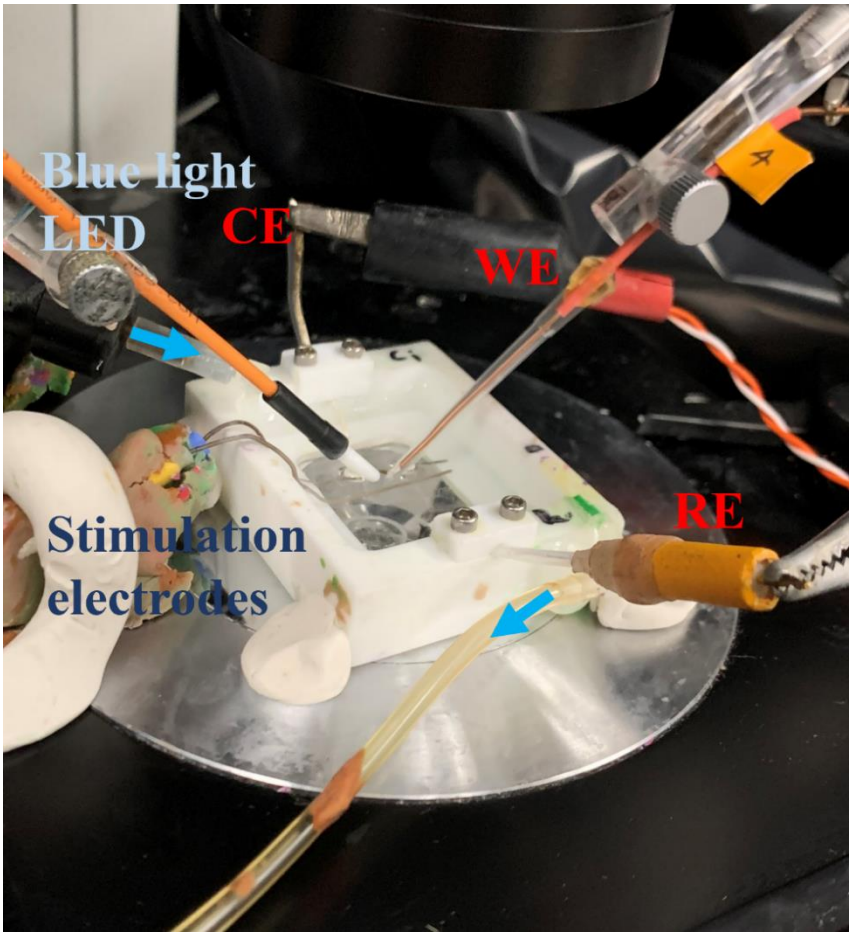

Figure 7.4. Experimental setup for *in vitro* electrochemical measurements using electrical and BLS. A window of circular muscle from mouse colon was pinned to the bottom of a Sylgard-lined recording chamber while oxygenated Krebs buffer pH 7.4 containing 1 µmol L^{-1} scopolamine and 1 µmol L^{-1} nifedipine to block spontaneous muscle contractions was perfused over the prep (marked by blue arrows) at 4 mL min^{-1} at 36-37°C. The Pt wire counter electrode (CE) and Ag/AgCl reference electrode (RE) were secured opposite of one another in the recording chamber and the Nafion/Pt/BDD working electrode (WE) was carefully lowered following a 30 min equilibrium period to gently touch a region of the tissue near a myenteric ganglion using a micromanipulator and low-power microscope. A pair of Ag/AgCl wires were placed on opposite ends of the tissue preparation, which were connected to an electrically isolated stimulator. The blue light LED was positioned at a 45° angle ~100 µm above the tissue preparation.

Figure 7.5 shows *i-t* traces from one *in vitro* CA experiment in which NO release was recorded in response to 1, 3, 5, and 7 pulses of electrical stimulation (black) and BLS (red) using a Nafion/Pt/BDD microelectrode polarized at 0.8 V vs Ag/AgCl. Short pulses of blue light (20 mW/mm^2, 10 Hz, 20 ms pulse duration) were delivered using an LED positioned ~100 µm from

the electrode tip. The responses were compared to an identical number of electrical stimuli delivered across two Ag/AgCl wires placed on opposing ends of the tissue preparation (80 V, 10 Hz, 0.5 ms pulse duration). Using one stimulus, almost no current response was observed for both electrical and BLS. At 3 pulses, a current response develops for both techniques, with a sharper profile for the electrical stimulation. A peak oxidation current is measured for both electrical and BLS at 5 pulses, but the oxidation current is much greater for the electrical stimulation. At 7 pulses, the current response starts to decrease and resembles that of 3 electrical and BLS pulses. This trend, in which a maximum current response is observed followed by a decrease in current with increasing pulse number, has been observed before in both our *in vitro* CA measurements[8] and electrophysiology studies using intracellular electrodes to measure membrane potential changes following electrical and BLS.[7] The decrease in current with the higher pulse number is likely linked to the depletion of intracellular Ca^{+2} with the higher pulse number, as NO is produced on demand when intracellular Ca^{+2} levels are elevated.

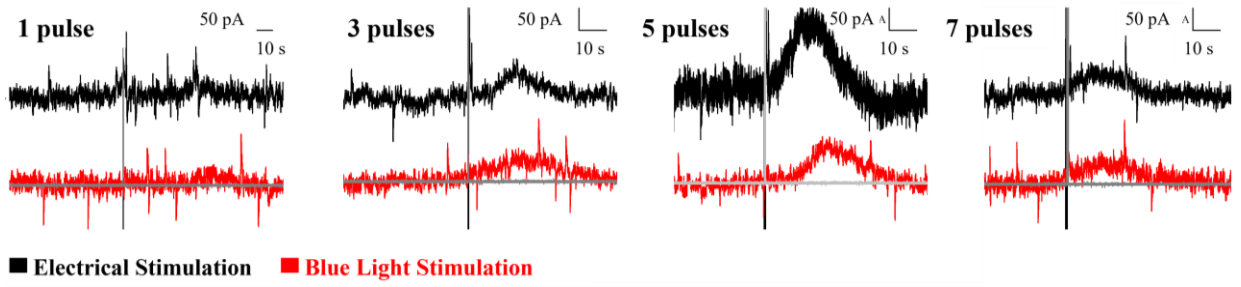

Figure 7.5. CA current-time (*i*–*t*) curves recording NO oxidation current using a Nafion/Pt/BDD microelectrode as a function of increasing number of electrical (black) or optical (red) stimuli delivered to a circular muscle preparation from the colon of a $NOS1^{cre}$/ROSA mouse. The grey trace serves as an event log and indicates the exact onset of the blue light stimuli. Electrical stimulation was performed at 80 V, 10 Hz, and 0.5 ms pulse duration. BLS was performed at 10 Hz with a 20 ms pulse duration. Detection of NO was performed at 0.8 V vs Ag/AgCl. The current was smoothed using a 10 Hz low pass filter.

NO measurements were also made from longitudinal muscle myenteric plexus (LMMP) preparations in addition to circular muscle preps. The myenteric nerve plexus is sandwiched

between the circular and longitudinal muscle layers of the gut wall. When detecting NO from the circular muscle, the tissue is thick, which prevents us from being able to clearly see myenteric ganglia using a low power microscope. However, if the tissue preparation is flipped over so that the longitudinal muscle faces upward and the longitudinal muscle cell layer is carefully peeled away, myenteric ganglia can easily be visualized making electrode placement easier. We prepared LMMP tissue preparations and visualized the myenteric ganglia using a low power microscope with a fluorescence attachment and YFP filter to see where ChR2 was being expressed and used that information to contact the electrode to a region of the tissue rich with ChR2/YFP expression. Figure 7.6 shows sample continuous amperometric *i-t* curves recorded from a LMMP preparation. The current response for 7 pulses of blue light can be seen in A, where the red bar marks the onset of the stimulus. The current response is low with the background current dipping far below baseline following the stimulation. To verify the source of the oxidation current, two pharmacological agents were used: tetrodotoxin (TTX) and L-nitro-N-arginine (L-NNA). TTX is a sodium channel blocker which prevents action potential propagation and L-NNA is a NOS antagonist which competes for L-arginine binding sites on NOS, preventing the on-demand synthesis and release of NO. Between drug applications, the chamber was rinsed with Krebs buffer and the stimulation was repeated to verify restoration of oxidation current. The current response was completely abolished in the presence of both TTX and L-NNA and the current response was restored following the rinse between drug application. This verifies that the current response, although unusual in profile, was the result of NO release and that NO release was neurogenic in origin. It was found that using both electrical and BLS produced identical current responses, both of which showed the same drop in baseline current following electrical or BLS. This data can be seen in panel B. To determine the cause of this drop in baseline current, the detection potential was lowered to 0.2 V vs Ag/AgCl and

the BLS was repeated. At 0.2 V, the potential is insufficiently positive to drive NO oxidation, but the electrode is still sensitive to ionic concentration changes. At 0.2 V we did not see an oxidation current spike, but we did observe a gradual decrease in current downstream of the BLS. This suggests that this drop in current is due to a local ionic concentration change in the extracellular fluid surrounding the microelectrode. As the current response from the LMMP preparations is much lower than the current response for NO oxidation observed from nerves of the circular muscle,[9] this local ionic concentration change obscures the current response, making it difficult to extrapolate peak current response and AUC of the oxidation peak.

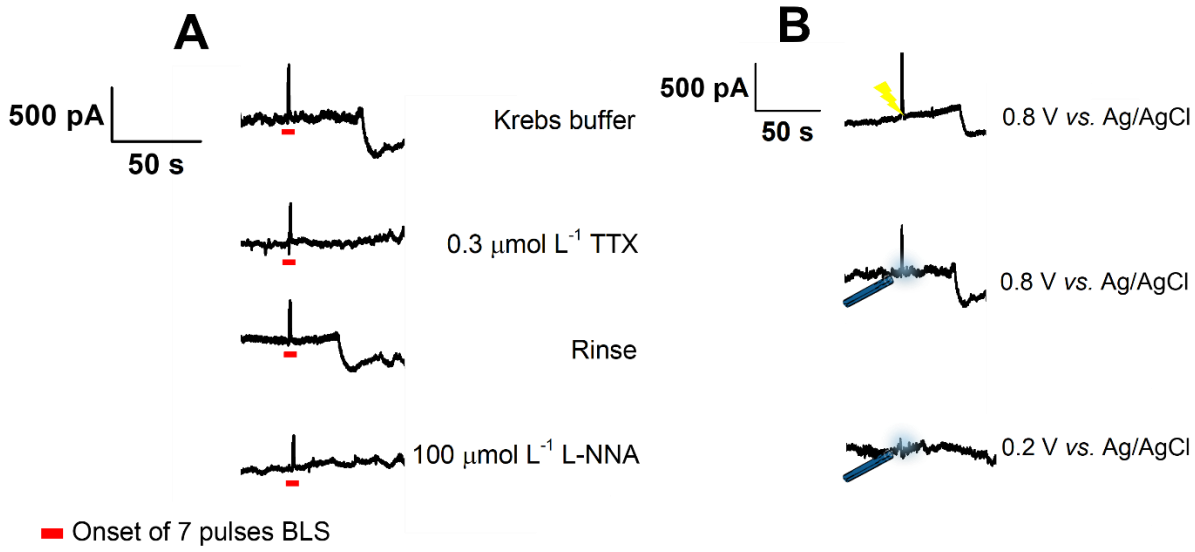

Figure 7.6. CA *i–t* curves recording NO oxidation current using a Nafion/Pt/BDD microelectrode following electrical or BLS delivered to a LMMP preparation from the colon of a NOS1^{cre}/ROSA mouse. The microelectrode was polarized at 0.8 V vs Ag/AgCl. (A) Oxidation current response following 7 pulses of blue light (indicated by red bar) in the presence and absence of the NOS inhibitor, 100 μmol L^{-1} L-NNA, and sodium channel blocker, 0.3 μmol L^{-1} TTX. A rinse with Krebs buffer was performed between drug applications to verify a restoration of current response. (B) Oxidation current responses following 7 pulses of electrical stimulation, 7 pulses of BLS, and 7 pulses of BLS after decreasing the detection potential to 0.2 V vs Ag/AgCl, a potential insufficient to drive NO oxidation. The *i–t* curves were passed through a 10 Hz low-pass filter for smoothing.

Most animals tested showed identical current responses for electrical and BLS. Figure 7.7 shows the results of two separate NOS1^{cre}/ROSA animals. The continuous amperometric *i-t* traces on the left show the current response to 1, 3, and 5 electrical and BLS pulses. There is an increase

in oxidation current with increasing pulse number as the concentration of extracellular NO increases. One can see that the peak current, AUC, rise slope, and fall slope are similar between the two stimulation techniques. That is, with exception of the BLS response at 5 pulses, which shows exceptional noise downstream of the stimulation that was caused from a bubble in the buffer line. The *i-t* traces on the right show an experiment using a separate animal in which the peak oxidation current at 5 pulses using electrical and BLS are overlaid with one another. For this experiment, the current responses are identical.

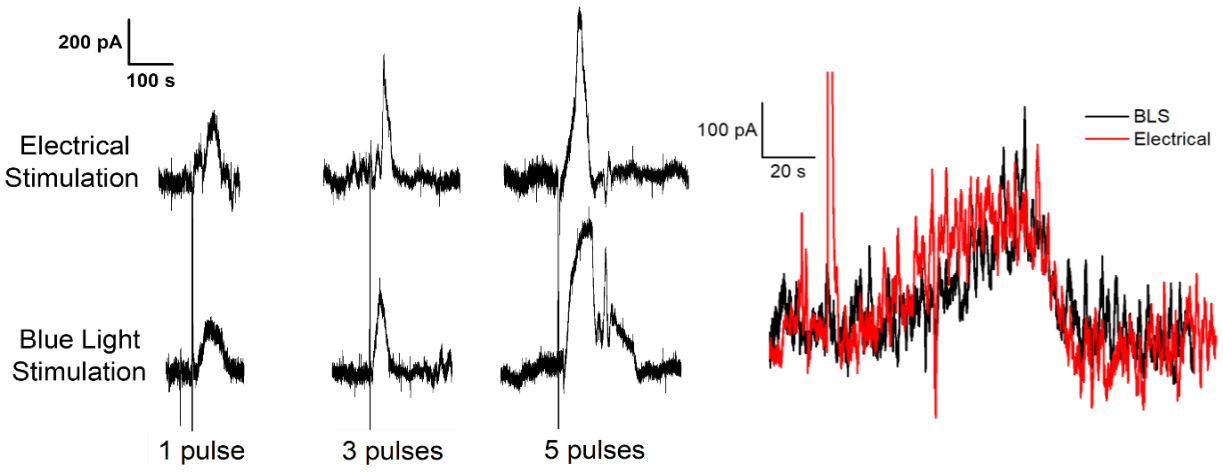

Figure 7.7. CA *i–t* curves recording NO oxidation current using a Nafion/Pt/BDD microelectrode as a function of increasing number of electrical (top left) or optical (bottom left) stimuli delivered to a circular muscle preparation from the colon of a NOS1^{cre}/ROSA mouse. A separate experiment using a different animal showing the overlaid electrical and BLS response to 5 pulses (right), showing an identical current response. Electrical stimulation was performed at 80 V, 10 Hz, and 0.5 ms pulse duration while BLS was performed at 10 Hz with a 20 ms pulse duration. Detection of NO was performed at 0.8 V vs Ag/AgCl. The current was smoothed using a 10 Hz low pass filter.

To determine if YFP/ChR2 was selectively expressed in nitrergic neurons, immunohistochemical labeling of NOS containing neurons and YFP was performed in the brain, colon, and small intestine of NOS1^{cre}/ROSA mice. These images can be seen in Figure 7.8. Staining was performed in the brain in addition to the ENS as the Nos1^{cre} driver line is expressed in all neuronal nitric oxide synthase (nNOS) expressing tissue, which includes discrete neuron

populations in the cerebellum, olfactory bulb, hippocampus, cortex, striatum, basal forebrain, and brain stem. Furthermore, the bulk of optogenetic studies using this driver line are performed in the brain where nNOS is expressed in several regions including the cerebral cortex, substantia nigra pars reticulata, and cerebellum.[10-13] Although there are few NOS^+ cells, there is no colocalization with the abundantly expressed YFP. A greater number of NOS^+ cells can be seen in the colon and small intestine. There is colocalization of YFP with NOS, however YFP seems to be expressed in all myenteric neurons rather than nitrergic neurons exclusively. This lack of selective expression is likely due to an error made during breeding. Somewhere along the breeding line, a heterozygous mouse for the Cre gene was mistaken for a homozygous mouse, resulting in severe ectopic expression. This explains why the bulk of measurements made showed identical current responses between electrical and BLS, as BLS was also stimulating all myenteric neurons and not nitrergic myenteric neurons exclusively.

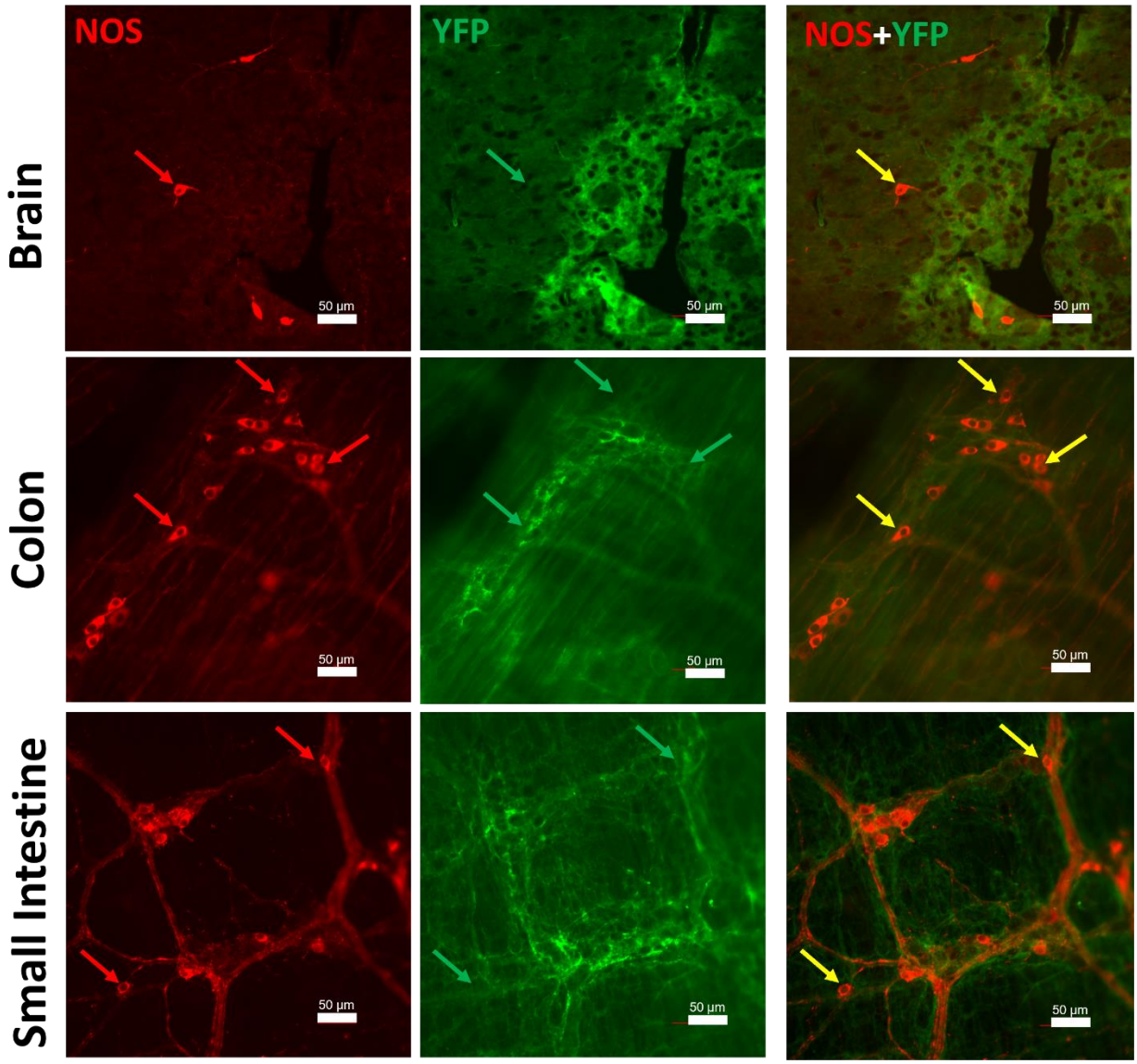

Figure 7.8. Immunohistochemical labeling of nitrergic neurons (left column) and YFP/ChR2 (middle column) in the brain, colon, and small intestine of NOS1^{cre}/ROSA mice using an antibody raised against NOS. The third column shows the merged image, which shows very little colocalization of YFP with NOS (shown as yellow). Select arrows mark the location of nitrergic neurons, which do not selectively express YFP. Images were collected by Dr. Hui Xu and Roxanne Fernandes from the Department of Pharmacology & Toxicology at MSU.

7.3 Discussion

Optogenetics combined with electrochemical detection is a powerful tool for the selective study of neural circuitry regulating peripheral and central nervous system function. This methodology has been frequently applied to the brain to study dopaminergic signaling. For

example, optically stimulated dopamine (DA) release has been measured from the nucleus accumbens in mice brain slice preparations using fast scan cyclic voltammetry (FSCV) and carbon fiber microelectrodes. This technique was especially advantageous, as the nucleus accumbens is highly heterogeneous, possessing afferent innervation from glutamatergic, serotonergic, dopaminergic, and GABAergic projections in addition to innervation from local GABAergic and cholinergic interneurons.[14] Not only are a multitude of different neurotransmitters released from this tissue (of which serotonin is electrochemically active), but several receptors, including but not limited to—metabotropic glutamate receptors, $GABA_B$ receptors, and nicotinic acetylcholine receptors—modulate terminal DA release.[14] DA release has also been measured from rat dorsal striatum *in vivo*[15] and mice striatal slices *ex vivo*[16] using carbon fiber microelectrodes and FSCV. In the gut, there has been extensive work by Spencer's group from Flinders University using optogenetics to control the ENS gastrointestinal motility,[1,17,18] however optogenetic tools have not been utilized alongside electrochemical detection in the gut.

Unfortunately, due to breeding errors and time constraints, we were unable to use the $NOS1^{cre}$/ROSA mice to their full potential in this dissertation project. The extensive degree of ectopic expression of ChR2 resulted in the bulk of myenteric neurons expressing the ion channel and consequently neuronal selectivity was lost. This explains why the electrical stimulation responses were identical to the BLS responses. There were a few cases where the BLS response was significantly lower in magnitude than the corresponding electrical stimulation response. As offspring from different breeding pairs were used, it is possible that some offspring showed the correct expression of ChR2 into NOS containing neurons. Regardless of if this is true or not, it is difficult to directly compare electrical stimulation and BLS. In a study recently performed by our group, electrical stimulation and BLS of ChR2/eYFP expressing cholinergic neurons were used to

elicit IJPs from colonic circular muscle. The authors utilized 1, 3, 5, and 7 stimulation pulses, and with exception of the single pulse, both the peak amplitude and AUC of the IJPs were significantly greater for electrical stimulation as compared to optogenetic stimulation.[7] This trend is expected for optogenetic neuronal selectivity. It is not uncommon to find significant differences between electrical stimulation and optogenetic stimulation.[14,16,19] However, these differences may be due to unmatched stimulation intensity between the methods rather than the difference in mode of action of the two techniques. One behavioral study attempted to mitigate those differences by matching self-stimulation rates between the two modalities. This was done by reducing the electrical stimulation currents to comparatively low values such that only the immediate surrounding area of the electrode was affected by the stimulation, much like it is in optical stimulation.[19] This study was performed in DAT::Cre and TH:Cre mice, two transgenic mouse lines commonly used in optogenetic studies of the central tegmental area.[19] Overall, the authors found no significant differences in stimulation-induced blood flow responses in the nucleus accumbens. However, differences became apparent in the frontal cortex and striatum, due to additional stimulation of glutamatergic neurons.[19] Overall, however, optical and electrical stimulation resulted in surprisingly very similar activity.[19] Therefore, if the cell population examined was overwhelmingly singular, one could expect identical responses between electrical and optogenetic stimulation.

It is worth noting that during some lengthier experiments conducted, the response to BLS gradually decayed with increasing number of stimuli and could not be restored like it could when electrical stimulation was being employed. In attempt to avoid this attenuated response, shorter experiments were conducted with limited use of the blue LED excitation. This is a phenomenon that has also been observed by other researchers when measuring DA release from mouse brain slices *ex vivo* using FSCV.[16] The authors observed a gradual rundown of evoked DA release with

repeated optical pulse-train stimulation at the same recording site.[16] This rundown was less-pronounced for single-pulse stimulations, and could also be mitigated by recording from a population of sites.[16] Although we cannot utilize multiple recording sites to directly compare electrical and optical stimulation, we can avoid long trains of stimuli and minimize the number of optical stimuli delivered during a single experiment. Besides using more caution in the future if ever regenerating these mouse lines, one could express ChR2 in specific regions of the gut by injecting a Cre inducible AAV9-EF1a-DIO-hChR2(H134R)-eYFP viral vector into homozygous $NOS1^{cre}$ mice. However, this technique requires a significant level of skill to precisely deliver the viral vector and a recovery period post-surgery.

7.4 Conclusions

It was demonstrated that optogenetics can be successfully used to optically stimulate NO release from myenteric neurons in the mouse colon. However, due to the high degree of ectopic expression observed in immunostaining and variability in YFP expression from animal to animal, this model proved unreliable for the selective study of NO release from nitrergic neurons. It is important to stress the importance of careful monitoring of the driver and reporter lines as the setup of improper breeding pairs can destroy an entire group of specifically bred mice. In summary, this preliminary work shows the promise of using a $NOS1^{cre}$/ROSA mouse model to selectively stimulate nitrergic neurons (or other specific types of neurons, e.g. cholinergic) in experiments that could provide new insights on neural circuitry regulating gastrointestinal motility.

REFERENCES

1. Spencer, N. J.; Hibberd, T.; Feng, J.; Hu, H. Optogenetic Control of the Enteric Nervous System and Gastrointestinal Transit. *Expert Rev. Gastroenterol. Hepatol.* **2019**, *13*(4), 281-284

2. Nagel, G.; Szellas, T.; Huhn, W.; Kateriya, S.; Adeishvili, N.; Berthold, P.; Ollig, D.; Hegemann, P.; Bamberg, E. Channelrhodopsin-2, a Directly Light-Gated Cation-Selective Membrane Channel. *Proc. Natl. Acad. Sci.* **2003**, *100*(24), 13940-13945.

3. Nagel, G.; Szellas, T.; Adesishvili, N.; Hegemann, P.; Bamberg, E. Channelrhodopsins: Directly Light-Gated Cation Channels. *Biochem. Soc. Trans*. **2005**, *33*(4), 863-866.

4. Abilez, O. J.; Wong, J.; Prakash, R.; Deisseroth, K.; Zarins, C. K.; Kuhl, E. Multiscale Computational Models for Optogenetic Control of Cardiac Function. *Biophys. J.* **2011**, *101*(6), 1326-1334.

5. Zeng, H.; Madisen, L. Mouse Transgenic Approaches in Optogenetics. *Prog. Brain Res.* **2012**, *196*, 193-213.

6. Tanaka, K.F. Optogenetics Research Using the Mouse as a Model System. In: *Optogenetics*; Springer, 2015; pp 227-237.

7. Perez-Medina, A. L.; Galligan, J. J. Optogenetic Analysis of Neuromuscular Transmission in the Colon of Chat-Chr2-YFP BAC Transgenic Mice. *Am. J. Physiol. Gastrointest. Liver Physiol.* **2019**, *317*(5), G569-G579.

8. Henderson, S.; Bhardwaj, K.; Perugachi, V.; Espinoza-Montero, P.; Galligan, J. J. *In Vitro* Monitoring of Nitric Oxide Release in the Mouse Colon Using a Boron-Doped Diamond Microelectrode Modified with Platinum Nanoparticles and Nafion. *Anal. Chem.* **2023**, *95*(2), 1027-1037.

9. Patel, B. A.; Galligan, J. J.; Swain, G. M.; Bian, X. Electrochemical Monitoring of Nitric Oxide Released by Myenteric Neurons of the Guinea Pig Ileum. *Neurogastroenterol. Motil*. **2008**, *20*(11), 1243-1250.

10. Gerashchenko, D.; Schmidt, M. A.; Zielinski, M. R.; Moore, M. E.; Wisor, J. P. Sleep State Dependence of Optogenetically evoked Responses in Neuronal Nitric Oxide Synthase-positive Cells of the Cerebral Cortex. *Neurosci*. **2018**, *379*(21), 189-201.

11. Chen, B.; Xu, C.; Wang, Y.; Lin, W.; Wang, Y.; Chen, L.; Cheng, H.; Xu, L.; Hu, T.; Zhao, J.; Dong, P.; Guo, Y.; Zhang, S.; Wang, S.; Zhou, Y.; Hu, W.; Duan, S.; Chen, Z. A Disinhibitory Nigra-Parafascicular Pathway Amplifies Seizure in Temporal Lobe Epilepsy. *Nat. Commun.* **2020**, *11*, 923.

12. Dubois, C. J.; Fawcett-Patel, J.; Katzman, P. A.; Liu, S. J. Inhibitory Neurotransmission Drives Endocannabinoid Degradation to Promote Memory Consolidation. *Nat. Commun*. **2020**, *11*, 6407.

13. Hai-Ying, L.; Chen, Z.; Xiao, H.; Lin, Y.; Hu, Y.; Chang, L.; Wu, H.; Wang, P.; Lu, W.; Zhu, D.; Luo, C. nNOS-Expressing Neurons in the vmPFC Transform pPvt-Derived Chronic Pain Signals into Anxiety Behaviors. *Nat. Commun.* **2020**, *11*, 2501.

14. Melchior, J. R.; Ferris, M. J.; Stuber, G. D.; Riddle, D. R.; Jones, S. R. Optogenetic Versus Electrical Stimulation of Dopamine Terminals In The Nucleus Accumbens Reveals Local Modulation of Presynaptic Release. *J. Neurochem.* **2015**, *134*(5), 833-844.

15. Bass, C. E.; Grinevich, V. P.; Vance, Z. B.; Sullivan, R. P.; Bonin, K. D.; Budygin, E. A. Optogenetic Control of Striatal Dopamine Release in Rats. *J. Neurochem*. **2010**, *114*(5), 1344-1352.

16. O'Neill, B.; Patel, J. C.; Rice, M. E. Characterization of Optically and Electrically Evoked Dopamine Release in Striatal Slices from Digenic Knock-in Mice with DAT-Driven Expression of Channelrhodopsin. *ACS Chem. Neurosci.* **2017**, *8*(2), 310-319.

17. Hibberd, T. J.; Feng, J.; Luo, J.; Yang, P.; Samineni, V. K.; Gereau IV, R. W.; Kelley, N.; Hu, H.; Spencer, N. J. Optogenetic Induction of Colonic Motility in Mice. *Gastroenterol.* **2018**, *155*(2), 514-528.

18. Spencer, N. J.; Travis, L.; Hibberd, T.; Kelly, N.; Feng, J.; Hu, H. Effects of Optogenetic activation of the Enteric Nervous System on Gastrointestinal Motility in Mouse Small Intestine. *Auton. Neurosci.* **2020**, *229*, 102733.

19. Weidner, T. C.; Vincenz, D.; Brocka, M.; Tegtmeier, J.; Oelschlegel, A. M.; Ohl, F. W.; Goldschmidt, J.; Lippert, M. T. Matching Stimulation Paradigms Resolve Apparent Differences Between Optogenetic and Electrical VTA Stimulation. *Brain Stimul.* **2020**, *13*(2), 363-371.

CHAPTER 8. CONCLUSIONS AND FUTURE WORK

The goal of this research was to develop and characterize electrochemical sensors and biosensors sensitive and selective for nitric oxide (NO), acetylcholine/choline (ACh/Ch), and ATP, and to apply those sensors *in vitro* to detect the real-time release of these signaling molecules from the mouse colon. The second aim was to apply these sensors in a transgenic mouse model of Alzheimer's disease (AD) to determine if nitrergic or cholinergic neuromuscular signaling is altered in AD in the gut. To electrochemically detect NO, we used a modified boron-doped diamond microelectrode prepared by platinizing a BDD microelectrode to reduce the working potential of NO oxidation, and coating that modified electrode with a thin film of Nafion to electrostatically repel negatively charged interferents such as the nitrite anion, an oxidative product produced during NO metabolism. Alternatively, because ACh is not electrochemically active, we utilized an enzyme-based sensor to measure ACh/Ch release from mouse myenteric ganglia, which relies on the enzymatic production of H_2O_2 to electrochemically detect ACh and Ch. These sensors were prepared by coating platinized-Pt microelectrodes with a thin film of poly(*m*-phenylenediamine), which acts as a permselective coating to restrict permeability of electroactive interferents, and depositing a multi-enzyme film onto those modified microelectrodes. The multi-enzyme film consisted of acetylcholinesterase (AChE), choline oxidase (ChOx), bovine serum albumin (BSA) to stabilize the enzymes, and glutaraldehyde, which acts as a cross-linking agent. The sensors respond with equal sensitivity to ACh and Ch, which is quickly formed following synaptic release into the extracellular space by action of AChE.

We directly detected NO and ACh/Ch release from colonic myenteric ganglia from a 5xFAD and APP/PS1 mouse model of AD. This was accomplished using transmural electrical stimulation and various pharmacological agents to validate the measured oxidation current

responses. As there is limited knowledge on the pathology of AD in the enteric nervous system (ENS), specifically whether the formation of Aβ plaques directly disrupts enteric neuron function, we addressed an important knowledge gap in AD research using a novel electrochemical and pharmacological approach. We could not detect Aβ accumulation in the 5xFAD mouse model nor any significant enteric dysfunction, suggesting that the 5xFAD mouse model is not suitable for studying myenteric amyloidosis. We were able to detect Aβ accumulation in the APP/PS1 mouse model, proving it to be a more suitable model for studying ENS dysfunction in AD. However, we did not detect any significant differences in amperometric NO or ACh/Ch release, though we did find significant sex differences in NO release. Although it is unclear as to the cause of this observed sex-difference, the formation of peroxynitrite, a potent oxidant produced in states of high oxidative stress, could be explored as a potential cause. Although further gastrointestinal (GI) studies and immunostaining need to be conducted, it appears that both nitrergic and cholinergic neuromuscular signaling are not altered in the APP/PS1 mouse model of AD. Future work on this front could benefit from electrochemical detection of serotonin overflow from enterochromaffin cells which line the digestive tract. We have used BDD microelectrodes in the past to measure this signaling molecule, and there is strong evidence that serotonergic signaling is altered in AD. It would be a worthwhile endeavor if alterations in serotonergic signaling could be detected and linked to GI dysfunction in AD.

Another aim of this research was to better understand the neural circuitry which regulates GI motility. We present some preliminary work using optogenetics to selectively stimulate nitrergic neurons and electrochemically measure NO release. Unfortunately, due to misgivings while generating the mice for these studies, we were unable to fully utilize this mouse model. If able to regenerate this mouse model such that selective expression of channelrhodopsin-2 is achieved in

nitrergic neurons with no ectopic expression, this work could be used to determine whether NO and ATP are co-released from the same neurons. Results from prior group work using optogenetics suggest that NO and ATP may be released from different classes of inhibitory motor neurons. It has always been assumed that NO and ATP are cotransmitters, i.e. neurotransmitters released from the same neurons, but there is no direct evidence that supports this. Although we were unable to successfully apply our ATP biosensors *in vitro*, if able to reduce the detection limit using an alternative enzyme immobilization strategy or even enzymatic detection scheme, these sensors could be applied alongside NO sensors in a $NOS1^{cre}$/ROSA mouse model and be used as direct evidence of cotransmission or alternatively the presence of two classes of inhibitory motor neurons. Furthermore, the selective detection of ATP *in vitro* from the mouse colon would provide insight as to whether ATP or another purine act as the primary purinergic neurotransmitter in the gut, a topic that has been heavily debated for some time.

In summary, the work presented here lays the foundation for further studies and demonstrates the utility of electrochemical sensors and biosensors in the periphery. These sensors could be applied in a variety of animal models to elucidate important information about the signaling mechanisms which mediate various physiological phenomena.